X-RAY PHASE CONTRAST IMAGING AT THE

MAINZ MICROTRON MAMI

Dissertation
zur Erlangung des Grades
"Doktor der Naturwissenschaften"
am Fachbereich Physik
der Johannes Gutenberg–Universität
Mainz

Vorgelegt von
Mahmoud El Ghazaly
geboren in Ägypten

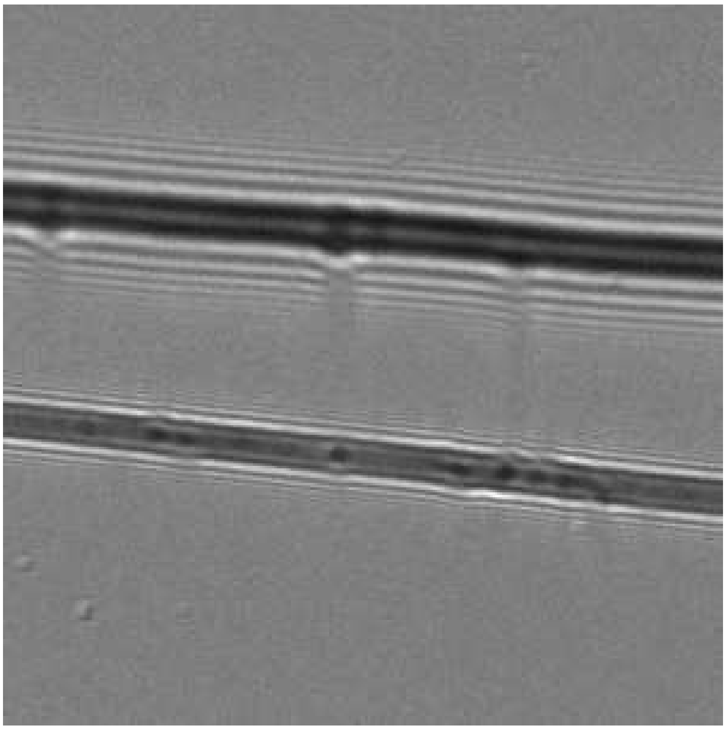

Mainz, im Oktober 2005

Tag der Mündlichen Prüfung: Mittwoch 7-12-2005

Abstract

Experiments have been performed to explore the potential of the low emittance 855 MeV electron beam of the Mainz Microtron MAMI for imaging with coherent X-rays. Transition radiation from a micro-focused electron beam traversing a foil stack served as X-ray source with good transverse coherence.

In a first series of experiments a polychromatic transition radiation X-ray source with typical photon energies in the range of 8-30 keV and a spot size of standard deviation $\sigma_h = (8.6 \pm 0.1)$ μm in horizontal and $\sigma_v = (7.5 \pm 0.1)$ μm in vertical direction was used to record refraction contrast radiographs of low absorbing materials, in particular polymer strings with diameters between 30 and 450 μm. As detectors X-ray films were used. The source-to-detector distance amounted to 13 m. The edge enhancement contrast $C_{ref} = (I_{max} - I_{min})/(I_{max} + I_{min})$ was investigated as a function of the distance between the object and the X-ray film which was varied between 0.5 and 5.5 m. The measured contrast C_{ref} of up to 20% can well be explained in the framework of a geometrical and a wave optical model.

In a second series of experiments holograms of strings were taken with a beam spot size $\sigma_v = (0.50 \pm 0.05)$ μm and a monochromatic X-ray beam of 6 keV energy. The good longitudinal coherence has been obtained by the (111) reflection of a flat silicon single crystal in Bragg geometry. It has been demonstrated that a direct exposure CCD chip with a pixel size of 13×13 μm^2 provides a highly efficient on-line detector. Contrast images can easily be generated with a complete elimination of all parasitic background. The on-line capability allows a minimization of the beam spot size by observing the smallest visible interference fringe spacings or the number of visible fringes.

In a third series of experiments it was demonstrated that X-ray films are very useful detectors for the micro-focused and monochromized transition radiation X-ray source at MAMI. The main advantage in comparison with the direct exposure CCD chip is the resolution. For the X-ray film Structurix D3 (Agfa) the standard deviation of the resolution was measured to be $\sigma_f = (1.2 \pm 0.4)$ μm, which is about a factor of 6 better as for the direct exposure CCD chip. With the small effective X-ray spot size in vertical direction of $\sigma_v = (1.4 \pm 0.5)$ μm and a geometrical magnification of up to 7.24 high quality holograms of tiny transparent and opaque strings were taken in which the holographic information is contained in up to 18 interference fringes.

X-ray radiography using coherent X-rays enhances also the visibility of highly absorbing materials via diffraction at edges. This was demonstrated with tungsten wires of various thicknesses between 4 and 40 μm diameter. In combination with a high geometrical magnification this effect allows the observation of small highly absorbing features with micrometer size in the investigated object.

Zusammenfassung

Am Mainzer Mikrotron MAMI wurden Experimente durchgeführt, um das Potential des 855 MeV Elektronenstrahles niedriger Emittanz für die Bildgebung mit kohärenter Röntgenstrahlung zu untersuchen. Als Strahlungsquelle mit guter transversaler Kohärenz diente Übergangsstrahlung, die von einem mikro-fokussierten Elektronenstrahl in einem Folienstapel erzeugt wurde.

In einer ersten Experimentserie wurden mit polychromatischer Übergangsstrahlung einer Photonenenergie im Bereich zwischen 8-30 keV Phasenkontrastradiographien von schwach absorbierenden Materialien - insbesondere Polymerfäden mit Durchmessern zwischen 30 und 450 μm - aufgenommen. Die Strahlfleckgrößen in horizontaler und vertikaler Richtung betrugen $\sigma_h = (8.6 \pm 0.1)$ μm bzw. $\sigma_v = (7.5 \pm 0.1)$ μm (Standardabweichungen). Als Detektoren wurden Röntgenfilme verwendet. Der Abstand zwischen Quelle und Detektor betrug 13 m. Der Phasenkontrast an Kanten von Polymerfäden $C_{ref} = (I_{max} - I_{min})/(I_{max} + I_{min})$ wurde als Funktion des Abstands zum Detektor untersucht, der zwischen 0.05 und 5.5 m variierte. Der gemessen Kontrast C_{ref} von bis zu 20% kann sowohl im Rahmen eines wellenoptischen Modells als auch eines Modells auf der Basis der geometrischen Optik gut beschrieben werden.

In einer zweiten Experimentserie wurden Hologramme von Polymerfäden bei einer Photonenenergie von 6 keV aufgenommen, wobei die Strahlfleckgröße $\sigma_v = (0.50 \pm 0.05)$ μm betrug. Die notwendige longitudinale Kohärenz wurde mit Hilfe des (111)-Bragg-Reflexes eines ebenen Silizium-Einkristalls erreicht. Es konnte gezeigt werden, dass ein offener CCD-Chip mit einer Pixelgröße von 13×13 μm^2 als ortsauflösender Röntgendetektor gut geeignet ist. Mit ihm können relativ einfach Kontrastbilder erzeugt werden, bei denen jeglicher parasitärer Untergrund durch Subtraktion eines Bildes ohne Objekt eliminiert wird. Der Echtzeiteinsatz dieses Detektors erlaubt über die Beurteilung der holographischen Interferenzstrukturen die Minimierung der Strahlfleckgröße der Röntgenquelle.

In einer dritten Experimentserie konnte gezeigt werden, dass Röntgenfilme gut geeignete ortsauflösende Detektoren für die Aufnahme von Hologrammen mit der mikrofokussierten, monochromatisierten Übergangsstrahlungsquelle an MAMI sind. Der Hauptvorteil im Vergleich zum offenen CCD-Chip liegt in seiner deutlich besseren Auflösung. Für den Röntgenfilm Structurix D3 (Agfa) wurde eine Auflösung $\sigma_f = (1.2 \pm 0.4)$ μm (Standardabweichung) gemessen, was im Vergleich zum CCD-Chip um einen Faktor 6 besser ist. Mit der kleinen effektiven Strahlfleckgröße des Röntgenstrahles in vertikaler Richtung von $\sigma_v = (1.4 \pm 0.5)$ μm und einer geometrischen Vergrößerung von 7.24 konnten qualitativ hochwertige Hologramme von sehr kleinen transparenten sowie vollständig absorbierenden Fäden aufgenommen werden. Die holographische Information ist dabei in bis zu 18 Interferenzringen enthalten.

Schließlich konnte gezeigt werden, dass die Radiographie mit kohärenten Röntgenstrahlen auch die Sichtbarkeit von stark absorbierenden Materialien infolge der Beugung an den Begrenzungen erhöht. Dies wurde anhand von Wolframdrähten mit Durchmessern zwischen 4 und 40 μm demonstriert. Bei hoher geometrischer Vergrößerung können über diesen Effekt stark absorbierende Strukturen mit Größen im Mikrometerbereich in einem zu untersuchenden Objekt sichtbar gemacht werden.

Contents

1 Introduction

X-ray imaging has been begun over 100 years ago, when Wilhelm Konrad Röntgen discovered X-rays in the year 1895 [Rö96]. Some of the intrinsic advantages over conventional imaging techniques, such as light and electron microscopy, is the penetration depth of X-ray photons. Among others this property allows, with the so-called non-destructive testing, the observation of thick specimens in its natural environment. X-ray imaging became rapidly an important diagnostic tool in medicine, material science, biology and environmental research [Ari94, Mon04].

The contrast in conventional absorption X-ray imaging is based on the difference in the absorption of different materials constituting the sample. Thin samples of light elements ($Z < 16$), such as soft tissues and organic materials, show a weak absorption contrast even at low X-ray energies, i.e., the big deficiency is that the conventional absorption radiography can not distinguish between materials with similar attenuation coefficients [Lui05]. In addition, it must be noted that the high absorbed dose within an object to be imaged may lead to radiation hazards. For low Z materials, however, a high contrast could be obtained if the phase shift of the X-rays introduced by the object could be measured instead of the intensity of the transmitted wave. The enhancement of the contrast is attributed to the fact that in particular for low-Z materials the phase shift for X-rays is higher than the absorption of incident X-rays. Also, for the radiography based on the phase shift mechanism, the absorbed dose is considerably lower in comparison to the conventional absorption radiography[Arf98, Kot99, Tur04].

X-ray phase contrast imaging can be carried out with a very simple experimental setup with polychromatic X-rays which are emitted from a small micro-focused source spot with a size in the order of some micrometers. This fact has been pointed out in [Wil96]. Information can be supplied on the sample morphology, i.e., its boundaries, interfaces and location of small features [Xiz03, Tak98, Lew04] can be obtained.

Phase contrast microscopy in the hard X-ray region has been done with different techniques with the common feature that all include crystal optics to render the phase visible. Two-beam Bonse-Hart interferometry [Bon65, Mom95, Mom02] and diffraction contrast imaging utilize an analyzer crystal [Cha97, Ing95]. Such techniques using several crystals lead to losses of X-rays photons. Also the experimental setup is rather sophisticated.

Phase information could be also obtained with an experimental setup similar to Gabor in-line holography [Gab49]. In principle such a setup is very simple but a severe restriction comes from the demand of a highly coherent X-ray source and also high spatial resolution detectors. The lack of coherent (transversal and longitudinal) X-ray sources prevented the development of X-ray holography for many years. With the advent of synchrotron radiation sources soft X-ray holography has been achieved [Mcn92] with sub-micrometer resolution. With third generation synchrotron radiation sources like ESRF, APS and SPRING8, hard X-ray phase contrast imaging, in-line holography and microtomography have been accomplished [Spa99, Col96, Hu01].

From the three requirements for phase contrast radiography, a brilliant X-ray source, an X-ray monochromator and a two dimensional high resolution detector, the X-ray source is of a particular importance. With the advent of electron accelerators, some new coherent X-ray sources have been developed which are based on synchrotron radiation, wiggler- or undulator radiation [Ste03]. The work presented here exploits the potential of the low emittance 855 MeV electron beam of the race track microtron MAMI to produce coherent X-rays. Our approach is based on transition radiation production in the X-ray region. Transition radiation is produced when the electron beam penetrates a thin foil or a periodic structure of thin foils. It features a broad band characteristics with a cut off energy of about 40 keV [Bac96], and is highly directional with an apex angle in the order of 0.6 mrad. A very good transverse coherence can be achieved by micro-focusing the low emittance electron beam of MAMI [Kph93]. The required longitudinal coherence is obtained by monochromizing the polychromatic transition radiation X-ray beam with the aid of a flat silicon single crystal. The radiographs are captured with high resolution X-ray films and a direct exposure CCD camera with a pixel resolution of 13×13 μm^2. Just the investigation of the novel on-line capabilities of the latter was an essential motivation of the investigations of this work.

The treatise is organized as follows. In chapter 2 an introduction to the principles of X-ray imaging will be presented. A comparison between the conventional radiography (based on X-ray attenuation) and phase radiography will be given. Since the X-ray beam coherence is a prerequisite for X-ray phase radiography, a brief review on the coherence will be given as well.

Chapter 3 deals with the transition radiation production from foil stacks which are used as a high brilliance X-ray sources. The optimization and construction of a foil stack which produces X-ray photons with a high flux at 6 keV will be presented. The accompanying bremsstrahlung which represents a serious background problem will be discussed as well.

In Chapter 4 the results of refraction or phase contrast imaging with a polymonochromatic X-ray beam from a transition radiation foil stack with good transverse coherence will be presented. The radiographs were recorded with an X-ray film. The imaged objects were low absorbing materials like polymer strings and green leaves which do not produce contrast in case of traditional absorption radiography.

Chapter 5 deals with the X-ray phase contrast imaging and hard X-ray in-line holography using monochromatic X-rays. The longitudinal coherence is achieved with the aid of a silicon crystal monochromator while the transversal coherence by microfocusing the electron beam at the transition radiation foil stack to values in the micrometer region. Advantages and disadvantages of X-ray detectors as a direct exposure CCD camera, and a luminescence screen which converts the X-rays into visible light in a combination with a lens and a CCD camera, will be discussed.

Moreover, high resolution X-ray films Structruix D3 has been recorded the X-ray phase contrast imaging and hard X-ray holography.

The paper closes with chapter 6 in which future prospects are discussed.

2 Principles of X-ray phase contrast imaging

In X-ray transmission imaging, a beam of hard X-rays in the energy range between approximately 6-60 keV traverses a sample. The intensity distribution in a plane perpendicular to the propagation direction somewhere downstream the sample is registered with a two-dimensional detector of high spatial resolution. The image, or more precisely the intensity distribution, depends strongly on the type of interaction between the X-rays with the sample material. In general, the contrast generation mechanism can be described by the introduction of the complex refractive index of the X-rays. In this chapter, a brief review on the complex refractive index and the principle of refraction contrast radiography will be presented.

2.1 Complex refraction index

When a parallel beam of X-rays penetrates matter, it suffers an attenuation and a phase shift. Such macroscopic interactions are described by the complex refraction index of X-rays [Jam65]

$$n(\omega) = 1 - \delta(\omega) + i\beta(\omega) \quad . \tag{2.1}$$

The real part $\Re[n(\omega)] = 1 - \delta(\omega)$ describes the refraction of the wave of angular frequency ω in a material, the quantity $\delta(\omega)$ gives the deviation of the refractive index of a material from unity (refraction index of vacuum). Therefore, it is also known as the decrement of the refractive index. In the current work it will be called dispersion index. The imaginary part $\Im[n(\omega)] = \beta(\omega)$ specifies the attenuation of the X-rays in matter [Com35]. It is known as the absorption index.

The transmission of an electromagnetic wave through a piece of matter of thickness d is illustrated schematically in Fig. 2.1. The undisturbed wave propagation in x-direction is described by the following expression

$$A_v = A_0 e^{i[\omega t - k_v d]}; \quad k_v = \frac{\omega}{c} \quad . \tag{2.2}$$

The amplitude of the outgoing wave behind the object is written as

$$A_m = A_0 e^{i[\omega t - k_m d]} = A_0 e^{i[\omega t - k_v d]} e^{i\frac{\omega}{c}\delta d} e^{-\frac{\omega}{c}\beta d} \tag{2.3}$$

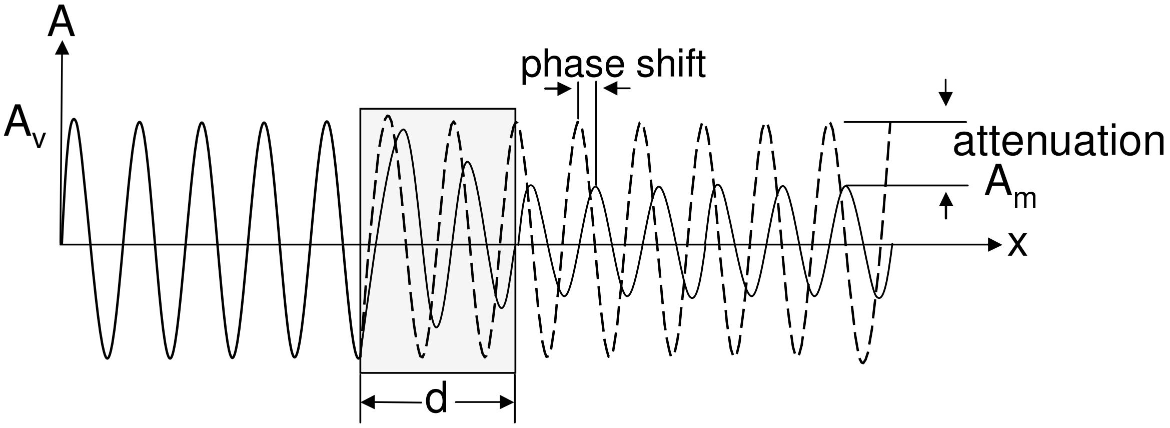

Figure 2.1: Transmission of an electromagnetic wave through a piece of matter of thickness d and complex refraction index $n = 1-\delta+i\beta$. The amplitude A_m is attenuated by the factor $e^{-\frac{\omega}{c}\beta(\omega)d}$ and has a phase shift $\frac{\omega}{c}\delta(\omega)d$ relative to the undisturbed wave A_v.

where $k_m = \omega n/c$ is the wave number in the medium. Comparing Eq. (2.2) and Eq. (2.3), the transmitted wave suffers a phase shift

$$\Delta\phi = \frac{\omega}{c}\delta(\omega)d \tag{2.4}$$

relative to the undisturbed wave, and an attenuation

$$\frac{|A_m|}{|A_v|} = e^{-\frac{\omega}{c}\beta(\omega)d} \quad . \tag{2.5}$$

The dispersion index $\delta(\omega)$ and absorption index $\beta(\omega)$ are expressed as [Aga91, Len94]

$$\delta(\omega) = \frac{2\pi r_e c^2 n_a}{\omega^2} f_1(\omega) \qquad \text{and} \qquad \beta(\omega) = \frac{2\pi r_e c^2 n_a}{\omega^2} f_2(\omega) \quad . \tag{2.6}$$

Here, $r_e = 2.818 \cdot 10^{-15}$ m is the classical electron radius and $n_a = N_A\rho/M_m$ is the atomic density, $N_A = 6.022 \cdot 10^{23}$ mol^{-1} the Avogadro's number, ρ the density of the material and M_m the molar mass. The values of the atomic scattering factors $f_1(\omega)$ and $f_2(\omega)$ are tabulated for a large range of energies [Hen93, Aga91]. For a given material the absorption index $\beta(\omega)$ falls off very steeply with increasing X-ray energy while the dispersion index $\delta(\omega) \sim 1/\omega^2$ decreases more smoothly. For energies higher than 6 keV the dispersion index of refraction $\delta(\omega)$ is more than three orders of magnitude larger than $\beta(\omega) \sim 1/\omega^4$. Fig. 2.2 shows the ratio δ/β as a function of the X-ray energy. The most important feature is the drastic difference of this ratio for the high-Z material Ni in comparison to the low-Z material polycarbonate at higher photon energies. For example, at $\hbar\omega = 30$ keV, δ/β for polycarbonate is approximately 40 times larger as for nickel. This clearly demonstrates that for low-absorbing materials the phase shift is the dominating effect in comparison to the attenuation. As a numerical example, for a polycarbonate plate of thickness 10 μm and a photon energy $\hbar\omega = 12$ keV for which

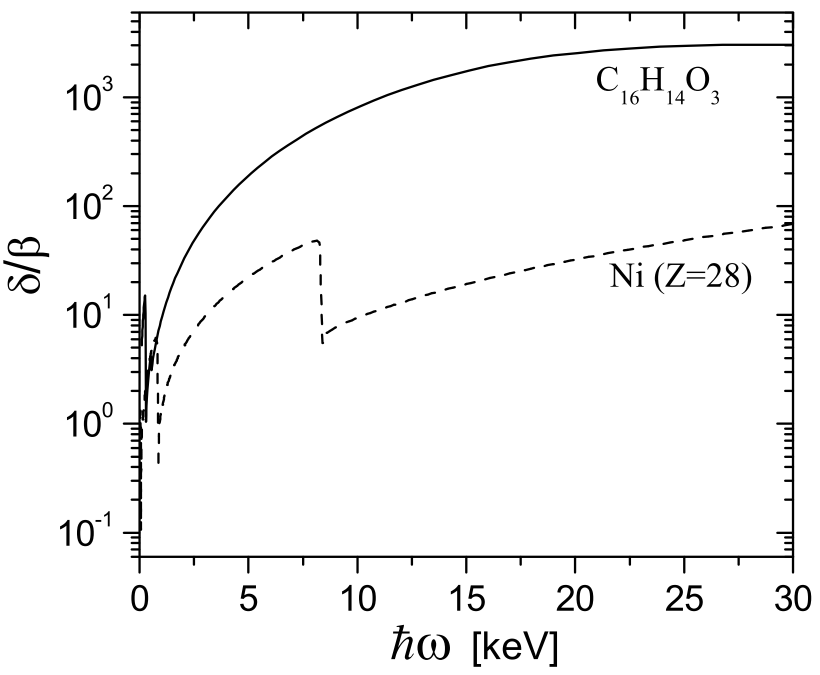

Figure 2.2: The δ/β ratio. This ratio is for low atomic number (Z) materials such as polycarbonate much larger as for high-Z materials as nickel [Hen93].

the complex refraction index parameters are $\delta = 1.826 \cdot 10^{-6}$ and $\beta = 1.573 \cdot 10^{-9}$ the phase shift is almost $11.35 \cdot \pi$ while the attenuation is only $1.3 \cdot \pi \cdot 10^{-4}$.

These considerations lead to the important conclusion that a high contrast combined with a low-absorbed dose could be achieved by using the phase shift mechanism to produce a radiograph [Wil96]. Radiography based on phase shift is referred to as refraction contrast, edge-enhanced contrast, refraction-enhanced or phase contrast. In the current work it will be called refraction-contrast radiography for imaging with polychromatic X-ray, and phase-contrast or holography for imaging with monochromatic X-ray.

2.2 Refraction contrast radiography

In the following section a novel kind of radiography is described which is based on refraction as a mechanism to produce a high contrast of low-absorbing materials using X-rays from a transition radiation source. The principles of refraction-contrast radiography will be explained as well as the interpretation according to geometrical and wave optics. The enhanced visualization of low-absorbing materials and its most important advantage that different objects of similar densities can easily be distinguished will also be presented.

2.2.1 Principles

X-rays as electromagnetic waves are subjected to reflection, diffraction, and refraction. The X-ray wavefront is deformed when passing through a sample of inhomogeneous thickness or refractive index. According to the geometrical approximation the phase difference $\Delta\phi$ for a ray path through an object with refraction index $n(\lambda; x, y, z) = 1 - \delta(\lambda; x, y, z) + i\beta(\lambda; x, y, z)$ relative to an undisturbed wave, assuming that the optical axis is parallel to the x-axis, is given according to Eq. (2.4) by

$$\Delta\phi(\lambda; x, y, z) = \frac{2\pi}{\lambda}\int \delta(\lambda; x, y, z)dx = r_e\lambda \int \rho_e(\lambda; x, y, z)dx \quad . \tag{2.7}$$

Here $\rho_e(z, y, x)$ is the electron density at the point (x, y, z), r_e the classical electron radius, and λ is the X-ray wavelength. The integration is carried out over the path of the X-ray beam [Wil96, Suz02].

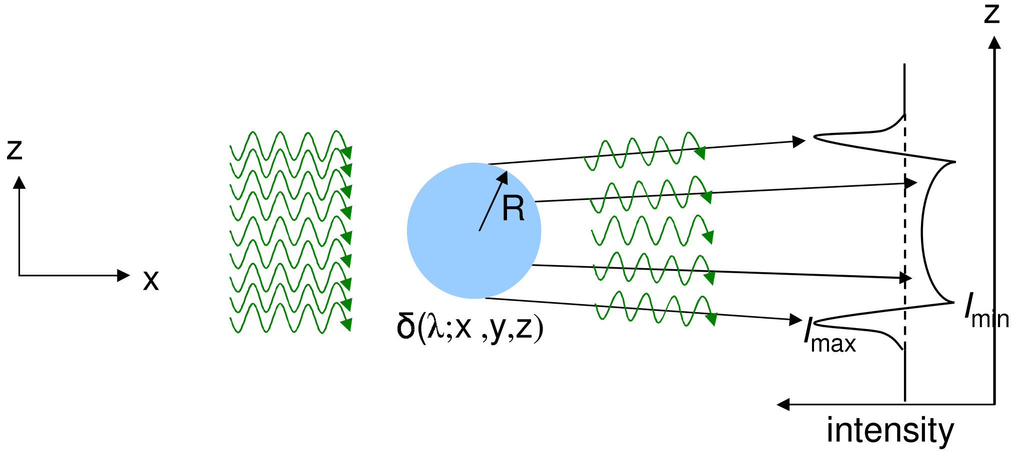

Figure 2.3: Formation of a refraction contrast radiograph according to geometrical optics. Refracted X-rays slightly deviate from rectilinear propagation at the interfaces in accordance with Snell's law of refraction. Since the refraction index for X-rays is slightly smaller than unity (about 10^{-6}), X-rays are refracted in opposite manner to visible light, i.e. they are focused by a concave and defocused by a convex object. For tangentially incident X-rays on an interface, X-rays encounter maximum deviation which results in the formation of a black/white contrast which enhances the visibility of the interfaces.

For simplicity in Fig. 2.3 a one dimensional object such as a string of radius R and a refraction index $n_2(\omega) = 1 - \delta_2(\omega) + i\beta_2(\omega)$ is considered, which is embedded in a medium of refraction index $n_1(\omega) = 1 - \delta_1(\omega) + i\beta_1(\omega)$ and which is illuminated with a parallel X-ray beam. The phase shift of the outgoing wave relative to wave in vacuum is given by

$$\phi = \frac{4\pi}{\lambda}(\delta_2 - \delta_1)R\sqrt{1 - (\frac{z_o}{R})^2} \quad . \tag{2.8}$$

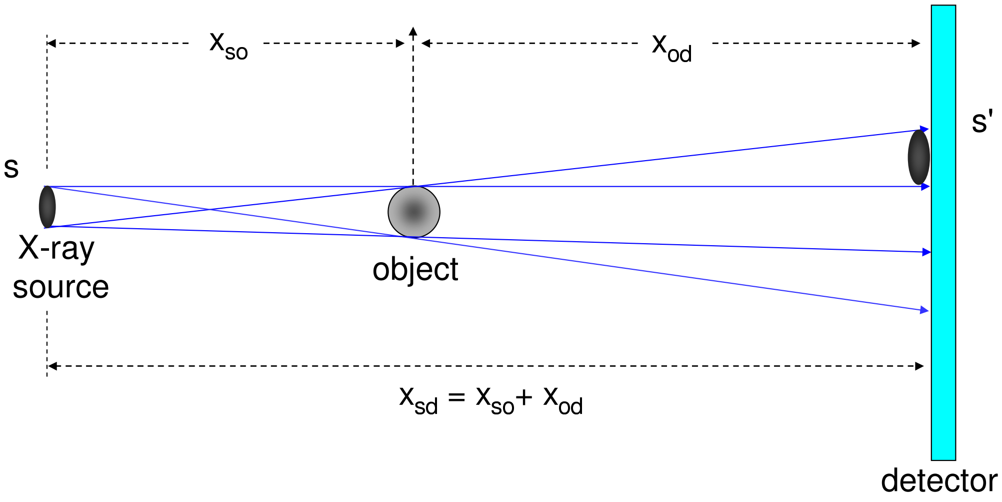

Figure 2.4: Schematic experimental setup for the refraction contrast radiography.

The angular deviation $\Delta\alpha$ of the normal to the wavefront is [Wil96]

$$\Delta\alpha = \frac{\lambda}{2\pi} | \bigtriangledown_z \phi| = \frac{4\pi(\delta_2 - \delta_1)}{R} \frac{z_o}{[1-(\frac{z_o}{R})^2]^{\frac{-3}{2}}} \quad . \tag{2.9}$$

The phase gradient diverges at $z = R$, the rays deviate by a large angle from the original propagation direction even though $(\delta_2 - \delta_1)$ is very small as in the case of X-rays. This leads to a loss of intensity at boundaries or a black/white edge contrast. This explains why the radiograph looks like a direct image of contours of the details which constitute the sample. More generally, any rapid variation of the refraction index or the thickness of the sample may be imaged as an intensity disturbance or a black/white contrast which appears at the corresponding points in the radiograph even when a polychromatic X-ray beam is used.

The black/white edge contrast is expressed as [Hec89]

$$C_{ref} = \frac{I_{max} - I_{min}}{I_{max} + I_{min}} \tag{2.10}$$

with I_{max} and I_{min} as shown in Fig. 2.3.

2.2.2 Principle of the experimental setup

The typical experimental setup for refraction contrast radiography is illustrated in Fig. 2.4. A polychromatic X-ray source illuminates a sample which is mounted at a distance x_{so} from the source. The detector is mounted at a distance x_{od} from the object. This configuration features a geometrical magnification M and a geometrical unsharpness S'.

The geometrical magnification is expressed as

$$M = \frac{x_{so} + x_{od}}{x_{so}} = 1 + \frac{x_{od}}{x_{so}} \quad . \tag{2.11}$$

In the current work the image can be magnified up to 7 times by increasing x_{od} to overcome the limited spatial resolution of the X-ray image detector of $13 \times 13\ \mu\text{m}^2$. A huge magnification of up to 65 times has been used to get ultra spatial resolution up to the sub-micrometer range as pointed out in [May02].

The geometrical unsharpness S', arising from the finite size of the focal spot projection on the detector plane, is given by

$$S' = S \cdot \frac{x_{od}}{x_{so}} = S(M-1) \quad . \tag{2.12}$$

Here S is the focal-spot size. The geometrical unsharpness is negligible small for M = 1, however, at an object-to-detector distance $x_{od} = 0$ the phase contrast vanishes as will be pointed out below in section 4.1.1.

2.3 Imaging with a coherent X-ray beam

The holograph records interference patterns between the disturbed waves by the sample and the undisturbed wave from the source. Fig. 2.5 shows the arrangement of in-line holography. A point source emanates a monochromatic wave (solid lines) and illuminates the sample of small size. The wave scattered by the sample (dashed lines) interfere with the undisturbed wave. The scattered wave and the unscattered wave form an interference pattern at the detector. The resulting hologram is recorded by an image detector of high spatial resolution. The amplitude at the detector plane

$$E(\vec{r}) = E_o(\vec{r}) + E_{scat}(\vec{r}) \tag{2.13}$$

consists of two different terms [Har96] $E_o(\vec{r})$ and $E_{scat}(\vec{r})$ which are the unscattered and scattered wave, respectively. The recorded intensity is expressed as

$$I(\vec{r}) = |E_o(\vec{r})|^2 + E_o^*(\vec{r})E_{scat}(\vec{r}) + E_o(\vec{r})E_{scat}^*(\vec{r}) + |E_{scat}(\vec{r})|^2 \quad . \tag{2.14}$$

The first term on the right hand side is the intensity of the undisturbed wave. The second and third term describe the interference between scattered and unscattered waves. This is the holographic diffraction pattern. The last term is the pure diffraction pattern of the scattered wave only. The diffraction pattern depends on the size of the object and its position relative to the source and the detector.

2.3.1 Coherence

For all X-ray beams produced by available X-ray sources, such as standard X-ray tubes, third-generation synchrotron insertion devices and transition radiation, the spectral

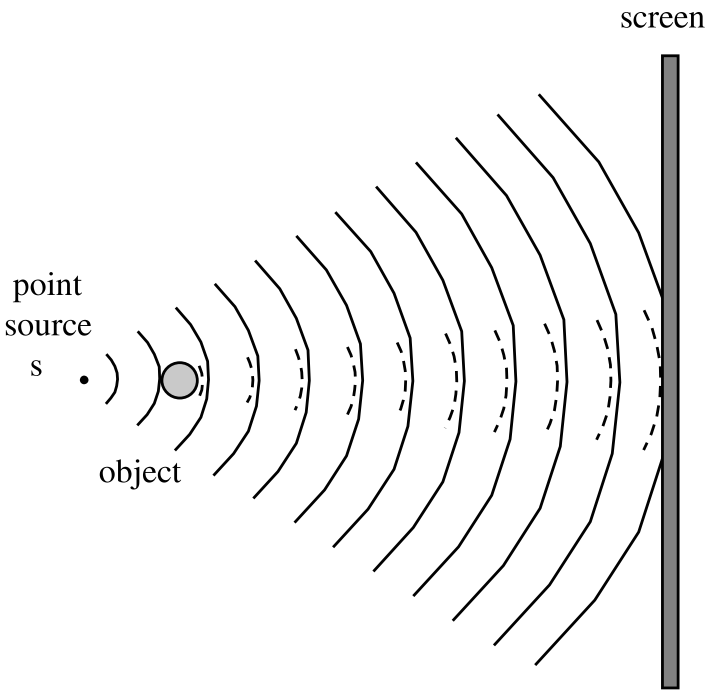

Figure 2.5: Schematic demonstration of in-line holography. A point X-ray source emanates a spherical wave of wavelength λ which illuminates a small object. The object is mounted close to a source and far from the imaging detector (CCD camera or high resolution X-ray film). The interference between the scattered wave by the object (dashed lines) and unscattered wave emanating from the source (solid lines) forms a hologram on the image detector.

bandwidth and finite spatial dimension of the source have to be taken into account. Finite spectral bandwidth and finite spatial dimension result in incoherent properties of the X-ray beam. A quantitative measurement of the effect of a source spot and a bandwidth on the coherence properties of the beam is the transverse and longitudinal coherence length or the degree of coherence of the beam. Coherence is connected to the ability of the waves to produce interference. This means that for imaging with coherent waves, the amplitude and phase of all individual waves are superimposed, rather than merely summing up individual intensities. The interference pattern is qualitatively described by the visibility V of the fringes.

$$V = \frac{I_{max} - I_{min}}{I_{max} + I_{min}} \tag{2.15}$$

where I_{max} and I_{min} are the maximal and minimal intensities of two neighboring fringes in the interference pattern.

The coherence properties of a source are divided conveniently into two categories, these are the transverse (spatial) coherence which is related to the finite extent of the X-ray source and the longitudinal (temporal) coherence which is related to the monochromaticity of the X-ray beam.

The transverse coherence originates from the fact that, as a rule, the individual source points emit radiation independently from each other. Transition radiation X-ray sources are quasihomogeneous [Car77]. But it can be shown that for the beam spot size realized in this work it can be considered in good approximation as a source for incoherent radiation. In this limit each electron passing the radiator foil stack emits X-rays independently. Therefore, every source point produces interference patterns shifted by $(x_{od}/x_{so})\Delta S$, with ΔS being the transverse displacement in the spot. This smears out any interference pattern which results in a deterioration of the holographic information. In order to avoid this deterioration, the X-ray source size must be kept as small as possible. To improve the transverse coherence the distance x_{so} can be increased and the distance x_{od} be reduced. However, the latter distance can not be made to small since restrictions imposed by the finite detector resolution must be taken into account. The transverse coherence length L_T is defined as the distance between points on the observation plane for which the relative phases of the wavefronts from outermost points in the source differ by $1/2\pi$. It is given by

$$L_T = \frac{\lambda \cdot x_{sd}}{2\pi \cdot S} \quad . \tag{2.16}$$

The longitudinal coherence length L_l describes the distance along a ray path over which a spectral distribution of width $\Delta\lambda$ retains its relative phases within the limits of π. It is in particular critical for X-ray holography because it restricts the maximum path length difference that can be accepted between rays passing from the source to the detector and rays which penetrate the object and then going to the detector. The longitudinal coherence length L_l is given by [Bor75]

$$L_l = \frac{\lambda^2}{2\Delta\lambda} \quad . \tag{2.17}$$

In case of an incoherent X-ray source every frequency component produces independently from the others an interference pattern resulting in a blurring of the interference pattern.

2.3.2 Coherence and visibility

In this section, the effect of a finite source size and a finite width of the spectral intensity distribution on the interference pattern will be demonstrated for a polymer string of radius R and complex refraction parameters δ and β, which is stretched along the y_o axis. For the definition of the coordinate system see Fig. 2.6. The normalized electric wave field $E(z_d)/E(z_0)$ at the detector plane can be calculated by means of the Fresnel-Kirchhoff integral. As shown in the appendix A.2 the result is

$$\begin{aligned} \frac{E(z_d,\lambda)}{E_0(z_d,\lambda)} &= 1 + \sqrt{\frac{x_{sd}}{i\lambda x_{so}x_{od}}} \int\limits_{-R}^{+R} \Big(\exp[-\frac{4\pi}{\lambda}(i\delta+\beta)\sqrt{R^2 - z_o^2}\,] - 1 \Big) \cdot \\ &\quad \cdot \exp[i\frac{\pi}{\lambda}\frac{x_{sd}}{x_{so}x_{od}}(z_o - z_d\frac{x_{so}}{x_{sd}})^2] dz_o \quad . \end{aligned} \tag{2.18}$$

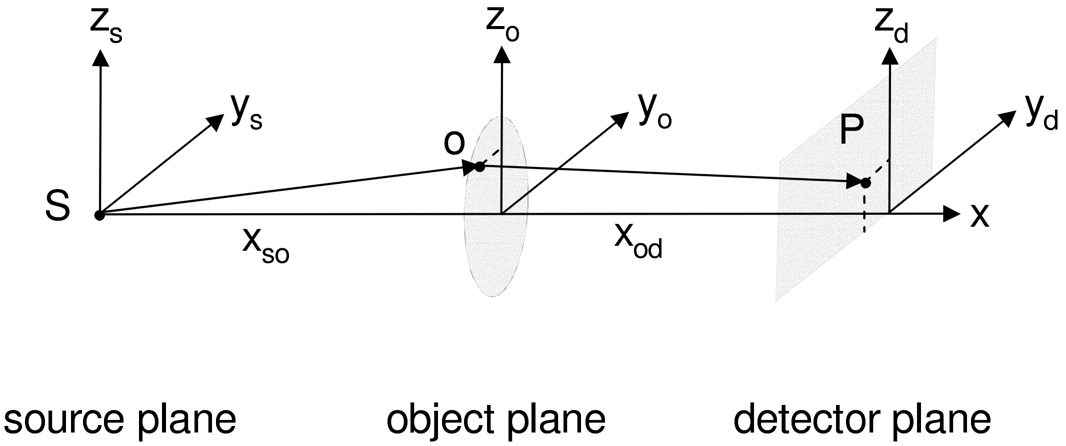

Figure 2.6: Standard geometry of refraction contrast and in-line holography. S is a point in the source, O is a point in the object plane and P is the point in the detector plane.

The normalized intensity distribution $I_n^{(\lambda)}(z_d, \lambda) = |E(z_d, \lambda)|^2 / |E_0(z_d, \lambda|^2$ is shown in Fig. 2.7 (a). The effect of a partial coherence, originating from the spectral distribution and a finite beam spot size of the X-rays, deteriorates the visibility of the interference fringes as shown in Fig. 2.7 (b) and (c). Source spot size and spectral distribution have been taken into account as convolutions with the normalized intensity distributions $g(z_s)$ of the beam spot and $f(\lambda)$ for the spectral distribution according to

$$I_n(z_d) = \int \int I_n^{(\lambda)}(z_d - \frac{x_{od}}{x_{so}} z_s, \lambda) \cdot g(z_s) \cdot f(\lambda) \cdot dz_s d\lambda \ . \tag{2.19}$$

In conclusion, radiography based on phase contrast is a useful technique to increase the contrast for low-Z materials with a small absorbed dose [Arf98]. For X-ray refraction contrast radiography, on the one hand, a good transverse coherence of the X-ray beam is required while the longitudinal coherence is not of major importance. The latter has been demonstrated with Fig. 2.7 (b). For X-ray in-line holography, on the other hand, both, a very good transverse coherence and a good longitudinal coherence of the X-ray beam are necessary since the holographic information is imprinted in the interference pattern. In the following chapters experiments at the Mainz Microtron facility (MAMI) will be presented in which the capabilities of a transition radiation X-ray source in combination with a micro-focused beam spot will be demonstrated for both, X-ray refraction radiography with broad band X-rays as well as in-line holography with monochromatic X-rays.

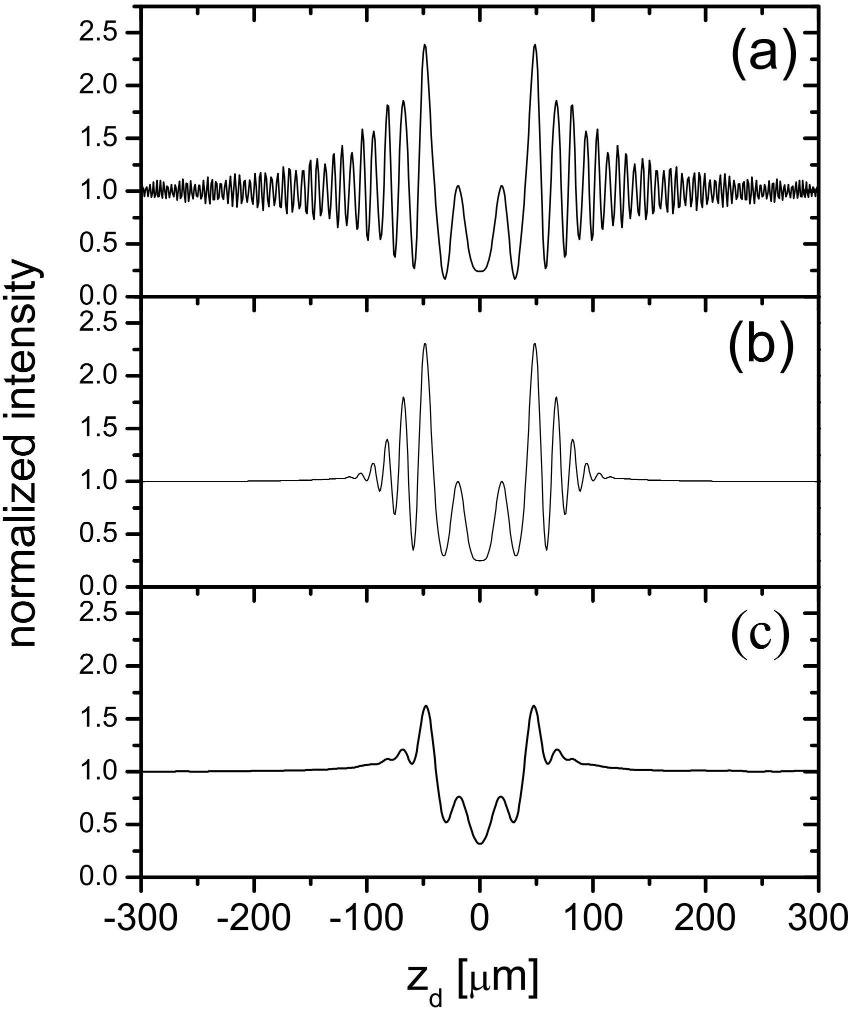

Figure 2.7: Effect of partial coherence on the visibility of fringes for a polymer string with a diameter of 30 μm, complex refraction index $\delta = 7.24 \cdot 10^{-6}$ and $\beta = 2.42 \cdot 10^{-8}$ at an X-ray energy of 6 keV, source-to-object distance $x_{so} = 10.45$ m, object-to-detector distance $x_{od} = 3.15$ m. (a) Normalized intensity distribution $|E(z_d, \lambda_0)|^2/|E_0(z_d, \lambda_0|^2$ according to Eq. (2.18) for a point source and monochromatic X-rays with $\lambda_0 = 2.067$ Å, corresponding to an energy of 6 keV, (b) for a point source but a Gaussian spectral distribution around λ_0 with standard deviation of $\sigma_\lambda = 0.2$ Å, (c) for a Gaussian intensity distribution of the X-ray source spot with standard deviation $\sigma_z = 6$ μm and monochromatic X-rays. Convolutions according to Eq. (2.19). Ideal detector resolution assumed.

3 The transition radiation X-ray source

X-ray sources are crucial elements in radiography. In principle, there are a lot of X-ray sources as, e.g., X-ray tubes, synchrotron or transition radiation sources. This chapter deals with transition radiation as a brilliant X-rays source. Transition radiation is produced when a relativistic electron beam crosses a polyimide foil stack. The production mechanism will be briefly discussed. Moreover, the feature of the radiation from optimized foil stacks to produce high flux radiation at a photon energy of 6 keV, using a 600 MeV electron beam, and at 33 keV with an 855 MeV electron beam will be presented.

3.1 The Mainz Microtron facility (MAMI)

The Mainz Microtron (MAMI) facility is three stage race-track electron accelerator. It is located in the Institute for Nuclear Physics on the campus of the Johannes Gutenberg University of Mainz. The first race-track microtron delivers a continues electron beam with an energy between 4 and 15 MeV. It was made available in the year 1979 for coincidence experiments. With two further race-track microtrons, an electron beam of low emittance, high energy resolution and stability with an energy up to 855 MeV can be delivered with a beam current ranging up to 10^{-4} A. A fourth accelerator stage is now being constructed, which will boost the electron beam energy up to 1500 MeV. The final device will be operational in the year 2006. The floorplan of MAMI together with the different experimental areas is shown in Fig. 3.1.

For the current work, the beam emittance in horizontal and vertical directions are of particular interest in view of the preparation of a micro-focused electron beam. In Fig. 3.2 both emittances are depicted as a function of the electron beam energy. The emittance in horizonal direction is bigger than the emittance in vertical direction because the electrons emit synchrotron radiation in the bending magnets resulting in a growth of the emittance. The emittance depends strongly on the energy of the electron beam while it is nearly independent from the current of the electron beam, see [Kph93]. The emittance in vertical direction decreases as a function of the beam energy, while in horizontal direction the emittance increases approximately exponentially at energies larger than 400 MeV. Therefore, the choice of the beam energy to prepare a microfocused electron beam for the experiments described in this work was 600 MeV. Measurements of the horizontal and vertical emittances and also Twiss parameters at

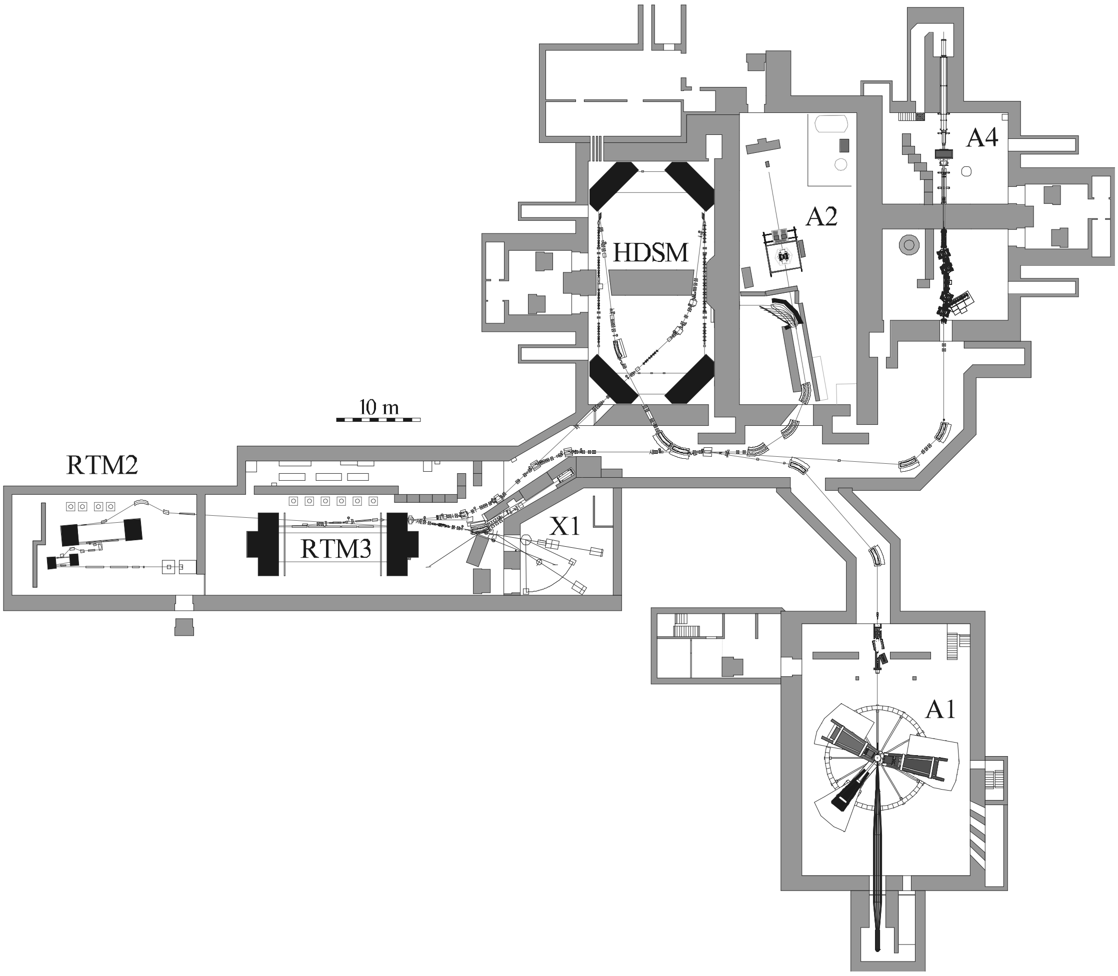

Figure 3.1: Layout of the MAMI accelerator with the race track microtrons RTM1-3 and the double sided microtron HDSM. Shown are also the experimental areas A1-A4 and X1 [KPHXX].

an electron beam energy 600 were performed with the method described in [Hag01]. The results are in horizontal direction:

$$\epsilon_h = A/\pi = 0.0023 \text{ mm mrad}$$

$$\beta = 39.03 \text{ m} \quad \alpha = -0.211 \quad \gamma = 0.027 \text{ 1/m} \quad ,$$

and in vertical direction:

$$\epsilon_v = A/\pi = 0.00052 \text{ mm mrad}$$

$$\beta = 9.599 \text{ m} \quad \alpha = 3.851 \quad \gamma = 1.695 \text{ 1/m} \quad .$$

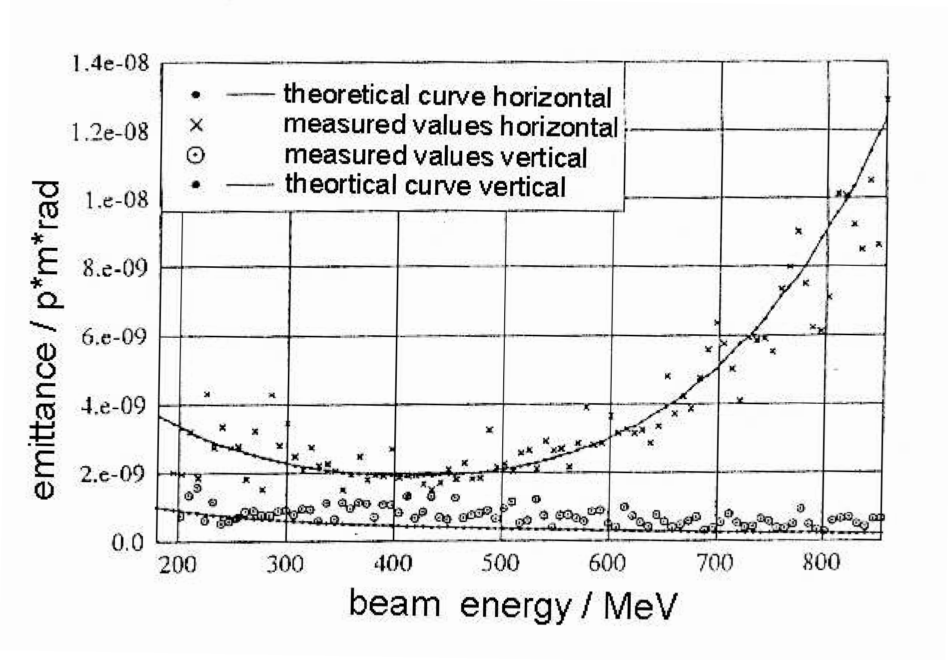

Figure 3.2: Emittance of the MAMI electron beam in vertical and horizontal direction as a function of the beam energy [Kph93].

These values have been used for simulation calculation with the program beamoptic described in 5.2.2 to get a microfocused electron beam[Roy84, ShvXX, Wil92].

3.2 Transition radiation

When an ultra relativistic electron beam crosses an interface between polyimide and vacuum a broad band of electromagnetic radiation is emitted which is known as transition radiation. The electron induces around its trajectory in the medium a time-dependent cylindrical symmetric dipole distribution that emits a cone of transition radiation which is radially polarized, see Fig. 3.3.

The mechanism of transition radiation of high relativistic charged particles has been investigated in extensive theoretical and experimental studies [Fra45, Rul97, Fab75]. In the current work highly relativistic electron beams with energies of 600 and 855 MeV have been used with relativistic factors $\gamma = 1/\sqrt{1-(\frac{v}{c})^2} \gg 1$. In the case of ultra relativistic electrons and for the energy of the emitted X-rays far from absorption edges of the medium, the permittivity ε_r can be expressed as $\varepsilon_r = 1 - \omega_p^2/\omega^2$ [Jac83] with the plasma frequency ω_p. The number of emitted X-ray photons with an energy $\hbar\omega$, emitted from a single interface at the angle θ with respect to electron velocity vector, is given per electron, per relative energy bandwidth interval $(d\hbar\omega/\hbar\omega)$, and per

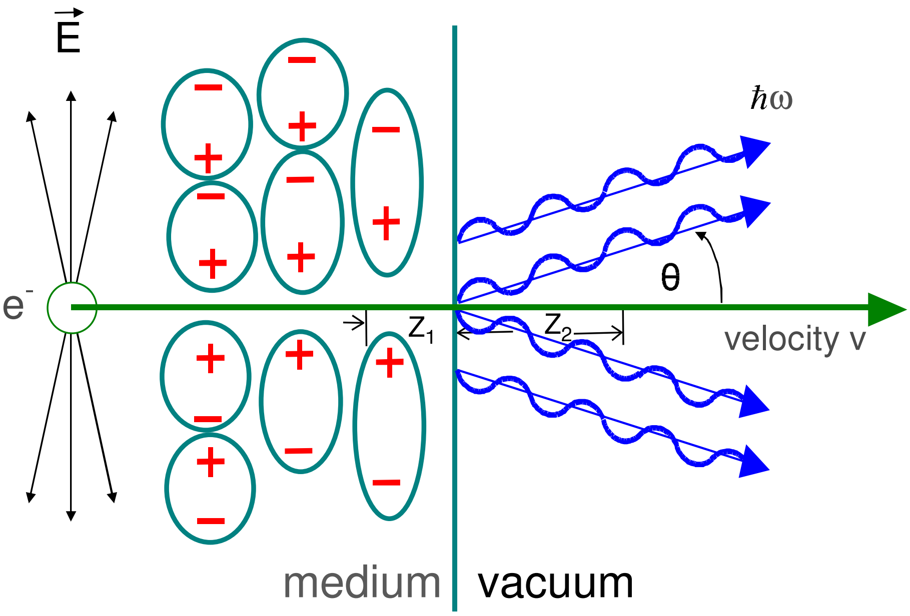

Figure 3.3: Transition radiation production at an interface between medium and vacuum. The electric field $\vec{E}$ of a highly relativistic electron produces a time-dependent, predominantly transversal polarization in the medium that leads to emission of dipole radiation. Just waves emitted from a formation zone in forward direction at the medium-vacuum interface contribute significantly to the transition radiation that is strongly peaked at small angles $\theta \simeq 1/\gamma$ with respect to the velocity vector of the electron.

solid angle $d\Omega$ by [Che74]

$$\frac{d^2N_0}{(d\hbar\omega/\hbar\omega)d\Omega} = F_1 = \frac{\alpha\ \theta^2\omega^2}{16\pi^2\upsilon^2}(Z_1 - Z_2)^2 \quad . \tag{3.1}$$

Here are $\alpha = 1/137.04$ the fine structure constant, υ the electron velocity, $\hbar$ the reduced Planck's constant, and Z_1, Z_2 the formation lengths of both media. The formation length Z is a characteristic property of the medium. It is defined as the length inside the medium where different points emit radiation coherently in forward direction. It is written as [Che74]

$$Z_i(\omega,\theta) = \frac{4\upsilon}{\omega}\frac{1}{\frac{1}{\gamma} + \theta^2 + (\frac{\omega_{pi}}{\omega})^2} \quad . \tag{3.2}$$

In this equation are $\omega_{pi} = \sqrt{\frac{4\pi\rho_{ei}e^2}{m_e}}$ the plasma frequencies of the media i=1,2 which are calculated from the electron densities ρ_{ei} of the media, e is the elementary charge, and m_e is the mass of the electron. The emitted radiation has its maximum intensity at angles $\theta \simeq 1/\gamma$ and a cut off energy limit at $\hbar\omega_c = \gamma\hbar\omega_p$. Above this value the spectrum falls off proportional to ω^{-4}. For a polyimide foil with a plasma frequency of 24.6 eV and an electron beam energy of 855 MeV, the critical energy is $\hbar\omega_c = 41.2$ keV.

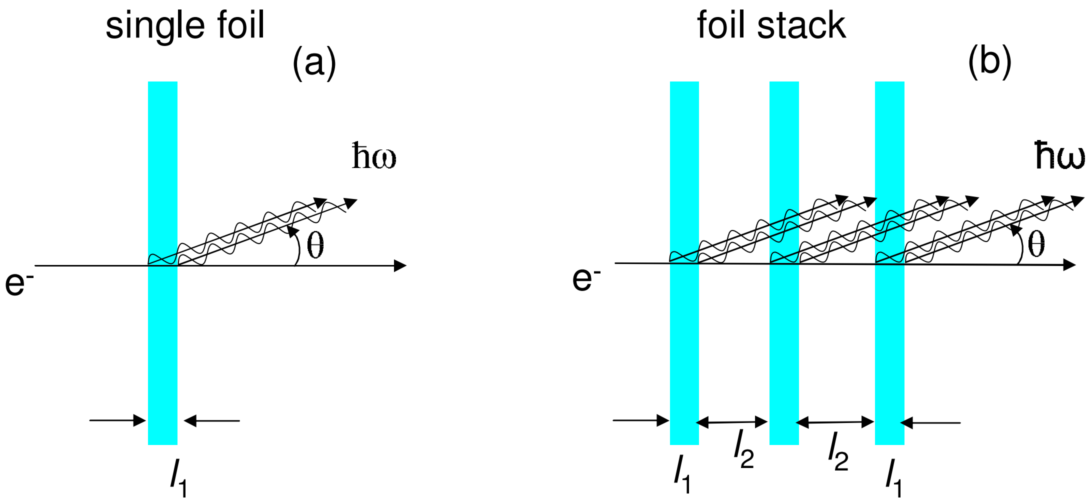

Figure 3.4: (a) Transition radiation from a single foil of thickness l_1. The emitted wave trains from the two surfaces may interfere constructively at a certain thickness l_1. (b) Transition radiation from several foils. The wave trains may interfere coherently at a certain distance l_2 and at a certain angle θ in forward direction.

The number of the emitted photons can be increased when the particles pass through several boundaries, see Fig. 3.4. The emerging waves from different interfaces may interfere constructively or destructively. The differential energy spectrum from a foil stack of M foils of thickness l_1 separated by equal spacing l_2 is given by [Che74, Bac94, Bac96]

$$\frac{d^2N_M}{(d\hbar\omega/\hbar\omega)d\Omega} = F_1 \cdot F_2 \cdot F_3 \ . \tag{3.3}$$

The factor $F_2 = 4\sin^2(l_1/Z_1)$ accounts for the interference of the radiation emitted from two interfaces of a single foil. For a foil stack having a number of foils M, the total amplitude of the radiation is given by the one-foil amplitude multiplied by the interference factor $F_3 = \sin^2(MX)/\sin^2(X)$, with $X = l_1/Z_1 + l_2/Z_2$. If the resonance conditions $l_1/Z_1 = (m - 1/2)\pi$ and $l_1/Z_1 + l_2/Z_2 = n\pi$ are satisfied simultaneously (m, n are integers with $m, n \geq 1$), the spectral intensity increases by a factor $4M^2$. The self-absorption of transition radiation within the foil stack results in a reduction of the outgoing photon intensity. It is especially relevant for lower-energy photons. Therefore, the radiator material must have a low atomic number (Z) in order to minimize the self-absorption ($\sim Z^2$) and also multi-scattering of electrons by the electric fields of atomic nuclei. The effects of electron beam divergence and electron multiple scattering in the foil stack result in an decrease of the enhancement factor $4M^2$. Also, as the beam divergence increases, the radiation cone with a minimum at the center begins to smear out and eventually the minimum may disappear.

The parameters of the two foil stacks used in the current work are tabulated in Tab. 3.1. The first foil stack has been optimized for a photon energy of 33 keV [Zah94, Joh95].

Table 3.1: Parameters of both foil-stacks used in this work.

X-ray energy optimization	33 keV	6 keV
Material	Polyimide ($C_{22}H_{10}N_2O_5$)	Polyimide ($C_{22}H_{10}N_2O_5$)
Number of foils	30	25
Thickness of foils [μm]	25	12.5
Distance between foils [μm]	75	100
Electron beam energy [MeV]	855	600
TR critical energy [keV]	41.6	28.9
Lorentz factor	1673	1174

However, it has its maximum flux at 10 keV. This foil stack has been used in the first set of experiments for refraction-contrast radiography. The calculated transition radiation characteristics are shown in Fig. 3.5. The estimated optimum X-ray energy to perform X-ray phase contrast imaging and in-line holography with the direct-exposure CCD camera, described in section 5.3, is 6 keV. Therefore a new foil stack has been constructed, which has its maximum photons flux at 6 keV. In doing this, a simulation program written by O. Kettig [Ket00] has been used. The simulation programm takes the multiple scattering of the electrons within the foils and also self absorption into account. The simulations showed that the optimal thickness of the polyimide foils is 12.5 μm, for which the transition radiation from the two interfaces of single foil interfere constructively. The optimal spacings between the foils are 100 μm at which the transition radiation from different foils interfere constructively. The number of foils is limited to 25 in order to minimize the self-absorption and electron multiple scattering. The calculated transition radiation characteristics are shown in Fig. 3.6.

3.3 Bremsstrahlung

When electrons are scattered in the positive electric fields of the nuclei in the radiator material they emit bremsstrahlung. The spectrum extends up to the maximum energy of the impinging electron. For bremsstrahlung produced by electrons with energy E at free atoms with atomic number Z, the number of photons d^3N_0 per electron, relative bandwidth $d\hbar\omega/\hbar\omega$, mass per unit area $d(\rho_i l_i)$, and solid angle $d\Omega$ amounts in Born approximation under the condition E [MeV] $\gg 100 \cdot Z^{-1/3}$ to [Jac83, Akh98]

$$\frac{d^3N_0}{(d\hbar\omega/\hbar\omega)d\Omega d(\varrho_i l_i)} = \frac{N_A}{M_m}\frac{3}{2\pi}\sigma_o F(\hbar\omega)\gamma^2\frac{1+\gamma^4\theta^4}{(1+\gamma^2\theta^2)^4} \quad , \tag{3.4}$$

with $\sigma_o = \alpha Z^2 r_e^2$, N_A the Avogadro-constant, M_m the molar mass, r_e the classical electron radius, γ the Lorentz factor of the relativistic electron, and θ the observation angle with respect to the electron beam velocity vector. The function $F(\hbar\omega)$ is given by

$$F(\hbar\omega) = 4[(1+\frac{(E-\hbar\omega)^2}{E^2} - \frac{2(E-\hbar\omega)}{3E})\ln(\frac{183}{Z^{1/3}}) + \frac{(E-\hbar\omega)}{9E}] \quad . \tag{3.5}$$

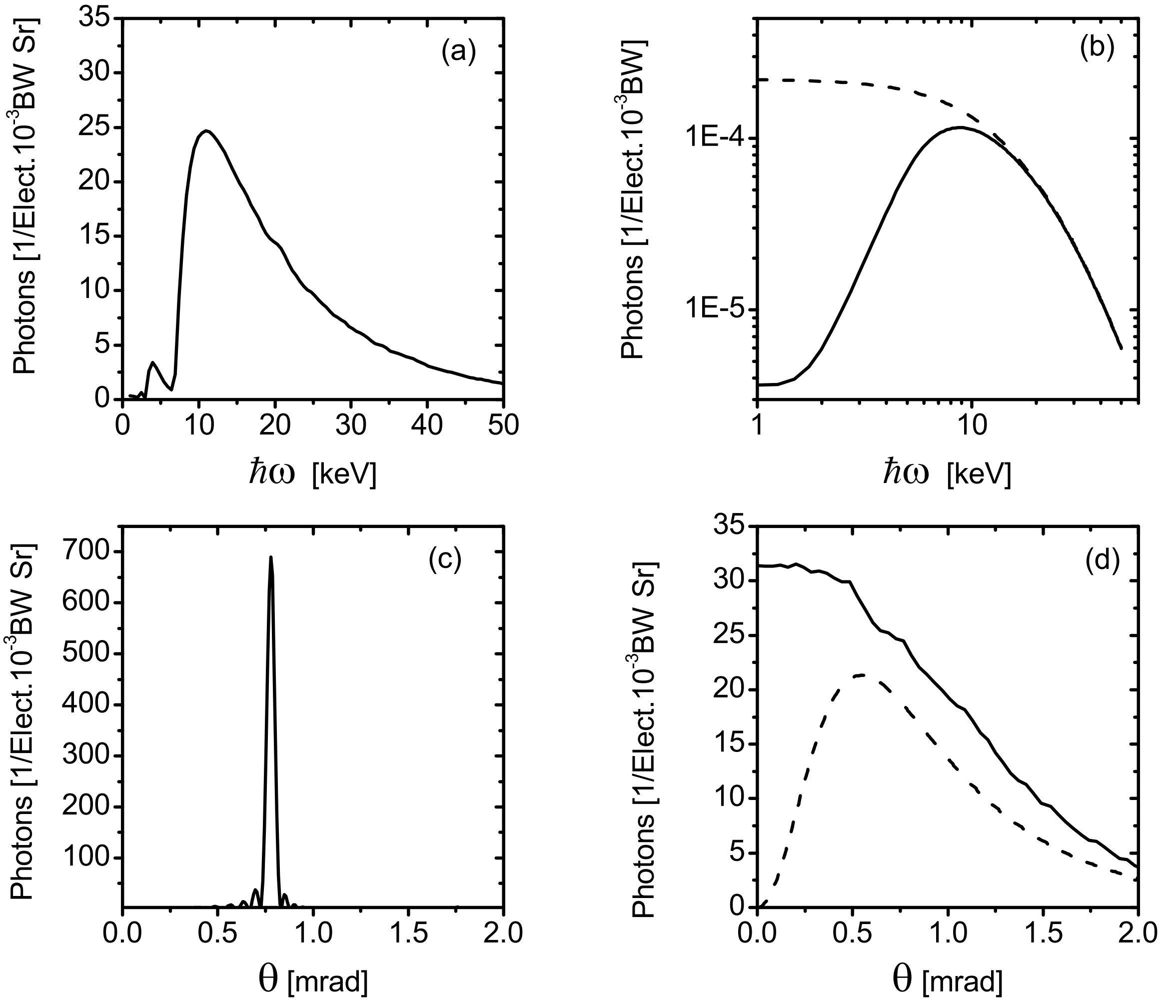

Figure 3.5: The calculated transition radiation spectra for 855 MeV electrons impinging perpendicularly on the foil stack which consists of 30 polyimide foils of 25 μm thickness and 75 μm separation. (a) Energy spectrum where multiple scattering, electron beam divergence (0.6 mrad) and self-absorption are taken into account. The spectrum peaks at about 10 keV. (b) Energy spectrum integrated over the solid angle. Dashed line: self-absorption neglected, full line: self-absorption taken into account. (c) Angular distribution of transition radiation at a fixed energy of 10 keV without beam divergence, multiple scattering and self absorption. (d) Angular distribution of the transition radiation at a fixed energy of 10 keV. Dashed line: electron multiple scattering is taken into account, full line: the electron beam divergence is included additionally [Ket00].

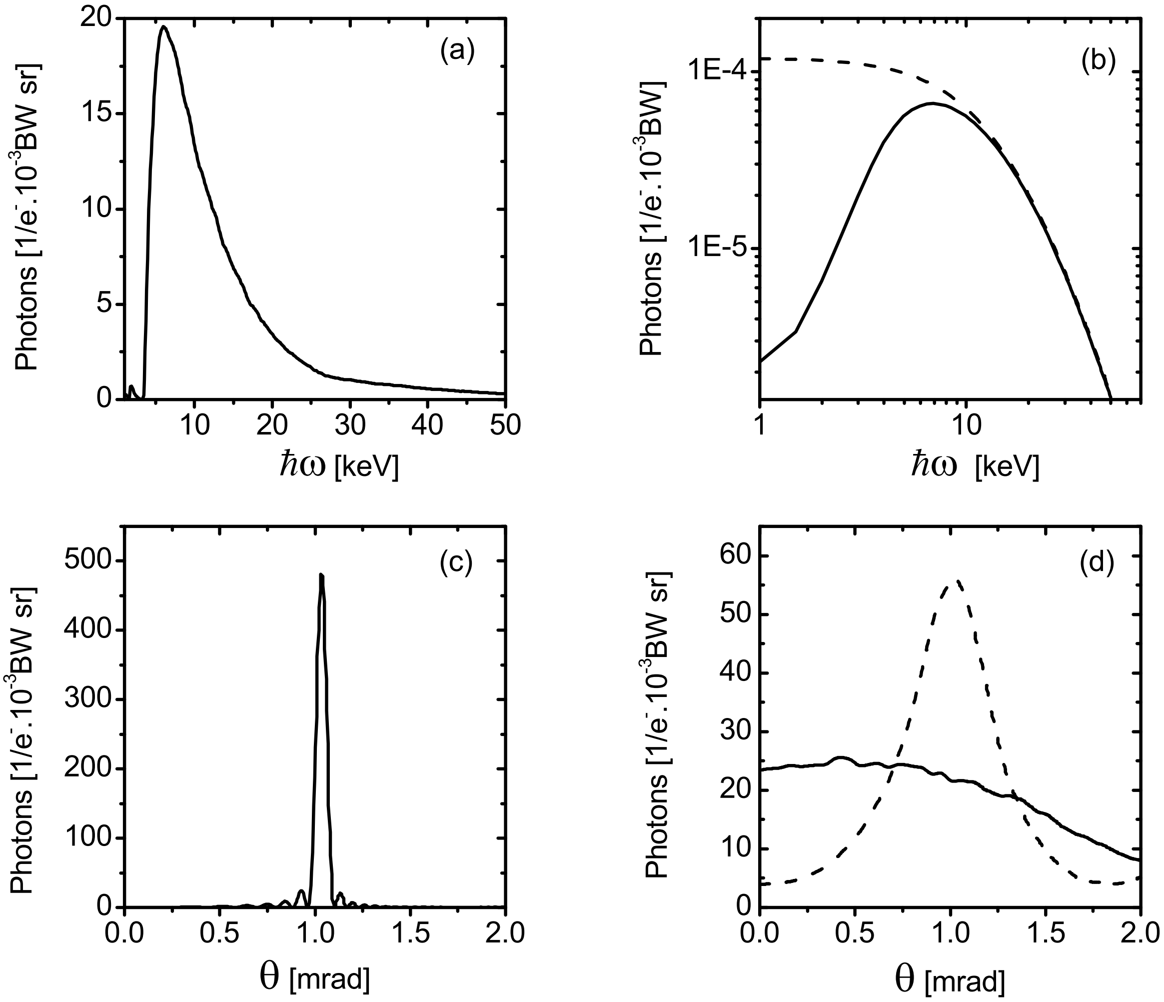

Figure 3.6: The calculated transition radiation spectra for 600 MeV electrons impinging perpendicularly on the foil stack which consists of 25 polyimide foils of 12.5 μm thickness and 100 μm separation. (a) Energy spectrum where multiple scattering, electron beam divergence (0.8 mrad) and self-absorption are taken into account. The spectrum peaks at about 6 keV. (b) Energy spectrum integrated over the solid angle. Dashed line: self-absorption neglected, full line: self-absorption taken into account. (c) Angular distribution of transition radiation at fixed energy of 6 keV without beam divergence, multiple scattering and self absorption. (d) Angular distribution of the transition radiation at a fixed energy of 6 keV. Dashed line: electron multiple scattering is taken into account, solid line: the electron beam divergence is included additionally [Ket00].

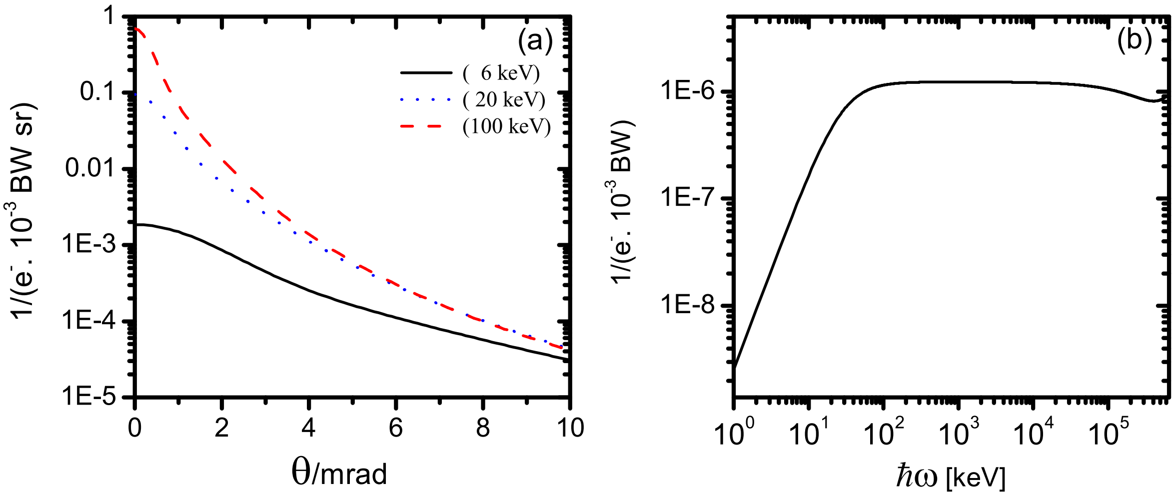

Figure 3.7: Calculated bremsstrahlung characteristics for the 6 keV polyimide foil stack at an electron beam energy of 600 MeV. (a) Angular distribution of photons with energies of 6 keV, 20 keV and 100 keV according to Eq. (3.6), (b) energy spectrum integrated over the solid angle. In the calculations the contributions of the spectra from the different elements comprising the polyimide radiator have been added according to their relative molecular weights.

In condensed materials the intensity and angular distribution of the bremsstrahlung is changed due to the density effect and is given by [Ter72, Bac98]

$$\frac{d^3N_0'}{(d\hbar\omega/\hbar\omega)d\Omega d(\varrho_i l_i)} = \frac{N_A}{M_m}\frac{3}{2\pi}\sigma_o F'(\hbar\omega)\gamma^2(\frac{\gamma'}{\gamma})^4\frac{1+\gamma'^4\theta^4}{(1+\gamma'^2\theta^2)^4} \qquad (3.6)$$

with

$$F'(\hbar\omega) = 4[(1+\frac{(E-\hbar\omega)^2}{E^2}-\frac{2(E-\hbar\omega)}{3E})\ln(\frac{183}{Z^{1/3}}\frac{\gamma}{\gamma'})+\frac{(E-\hbar\omega)}{9E}] \quad . \qquad (3.7)$$

and the modified Lorentz-factor

$$\gamma' = \frac{\gamma}{\sqrt{1+(\frac{\gamma\omega_p}{\omega})^2}} \quad . \qquad (3.8)$$

For high energy X-rays, i.e for $\lim_{\omega\to\infty}\gamma' = \gamma$, Eq. (3.6) reduces to Eq. (3.4).

Fig. 3.7 (a) shows the angular distribution of bremsstrahlung at some photon energies. The density effect manifests itself in a suppression of bremstrahlung emission at photon energies $\hbar\omega < \gamma\hbar\omega_p$. In addition, it can be seen that the angular distribution broadens the smaller the photon energy gets. However, the total emitted number of photons remains reduced despite this broadening. To demonstrate this, Eq. (3.6) has been integrated over the solid angle. With the aid of the integral

$$\int_0^\infty \frac{1+\gamma^4\theta^4}{(1+\gamma^2\theta^2)^4}2\pi\theta d\theta = \frac{2\pi}{3\gamma'^2} \qquad (3.9)$$

one obtains

$$\frac{d^2N_0'}{(d\hbar\omega/\hbar\omega)d(\varrho_i l_i)} = \frac{N_A}{M_m}\sigma_o(\frac{\gamma'}{\gamma})^2F'(\hbar\omega) \quad . \tag{3.10}$$

The corresponding spectral distribution is shown in Fig. 3.7 (b). Comparing the transition radiation spectrum Fig. 3.6 with the bremsstrahlung spectrum Fig. 3.7 (b) it can be concluded that the spectral distribution of transition radiation at a photon energy of 6 keV is about a factor 50 larger as the high energy bremsstrahlung spectrum in the region where the density effect can be neglected. However, the integrated high energy part of the bremsstrahlung spectrum yields $4.3{\cdot}10^{-3}$ photons per electron in the photon energy interval ranging from 10 MeV to the maximum energy of 600 MeV. This contamination of the transition radiation spectrum represents a background problem in the experimental area since photons which hit matter produce electromagnetic showers. We come back to this problem in appendix C.

4 Refraction contrast radiography

The counterpart of normal absorption contrast radiography with polychromatic X-rays for absorbing objects is the refraction contrast radiography for low absorbing, nearly transparent objects. The geometrical arrangement for this kind of radiography is very similar as that for the absorption contrast radiography with the fine difference that the transparent object must not be in direct contact with the detector plane but be positioned in some distance from it. The reasons will be outlined in more detail at the beginning of this chapter on the example of polyamide fibers before the experimental setup, measurements and the results are described to take refraction contrast radiographs at MAMI. Finally, further examples of some green leaves (*Rumex crispus* and *Ficus benjaminus*) will be presented in order to show how the contrast is significantly improved with a low absorbed dose.

4.1 Basic background

Principally, any kind of imaging also with X-rays is a wave optical phenomenon. However, indications of wave optics depend strongly on the geometrical arrangement of source, object and the detector. In Fig. 4.1 one can distinguish in essence four arrangements of the object between the source and detector plane. The source-to-detector distance will be assumed to be a constant. In this section the contact region (I) and the near field region (II) will be discussed in more detail.

4.1.1 Contact region

To start with, Eq. (2.18) is rewritten as $E(z_d,\omega)/E_0(z_d,\omega) \;=\; 1 + a(z_d,\omega)$ with

$$a(z_d,\omega) = \sqrt{\frac{\omega x_{sd}}{i2\pi c x_{so} x_{od}}} \int\limits_{-\infty}^{+\infty} [q(z_o,\omega)-1] \exp[i\frac{\omega}{2c}\frac{x_{sd}}{x_{so}x_{od}}(z_o - z_d\frac{x_{so}}{x_{sd}})^2] dz_o \;. \qquad (4.1)$$

Here are $\omega/c \;=\; k \;=\; 2\pi/\lambda$, and for a string with radius R

$$q(z_o,\omega) \;=\; \exp[-2(\omega/c)(i\delta+\beta)\sqrt{R^2 - z_o^2}\;]\;\theta(1-|z_o|/R) \qquad (4.2)$$

with $\theta(x)$ the unit step function, equal to zero for $x < 1$ and 1 for $x \geq 1$. At small distances $x_{od} \to 0$, for which $x_{so} \to x_{sd}$, the exponential in Eq. (4.1) oscillates rapidly

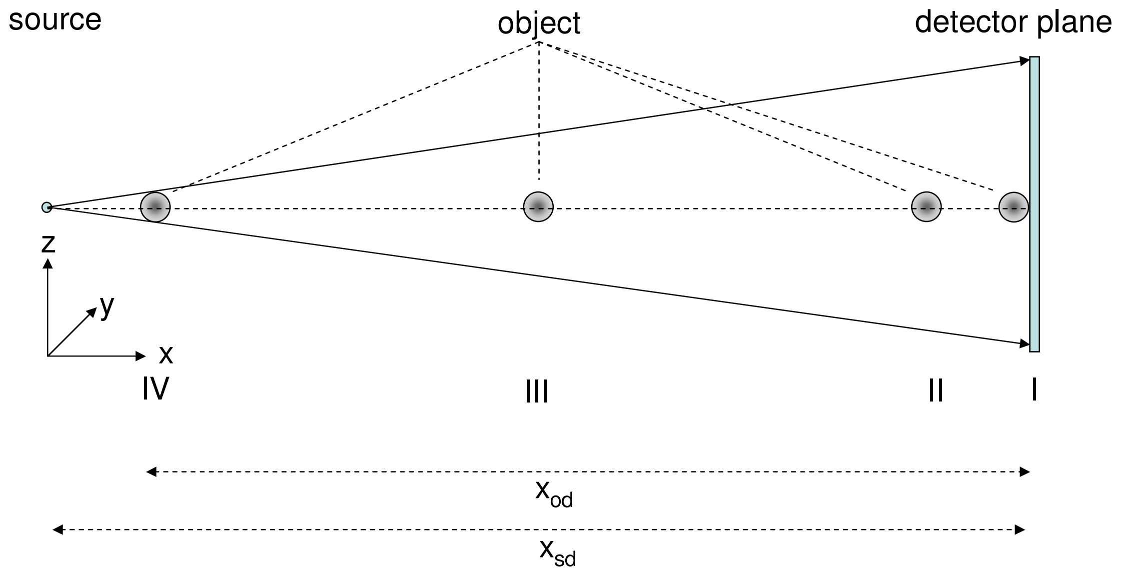

Figure 4.1: Imaging regimes as a function of the distance between object and detector plane x_{od}. The distance x_{sd} between source and detector is assumed to be given by the geometrical restrictions of the setup and kept constant. Four regions can be distinguished by the imaging distance x_{od}. For the contact region (I), i.e. $x_{od} = 0$, only the absorption within the object is of relevance (conventional radiography). In the near field region (II) a contrast can be generated even from low absorbing materials at sharp changes of the refraction index. In the intermediate region (III) and the region (IV) at close distance to the source a magnification of the object can be achieved. However, the image loos more and more resemblance with the object due to diffraction.

and a replacement with a δ_ε function can be performed according to

$$\delta_\varepsilon(z_o - z_d) = \lim_{x_{od}\to 0} \sqrt{\frac{\omega x_{sd}}{i2\pi c x_{so} x_{od}}} \exp[i\frac{\omega}{2c}\frac{x_{sd}}{x_{so}x_{od}}(z_o - z_d)^2]dz_o \quad . \tag{4.3}$$

Then Eq. (4.1) reduces to

$$a(z_d, \omega) = \int_{-\infty}^{+\infty} [q(z_o, \omega) - 1]\ \delta_\varepsilon(z_o - z_d)]dz_o = q(z_d, \omega) - 1 \ . \tag{4.4}$$

The amplitude ratio at the detector is $E(z_d, \omega)/E_0(z_d, \omega) = q(z_d, \omega)$. The function $q(z_o, \omega)$ can be written as $q(z_o, \omega) = \exp[-t_o(z_o)(i\delta(z_o) + \beta(z_o))]$ with $t_o(z_o)$ a function which characterizes the thickness dependence of the object. The intensity $|E(z_d, \omega)|^2$, the detector measures, is $|E(z_d, \omega)|^2 = |q(z_d, \omega)|^2 |E_0(z_d, \omega)|^2 = \exp[-2t_o(z_d)\ \beta(z_d))]|E_0(z_d, \omega)|^2$. Notice, that in the contact region $z_o = z_d$ holds. This is the commonly accepted result that only an absorption contrast of the object can be observed in X-ray imaging. Any phase changes caused by the object are unobservable in this geometry in which the object is in close contact with the detector.

4.1.2 Small distance between object and detector - phase contrast

An object with negligible absorption, i.e. with $\beta(z) \rightarrow 0$ anywhere, generates almost no contrast. This is, however, only true if the object is brought in close contact with the detector. If an object with still negligible absorption but with a rapid phase variation in some small domain is positioned at a finite but small distance $x_{od} \ll x_{sd}$ with respect to the detector plane a phase contrast may be observed. This has already been pointed out in section 2.2.1 in terms of geometrical arguments. In the picture of wave optics the exponential in Eq. (4.1) has now a typical width $\sigma_o = \sqrt{\lambda x_{so} x_{od}/(2\pi x_{sd})}$ in which it oscillates for a given z_d as a function of z_o not too rapidly. It can be seen from Eq. (4.2) that at the string border a large phase change $\Delta\phi_{string} = 2(\omega/c)\delta \cdot R\sqrt{1-[(R-\Delta z_o)/R]^2}$ may occur in a small distance Δz_o close to $z_o = R$, and around $z_d \simeq Rx_{sd}/x_{so}$ now interference fringes may show up, similar as those shown in Fig. 2.7 (a), provided $\Delta z_o < \sigma_o$ holds. If this condition would not be fulfilled, but instead if $\Delta z_o \gg \sigma_o$ would apply, the rapidly oscillating integrand would give an integral value close to zero for any z_d around Rx_{sd}/x_{so}.

For polychromatic X-rays the contrast is generated by an incoherent superposition of the interference patterns of the various differentially small monochromatic components of the spectrum. The interference pattern has been calculated on the basis of the Fresnel- Kirchhoff integral Eq. (2.18) for a string with the normalized intensity $I^{(\omega)}_{n,w}(z_d, \omega) = |E(z_d, \omega)|^2/|E_0(z_d, \omega|^2$ as

$$I_{n,w}(z_d) = \frac{1}{\sqrt{2\pi}\sigma} \int\int I^{(\hbar\omega)}_{n,w}(z'_d, \hbar\omega) \cdot \exp[-\frac{(z_d - z'_d)^2}{2\sigma^2}] \cdot f(\hbar\omega) \cdot dz'_d \cdot d\hbar\omega \quad . \tag{4.5}$$

A realistic X-ray energy distribution function $f(\hbar\omega)$, the X-ray film records, has been assumed, the spectrum of which is shown in Fig. 4.6. How it comes about will be explained in the subsection 4.2.2 below. To save computer time, only discrete values $f_i, i = 8, 30$ in steps of 1 keV were taken in the photon energy interval between 6 and 30 keV. The results of these calculations are depicted in Fig. 4.2 (a) for a transparent object. Just the main two fringes are visible while the others more or less are wiped out. The reason is that, because the first maximum and minimum for different wavelengths appear nearly at the same position, all other fringes overlap incoherently and cancel each other. The final radiograph contains just one maximum and one minimum at the geometrical borders of the object and the resulting black/white contrast images the object. The contrast at the edges of the object is also called "edge enhancement" or simply "phase contrast".

The projected beam spot size $(x_{od}/x_{so})\sigma_s$, the finite resolution of the detector σ_d and the pixel resolution σ_p of the optical film scanner are taken into account by the Gaussian in Eq. (4.5) with

$$\sigma = \sqrt{(x_{od}/x_{so})^2\sigma_s^2 + \sigma_d^2 + \sigma_p^2} \quad . \tag{4.6}$$

They further reduce the contrast as can be seen at Fig. 4.2 (b).

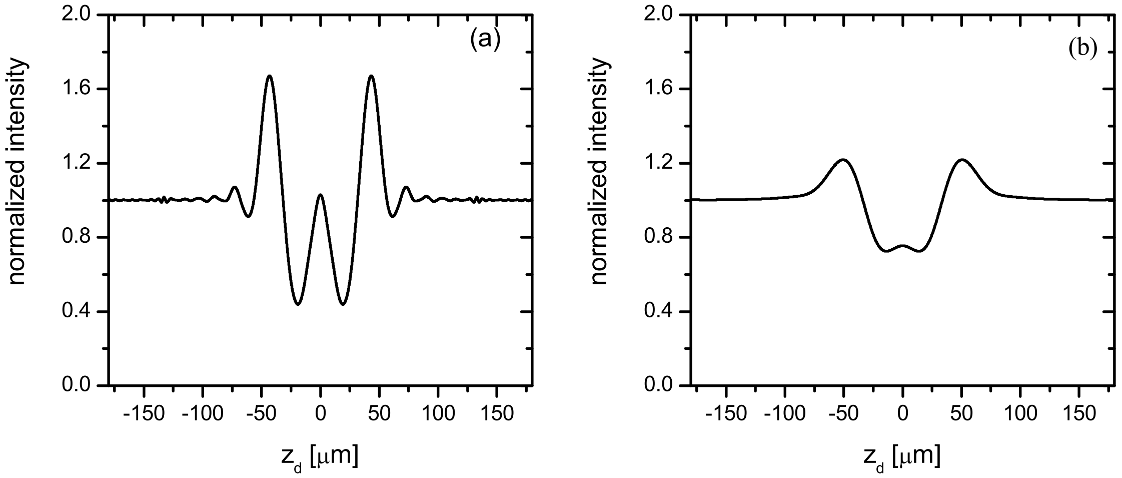

Figure 4.2: Calculated intensity pattern for a polyamide string of 30 μm diameter in case of polychromatic X-rays. Standard deviation of the X-ray source spot size $\sigma_h = 8.6$ μm, of the detector resolution $\sigma_d = 1.96$ μm, and the film scanner resolution $\sigma_p = 9.77$ μm. The source-to-object distance is $x_{so} = 5.88$ m and the object-to-detector distance $x_{od} = 5.5$ m. (a) The weighted intensity profile produced by the X-ray spectrum recorded by the X-ray film, see Fig. 4.6 (c). (b) After convolution with a Gaussian which takes into account X-ray source size projection on the detector plane and detector resolution according to $\sigma = \sqrt{(x_{od}/x_{so})^2\sigma_v^2 + \sigma_d^2 + \sigma_p^2} = 12.8$ μm.

4.1.3 Refraction contrast in the picture of geometrical optics

The calculation of the refraction contrast in the framework of wave optics is the only correct description. However, the examples shown in the last subsection on this basis require considerable computational effort and can not easily be used for involved simulations of the experiments to be carried through. Therefore, a simple model has been developed in the framework of geometrical optics [Bac05] which is described in Appendix A.1.

The normalized total intensity distribution $I_{n,g}^{(\omega)}$ of a refraction contrast radiograph for a transparent string of a radius R and refractive index decrement δ_2, which is surrounded by a medium of refractive index decrement δ_1, is expressed by

$$\begin{aligned} I_{n,g}^{(\omega)}(z_d/R,\omega) &= \theta(\frac{z_d}{R\cdot(1+x_{od}/x_{so})}-1)+\frac{dN}{d(z_d/R)}/\frac{dN_0}{d(z_d/R)} = \\ &= \theta(\frac{z_d}{R\cdot(1+x_{od}/x_{so})}-1)+\frac{(1+x_{od}/x_{so})}{(1+x_{od}/x_{so})+A(\omega)/(1-(z_o/R)^2)^{\frac{3}{2}}} \end{aligned} \tag{4.7}$$

with z_o/R a solution of the equation

$$\frac{z_d}{R} = \frac{z_o}{R}(1+\frac{x_{od}}{x_{so}}) + A(\omega)\frac{z_o/R}{\sqrt{1-(z_o/R)^2}} \quad , \tag{4.8}$$

with $\theta(x)$ is the unit step function, and $A(\omega) = 2x_{od}\delta(\omega)/R$. A typical intensity distribution $I_{n,g}^{(\hbar\omega)}(z_d/R, \hbar\omega)$ as a function of the reduced detector coordinate z_d/R is shown in Fig. 4.3 (a), dashed curve. The sharp increase of the intensity at the geometrical borders of the string originates from the fact that in this model wave optical phenomena are omitted ($\lambda \rightarrow 0$). However, these can be approximately taken into account by a convolution with a Gaussian of standard deviation $\sigma_w = \sqrt{\lambda x_{sd} x_{od}/(2\pi x_{so})}$ which can be estimated from the exponential in Eq. (4.1). The argument is that for a fixed point z_o in the object the typical spread in the detector plane is given by a region $|z_o x_{sd}/x_{so} - z_d| < \sigma_w$. For $|z_o x_{sd}/x_{so} - z_d| \gg \sigma_w$ the exponential oscillates rapidly and the mean value in z_d approaches zero. Again, projected source size σ_s, detector resolution σ_d and pixel resolution of the film scanner σ_p deteriorate the contrast. The total standard deviation of the Gaussian with which the initial distribution must be convoluted is given by

$$\sigma = \sqrt{(\frac{x_{od}}{x_{so}})^2 \sigma_s^2 + \sigma_d^2 + \sigma_p^2 + \frac{\lambda x_{od} x_{sd}}{2\pi x_{so}}} \quad . \tag{4.9}$$

In the final intensity distribution $I_{n,g}(z_d/R)$ also the energy distribution of the primary polychromatic X-ray beam, including the response of the X-ray detector, has to be taken into account. It is obtained by an integration with the normalized distribution function $f(\hbar\omega)$ which is the X-ray spectrum recorded by the X-ray film, see below subsection 4.2.2. The result is

$$I_{n,g}(z_d/R) = \frac{1}{\sqrt{2\pi}\sigma} \int \int I_{n,g}^{(\hbar\omega)}(z'_d/R, \hbar\omega) \cdot \exp[-\frac{(z_d - z'_d)^2}{2\sigma^2}] \cdot f(\hbar\omega) \cdot dz'_d \cdot d\hbar\omega \quad , \tag{4.10}$$

with σ given by Eq. (4.9).

In Fig. 4.3 (b) the calculated contrast is shown. With a beam spot size approaching zero and ideal resolution of the X-ray film the contrast C_{ref} in the limit of geometrical optics ($\lambda \rightarrow 0$) is larger than 55%. Wave optical phenomena considerably diminish the contrast at small distances between object and detector and a large distance would be favorable. However, the finite source spot size and the finite detector resolution diminish the contrast as well. To keep the influence of the finite beam spot size as small as possible, the object-to-detector distance should be small. Then, also the detector resolution must be increased, however, it must not be much better than the wave optical value $\sigma_w = \sqrt{\lambda x_{sd} x_{od}/(2\pi x_{so})}$. In addition, it must also be taken into account that, despite at larger object-to-detector distances x_{od} the contrast increases, the quality of the edge enhancement deteriorates because of a broadening of the edge.

As discussed in the last paragraph, there are many conflicting requirements for the optimum object-to-detector distance x_{od} and an experimental investigation of this subject is absolutely imperative.

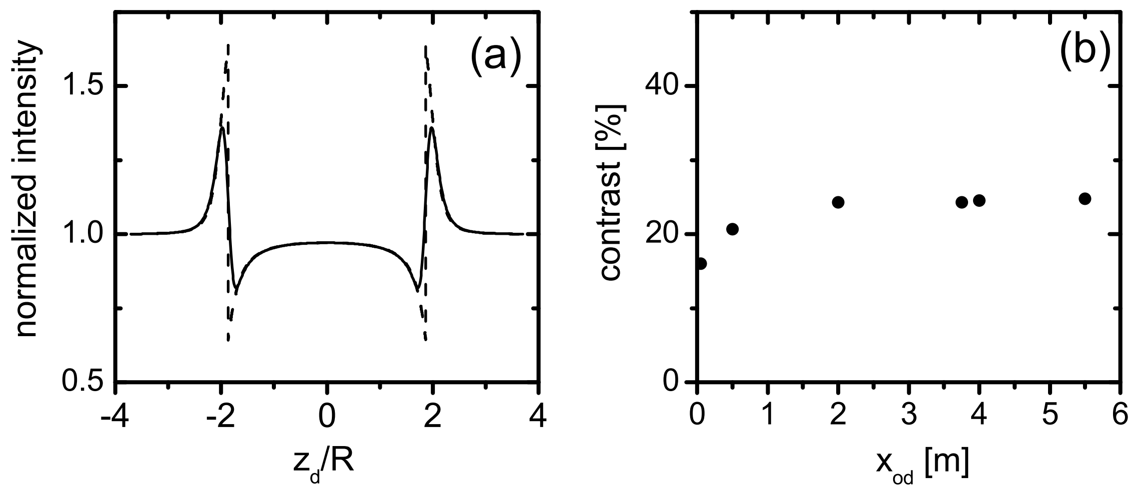

Figure 4.3: Calculated normalized intensity profiles of a polyamide string. Photon energy $\hbar\omega_0$=19.6 keV, string diameter 135 μm, source-to-object distance $x_{so} = 5.88$ m, object-to-detector distances $x_{od} = 5.5$ m , $\delta(\hbar\omega_0) = 6.75 \cdot 10^{-7}$, $\beta(\hbar\omega_0) = 2.6 \cdot 10^{-10}$. (a) Dashed line: calculations based on geometrical optics according to Eq. (4.8), full line: wave optics approximately taken into account according to Eq. (4.10) with $f(\hbar\omega) = \delta_\varepsilon(\hbar\omega - \hbar\omega_0)$ and $\sigma = \sigma_w = \sqrt{\lambda x_{sd} x_{od}/(2\pi x_{so})}$. (b) Contrast C_{ref} as a function of the object-to-detector distance x_{od}.

4.2 Experimental

4.2.1 Set-up

The principle of the refraction contrast radiography is depicted in Fig. 4.4. The 855 MeV electron beam produces in a transition radiation foil stack a polychromatic X-ray beam which propagates in forward direction. The electron beam is deflected by a bending magnet and guided into the beam dump. In a distance x_{od} from the X-ray film the objects to be imaged are located.

An overview of the experimental setup at MAMI with all relevant components for the refraction contrast radiography is shown in Fig. 4.5. The beam line has been designed and constructed by F. Hagenbuck [Hag01]. The electron beam of an energy 855 MeV is focused at the center of the target chamber by means of the quadrupole doublet Q1. Inside the target chamber the transition radiation foil stack and beam diagnostic elements are installed.

The foil stack consists of 30 polyimide foil with a thickness of 25 μm and spacings between the foils is of 75 μm (the 33 keV foil stack in Table 3.1). The spot size of the electron beam has been measured by a tungsten wire of 10 μm diameter. The electron beam is guided behind the target chamber to the beam dump. The beam guide system is shielded by a concrete wall of 1 m thickness and 3.5 m height from the experimental

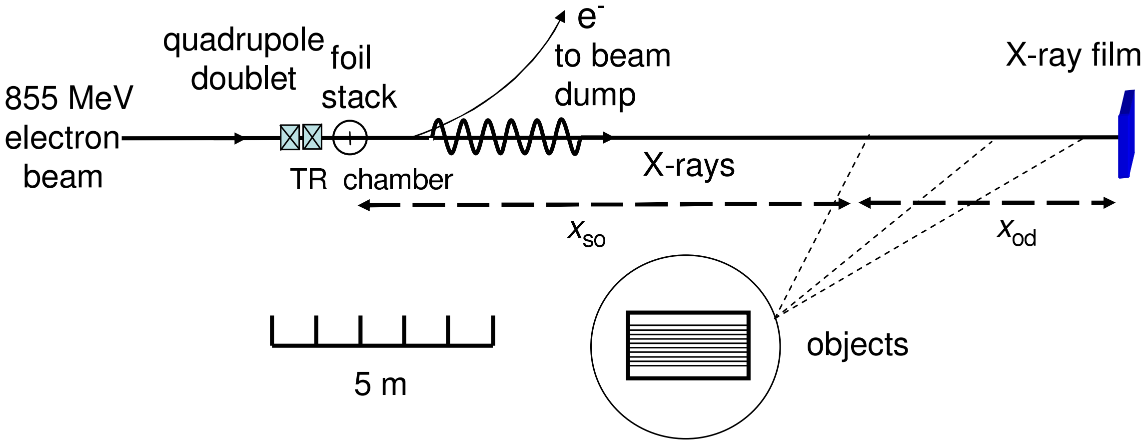

Figure 4.4: Schematic diagram showing the experimental setup for refraction contrast radiography. The maximum source-to-detector distance is $x_{sd} = 13$ m, measurements at object-to-detector distances $x_{od} = 13$ from 0 to 7.12 m.

area to reduce the background produced by electrons which emitted a bremsstrahlung photon in the TR foil stack and left the beam line behind the bending magnet BM2, as well as the background from the beam dump. The polychromatic X-rays proceed in forward direction and leave the vacuum system through a polyimide exit window of 120 μm thickness in a distance of 5.88 m from the foil stack. The objects to be imaged are mounted in air at different distances from the target x_{so} and from the X-ray film x_{od}, with 5.88 m $< x_{so} <$ 13 m and 0 m $< x_{od} <$ 7.12 m. The maximum available source-to-detector distance x_{sd} is about 13 m.

4.2.2 X-ray film

For the refraction contrast radiography experiments as position sensitive detectors X-ray films have been used. X-ray films have a high spatial resolution of up to 2 μm (FWHM), a large working area and a high quantum efficiency over a wide range of photon energies. These advantages are the reason that X-ray films continue to be used to record intensity information despite of the disadvantage of their limited dynamic range which is typically in the order of 1:1000.

The X-ray film used in the current work is Mamoray MR5 II PQ produced by Agfa[1]. It is based on silver bromide with an emulsion thickness of $d_f = 12$ μm [Hen86]. The X-ray films have been used without intensifier screens (direct exposure) to keep the benefit of high spatial resolution of about 200 lp/mm[2]. The utilization of an intensifier screen would degrade the spatial resolution to (15-2)0 lp/mm [Spy02]. The

---

[1] Agfa-Gevaert N.V., B2640 Mortsel Belgium

[2] lp means line pair

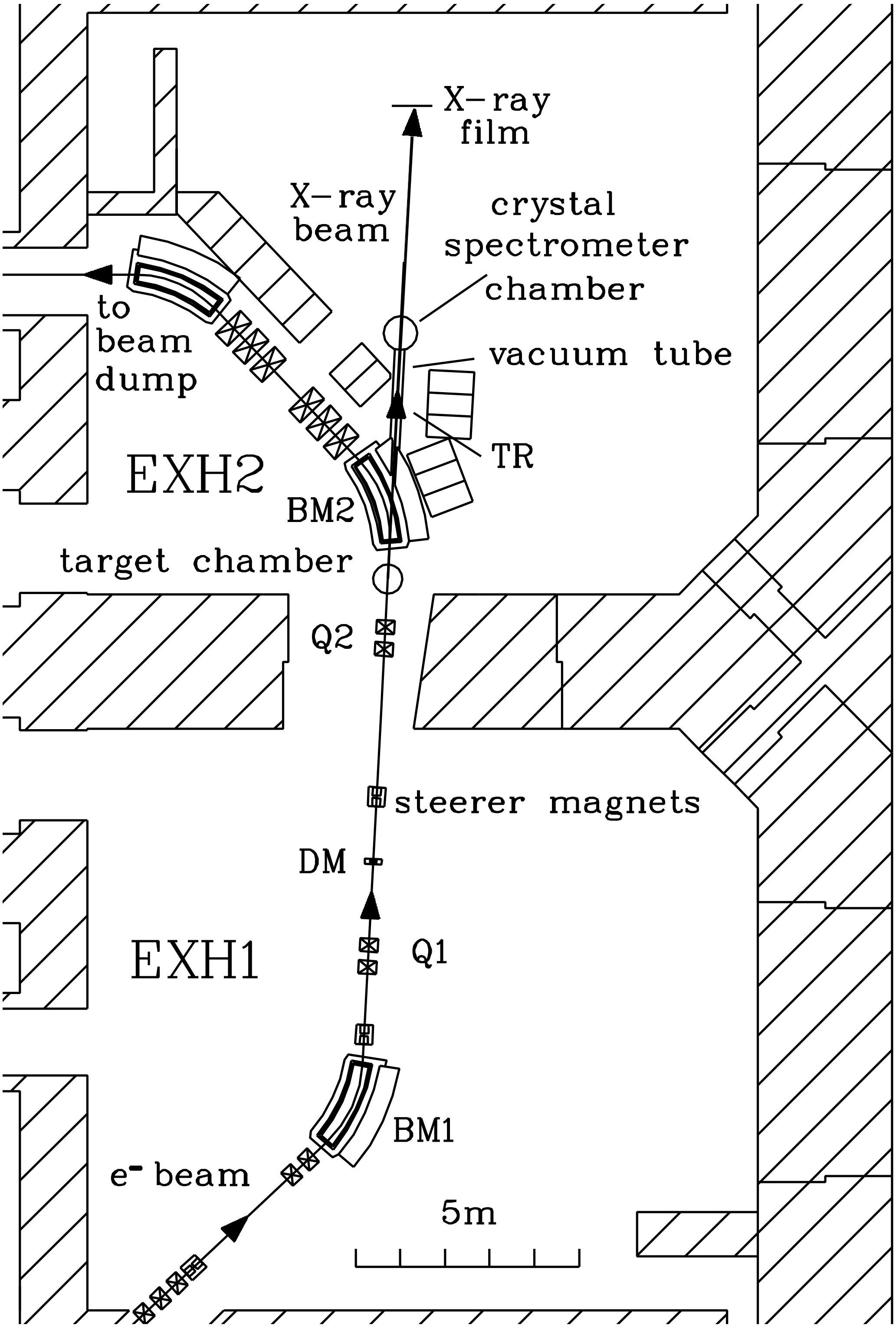

Figure 4.5: Overview of the experimental setup for the refraction contrast radiography in the experimental areas EXH1, EXH2 of MAMI. The relevant components are a focusing quadrupole doublet Q2 in a distance of 0.94 m from the transition radiation (TR) foil stack in the target chamber, the bending magnet BM2, which deflects the electron beam, a vacuum tube which connects the target chamber with an additional crystal spectrometer chamber and the X-ray film. A quadrupole doublet Q2 installed in EXH1 is used to prepare the electron beam for an optimal focusing by the quadrupole doublet Q1.

typical absorption efficiency of the X-ray film is given by the factor $\exp[-\mu_f(\hbar\omega)d_f]$, with $\mu_f(\hbar\omega)$ the linear attenuation coefficient, d_f the thickness of the emulsion, and is shown in Fig. 4.6 (a). It varies between about 2-60% for energies between 6 and 50 keV [Dia74]. As shown in Fig. 4.6(b) the low energy X-ray spectrum at the position of the X-ray film hardens since photons of the radiator foil stack are absorbed in the exit window made of polyimide with thickness $d_p = 120$ μm and in the distance of $d_a \simeq 5.5$ m the photons travel in air. The hardening is taken into account by the factor $(1 - \exp[-\mu_p(\hbar\omega)d_p]) \cdot (1 - \exp[-\mu_a(\hbar\omega)d_a])$. The effective photon spectrum impinging the X-ray film is shown in Fig. 4.6 (c). The quantities $\mu_p(\hbar\omega)$, and $\mu_a(\hbar\omega)$, are the linear attenuation coefficients, of the polyimide exit window, and of air, respectively. They were taken from [PhyXX, Sto70, Hen93].

The exposed X-ray films were processed manually. They were developed with G135A and G153B developer for three minutes at 20 °C. Then they were fixed with G354 fixer for three minutes at the same temperature. Finally the films were rinsed with water for 5 minutes and then dried. The X-ray films were digitized with a Nikon film scanner Super CoolScan 4000 ED which has a spatial resolution of 4000 dpi [3] corresponding to a pixel size of (6.35×6.35) $\mu\mathrm{m}^2$ or by a Nikon film scanner Super CoolScan 2700 ED with spatial resolution 2700 dpi corresponding to (9.4×9.4) $\mu\mathrm{m}^2$ pixel size.

The spatial resolution of the X-ray film has been determined by measuring the edge spread function of a razor-blade mounted in contact with the film. The light emitted from a condenser lens light source of 500 μm diameter was used, mounted at a distance of 70 cm from the film. A small razor-blade-to-film distance, a long light source-to-razor-blade distance and a small light source size avoid the deterioration of the edge spread function by the source projection on the film and also diffraction. The X-ray films, as usual, have been developed under the instructions specified by the manufacturer in order to get maximum performance. The film was digitized with an optical microscope equipped with a high resolution CCD camera and an 8 bit ADC of type F-View XS [OlyXX]. A projection of the intensity profile parallel to the edge has been produced to improve the statistics. The intensity profile of the edge spread function was smoothed and differentiated to get finally the spatial resolution (4.6 ± 0.2) μm (FWHM) of the film as shown in Fig. 4.7. Unfortunately, no other published results are reported on the spatial resolution of this film in case of direct exposure since it is originally designed to be used in combination with intensifier screens.

4.3 Measurements

At the beginning of each measurement the electron beam spot size was optimized. Its size at the foil stack determines the X-ray spot size. The electron spot size was measured by a tungsten wire of (10 ± 1) μm diameter. Two crossed tungsten wires were mounted in the transition radiation chamber on a goniometer. The goniometer gives the possibility to adjust the target position with respect to the electron beam

---

[3] dots per inch

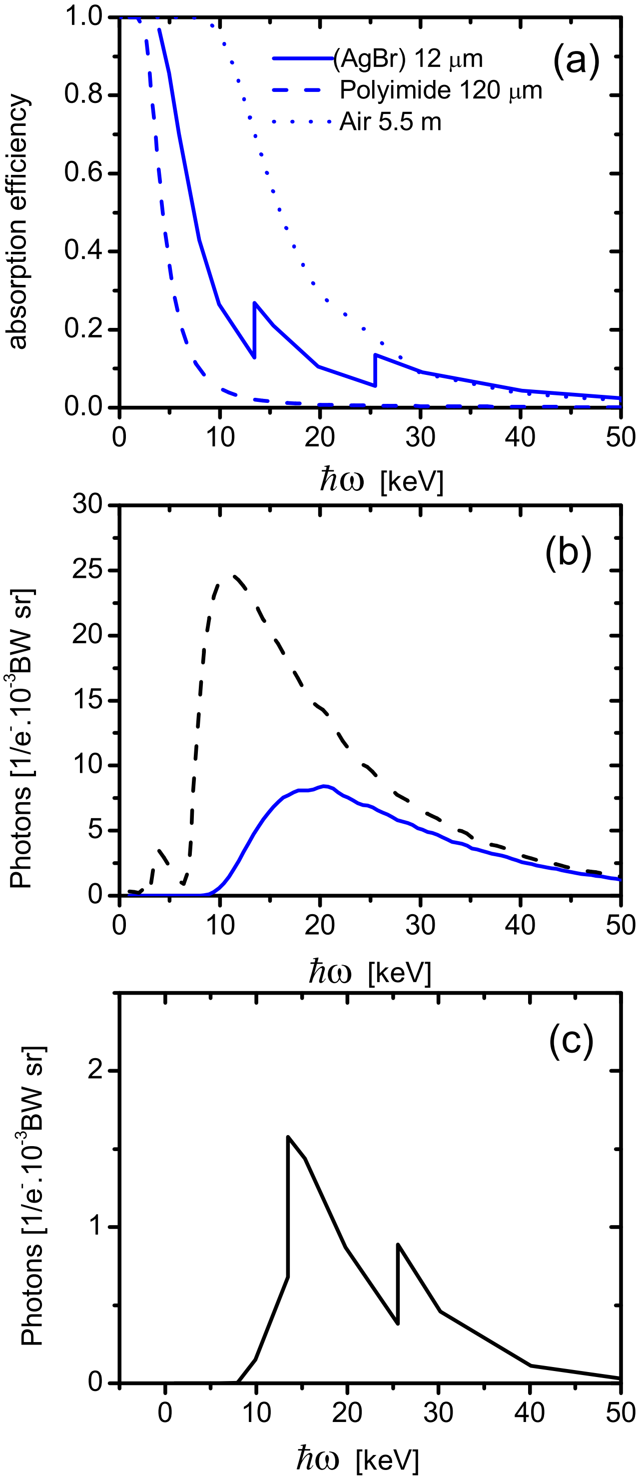

Figure 4.6: X-ray spectrum recorded by the X-ray film. Part (a) represents the absorption coefficients $\mu_f(\hbar\omega)$, $\mu_p(\hbar\omega)$ and $\mu_a(\hbar\omega)$ of the X-ray film emulsion of thickness 12μm with a composition of 3.1 mg/cm^2 Ag and 4.66 mg/cm^2 Br, polyimide, and air, respectively. Part (b) shows as dashed line the transition radiation spectrum of the 33 keV foil stack, produced by 855 MeV electrons, see chapter 3, and as solid line the spectrum after transmission through the polyimide window with thickness of 120 μm and travel of a distance of 5.5 m in air. Part (c) is the recorded spectrum by the X-ray film [PhyXX].

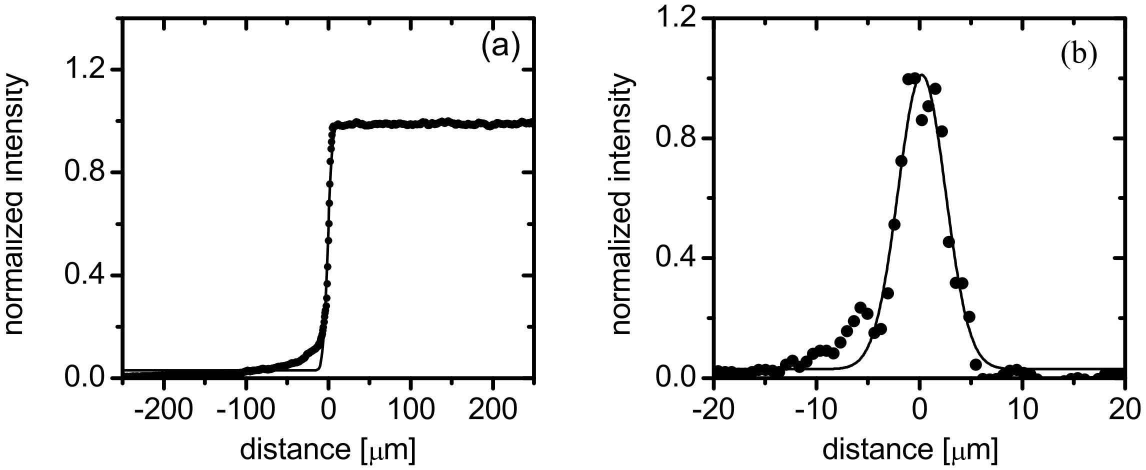

Figure 4.7: Edge spread function (a) and spatial resolution (b) of the X-ray film Mamoray MR5 II PQ (Agfa). Points are the experimental results, solid lines fits with an error function (a) and a Gaussian (b). The spatial resolution of the film amounts to (4.6±0.2) μm (FWHM).

direction. When the tungsten wire moves across the electron beam, bremsstrahlung is emitted. Its intensity is recorded by a photodiode, positioned in forward direction close to the X-ray film position in Fig. 4.5, as a function of the position of the tungsten wire. The measured electron beam profiles are shown in Fig. 4.8. The electron beam spot size after deconvolution with the wire scanner sensitivity profile function (semicircle), representing approximately the response function of the tungsten wire, was $\sigma_h = (8.6 \pm 0.1)$ μm in the horizontal direction and $\sigma_v = (7.5 \pm 0.1)$ μm in the vertical direction.

In the next step the X-ray beam spot size at the position of the X-ray film has been measured. It is shown in Fig. 4.9 and the corresponding intensity profiles in Fig. 4.10. The illuminated area at a distance of 10 m from the source amounts to approximately (100 × 30) mm^2 (FWHM) which gives the opportunity to image objects up to the same size. The expected X-ray beam size at 10 m from the source can be estimated from Fig. 3.5 to be about 28 mm (FWHM) in both directions. However, with the measured electron beam spot size and the beam emittances $\epsilon_h = 7.4 \cdot 10^{-3}$ mm mrad and $\epsilon_v = 6.6 \cdot 10^{-4}$ mm mrad, standard deviations of the beam divergence $\sigma_h^{'} \geq 0.9$ mrad and $\sigma_v^{'} \geq 0.09$ result, respectively. From these numbers an emittance-given spot size in 10 m distance of (90×9) mm^2 (FWHM) can be calculated. From these considerations it can be concluded that the measured width in horizontal direction is determined by the emittance of the electron beam while in vertical direction by the TR emission characteristics.

The objects to be imaged were polyamide fibres with the chemical formula $C_{12}H_{22}N_2O_2$, a density of 1.14 g/cm^3, and complex refraction index parameters $\delta = 6.75 \cdot 10^{-7}$ and $\beta = 2.6 \cdot 10^{-10}$ at a photon energy of 19.6 keV. The strings have different diameters of 30, 170, 270, 350 and 450 μm. These objects have negligible absorption at a photon energy of 19.6 keV ranging from 0.1% to 1.26%, which assures that they are optimal

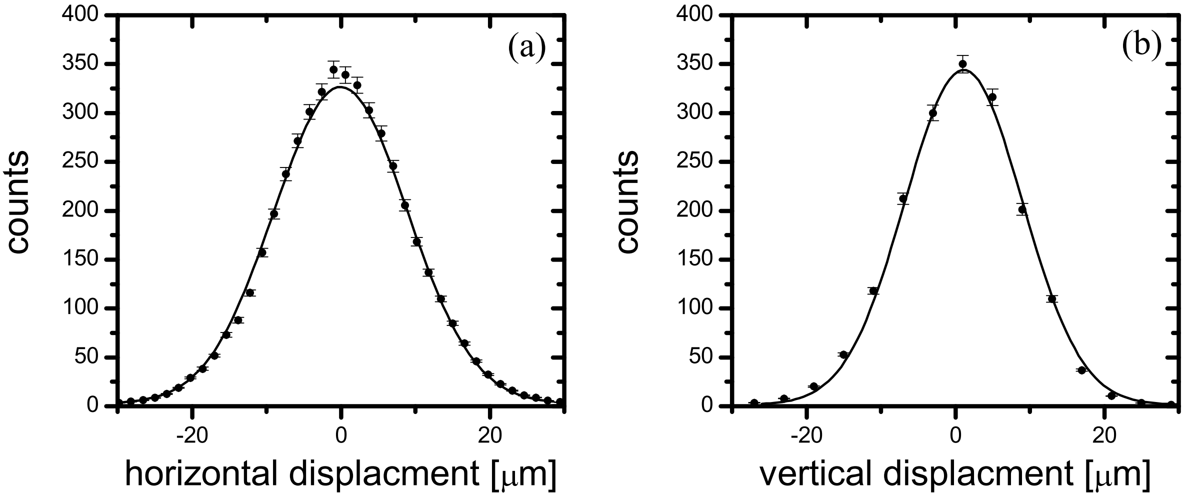

Figure 4.8: Measured electron beam spot size at an electron beam energy of 855 MeV, (a) in the horizontal direction, and (b) in the vertical direction. The electron beam current was 335 nA, the step increment horizontally 1.6 μm and vertically 4 μm and the recording time 2.5 s per point. The measured standard deviations of the spot size after deconvolution are $\sigma_h = (8.6 \pm 0.1)$ μm in the horizontal and $\sigma_v = (7.5 \pm 0.1)$ μm in vertical direction. Taken from [Hag01].

phase objects. In addition, two dimensional objects as green leaves, *Rumex crispus* and *Ficus benjaminus*, were imaged.

Different radiographs have been recorded at different object-to-detector distances x_{od} ranging from 0 to 5.5 m and also with different exposure times depending on the source-to-detector distance x_{sd}, and also on the electron beam current. An example of a measurement is shown in Fig. 4.11, where the visibility enhancement of low absorbing materials like polyamide strings can clearly be recognized.

4.4 Determination of the normalized contrast

The conversion of the high resolution information on the X-ray film requires a point by point conversion of the film images into digital form. This procedure may also limit the dynamical range of the radiograph if the digitizing depths of the scanning densitometer is not sufficient. Since our laboratory is neither equipped with a high performance developing station for X-ray films (the exposed X-ray films must be carefully processed) nor a high performance densitometer, reductions in the obtainable accuracy could not be avoided. In this section the applied procedure to obtain quantitative intensity information from the radiographs despite these shortcomings is described.

The primary quantity which is measured by an X-ray film is the photographic density

Figure 4.9: X-ray beam spot size in a distance of 10 m from the X-ray source as taken by the X-ray film. The spot size amounts to about 100 mm in horizontal and 30 mm in vertical direction. This shape results from the electron beam divergence and the transition radiation emission cone.

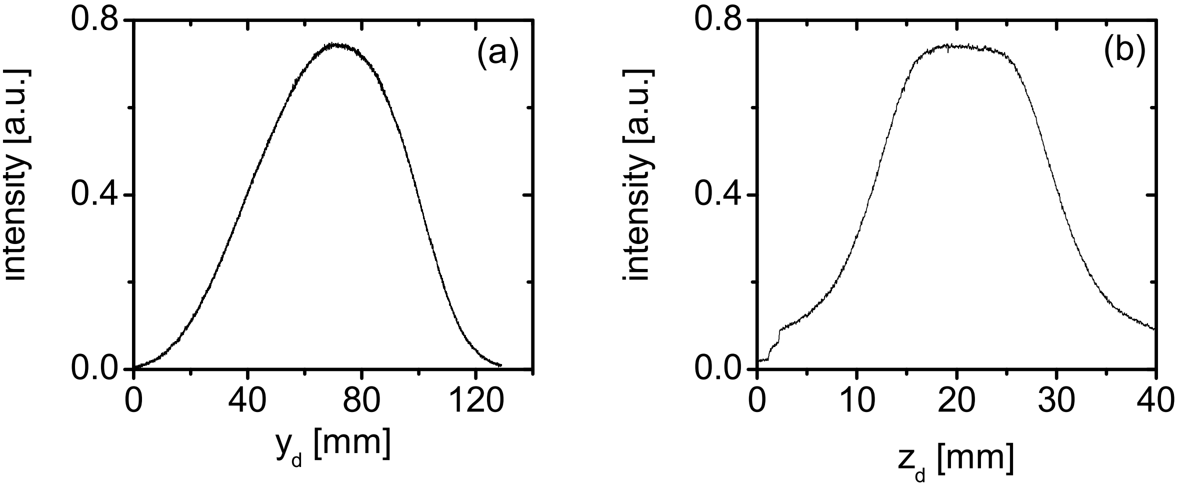

Figure 4.10: Intensity profile of the radiograph shown in Fig. 4.9. (a) Horizontally and (b) vertically

D_p. It is defined as the basis 10 logarithm as $D_p = \log(i_0/i)$ with i_0 the optical light intensity impinging on the film and i the intensity measured by the detector of the densitometer. From this primary quantity the so called fog $D_f = \log(i_0/i_{0f})$ of an unexposed part of the film must be subtracted to obtain the density $D = D_p - D_f = \log(i_{0f}/i)$ which must be related to the exposure b of the film, i.e. the energy per unit area dE/dA deposited by the X-ray photons at a certain location $\overrightarrow{r}$ at the film. The latter is given here by the angles θ and φ which describe the photon emission characteristics of the X-ray source. The exposure is given by

$$\begin{aligned}\frac{dE}{dA}(\theta,\varphi) &= \frac{(I_e/e)\cdot t_{exp}}{x_{sd}^2}\int\left(\frac{d^2N(\theta,\varphi,\hbar\omega)}{(d\hbar\omega/\hbar\omega)d\Omega}\right)_s \cdot (1-\exp[-\mu_p(\hbar\omega)d_p])\cdot \\ &\quad \cdot(1-\exp[-\mu_a(\hbar\omega)d_a])\cdot(1-\exp[-\mu_o(\hbar\omega)d_o])\cdot\exp[-\mu_f(\hbar\omega)d_f]\cdot d\hbar\omega\ .\end{aligned}$$

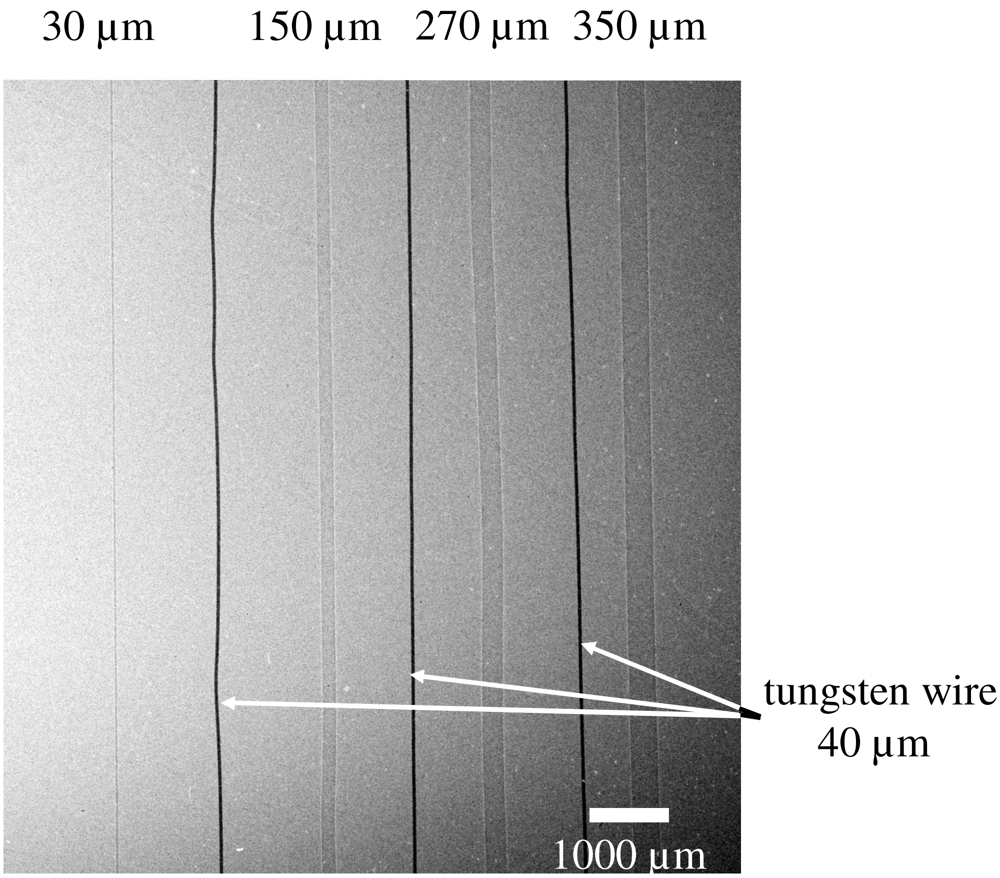

Figure 4.11: Radiograph of a set of polyamide strings of different diameters as given at the top of the view graph, and tungsten wires of 40 μm diameter. The source-to-object distance was $x_{so} = 8.11$ m and the object-to-detector distance $x_{od} = 3.27$ m. The exposure time was 40 sec at an electron beam current of 6 nA. The visibility of the polyamide strings is strongly enhanced at the interfaces. The object wires were mounted vertically.

(4.11)

Here, $\left(\frac{d^2N(\theta,\varphi,\hbar\omega)}{(d\hbar\omega/\hbar\omega)d\Omega}\right)_s$ is the emitted X-ray photon spectrum from the 33 keV foil stack described above, see also chapter 3, I_e is the electron current impinging on the foil stack, e the elementary charge, t_{exp} the exposure time, and x_{sd} the distance between the foil stack and the X-ray film. The quantities $\mu_p(\hbar\omega)$, $\mu_a(\hbar\omega)$, $\mu_o(\hbar\omega)$, and $\mu_f(\hbar\omega)$ are the linear attenuation coefficients of the polyimide exit window (thickness of $d_p = 120$ μm), of air (distance $d_a \simeq 5.5$ m), the object under investigation (thickness d_o), and the X-ray film emulsion (thickness d_f), respectively. The integral extends over the complete photon emission spectrum, including the bremsstrahlung part.

In a simple theoretical model [Geo58] the photographic density can be described by

$$D(\overrightarrow{r}) = D_{sat}(1 - \exp(-b(\overrightarrow{r})/b_0)) \tag{4.12}$$

with $b(\overrightarrow{r}) = dE(\overrightarrow{r})/dA$ the exposure at the position $\overrightarrow{r}$ at the film. The saturation density D_{sat} and b_0 are characteristic quantities of the X-ray film.

From Eq. (5.13) the relative exposure is obtained as

$$\frac{b(\overrightarrow{r})}{b_0} = \ln\left(\frac{D_{sat}}{D_{sat} - D(\overrightarrow{r})}\right) \quad . \tag{4.13}$$

Since we are interested in contrast ratios $(b(\overrightarrow{r})/b_0)/(\bar{b}/b_0)$ with $\bar{b}$ a mean value on some position outside the domain of interest, the unknown quantity b_0 cancels. The still unknown saturation density must, in principle, be determined. However, since the digitization devices to our disposal had only a depths of 8 bits the main restriction in the dynamical range is expected to originate from the digitization procedure and not the dynamical range of the X-ray film.

The procedure we adapted to obtain the contrast ratio of a string was the following. At first, domains on the X-ray film were selected in which the photographic density was assumed to be in the linear region. In this case Eq. (5.13) reduces to $D(\overrightarrow{r}) = D_{max} \cdot b(\overrightarrow{r})/b_0$ and in the contrast ratio also the saturation density cancels. Thereafter, we determined the contrast ratio at various positions of the string for which the exposure varied, see e.g. Fig. 4.12, and selected the maximum value as the experimental contrast.

4.5 Results

An extensive study of the contrast generation as a function of the object-to-detector distance x_{od} has been performed for polyamide strings of different diameters and also for a strongly absorbing tungsten wire. The calculated absorption contrast for a polyamide string with a diameter of 270 μm dos not exceed 1%. Therefore, no absorption contrast can be observed with the traditional contact radiography, i.e. for $x_{od} \cong 0$, in accord with our measurements. By moving the object away from the detector, the imaging regime is changed from absorption radiography to phase contrast radiography and phase shift is the mechanism to produce the contrast. The contrast appears at the borders of the polyamide string where the density gradient reaches its maximum value and is measured by the quantity $C_{ref} = (I_{max} - I_{min})/(I_{max} + I_{min})$, see Fig. 2.3.

Figs. 4.13, 4.14, and 4.15 show a set of radiographs of a polyamide string[4] [GooXX] with a diameter of about 270 μm at different object-to-detector distances. In Fig. 4.13 (a) the object-to-detector distance was $x_{od} = 0.5$ m and a contrast $C_{ref} = (5.2\pm3.1)$ % has been observed. In Fig. 4.14 the object-to-detector distance was increased to $x_{od} = 3.27$ m and a contrast of $C_{ref} = (17.8\pm2.1)$ % was determined. For the long object-to-detector distance $x_{od} = 5.5$ m, the contrast $C_{ref} = (16.7 \pm 1.9)$ % seems to decrease again slightly, see Fig. 4.13. It can be seen from Figs. 4.13, 4.14, and 4.15 that the borders of the black/white contrast broaden with increasing distance between object and film x_{od}. To this broadening the projected beam spot size contributes at the largest $x_{od} = 5.5$ m according to Eq. (2.12) to 19 μm (FWHM) which is already a rather large fraction in

---

[4] supplied by Goodfellow

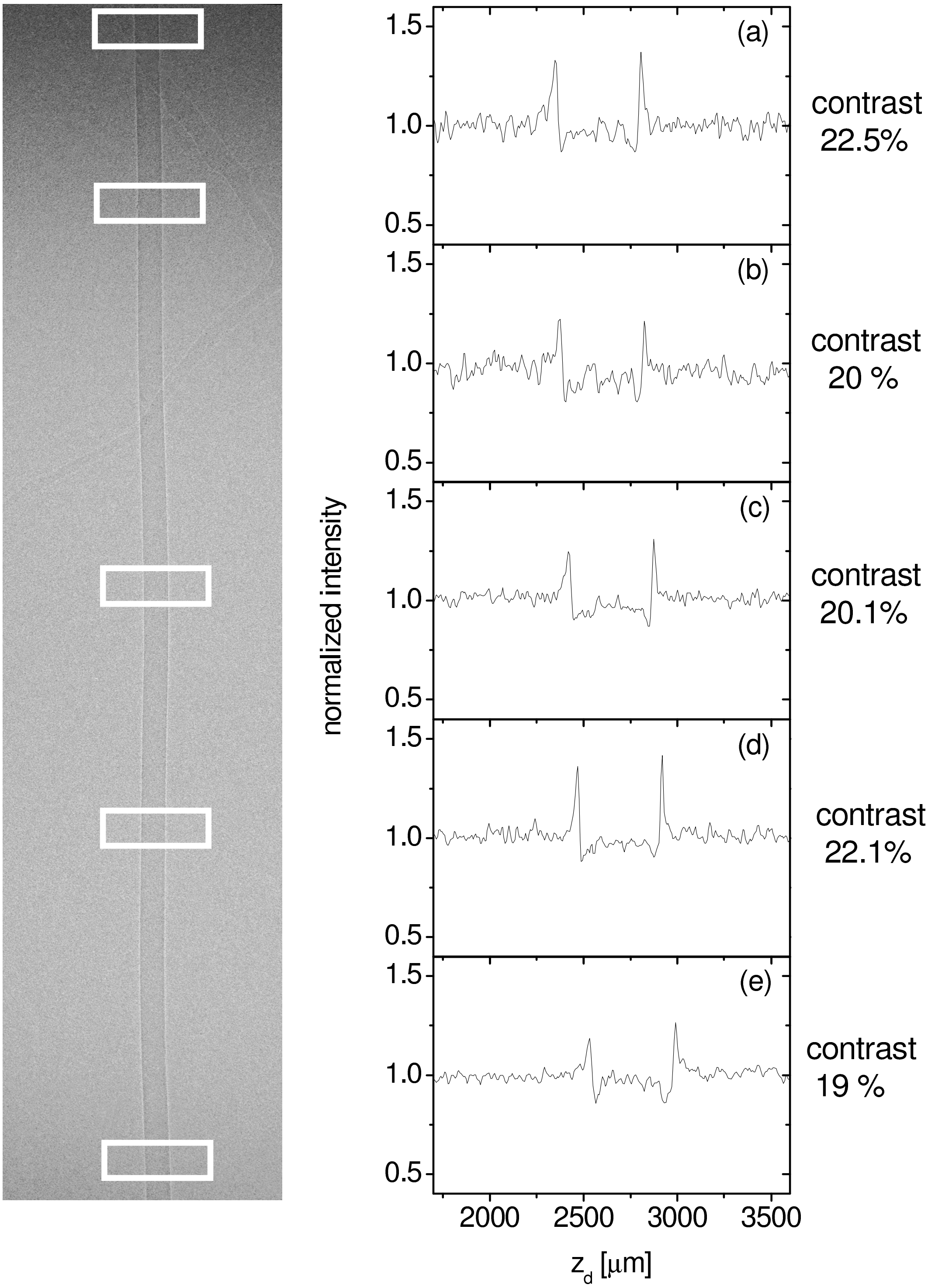

Figure 4.12: Radiograph of a polyamide string with a diameter of 270 μm. Source-to-object distance $x_{so} = 7.38$, object-to-detector distance $x_{od} = 4$ m, X-ray source size $\sigma_h = (8.6 \pm 0.1)$ μm, and $\sigma_v = (7.5 \pm 0.1)$ μm. The white rectangles show the positions where the intensity profiles shown at the right hand side were generated, 100 pixels are summed up vertically. The change in blackness is due to the change of the X-ray flux incident on the different parts. The contrast C_{ref} reaches a maximum in panel (a).

comparison to the difference between maximum and minimum at the border of about 40 μm.

The contrast C_{ref} is depicted in Fig. 4.16 for all measurements as a function of the object-to-detector distance x_{od}. The contrast increases with increasing object-to-detector distance x_{od}, reaches a maximum at about 4 m, and decreases again for larger x_{od}. The latter is a consequence of the increasing projected beam spot size on the detector plane. Further results for a nylon string of 30 μm diameter are presented in the appendix B.

Fig. 4.17 (a), (b) and (c) show radiograph, intensity profile and calculation of a tungsten wire. It is interesting to notice, that also a weak edge enhancement is observed for this strongly absorbing object.

4.6 Discussion

The most interesting feature of the radiographs shown in Figs. 4.13, 4.14, and 4.15 is that an edge enhancement or phase contrast can be observed with a polychromatic X-ray beam. This fact has been discussed in a number of papers also in connection with the interplay between refraction and diffraction [Wil96, Hwu99]. The general features of refraction contrast imaging will be discussed by means of Fig. 4.16, where all measurements of the contrast C_{ref} are shown as error bars as a function of the object-to-detector distance x_{od}. It can be stated that the distance between object and detector x_{od} must be at least so large that the wave optical spread of the diffracted X-rays at an interface of the object becomes comparable with the detector resolution. Otherwise the interference fringes are blurred and the contrast is low. With increasing distance x_{od} the contrast increases about linearly. However, at the same time the projected X-ray spot size on the detector plane increases what worsens the contrast at larger distances. The maximum of the contrast is a function of beam spot size and film resolution. But contrast is not the only figure of merit. It must also be taken into account that with increasing x_{od} the edge spread increases and the resolution deteriorates. The latter might be undesirable in case that resolution is of importance and nearby objects must be resolved.

Next, the question will be addressed whether the measured edge enhancement structures can be understood quantitatively in the framework of the wave optical and geometrical models. As has already been pointed out in subsection 4.1.2, the refraction contrast is in a strict sense a wave optical phenomenon, however, with some care it can also be explained in the framework of geometrical optics as shown in subsection 4.1.3. Both models have two free parameters which are the standard deviation of the beam spot size and the resolution of the X-ray film including the film scanner. The standard deviations of the beam spot size and the intrinsic resolution of the X-ray film have been measured to be $\sigma_h = 8.6$ μm and $\sigma_f = 2.0$ μm, respectively. The pixel size of the scanner is (9.4×9.4) μm^2. The total resolution of the film and the scanner was measured to be $\sigma_t = (10.0 \pm 0.4)$ μm.

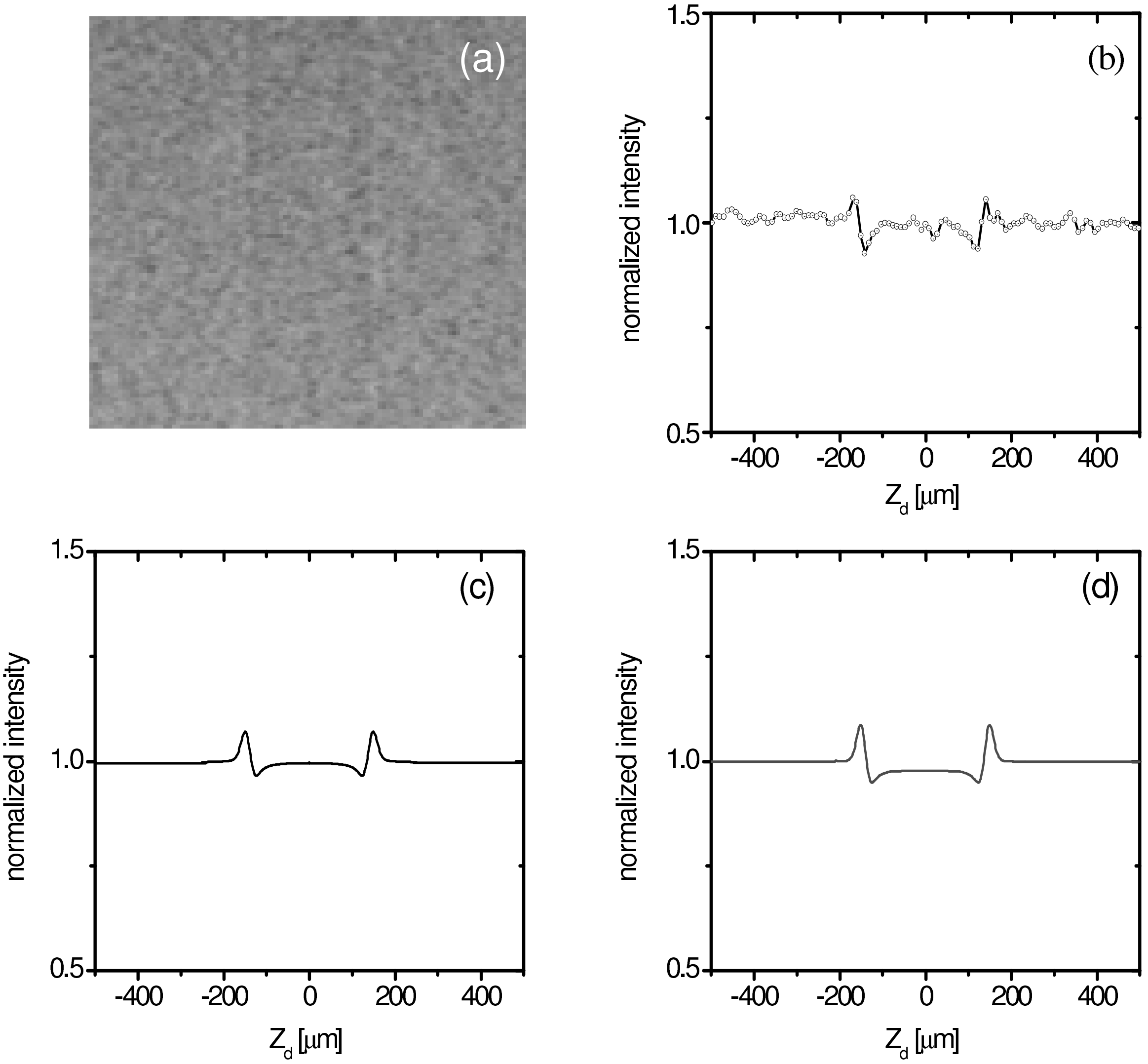

Figure 4.13: (a) Refraction enhanced radiograph of a polyamide string with a diameter of 270 μm at an object-to-detector distance $x_{od} = 0.5$ m, and a source-to-detector distance $x_{sd} = 11.38$ m. The polychromatic X-ray beam from transition radiation with spectral distribution shown in Fig. 3.5 has been used. At the spectrally weighted energy of 19.6 keV the refractive index parameters are $\delta = 7.2 \cdot 10^{-7}$ and $\beta = 2.74\ 10^{-10}$. The electron beam current was 6 nA, the exposure time amounted to 60 sec. X-ray source sizes were $\sigma_h = (8.6 \pm 0.1)$ μm and $\sigma_v = (7.5 \pm 0.1)$ μm in horizontal and vertical direction, respectively. The radiograph (a) was captured by an X-ray film (Agfa Mamoray MR5 II PQ). The developed film was digitized by an X-ray scanner (Nikon Super CoolScan 2700 ED) with a pixel size of $9.4 \cdot 9.4$ μm^2. (b) Intensity profile for which 100 vertical pixels were added together to improve the statistics. (c) Normalized intensity profile according to geometrical optics as described in subsection 4.1.3 with the following parameters: film and scanner resolution $\sigma_d = (10.0 \pm 0.4)$ μm, and the wave optical contribution $\sigma_w = \sqrt{\lambda x_{sd} x_{od}/(2\pi x_{so})} = 2.3$ μm with $\lambda = 0.633$ Å. (d) Same as (c) on the basis of wave optics

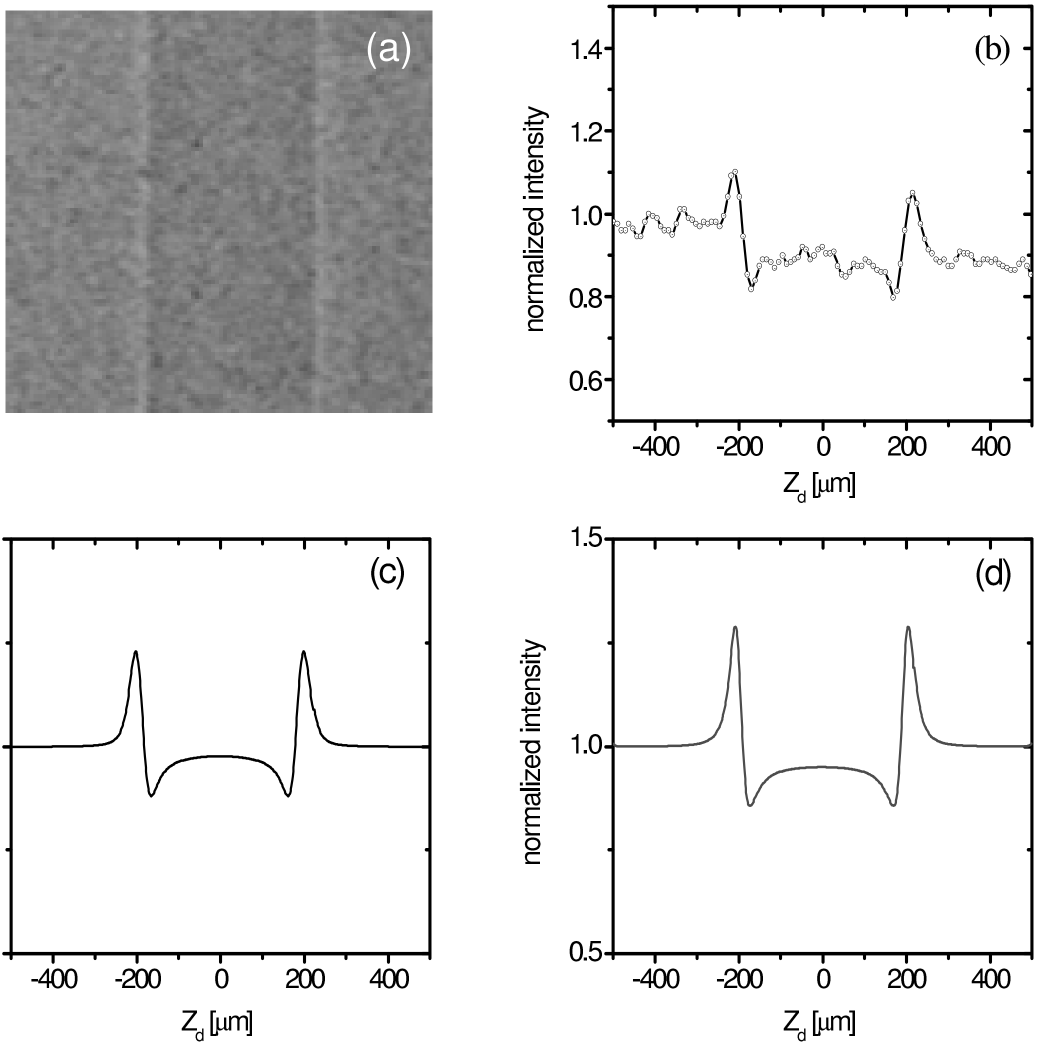

Figure 4.14: (a) Refraction enhanced radiograph of a polyamide string with a diameter of 270 μm at an object-to-detector distance $x_{od} = 3.27$ m. For further explanations see caption of Fig. 4.13.

Figs. 4.13 (c), 4.14 (c), 4.15 (c) show calculations with the geometrical model presented in section 4.1. Figs. 4.13 (d), 4.14 (d), 4.15 (d) show calculations with the wave optical model presented in appendix A.2. For both calculations beam spot size and X-ray film resolution have been taken as explained above. For the geometrical model the X-ray spectrum has been approximated by a delta-function at the mean photon energy $\hbar\omega = 19.6$ keV since model calculations showed a rather weak energy dependence of the edge structure. The wave optical calculations were performed with the detected X-ray spectrum shown in Fig. 4.6 which was approximated with 22 discrete values in the energy range between 8 and 30 keV. As can be seen, both, the geometrical and the wave optical model describe the general features of the measurement well.

The rather good results for the contrast ratio C_{ref} of the geometrical model as shown in Figs. 4.13 (c), 4.14 (c) , 4.15 (c) are somehow surprising since in the model an additional

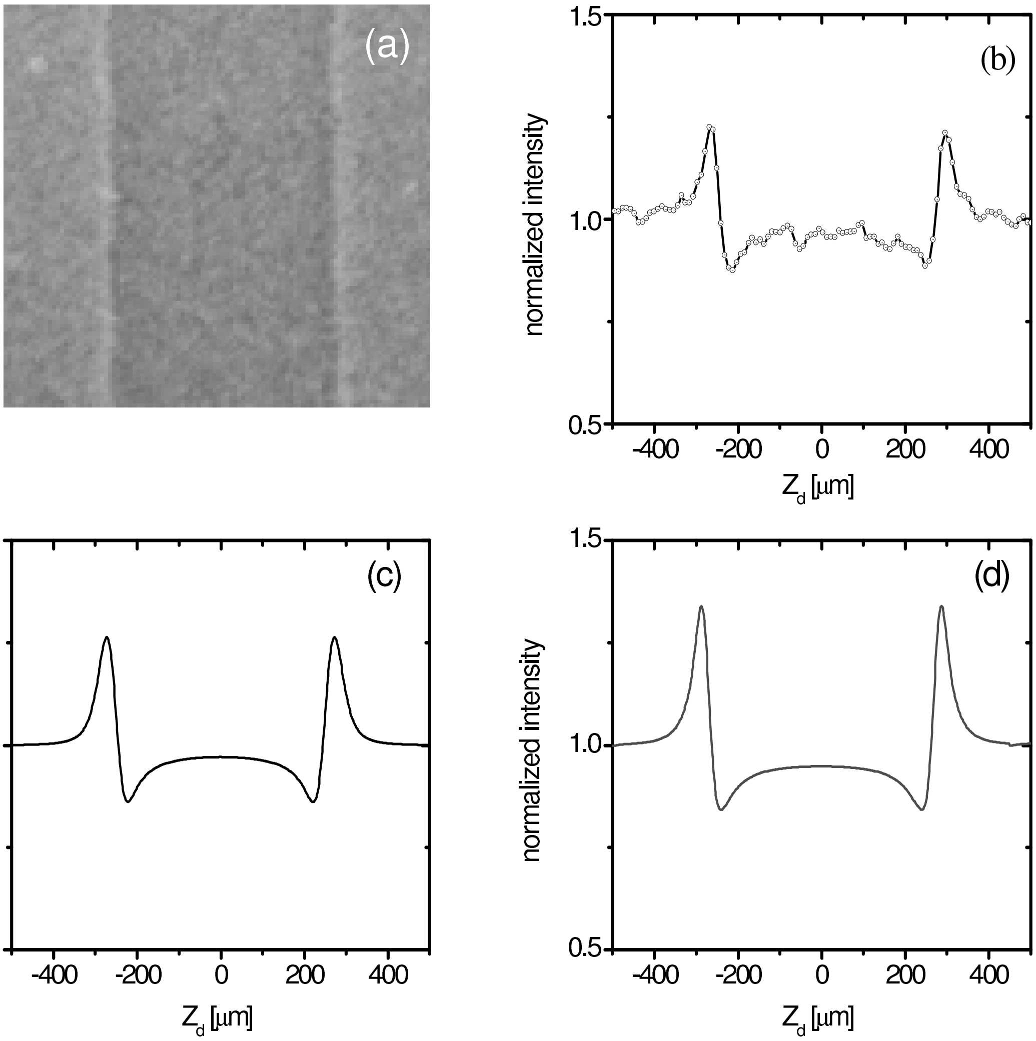

Figure 4.15: (a) Refraction enhanced radiograph of a polyamide string with a diameter of 270 μm at an object-to-detector distance $x_{od} = 5.5$ m. For further explanations see caption of Fig. 4.13.

parameter $\sigma_w = \sqrt{\lambda x_{so} x_{od}/(2\pi x_{sd})}$ was introduced which accounts for the diffraction. The real parameter may differ from the assumed one. However the good agreement may be a consequence of the rather poor total film resolution $\sigma_t = (10.0 \pm 0.4)$ μm. The results are collected in Tab. 4.1.

In addition to the edge enhancement there is also an area contrast for the string which increases with increasing object-to-detector distances. This can be explained as follows. Since the X-ray refraction index is smaller than unity, the string with cylindrical shape behaves like a concave lens. The focal length f can be calculated with the lens maker's formula [Hec89]:

$$\frac{1}{f} = \frac{2 \cdot (\Re(n) - 1)}{r} = -\frac{2\delta}{r} \quad . \tag{4.14}$$

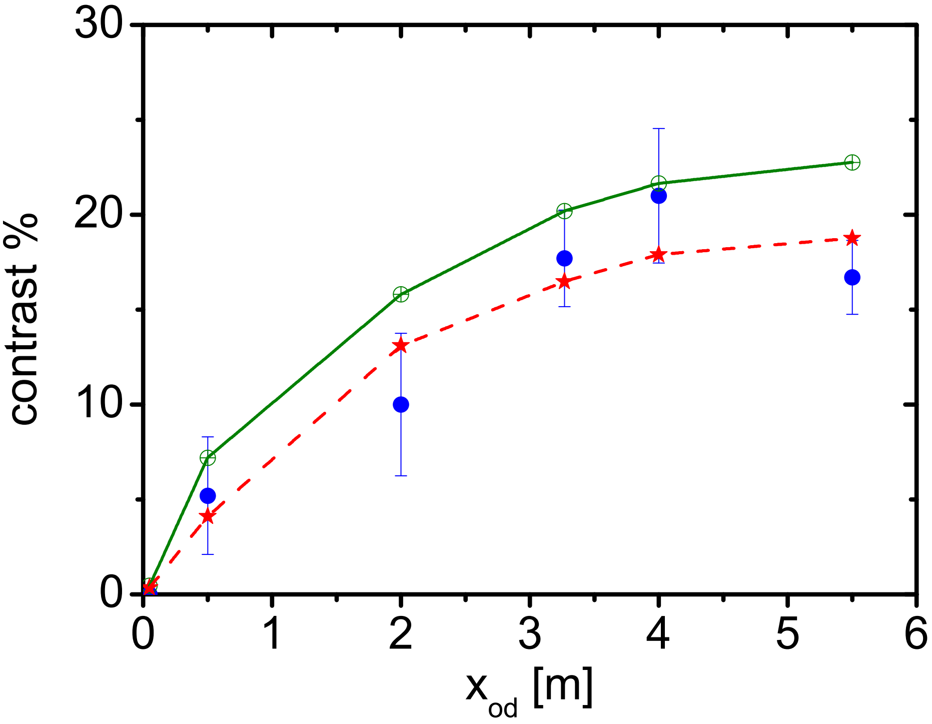

Figure 4.16: Contrast C_{ref} for a polyamide string of 270 μm diameter as a function of the object-to-detector distance x_{od}. The source-to-detector distance $x_{so} = 11.38$ m was kept constant during the measurements. Error bars are measurements, crossed circles calculations with the wave optical model with a beam spot size $\sigma_h = 8.6$ μm and a total X-ray film resolution and the scanner resolution $\sigma_t = (10.0 \pm 0.4)$ μm. Stars designate calculations according to geometrical optics

For a polyamide strings with diameters of 270 μm and 30 μm and a dispersion index $\delta = 7.2 \cdot 10^{-7}$ at an X-ray energy of 19.6 keV, the focal length is about 93.8 and 10.3 m, respectively.

It is very interesting that for the radiograph of a strongly absorbing tungsten wire with a diameter of 40 μm also a weak edge enhancement can be observed with a polychromatic X-ray beam, see Fig. 4.17. The calculated intensity profile of the radiograph on the basis of the wave optical description, Eq. (4.5), is shown in Fig. 4.17 (c). It was calculated again for 22 discrete energy values ranging form 8 to 30 keV and then convoluted with the X-ray source spot size $\sigma_h = 8.6$ μm and the detector spatial resolution function with a standard deviation $\sigma_t = (10.0 \pm 0.4)$ μm. It can be seen that just one maximum remains which brings about the edge enhancement, and all other fringes have disappeared.

The comparison between the experimental results and the simulations based on geometrical optics and wave optics shows that the edge enhancement of low absorbing materials can be explained on the bases of wave optics alone. In other papers [Hwu99], the interplay between refraction contrast and diffraction depends on the object mor-

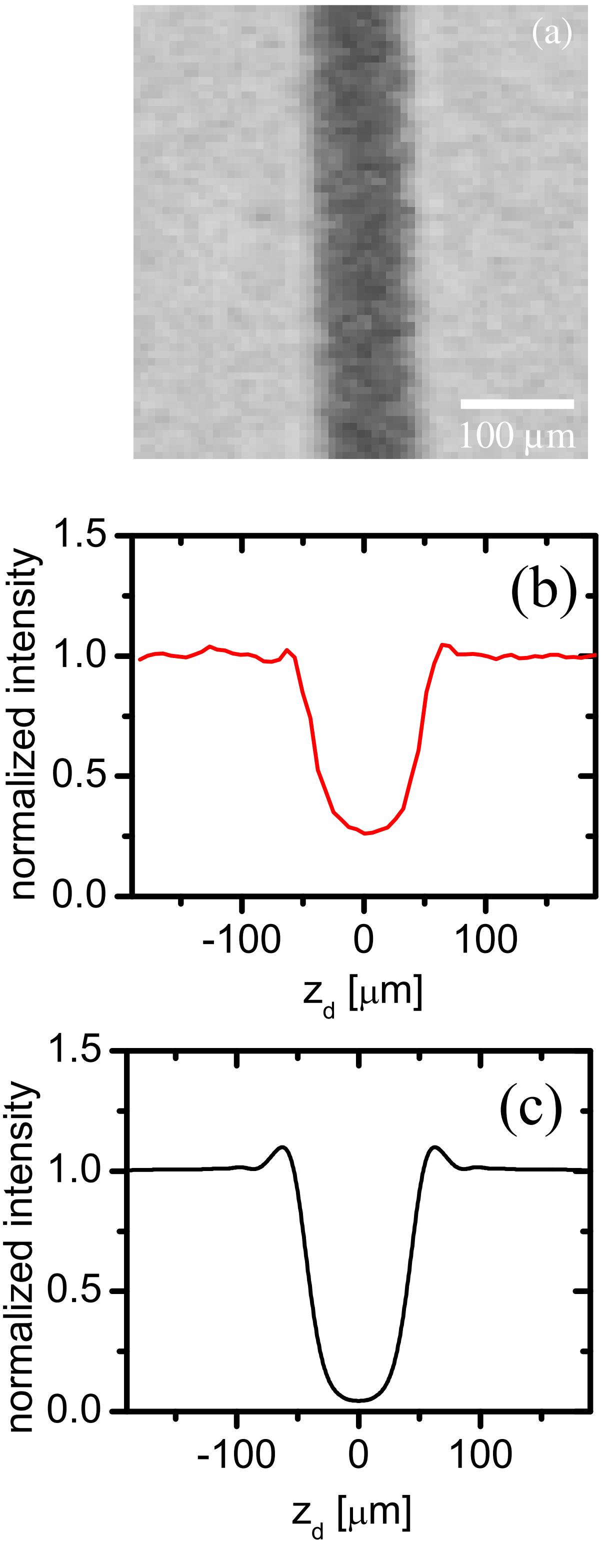

Figure 4.17: (a) Radiograph of a tungsten wire with a diameter 40 μm at an object-to-detector distance x_{od} = 3.27 m, and a source-to-detector distance x_{od} = 8.11 m, imaged with polychromatic X-rays of a mean energy of 19.6 keV. The exposure time amounted at an electron beam current of 6 nA to 40 s. (b) Intensity profile and (c) a simulation based on wave optics assuming a polychromatic X-ray beam with a spectral distribution as shown in Fig. 4.6.

Table 4.1: Comparison of the measured contrast C_{ref} with calculations on the basis of the geometrical model C_g and the wave optical model C_w for a polyamide string of 270 μm diameter for various object-to-detector distances x_{od}. The source-to-detector distance $x_{sd} = 11.38$ m was kept constant. The calculations were performed in both cases with a beam spot size $\sigma_h = 8.6$ μm and a total X-ray film resolution and the scanner resolution of $\sigma_t = (10.0 \pm 0.4)$ μm. The magnification is denoted by M.

x_{so} [m]	x_{od} [m]	M	C_g	C_w	C_{ref}[%]
11.33	0.05	1	0.35	0.45	0
10.88	0.5	1.05	4.1	7.2	(5.2±3.1)
9.38	2.0	1.21	13.1	15.8	(10±3.8)
8.11	3.27	1.4	16.48	20.2	(17.8±2.1)
7.38	4.0	1.54	17.9	21.65	(21.0±3.6)
5.88	5.5	1.94	18.76	22.76	(16.7±2.0)

phology and the object-to-detector distance.

A big advantage of X-ray phase contrast imaging is the reduction of the absorbed dose by the sample. This reduction can be explained in the framework of the X-ray interaction with matter. The X-ray phase contrast imaging is based on the elastically scattered photons by the object (forward direction). Therefore it is proportional to f (atomic scattering factor), whereas the absorption contrast is proportional to f^2 [Hen93]. As reported in [Car98] the absorbed dose in case of the phase contrast imaging is 10 times smaller than the absorbed dose for absorption contrast imaging.

4.7 Further examples

Green leaves, objects of biological interest with a rather complex three dimensional structure, were used to test the performance of refraction contrast radiography on two dimensional images at MAMI using hard polychromatic X-rays from the transition radiation source. Such objects with a thickness smaller than 1 mm, have negligible attenuation contrast for hard X-rays (19.6 keV). X-ray examinations are difficult because green leaves consist of tissues with similar densities and rather similar attenuation coefficients.

To demonstrate, how the refraction contrast radiography enhances the visualization of low-Z materials and also to show the difference to the conventional radiography, Fig. 4.18 shows two radiographs of a green leaf of *Ficus benjaminus* at different object-to-detector distances. *Ficus benjaminus* is a very interesting object because it contains calcium carbonate ($CaCO_3$) crystals of sizes about 50 μm which have complex refraction index parameters $\delta = 1.37 \cdot 10^{-6}$ and $\beta = 3.46 \cdot 10^{-8}$ at 19.6 keV. These inclusions are similar to the calcification in a female cancer breast.

In Fig. 4.18 (a) the object is in contact with the detector ($x_{od} = 0$) as in the case of conventional radiography. For this geometry the contrast is mainly due to the

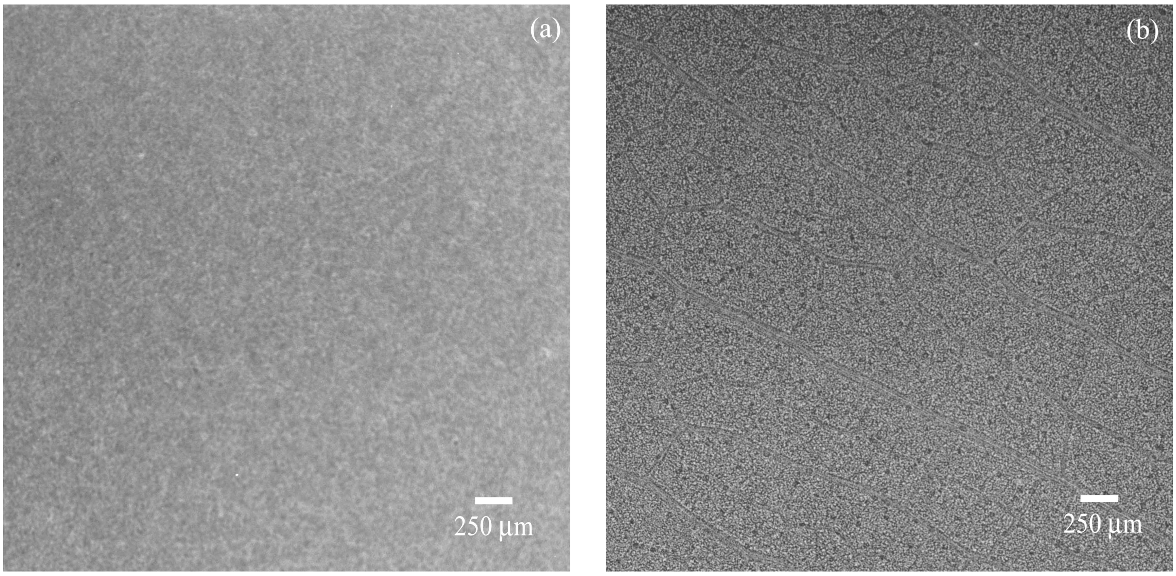

Figure 4.18: Refraction contrast radiographs of a part of a green leaf of *Ficus benjaminus*. The radiographs were recorded by the X-ray film (Agfa MAMORAY MR5 II PQ). The electron beam current was 6 nA, the exposure time 40 s. The source-to-detector distance was $x_{sd} = 11.38$ m. (a) Picture taken at an object-to-detector distance $x_{so} \cong 0$ m, (b) at $x_{od} = 2.5$ m. The 33 keV kapton foil stack was used. The electron beam energy was 855 MeV, the electron beam spot size had standard deviations of $\sigma_h = (8.6 \pm 0.1)$ μm and $\sigma_v = (7.5 \pm 0.1)$ μm in the horizontal and vertical direction, respectively.

absorption of X-ray photons by the object. As expected, no contrast is observed in accord with expectations. In Fig. 4.18 (b) the object-to-detector distance is increased to $x_{od} = 2.5$ m. The radiograph shows an excellent visualization of all fine details including calcifications in the green leaf.

Two important features are observed for refraction contrast radiograph of Fig. 4.19 in which the image of a green leaf of *Rumex crispus* is shown. Firstly, in the part labelled with (a) where the leaf is thinner than 1 mm, the visibility of a bundle of vascular tissue (veins) could be resolved with high contrast. Secondly, in the middle part labelled by (b), the object is about 3 mm thick and contains a bundle of vascular tissue (veins). However, the identification of an individual vein is difficult since images from the different veins in the radiograph are overlapping.

For complex and thick objects the refraction contrast radiography faces, in principle as every radiographic method, a deficiency due to multi-refraction at different details comprising the object. Fig. 4.21 shows a radiograph of a polymer fiber bundle with an external diameter of about 450 μm and individual fibers with about 30 μm diameter. At the mean photon energy of 19.6 keV the maximum absorption is less than 1.26 % for the bundle as a whole and less than 0.1 % for the individual fiber of 30 μm diameter. However, the radiograph demonstrates an excellent visualization of the individual fibers.

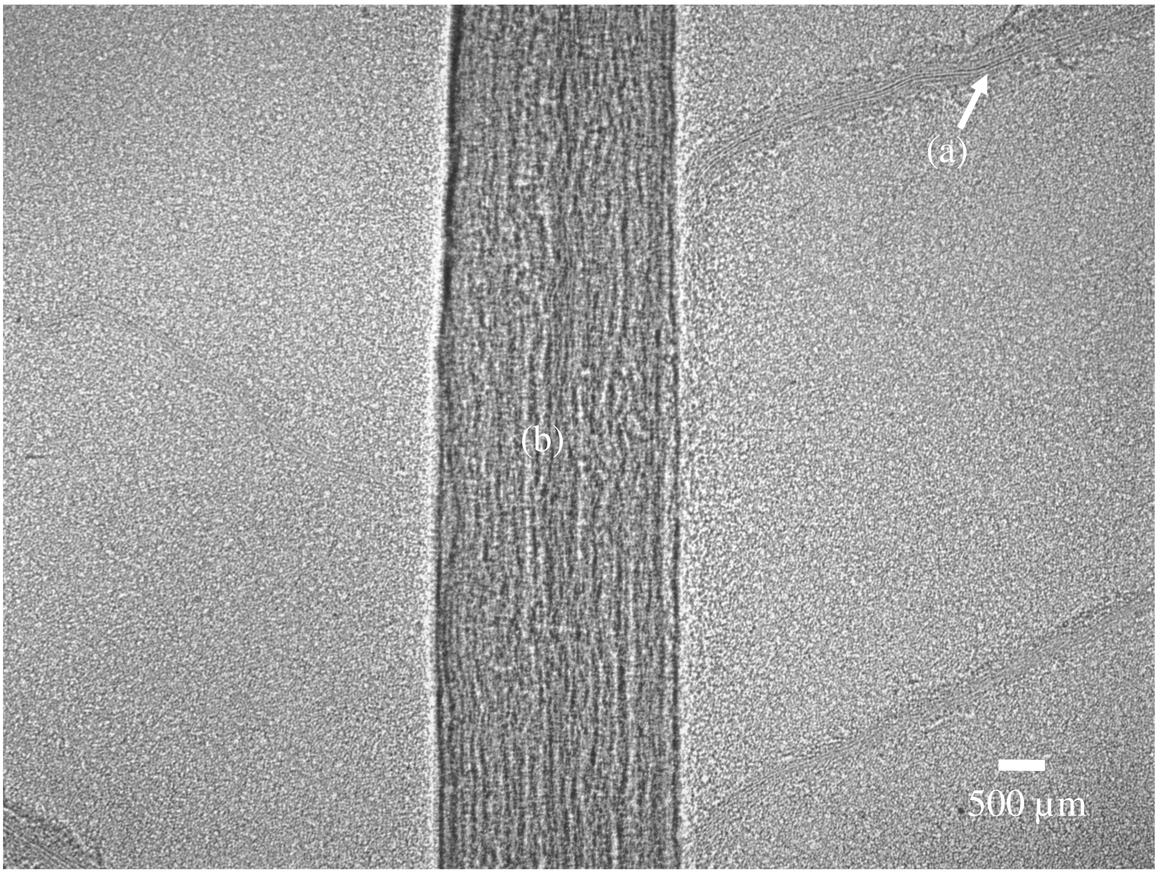

Figure 4.19: A refraction contrast radiograph of a part of green leaf *Rumex crispus*. The radiograph was recorded by the X-ray film MAMORAY MR5 II PQ (Agfa). The object-to-detector distance was $x_{od} = 5.5$ m at a source-to-object distance of $x_{so} = 5.88$ m. With these parameters the magnification was about 2 times. The electron beam current was 6 nA, the exposure time 40 s. The 33 keV kapton foil stack was used. The electron beam energy was 855 MeV, the electron beam spot size had standard deviations of $\sigma_h = (8.6 \pm 0.1)$ μm and $\sigma_v = (7.5 \pm 0.1)$ μm in the horizontal and vertical direction, respectively.

4.8 Concluding remarks

It has been shown in this chapter that the highly directional transition radiation X-ray beam at MAMI is well suited for normal and, in particular, refraction contrast radiography. Due to the low divergence angle of the beam of about 0.8 mrad the object can be placed at large distances from the X-ray source in a still considerable photon flux. At close object-to-detector distances the deteriorating influence of the finite X-ray beam spot size on the resolution becomes negligibly small. Assuming an ideal X-ray detector and considering the limitation by the effective X-ray source size, the minimum achievable spatial resolution is $S' = S \cdot x_{od}/x_{so}$. The spatial resolution can be further reduced by micro-focusing the electron beam. In general, the smaller the distance between object and detector the higher the spatial resolution in the radiographs. A transition

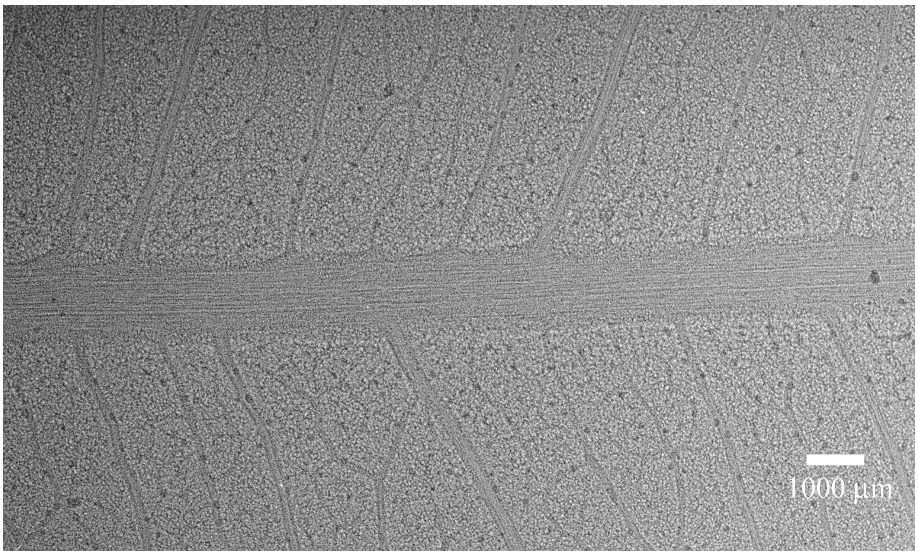

Figure 4.20: Refraction contrast radiograph of a part of a green of leaf *Ficus benjaminus*. The radiograph was recorded by X-ray film (Agfa Mamoray MR5 II PQ). The exposure time was 50 s at an electron beam current of 6 nA. The object-to-detector distance was $x_{od} = 6.18$ m at a source-to-object distance of $x_{so} = 5.88$ m. The 33 keV kapton foil stack was used. The electron beam energy was 855 MeV, the electron beam spot size had standard deviations of $\sigma_h = (8.6 \pm 0.1)$ μm and $\sigma_v = (7.5 \pm 0.1)$ μm in the horizontal and vertical direction, respectively.

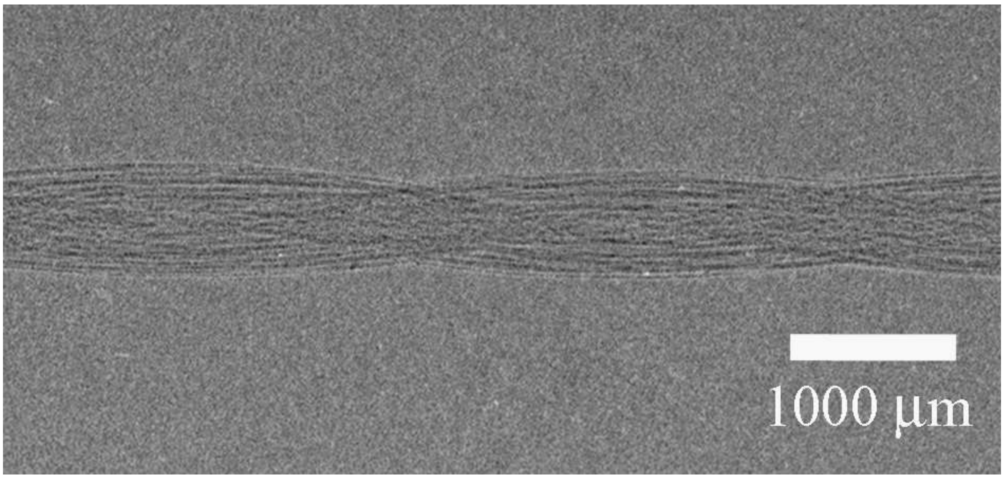

Figure 4.21: Refraction contrast radiograph of a polymer fiber bundle wire with an outer diameter of about 450 μm and single fibers of a diameter of about 30 μm. The radiograph was captured with the X-ray film (Agfa Mamoray MR5 II PQ). The electron beam current was 6 nA, the exposure time 40 s. The object-to-detector distance was 3 m at a source-to-object distance of 7 m. The 33 keV kapton foil stack was used. The electron beam energy was 855 MeV, the electron beam spot size had standard deviations of $\sigma_h = (8.6 \pm 0.1)$ μm and $\sigma_v = (7.5 \pm 0.1)$ μm in the horizontal and vertical direction, respectively.

radiation X-ray source with a micro-focused electron beam could be a valuable source in various applications, such as medical radiography, material science, environmental applications, etc. However, a disadvantage which limits the medical applications may be the contamination of the X-ray beam with high energy bremsstrahlung photons.

At finite but still close distances between object and detector refraction contrast (phase contrast or edge enhancement) occurs. X-ray phase contrast radiography can be carried out using a very simple experimental setup which consists of the transition X-ray source, the objects and an X-ray detector. Demands on the transverse coherence of the X-ray beam to observe phase contrast are not severe since the projected source size at the detector plane can be kept small by a small distance between object and detector. A good longitudinal coherence is not at all a prerequisite since the position of the first interference maximum at discontinuities does essentially not alter with the photon energy.

There is no need for sophisticated calculations to realize that for refraction contrast radiography a significant high contrast is obtained with low absorbed dose. The latter arises from the fact that only few photons are absorbed in low absorbing materials to be radiographed.

It might be worth to compare the refraction contrast radiographs obtained at MAMI with similar measurements at big synchrotron radiation facilities as ESRF, APS and Spring8, etc. At these facilities the primary X-ray spot size is in the order of 20-35 μm [Mor02, Koh00] which is much larger than the spot size which can be obtained with the low emittance electron beam of MAMI. Although the transition radiation brilliance of the MAMI X-ray beam may be much lower as that of the mentioned synchrotron radiation sources, the quality of refraction contrast radiographs is comparable [Kun01].

In this chapter a polychromatic X-ray source has been used to record high quality refraction contrast radiographs of low absorbing materials. In the following chapter, the hard X-ray phase contrast imaging and in-line holography using a monochromatic X-ray beam will be investigated.

5 Towards hard X-ray in-line holography

In the preceding sections it has been shown that the transition radiation (TR) X-ray source is well suited for refraction contrast imaging. This chapter deals with the investigation of the possibility of X-ray phase contrast imaging and hard X-ray in-line holography with monochromatic X-rays at MAMI. The good emittance of MAMI allows the preparation of a micro-focus which is a prerequisite of the required transverse coherence of the TR X-ray source. The longitudinal coherence can be achieved by a single crystal monochromator. The experimental setup, the preparation of the micro-focused electron beam and the results obtained so far will be described in this chapter.

5.1 Basic Background

In chapter 2 it was already shown that the holographic information of an object is imprinted in the interference pattern at the detector plane which originates from the interference of the wave scattered by the object and the original wave emanating from the X-ray source. This section deepens these considerations.

A wave emanating from a "point" source may illuminate an object from which it is scattered. The wave amplitude $E(\vec{r})$ can be split into the reference wave $E_0(\vec{r})$ and a scattered wave $E_{scat}(\vec{r}) = a(\vec{r}) \cdot E_0(\vec{r})$ and the amplitude ratio can be written as $E(\vec{r})/E_0(\vec{r}) = 1 + a(\vec{r})$, for details see appendix A.2. The scattering amplitude $a(\vec{r})$ contains the required information on the object. On a detector screen, as an X-ray film or a CCD detector, the squared absolute values of the amplitudes $|E(\vec{r})|^2$ and $|E_0(\vec{r})|^2$ are measured from which the normalized contrast ratio

$$I_{norm}(\vec{r}) = \frac{|E(\vec{r})|^2 - |E_0(\vec{r})|^2}{|E_0(\vec{r})|^2} = 2\ \Re[a(\vec{r})] + |a(\vec{r})|^2 \qquad . \qquad (5.1)$$

can be determined. The nominator is the contrast image, by division through the reference wave $|E_0(\vec{r})|^2$ the normalized contrast image is obtained.

The appearance of $2\ \Re[a(\vec{r})] = a(\vec{r}) + a^*(\vec{r})$ on the right hand side of Eq. (5.1) shows that the hologram contains also information on the real part of the scattering amplitude rather than only its absolute value squared $|a(\vec{r})|^2$ which may be referred to as "classical diffraction pattern" of the complementary transmission function of the object, see appendix A.2. Such classical diffraction patterns are observed in diffraction experiments in which the reference wave is absent, e.g., at diffraction on a slit which is the complementary to an opaque object as, e.g., an opaque wire. While the classical diffraction pattern is rather smooth, see Fig. 5.1 (a), the holographic diffraction pattern oscillates rapidly, see Fig. 5.1 (b). These oscillations have a rather small amplitude and can hardly be seen in a measurement of the hologram which is shown in Fig. 5.1 (c). Much more pronounced oscillations are observed for transparent objects as polymer strings, see Fig. 5.1 (d), (e) which are maintained in the sum of the classical and the holographic diffraction pattern, see Fig. 5.1 (f). These oscillations contain information on the distance between the object from the detector or the source, see also appendix A.2, and via the refractive index decrement δ and the absorption β also information on the bulk of the string. Finally, the hologram contains via the transverse coherence length also information on the beam spot size. All together, a hologram of transparent objects contains a lot of information. Which information can be extracted from holograms of transparent objects will be discussed in section 5.5.3.

With reference to Fig. 4.1, our experiments were performed in the intermediate region (III). As has been pointed out in more detail in appendix A.2 we do not approach in this region a simple situation in which the Fresnel-Kirchhoff integral Eq. (2.18) may reduce to a Fourier-transform of the complementary transmission function $p(z_o)$ of the object, in our case a string with radius R. The reason is that the total Fresnel number $N_F = R^2/(\lambda x_{so}) + R^2/(\lambda x_{od})$ is even in the most favorable case of equal source-to-object, x_{so}, and object-to-detector, x_{od}, distances not small in comparison to one. For example, for $R = 15$ μm, an X-ray wave length $\lambda = 2$ Å and a source-to-detector distance $x_{sd} = 13.6$ m, which is given by our experimental boundary conditions, the Fresnel number is $N_F = 0.33$. Sophisticated reconstruction codes may be required to obtain the geometrical information from the hologram under these circumstances, but the development of such codes is beyond the scope of the experimental investigations of this work to be described in the following.

5.2 Experimental set-up and test measurements

5.2.1 Principle of the experiment and overview

The observation of interference patterns as shown, for instance, in Fig. 5.1 requires both, a good transverse and a good longitudinal coherence which can be achieved with a microfocused and monochromatic X-ray beam. These requirements led to an experimental arrangement at MAMI which is schematically depicted in Fig. 5.2. As monochromator a flat single crystal in Bragg geometry is used. The objects to be imaged can be placed between TR radiator and monochromator crystal close to the TR source resulting in a magnification of the object up to a factor of 7.4 or, alternatively, between monochromator and X-ray detector. The magnification may be of importance to compensate for a moderate detector resolution if, e.g., CCD-chips in a direct exposure mode are used.

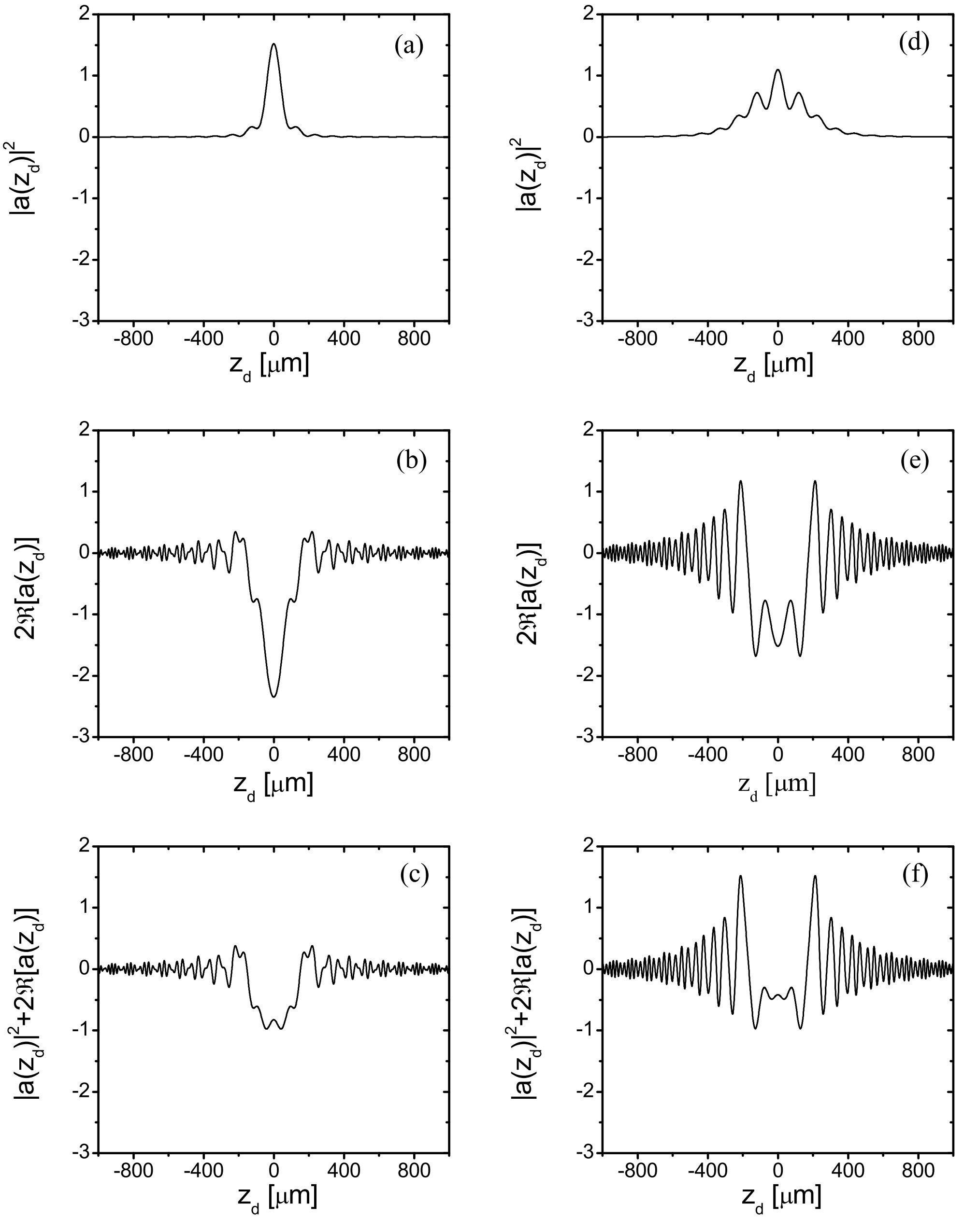

Figure 5.1: Analysis of the normalized contrast image into distinct patterns for a totally opaque tungsten wire, left column (a), (b) and (c), and for an approximately transparent polymer string, right column (d), (e) and (f). Both wires have the same diameter of 25 μm. The X-ray photon energy is 6 keV (λ=2.067 Å), the complex refraction index parameters are $\delta_W = 8.5 \cdot 10^{-5}$ and $\beta_W = 1.1 \cdot 10^{-5}$ and $\delta_P = 7.3 \cdot 10^{-6}$ and $\beta_P = 2.55 \cdot 10^{-8}$ for tungsten and polymer, respectively, at this energy. The source-to-object distance is $x_{so} = 1.92$ m and the object-to-detector distance $x_{od} = 11.68$ m. Panels (a) and (d) show the classical diffraction pattern $|a(z_d)|^2$ which is the diffraction pattern of the complementary object, (b) and (e) the holographic diffraction pattern $2Re[a(z_d)]$ which come about by the interference between the disturbed wave front by the object and the reference wave emanating from the source, (c) and (f) show the normalized contrast images.

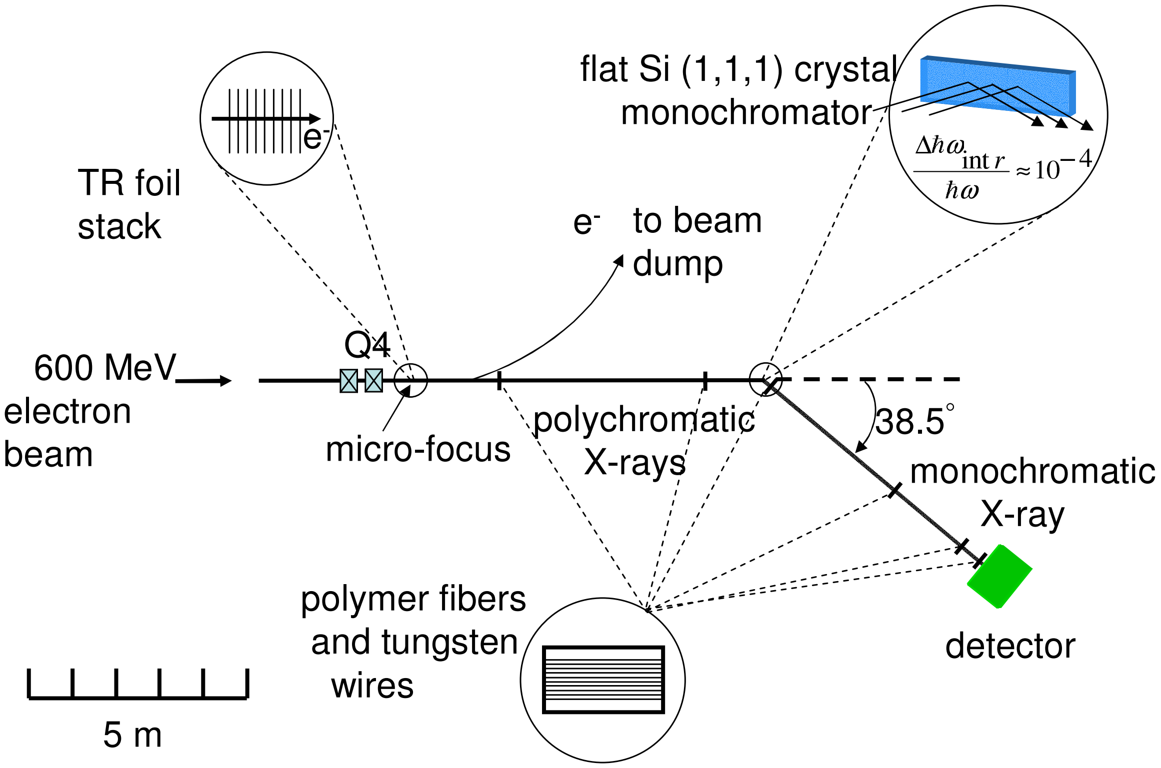

Figure 5.2: Schematic experimental setup for X-ray in-line holography at MAMI. Shown are also the main components and the locations of the objects to be imaged which can be positioned in distances of 1.88, 4.3, 7.47, 10.78, 12.71 and 13.6 m from the X-ray source.

A full-scale overview of the experimental setup is shown Fig. 5.3. It consists of the electron beam line with various focusing elements for preparation of the micro-focus, the target setup with TR foil stacks, the single crystal monochromator in a distance of 7.8 m from the target, and a CCD detector or an X-ray film in a distance of 5.8 m from the monochromator. The position of the objects between X-ray source and detector depends on the desirable magnification which is connected with the spatial resolution of the X-ray detector. All components are housed in a connected vacuum system to avoid self absorption of the X-rays. The essential components are described in the following in more detail.

5.2.2 The electron beam line

The electron beam line is located in the hall B of the MAMI accelerator facility. The 7.1° bending magnet BM0 at the exit of RTM3 guides the electron beam with a maximum energy up to 855 MeV into the X1 beam line. After the X-ray production in the target chamber the electron beam is deflected by the bending magnet BM1 by an angle of 43.5° with respect to the original direction which coincides with the X-ray

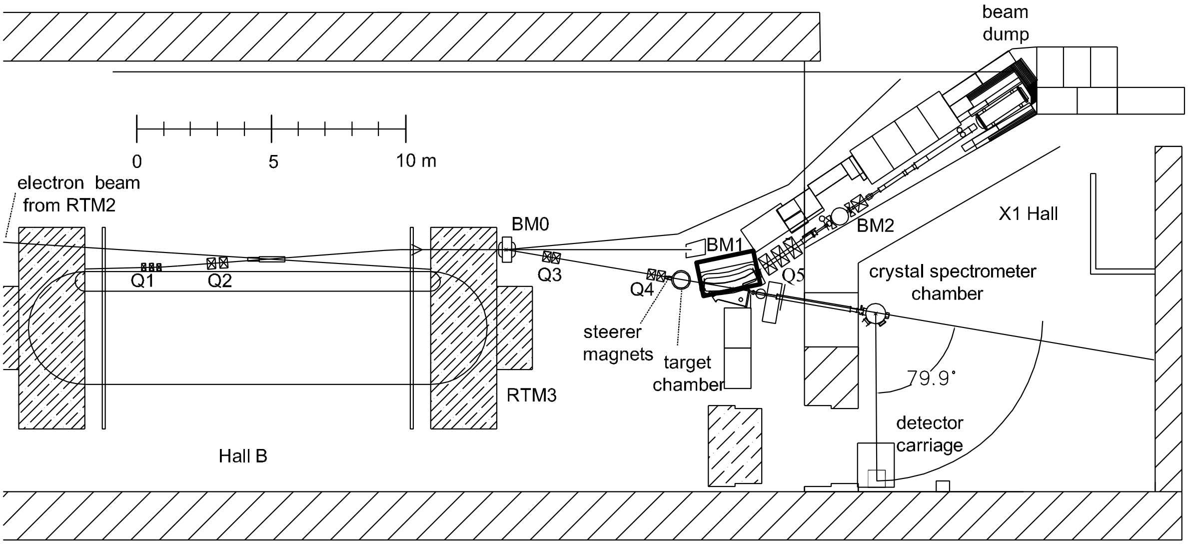

Figure 5.3: Layout of the experimental area of the X1 collaboration with MAMI B. Shown is the X1 beam line with bending magnets BM and quadrupoles Q. X-ray transition radiation, generated by the electron beam up to an energy of 855 MeV in a foil stack located in the target chamber, is monochromized by a silicon single crystal in the crystal spectrometer chamber and detected with X-ray detectors located on the detector carriage

emission cone and thereafter by the dipole magnet BM2 by 7.2° down into the water cooled beam dump which is designed for a maximum available beam current of 100 μA. The micro-focus of the electron beam demands a large beam spot size just prior to the focusing quadrupole doublet Q4. To accomplish this, it was necessary to install an additional quadrupole doublet Q2 in the extraction beam line of the RTM3 accelerator. Ray trace calculations were performed to optimize the location of the beam optical elements and current settings to achieve a spot size as small as possible in the target chamber. A typical result of such a calculation obtained with the interactive computer code beamoptic [ShvXX] is shown in Fig. 5.4.

The standard deviation of the beam spot amounts to $\sigma_h = 1.76$ μm and $\sigma_v = 1.20$ μm in horizontal and vertical direction, respectively. Transition radiation with an energy of 6 keV corresponding to a wavelength of 2.067 Å produced by such a small beam spot results, according to the equation $\sigma_v \cdot \theta_{coh} \simeq \lambda/2\pi$ and $\theta_{coh} = L_T/x_{sd}$, in a transverse coherence length L_T= 373 μm (standard deviation) at a distance $x_{sd} = 13.6$ m between source and detector. Such a transverse coherence length is a prerequisite to carry out experiments on hard X-ray in-line holography at MAMI.

5.2.3 Target setup

The target setup is shown in Fig. 5.5. It consists of beam diagnostic elements and foil stacks for the production of transition radiation in the X-ray region. These components are described in the following subsections.

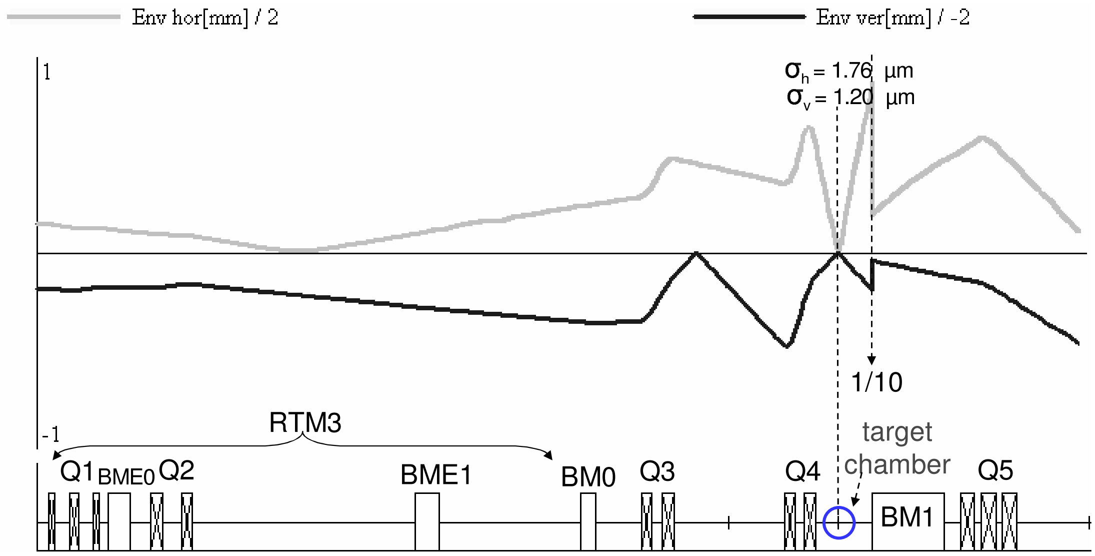

Figure 5.4: Simulation of the micro-focused electron beam using the program beamoptic. Quadrupole triplet Q1 and quadrupole doublet Q2 were used to optimized the electron beam size at the entrance of Q3. Bending magnets BME0 and BME1 deflect the electron beam by angles of 2.85° and 4.38°, respectively, to extract it from the RTM3. Bending magnet BM0 deflects the electron beam by an angle of 7.1° into the X1 beam line. Quadrupole doublet Q3 prepares the electron beam for the microfocusing quadrupole doublet Q4. The bending magnet BM1 deflects the electron beam to the beam dump. Because the lateral size of electron beam behind the microfocus rapidly increases, the gap of BM1 is 80 mm. The quadrupole triplet Q5 focuses the electron beam again to a small size so that it can be guided without losses through the following lattice elements into the beam dump. Both, the horizontal beam envelope (grey) and the vertical envelope (black) are shown along the beam line in terms of standard deviations (RMS-values) in a mm scale.

5.2.3.1 Electron beam diagnostics

For the preparation of the electron micro-focus ZnS fluorescence screens and a tungsten wire scanner were used. The ZnS fluorescence screen permits a rough preparation of the spot size. In a first step the spot size was minimized visually. In a second step the beam was focused on one of the pin-holes in the ZnS fluorescence screen with diameters of 150 μm, 200 μm and 300 μm. Thereafter the spot was optimized by minimizing the fluorescence light emitted from electrons which impinge on the fluorescence screen close to the periphery of the pin-hole.

To further optimize and to measure the spot size quantitatively the electron beam was swept across tungsten wires. As shown in Fig. 5.6, two steerer magnets were used for that purpose which are located downstream the quadrupole doublet Q4 in a distance of 0.45 m from the target. The wires have thicknesses of either 10 μm for a rough or 4 μm for a precise measurement. The electrically isolated wire forms a loop with two straight sections which are perpendicularly to each other to monitor the spot size in

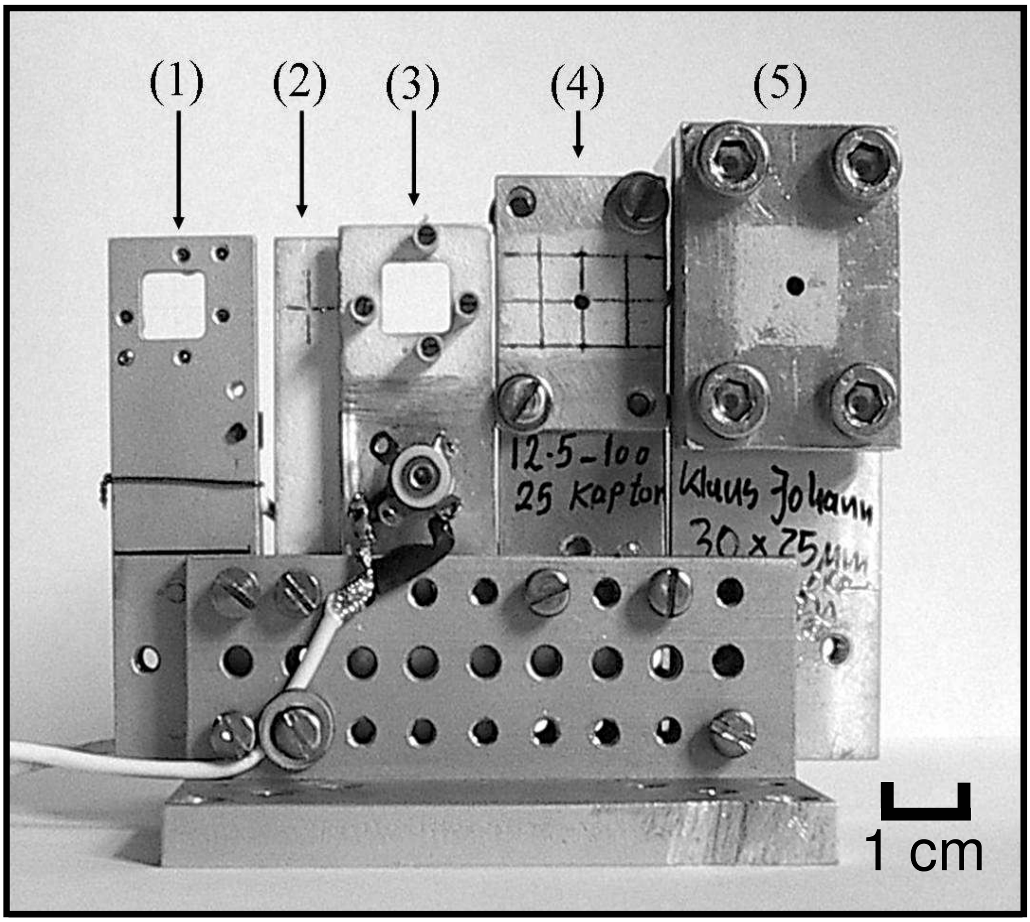

Figure 5.5: Picture of the target setup. The electron beam direction shows inward the picture. (1) Wire scanner with tungsten wires of 10 μm diameter, (2) ZnS fluorescence screen with pin-holes of 150 μm, 200 μm and 300 μm diameter, (3) wire scanner with tungsten wires of 10 μm diameter, (4) polyimide foil stack optimized for emission of 6 keV photons at a beam energy of 600 MeV, (5) polyimide foil stack optimized for emission of 33 keV photons at a beam energy of 855 MeV

horizontal and vertical direction. The current signal is generated by the emission of low energy secondary electrons [Hag95, Hag01]. In the captions of Fig. 5.6 and Fig. 5.7 the procedure is explained in more detail.

Fig. 5.8 shows a measurement of the horizontal and vertical beam spot size at a beam energy of 600 MeV. The originally measured current signal is a function of the time. It was converted into a function of distance by measuring a calibration factor in terms of μm/s. The spot size has a FMHM of 5.2 μm and 4.9 μm horizontally and vertically, respectively. To extract the beam spot size, the measured distributions must be deconvoluted from the response of the tungsten wire to the emission of secondary electrons. For the latter a rectangular function with a width of the wire diameter of 4 μm was assumed. The beam spot was assumed to be of Gaussian shape in both dimensions. Both distributions were convoluted and fitted to the measured distribution with the

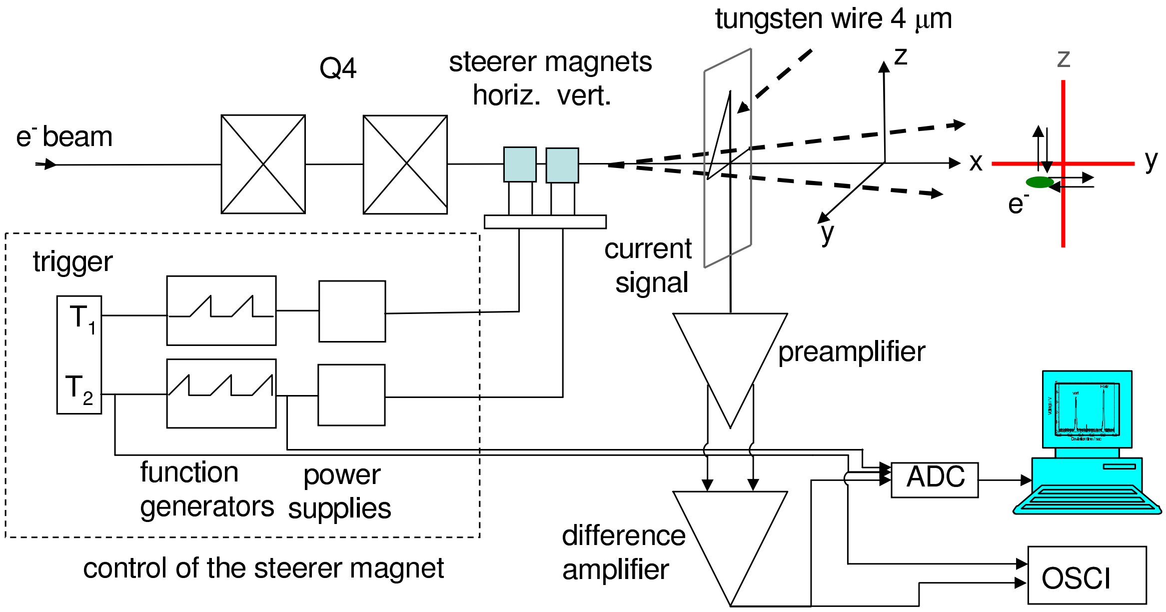

Figure 5.6: Arrangement to measure the electron beam spot size. The steerer magnet currents of ±4 A are delivered by power supplies (Electronic Measurement Inc.) supplying saw tooth pulses. The horizontal trigger (Scientific Instruments GmbH model 9410) is delayed by 0.5 s with respect to the vertical one resulting in a contour as shown in the insert. The repetition rate was typically 2 Hz. The current from the wire is amplified with a preamplifier (homemade by Inst. of Nuclear Physics, Mainz) and converted in a voltage signal. Signal and ground signal of the preamplifier are sent to the control room of MAMI where a difference signal is formed to suppress electrical pick-up and noise. The final signals are correlated to the signals from the function generators, and displayed and saved on a storage oscilloscope (Tektronix TDS 744A) or on a PC after analog-to-digital conversion (ADC-212, Pico 212) [PicXX]

standard deviation of the Gaussian as a free parameter. The best fit is shown as full line in Fig. 5.8. The horizontal and vertical standard deviations are (4.5 ± 0.8) μm and (3.8 ± 0.7) μm, respectively. With the emittance of 0.002 mm mrad and 0.00052 mm mrad the beam divergence turned out to be 0.41 mrad and 0.13 mrad, respectively.

The electron beam current stability at Mainzer Microtron MAMI is measured in a lot of other works and it is smaller than 3%, see for example [Ket00, Hag01].

5.2.3.2 Transition radiation foil stacks

Two polyimide foil stacks have been used to produce transition radiation. As described in section 3.2, one is optimized for a high X-ray flux at 6 keV at an electron beam energy of 600 MeV. A number of 25 polyimide foils with a thickness of 12.5 μm are spaced out by aluminium foils of 100 μm thickness, the latter with centric holes of 2 mm diameter

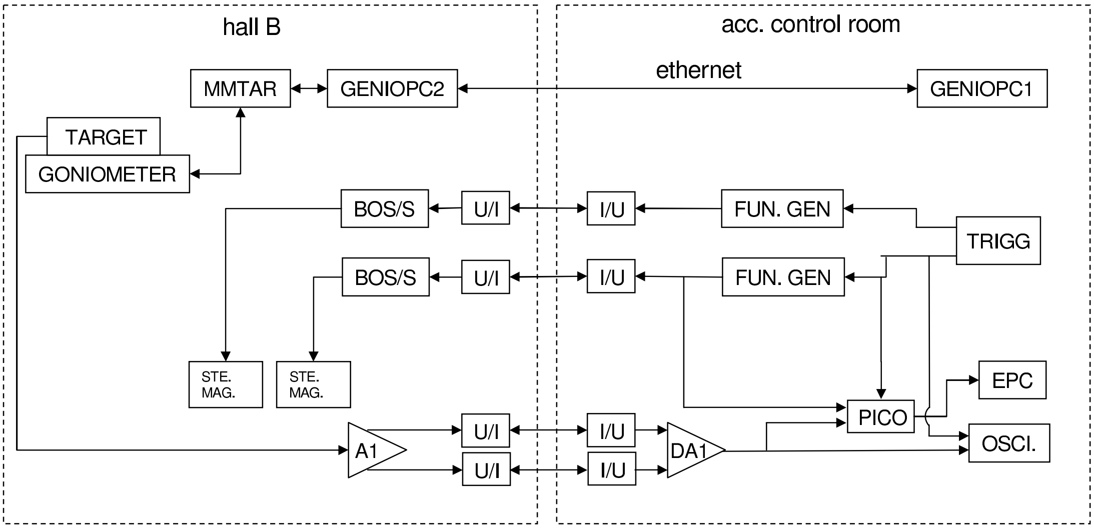

Figure 5.7: Block diagram showing the control units for the measurement of the electron beam spot size and the positioning of the target components, such as tungsten wires and foil stacks, with respect to the electron beam. The goniometer with the target components in Hall B are controlled from the control room of MAMI with the computer GENIOPC1. It communicates by ethernet with the computer GENIOPC2 in experimental hall B which controls via the motor-controller MMTAR all tables of the goniometer. Two function generators (FUN.GEN) generate a sawtooth signal. One signal is delayed with respect to the other one by using an external trigger TRIGG. The signals from the function generators control two bipolar operational power supplies BOS/S (Electr. Meas. Inc.) which are connected to two dipoles steerer magnets. The current signal produced in the wire scanner is amplified by preamplifier A1. A difference amplifier DA1 is used to suppress pick-up and noise. The output signal of DA1 is recorded with a storage oscilloscope OSCI (Tektronix) or by the oscilloscope PICO. The signals are recorded with a personal computer (EPC)

for the passage of the electron beam. Foils and spacers are tightly pressed together. The other foil stack is optimized for emission of 33 keV photons at a beam energy of 855 MeV [Joh95]. It consists of 30 polyimide foils of 25 μm thickness and 75 μm spacing. In order to find the center of the foil stack, ZnS screens are mounted in front of the stacks with holes of 2 mm diameter.

The whole target assembly is mounted on a four axis goniometer, see Fig. 5.9, permitting precise adjustments in the y and z coordinates perpendicular to the beam direction. The movement of the target setup in x direction allows a measurement of the beam spot size at different positions along the beam axis. Such measurements provide information whether the focus is located directly in the foil stack rather than before or behind it.

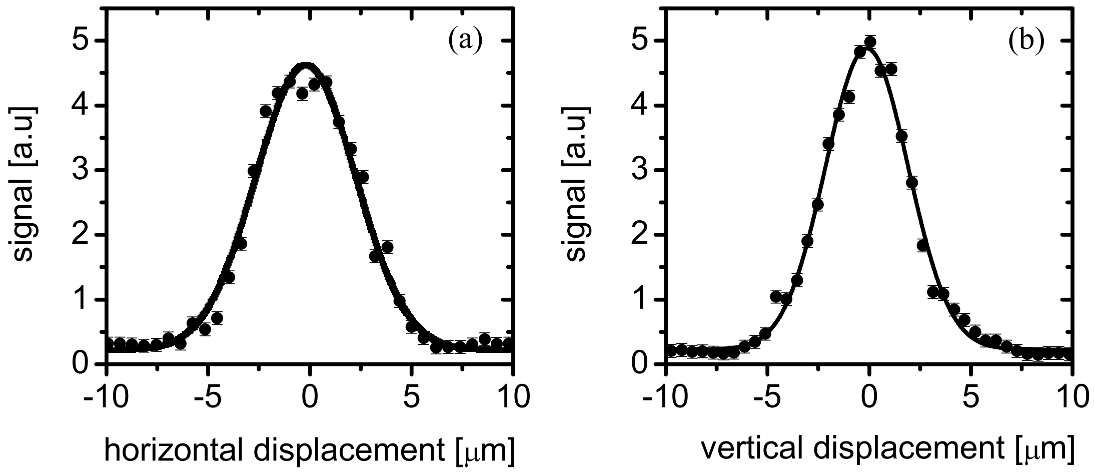

Figure 5.8: Electron beam spot size as measured with a tungsten wire of 4 μm diameter at a beam energy of 600 MeV. The electron beam current was 50 nA. Shown are (a) the horizontal and (b) the vertical profile. The full line represents a best fit with standard deviations of the beam spot of $\sigma_h = (1.9 \pm 0.3)$ μm and $\sigma_v = (1.6 \pm 0.3)$ μm

5.2.4 Single crystal monochromator

The transition radiation X-rays are monochromatized with a flat silicon single crystal in Bragg geometry with its surface parallel to the (111) crystal plane. An appropriate monochromatic X-ray energy can be selected by the angle of the detector arm that can be rotated up to 80° with respect to the forward direction of the X-ray beam.

The monochromator setup is depicted in Fig. 5.10. Residual strains on the rectangular crystal with dimensions of $160 \times 40 \times 1$ mm^3 are minimized by fixing the crystal just from one side with the aid of final dimension plates, while the other side is sitting on a stand. For the positioning of the monochromator crystal in the X-ray cone and accurate orientation at the appropriate Bragg angle, the crystal is mounted on a four axis goniometer. The Bragg angle must be adjusted with high precision, therefore the rotatable table ROT1 is equipped with a highly accurate rotation encoder (ENC) which has an angular resolution of 0.0002°. Further details of the monochromator setup are described in Ref. [Ket00, Lin97].

The goniometer of the monochromator in the crystal spectrometer chamber is computer controlled. Details are shown in Fig. 5.11.

5.2.5 Detector carriage

In a distance of 5.8 m from the monochromator crystal X-ray detectors can be mounted on a carriage which is shown in Fig. 5.12. The vacuum chamber is evacuated in order to avoid self absorption of the X-rays. As detectors either X-ray films or charged-coupled

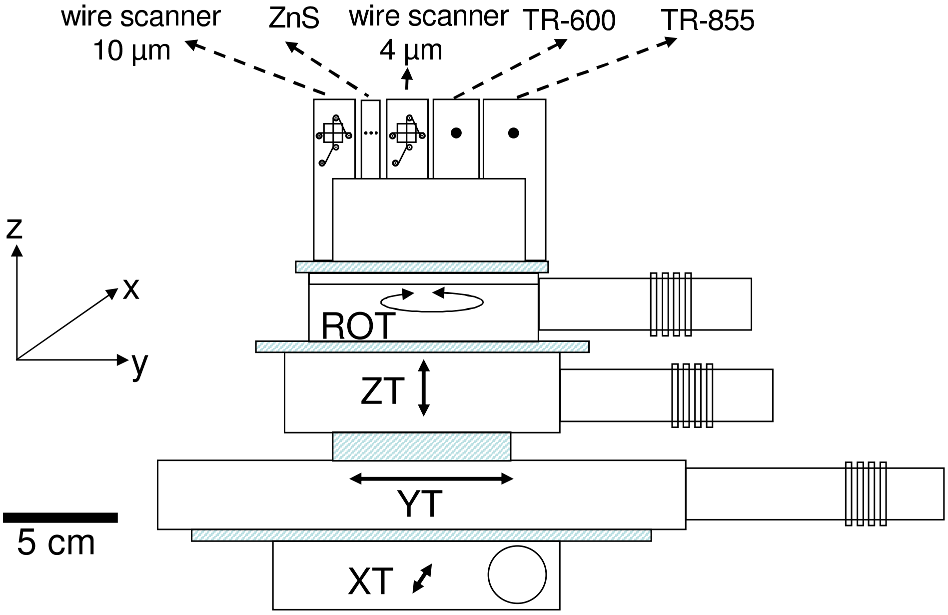

Figure 5.9: Target and goniometer setup in the TR-chamber. The electron beam moves in x direction. The goniometer consists of four tables that allow motions in x, y, and z directions with an accuracy of 1 μm, 0.1 μm, and 1 μm, respectively, as well as rotation around the z axis with an accuracy of 0.01°

devices (CCD's) were used. For experiments with films the X-rays pass through a polyimide window of 25 μm thickness and with a diameter 50 mm, as shown in Fig. 5.13. The films are located in air close to the exit window to minimize self absorption in air.

As already pointed out in section 4.2.2, the advantage of X-ray films is the good spatial resolution of about 2 μm which actually can be achieved with hard X-rays. The disadvantage is that X-ray films are slow, off-line detectors with a small dynamic range. Electronic detectors like CCD's allow fast on-line imaging. The resolution in a direct exposure mode is limited by the pixel size. However, luminescent screens in conjunction with a CCD offer, in principle, on-line operation with a resolution that is limited by diffraction of visible light to about 0.5 μm. Both detector systems have been implemented and are described in the next section.

5.3 Charge-coupled device (CCD) as X-ray detector

5.3.1 Description of the back-illuminated CCD chip

Quantitative radiography applications, such as phase contrast and hard X-ray holography, require a digitization with low noise, large dynamic range and linear relationship

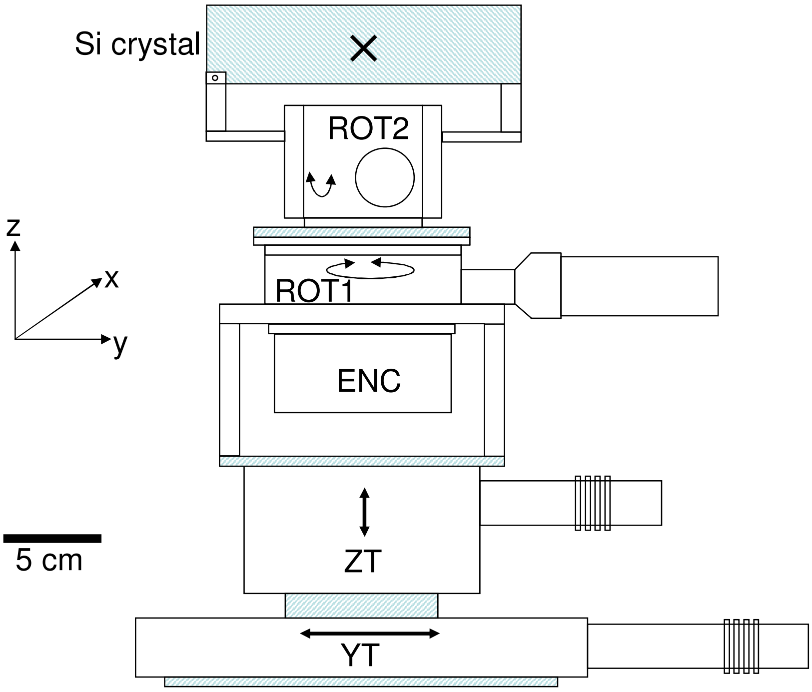

Figure 5.10: Monochromator crystal and goniometer setup in the spectrometer chamber. The X-ray beam moves in x direction. The silicon single crystal is installed on a goniometer which consists of four tables which allow motions in the orthogonal y and z directions with an accuracy of 1 μm, as well as rotation around the vertical z axis (ROT1) and tilts with respect to the propagation direction of the X-ray beam (ROT2). With a high precision encoder (ENC) for table ROT1 the Bragg angle can be adjusted with a precision of 0.0002°

between the incident radiation intensity and the response of the detector. Such conditions can be fulfilled by charge-coupled devices (CCD$_s$) which had been developed at AT &T by W.S Boyle and G.E. Simth in 1970 [Boy77]. For the current experiments the CCD system ANDOR DO-434 BN CCD [AndXX] was used. It contains a back-illuminated CCD low noise sensor from Marconi CCD47-10 [MirXX] with 1024 × 1024 pixels of a size of 13 × 13 μm^2. The ANDOR DO 434 BN CCD chip is depicted in Fig. 5.15, the main properties of the system are tabulated in Tab. 5.3.1. The integrated Peltier cooling system provides a cooling temperature of the CCD chip of -65°C with air-cooling, and -80°C at additional water cooling. The low dark current at -65°C of 0.002 eles/pixel.sec or even 0.00083 eles/pixel.sec at -80°C allows long exposure times and provides a wide dynamic range.

At back illumination the incident photons enter the sensitive layer of the CCD from the opposite side of the electrode system and must penetrate only a thin layer with a thickness of about 10 nm resulting in a good quantum efficiency. For visible light this layer serves as an anti-reflection coating to reduce surface reflection losses. As shown in Fig. 5.14, the back illuminated Marconi CCD47-10 chip has a good quantum efficiency over a wide spectral range. For hard X-rays of 6 keV energy it amounts to

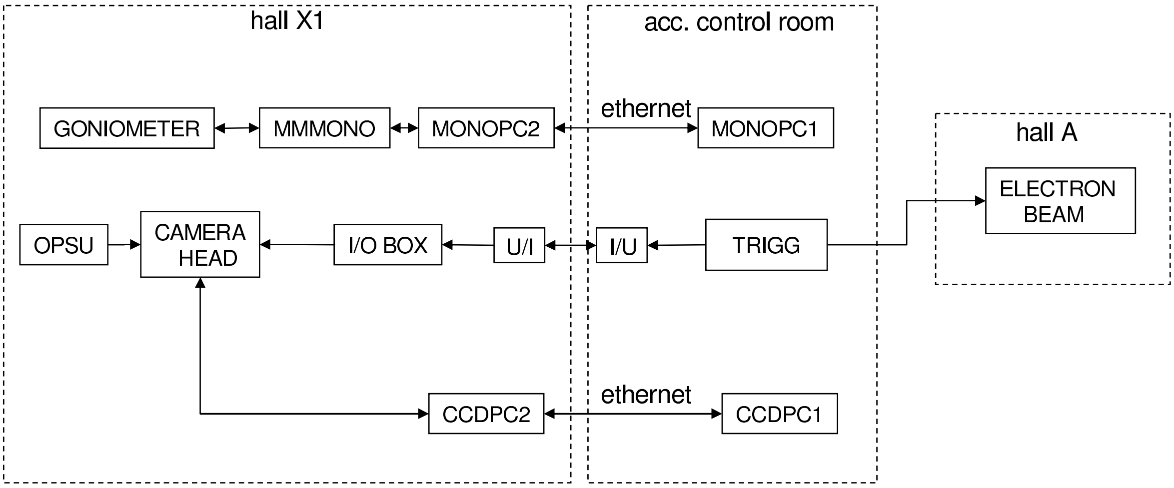

Figure 5.11: Block diagram showing the control units for the monochromator goniometers and data acquisition of the CCD camera. A computer (MONOPC1) communicates via ethernet with a computer in the X1 hall (MONOPC2) which controls the motion master MMMONO of the goniometer tables. The direct exposure CCD camera is controlled from the measuring room with the computer CCDPC1, which communicate by ethernet with computer CCDPC2 in the experimental hall X1. By using external trigger TRIGG the electron beam-on signal and the start signal for the data acquisition with the direct exposure CCD camera are synchronized. The electron beam is switched off during the read out.

still about 45%. These features offer the opportunity to use the CCD chip either in the direct exposure mode in which the signal is generated by direct energy deposition of hard X-rays in the sensitive layer, or in combination with a luminescent screen which converts the X-ray photon energy partly into visible light which is detected by the CCD.

5.3.2 Electronics and data acquisition

After exposure the charge acquired in the pixels of the CCD is digitized pixel by pixel by means of a 16 bit ADC. The read out sequence is described in the caption of Fig. 5.15. Essential part is a low noise amplifier integrated on the chip. To achieve a good energy resolution, the time constant of the amplifier must be sufficiently long, about in the order of is 1 μs. The digitization time per pixel 1 μs. Consequently, the used CCD chip is a slow scan device with a read out time of 1.05 s. In contrast, the requirements on noise and dynamical range of fast scan CCD chips, as used in video-or photographic cameras, are much less demanding.

The software supplied by ANDOR allows integration of successive frames. In the current work, typically 100 frames were integrated before the resultant composite frame was downloaded to the hard disk of a PC. Such mode is known as accumulation mode

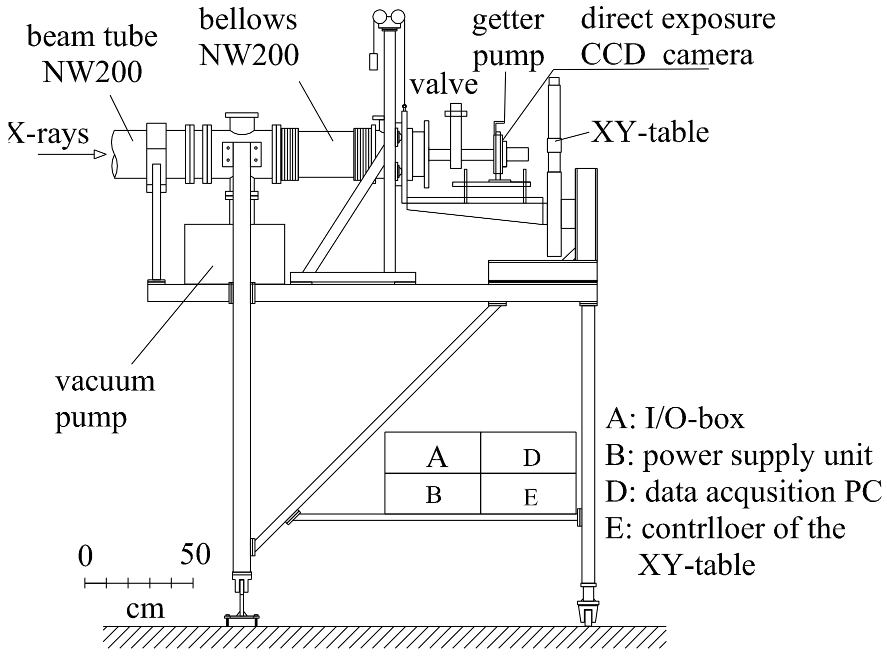

Figure 5.12: Side view of the detector arrangement. For X-ray detection with films the vacuum tube has a polyimide window with 25 μm thickness at a distance of 5.8 m from the crystal. The direct exposure CCD unit is directly connected to the vacuum tube without any window. A membrane bellow (NW 200) is mounted between CCD and beam tube for the purpose of a precise positioning of the CCD unit by means of the XY table with an accuracy of 5 μm

[Mah95] and has the advantage of saving memory space on the storage medium. The CCD camera must not be exposed to X-ray photons during the read out to avoid image deterioration. Therefore, the electron beam was switched off during the read out of the CCD. Typical exposure and read out cycles are shown in Fig. 5.16. The timing is achieved by an external reference signal TRIGG, see Fig. 5.11. The CCD is controlled from the MAMI accelerator control room or from the X1 measuring room with a PC running on windows XP.

5.3.3 The direct exposure mode

In the direct exposure mode the signal is generated by direct energy deposition of the hard X-ray photons in the sensitive layer of the CCD. The primary mechanism is photo absorption. The resulting photo electrons create electron-hole pairs which are collected in the potential well of the pixels.

Fig. 5.12 depicts the installation of the direct exposure CCD at the detector carriage. To avoid condensation of moisture or oil on the cooled CCD chip an oil-free high vacuum at a pressure smaller than 10^{-6} mbar is required. For that purpose oil-free

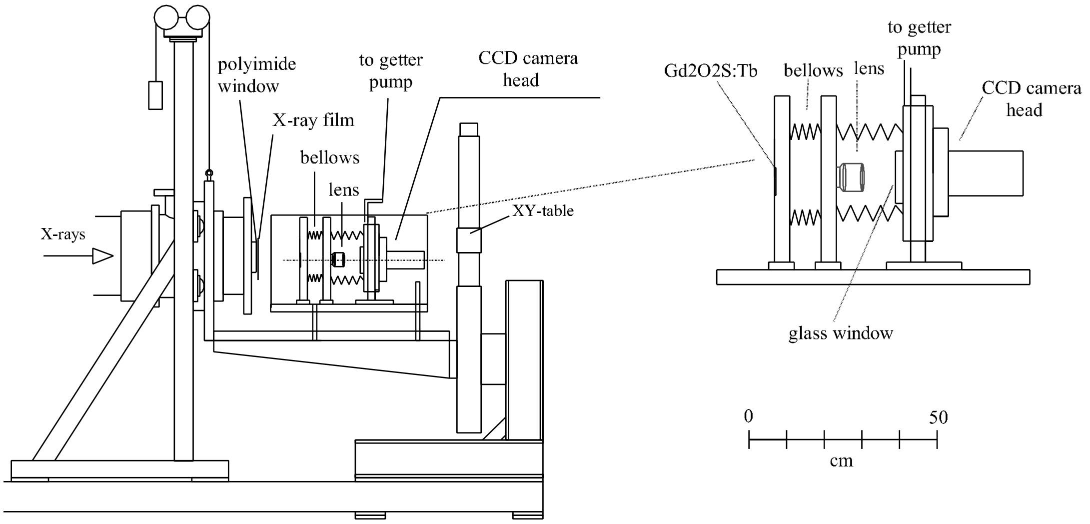

Figure 5.13: Side view of the central part of the detector arrangement for X-ray film exposure and measurements with the luminescent imaging system. X-ray photons impinge from the left and enter into the air through a polyimide foil of 25 μm thickness. The end flange of the vacuum tube has a clearance of 50 mm. The X-ray film is positioned directly behind the end flange. The entrance of the luminescent imaging system is made light tight by two aluminized Hostaphan foils with $\varrho d = 250$ μg/cm^2 covered with 20 μg/cm^2 aluminum. The Gd_2O_2S:Tb luminescent screen has 12 μm thickness and an area of (26×20) mm^2. A Canon camera lens with a focal length $f = 50$ mm and an F-number of 1.4 focuses the picture onto the cooled CCD chip which is located in a high vacuum environment. The picture can be focused remotely by a mechanical drive at the lens.

pumps have been used with which the CCD camera chamber can be evacuated up to a pressure of 10^{-8} mbar. In order to avoid absorption losses in windows, the CCD was operated in the common vacuum system of the monochromator and target chamber. However, the CCD must be protected against visible light which might be generated in the transition radiation foil stack. Two 250 μg/cm^2 thick aluminized Hostaphan foils, with an aluminum thickness of 20 μg/cm^2, are mounted in a distance of 20 cm from the CCD chip. Two foils were used to cover pin-holes in the foils.

A number of test measurements in the direct exposure mode were performed using an ^{55}Fe source which emits K_α photons with an energy of 5.899 keV and K_β photons with 6.49 keV. The source with an activity of 3 MBq was positioned in vacuum at a distance of 21 cm from the CCD chip. The geometrical arrangement is similar as that shown in Fig. 5.13, with the CCD decoupled from the main vacuum system. The CCD camera was cooled down to -80 °C. The exposure time for one frame amounted to 10 s in which about 6000 events were collected at the CCD. This number is small enough to avoid double hits in one pixel (pile up). The pulse hight distribution is shown in Fig. 5.17 (a). The K_α and K_β photon peaks are clearly resolved, see also Fig. 5.17 (b). However, a significant part of the intensity appears in the low energy tail of the lines. The reason for this tail is split-event generation which will be explained in the following.

Table 5.1: ANDOR DO 434 BN CCD detector characterization [AndXX].

CCD chip	Marconi 47-10
Depletion layer thickness [μm]	$\simeq 10$
dark current [eles/pixel.sec]	0.00083 at -80°C
minimum temperature [°C]	-80
pixel size [μm^2]	13×13
effective area [mm^2]	13.312×13.312
R.m.s. read out noise [eles/pixel]	6.8 at 1MHz
full well [eles/pixel]	100000
gain [e^-count] @ 1 & 2,16,32 μs	2, 1.4, 0.7

When an incident photon with an energy of 6 keV is absorbed within the 10 μm thick depletion layer it produces a number of n_e = 6000 eV/3.65 eV = 1644 electron-hole pairs, since for the production of one electron-hole pair an energy of 3.65 eV is required [Deb88]. Electrons and holes are separated in the electrical field of the depletion layer and the electrons are collected at the electrodes. For X-ray photons with an energy of 6 keV, the initial diameter D of the electron cloud can be estimated to be $D[\mu\text{m}] = 0.017\cdot[E[\text{keV}]]^{1.75} = 0.39$ μm [Bau86]. During the transport to the electrodes the diameter increases because of the electrostatic repulsion between the many electrons and diffusion. This may lead to a distribution of the electron cloud over more than one pixel and split events are generated. Only for 17% of all events the charge is collected in a single pixel, as has been determined by analyzing single frames. It was found that the charge may be splitted in up to 7 neighboring pixels. On the one hand, such split events deteriorate the spatial resolution of a radiograph but, on the other hand, they can be exploited to improve the resolution by the determination of the center of gravity of the split events. Algorithms have been developed [Tsu02] with which sub-pixel resolutions were obtained. However, preparatory experiments showed that in our case at least 23000 single frames are required to produce just one radiograph with sub-pixel resolution and good statistics [1]. At a read out time of 1.05 s per frame this leads to an unreasonable long collection time of nearly 7 hours. Therefore, this idea was not further pursued, and for all experiments described in the following the accumulation mode has been applied. However, it must be concluded from the test experiments described in this section that only a spatial resolution can be achieved which is worse than the pixel size of 13 μm.

---

[1] As will be shown in the section **??**, a radiograph with good statistics requires a summed pulse hight of about 350,000 ADC-counts/pixel, offset subtracted. To reach such a pulse height, 580 photons with an energy of 6 keV must be absorbed by a single pixel since one 6 keV photon generates an ADC-count number of 600, see Fig. 5.17. For a reconstruction with sub-pixel resolution, pile up must be absent which means that exposure time and X-ray flux must be reduced. This requirement leads to an enlargement of the collected frames by about a factor of 20 in comparison to a normal exposure. Therefore, the required single frames are 11600. Since for a normalized contrast radiograph the image must be background corrected, we need additionally 11600 single frames for the corrected the radiograph.

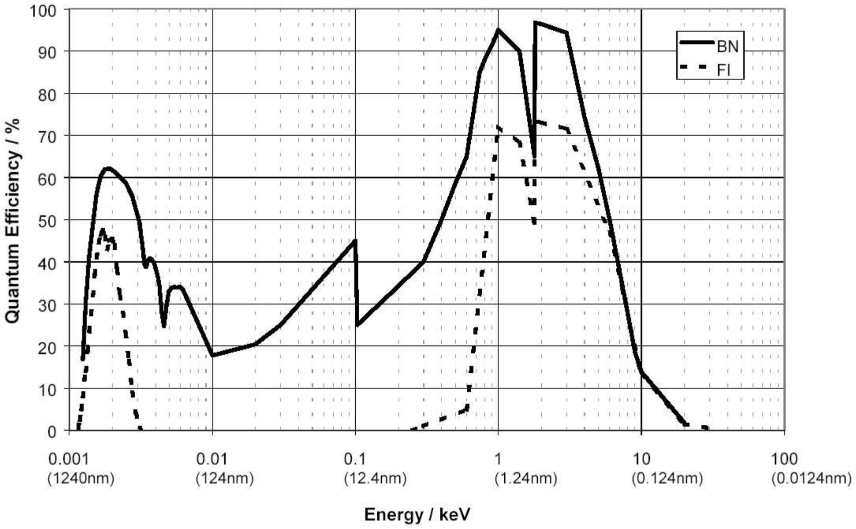

Figure 5.14: Quantum efficiency of a back illuminated (BN) and a front illuminated (FI) Marconi CCD47-10 chip. In comparison to the front illuminated chip, the back illuminated CCD has high quantum efficiency over a wide spectral range which extends from visible light to hard X-rays. [AndXX].

The section will be closed with a discussion of the energy resolution. It is demonstrated in Fig. 5.17 (b) and (c), that a resolution of (127±4) eV was achieved with the CCD chip. The theoretical limit of the energy resolution is determined by the statistics of the produced electrons (Fano-noise-limited performance) and the readout noise σ_r. Not all energy of the absorbed photon generate electron-hole pairs since some amount of energy is transferred to Si lattice in which phonons are excited. The resulting statistical fluctuations are taken into account by the Fano factor [Ber68] which is $F = \ 0.115$ for silicon, and the resolution (FWHM) is expressed as

$$\Delta\hbar\omega[\mathrm{eV}] = 2.355 \cdot 3.65\sqrt{\sigma_r + F\frac{E[\mathrm{eV}]}{3.65}}. \tag{5.2}$$

At a read out rate of 1 MHz the read out noise is $\sigma_r = 6.5$ electron (rms) per pixel and the best achievable energy resolution for monochromatic 6 keV photons is $\Delta\hbar\omega = 120$ eV. The experimental result is rather close to this number.

5.3.4 X-ray imaging with a luminescent screen

The direct exposure mode of the CCD has the advantage of a good detection efficiency, however, as discussed in the preceding section the spatial resolution in the accumulation mode can not be better than the pixel size. In this section another possibility will be discussed to achieve a good spatial resolution with a CCD detector which preserves the on-line capability. It based on the fact that with the aid of a luminescent screen the X-ray picture can be transformed into a visible light picture which can be magnified

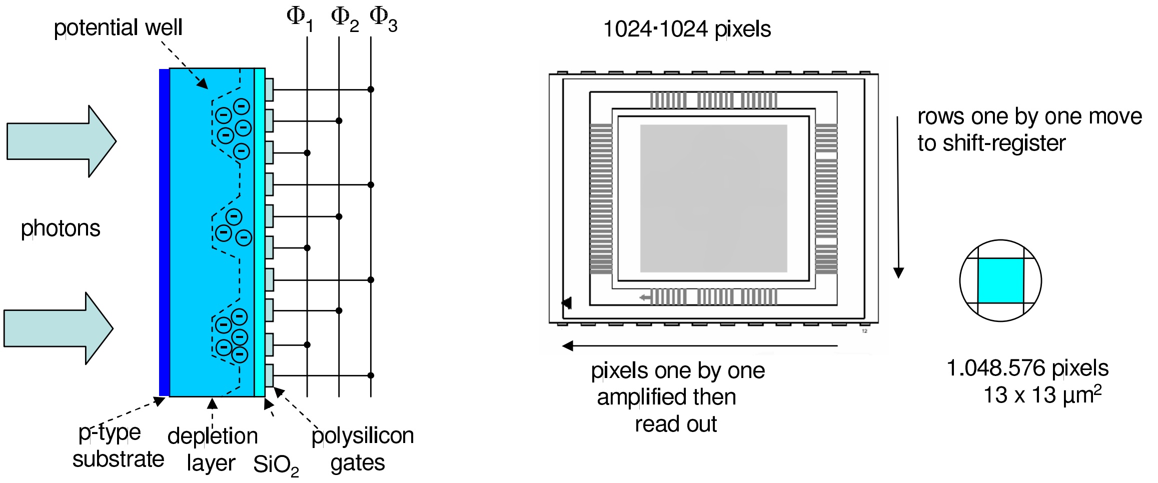

Figure 5.15: Scheme to illustrate the operation principle of a charge coupled device (CCD). Left: Side view to illustrate direct detection of photons at back illumination. Right: Front view to illustrate the read-out mechanism of the back-illuminated CCD sensor Marconi CCD47-10. (a) The stored charges in a frame are shifted by one row so that the bottom row moves to the shift register. (b) The charge in the shift register is moved horizontally by one pixel. This way the charge at the endmost pixel of the shift register is moved into the input node of the amplifier. (c) The charge in the output node of the amplifier is moved to the analog-to-digital converter and is digitized. (d) Steps (b) and (c) are repeated until the shift register is worked out. (d) The frame is shifted vertically again by one row, i.e. the next row of charge moves down into the shift register. Steps (b), (c) and (d) are repeated until the whole frame is read out [AndXX]

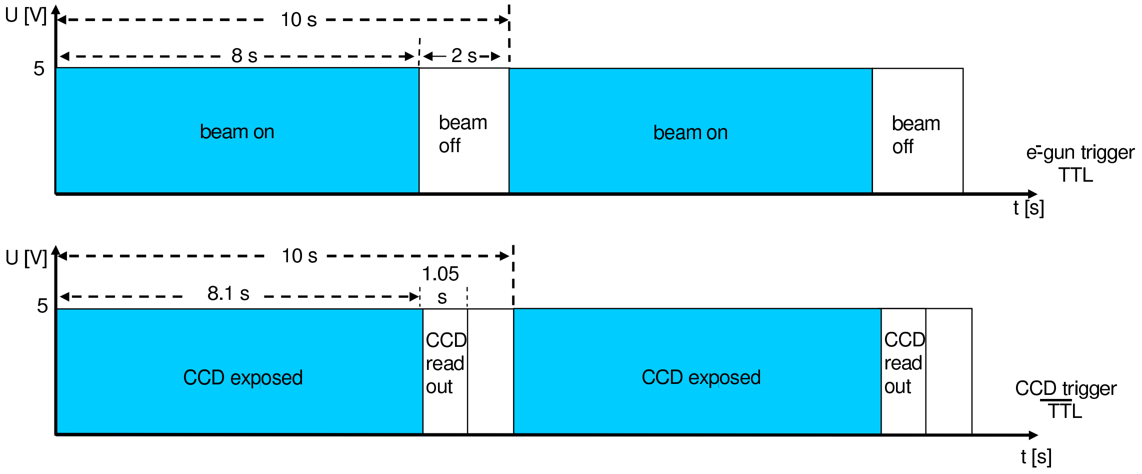

Figure 5.16: Readout of the CCD. After 8 s exposure of the CCD the electron beam is switched off, 0.1 s later the read out starts which lasts 1.05 s, and 0.85 s later a new cycle starts.

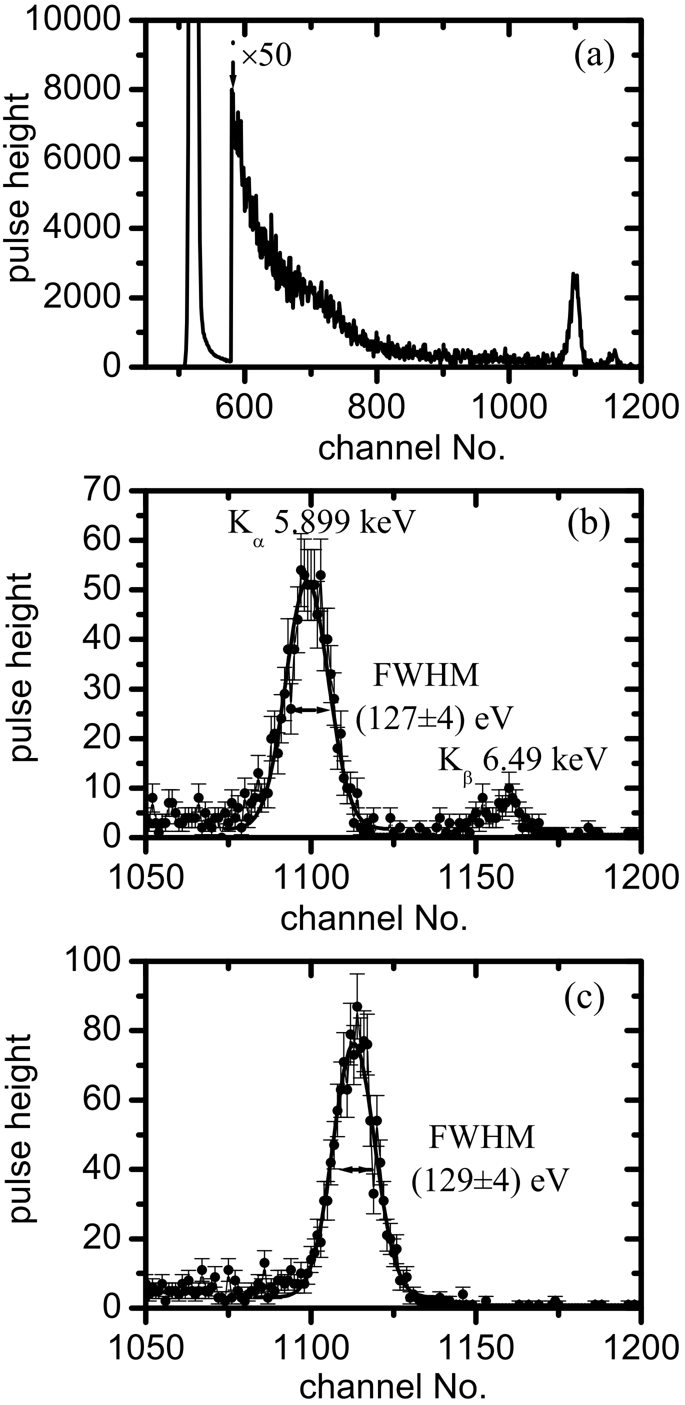

Figure 5.17: Photon energy spectra recorded by the CCD detector chip. (a) Spectrum taken with an ^{55}Fe source at a temperature of the CCD chip of −80 °C, exposure time 10 s. (b) Enlargement of the K-line region. The measured energy resolution amounts to $\Delta\hbar\omega = (127 \pm 4)$ eV. (c) Spectrum taken on-line with the silicon (111) reflex at the Bragg angle of $\theta_0 = 19.25°$ which corresponds to a photon energy of 6 keV. Electron beam current 1 nA, exposure time per frame 1 s. Pile up can be completely neglected. CCD temperature −50 °C. The energy resolution $\Delta\hbar\omega = (129 \pm 4)$ eV is about the same as the energy resolution obtained at the lower temperature of -80 °C.

by optical imaging with lenses and detected by the CCD chip [Bus94]. In principle, a diffraction limited resolution in the sub-μm region can be obtained by such a method [Koc98]. However, although the CCD has a high quantum efficiency in the visible spectral range, as can be seen from the Fig. 5.14, the detection efficiency is reduced in comparison to the direct exposure mode due to a low conversion efficiency of the X-ray photons into visible light of 15-20 %, and a low light collection efficiency of the lens system of 0.6%. A rather faint optical picture may result which can be deteriorated by background processes originating from the hard gamma-ray (bremsstrahlung) part in the transition radiation spectrum, see section 3.3. In this section the results of experiments with such a detection system are summarized. Details are presented in the appendix C.

The imaging system with a Gd_2O_2S:Tb luminescent screen is depicted in Fig. 5.18, and a radiograph taken with monochromatic X-rays of 6 keV energy of different polymer strings is shown in Fig. 5.19. The essential feature is that the radiograph is littered with white points. These were generally observed with this kind of imaging system, see appendix C. The reason was found in the high energy bremsstrahlung background which is emitted simultaneously with the X-rays in the transition radiation foil stack. Since the bremsstrahlung production cross section scales with Z^2 this background could be diminished by employing foils with lower atomic numbers Z as, e.g., beryllium or lithium. In addition, a sophisticated shielding of the CCD chip may help to suppress the background. However, we refrained from an optimization of this type of detector system since it would have required a great deal of developments and tests.

5.4 Investigation of the features of the monochromized photon beam

5.4.1 Energy width and longitudinal coherence length

The flat silicon single monochromator crystal, cut with the (111) lattice plane parallel to the surface, acts as a mirror for the transition radiation photons emitted from the foil stack [Bea74, Har71, Pin84]. However, this mirror is energy dispersive in the horizontal direction. The deviation ε of the photon energy, defined by the equation $\hbar\omega = \hbar\omega_B(1+\epsilon)$, from the nominal Bragg energy

$$\hbar\omega_B = \frac{2\pi\sqrt{h^2+k^2+l^2}}{a_0}\frac{\hbar c}{2\sin\theta_B} \tag{5.3}$$

is given by the expression

$$\varepsilon = \frac{\Re(\chi_0)}{2\sin^2\theta_B} - \frac{\theta_x}{\tan\theta_B} \tag{5.4}$$

where $\theta_x = \theta - \theta_B$ is the deviation from the nominal Bragg angle θ_B. The integers h, k, l are the Miller indices, and a_0 the lattice constant. In our experiment the (111) reflection was selected. The Bragg angle for $\hbar\omega_B = 6$ keV amounts to $\theta_B = 19.25°$.

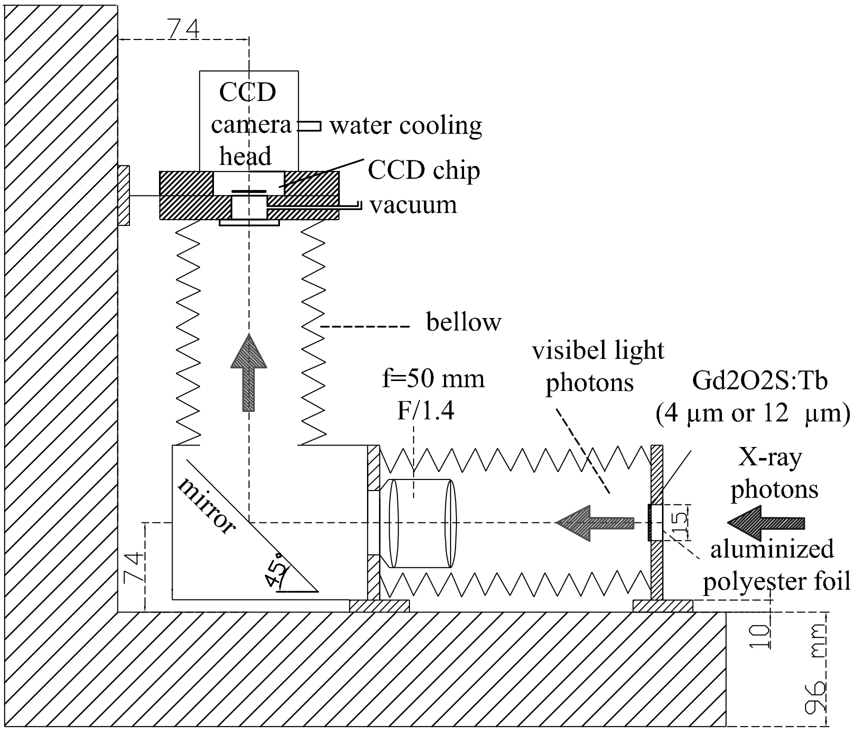

Figure 5.18: Imaging system (not to scale). X-ray photons impinge from the right onto the Gd_2O_2S:Tb luminescent screen of 4 and 12 μm thickness for polychromatic and monochromatic X-ray detection, respectively [ProXX, SICXX]. An f = 50 mm Canon camera lens with F-number of 1.4 has been used [CanXX]. The principal points are located in front of the lens. The picture at the luminescent screen can be focused remotely by a mechanical drive at the lens. For a detailed description of the CCD camera head see section 5.3.

In in-line holography a scattered wave from the object interferes with an unscattered wave from the source. For a transverse coherence length of L_T = 250 μm a θ_x=18.4 μrad results in a distance of 13.6 m. The angular spreads which originate from the beam spot size and the pixel resolution are less than 1 μrad and can be neglected. The angle θ_x corresponds according to Eq. (5.4) to a relative energy shift of 5.3 $\cdot 10^{-5}$ or 0.32 eV. This means that two waves with slightly different energies must interfere what is only possible if the longitudinal coherence length L_l is long enough. To judge this, we first calculate the longitudinal coherence length of the Bragg reflected X-rays itself.

The finite energy width of the Bragg reflection can be calculated from the reflecting power ratio $|R^P|^2$ with the amplitude ratio given by [Cat89, Eq. (3.2)]

$$
\begin{aligned}
R^P(\theta_x, \varepsilon_\theta) &= -y_P(u) + \mathrm{sign}[\Re(y_P(u))]\sqrt{y_P^2(u) - 1} && (5.5)\\
y_P(u) &= \frac{u + i\Im(\chi_0)}{P\chi_H} && (5.6)\\
u &= 2\sin\theta_B[\theta_x\ \cos\theta_B + \varepsilon\ \sin\theta_B] + \Re(\chi_0). && (5.7)
\end{aligned}
$$

Here are χ_0 and χ_H the Fourier components of the dielectric susceptibilities of the analyzer crystal, and P the polarization factor, with $P = \cos 2\theta_B$ for π polarization

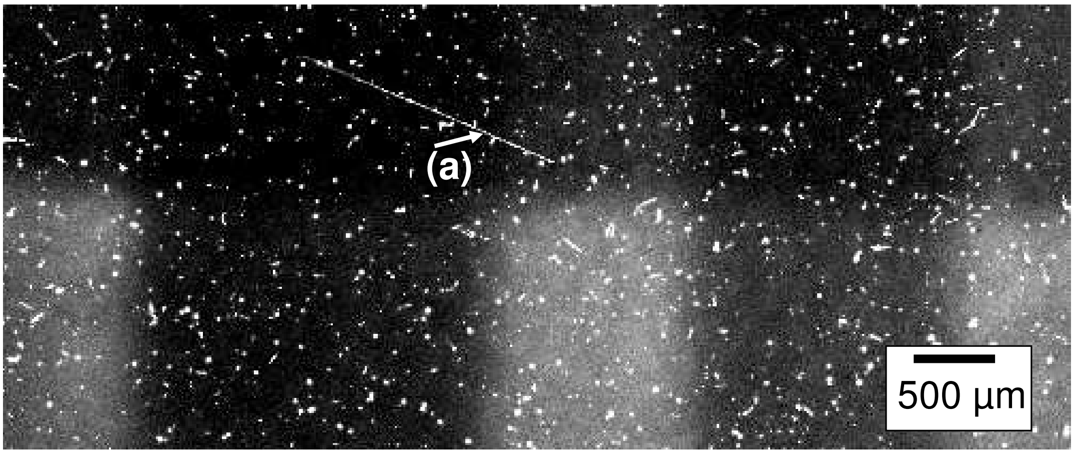

Figure 5.19: Magnified part of a radiograph taken with the setup shown in Fig. 5.18. The image was taken with monochromatic X-rays of 6 keV energy. The white points originate from electrons or positrons, produced in a shower by high energy bremsstrahlung photons, which pass through the CCD detector. In the part labelled with (a) a heavy particle moves through the depletion layer nearly parallel to the surface of the CCD

with the polarization vector in the reflection plane, and $P = 1$ for σ polarization with the polarization vector perpendicular to the reflection plane. The result of the calculation for a polychromatic X-ray beam impinging the crystal at a well defined observation direction is depicted in Fig. 5.20.

The width of the reflecting power ratio shown in Fig. 5.20 is $\Delta\varepsilon = 1.4 \cdot 10^{-4}$ corresponding to 0.84 eV. This energy exceeds somewhat the relative energy difference of 0.32 eV of the two waves which must interfere. The estimation of the longitudinal coherence length will be performed with the larger value resulting in $L_l = 0.5\lambda^2/\Delta\lambda = 0.5\lambda/\Delta\varepsilon = 0.74$ μm. This value is sufficiently large for all objects investigated in this work which had thicknesses in the sub-mm range since at a refractive index decrement of $\delta = 1{\cdot}10^{-6}$ the optical path difference is less than 0.01 μm.

5.4.2 Higher order reflexes

Beside the (111) reflection of the silicon monochromator crystal also the higher orders as (333), (444), and (555) are allowed too. If a continuous X-ray spectrum impinges on the crystal the corresponding higher order photons may perturb a measurement. To study the intensity of these higher order reflexes a CdZnTe detector with an active volume of 3 mm × 3 mm × 2 mm was installed directly behind the polyimide exit window with a thickness 25 μm. At a Bragg angle of 19.25° monochromatic lines are expected at photon energies of 6 keV, 18 keV, 24 keV, and 30 keV. The measured energy spectrum is shown in Fig. 5.21.

The spectrum is dominated by the 6 keV line, however, lines with smaller intensities are observed as well which can be identified to belong to the higher order reflexes. Since

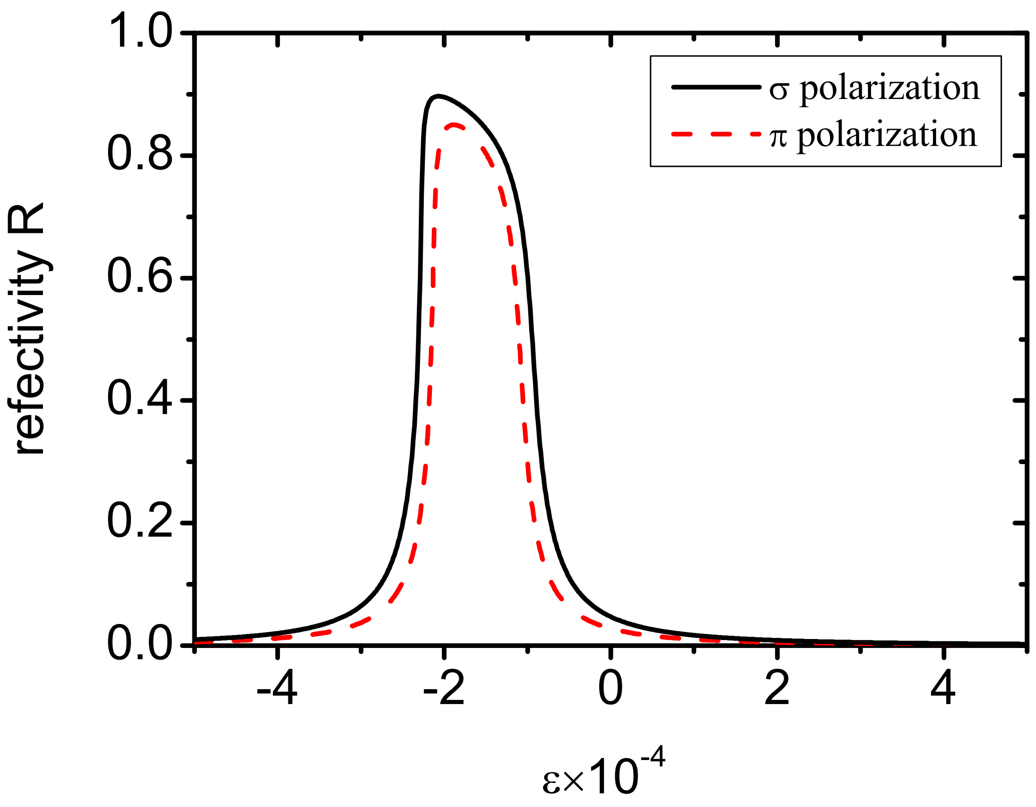

Figure 5.20: Reflecting power ratio for the (111) reflection in Bragg geometry of a perfect silicon single crystal at an observation angle which coincides with the Bragg angle of 19.25°. The abscissa is a the relative energy deviation from the exact Bragg energy. Dielectric susceptibilities are χ_0' = -0.27354$\cdot 10^{-4}$, χ_0'' = 0.10968$\cdot 10^{-5}$, χ_H' = 0.14454$\cdot 10^{-4}$, χ_H'' = 0.76250$\cdot 10^{-6}$ [SerXX]. The width for the π polarization curve is $\Delta\varepsilon = 1.4 \cdot 10^{-4}$.

the efficiency of the CdZnTe detector in the energy range up to 30 keV is approximately constant, it can be seen that the contributions are 3.1%, 2.0%, and 0.8% for the (333), (444) and (555) reflexes, respectively. Therefore, the flux of X-ray photons with 6 keV is about a factor of 20 higher. In addition, for the direct exposure CCD camera the detection efficiency at an energy of 18 keV and larger is very small, see Fig. 5.14, consequently the detection of high energy photons can be neglected. For X-ray films based on silver bromide (AgBr) [PhyXX] with nominal thickness 12 μm the detection efficiency at 6 keV is about 93% while it decreases at 18 keV to 28.6% and at 24 keV to 14.2%. At 30 keV the detection efficiency increases again to 19.6% due to the increase of the absorption coefficient at the absorption edge of Ag at 25.514 keV. From this discussion it can be concluded that the contribution of higher order reflexes is rather small, and it will be neglected in the following.

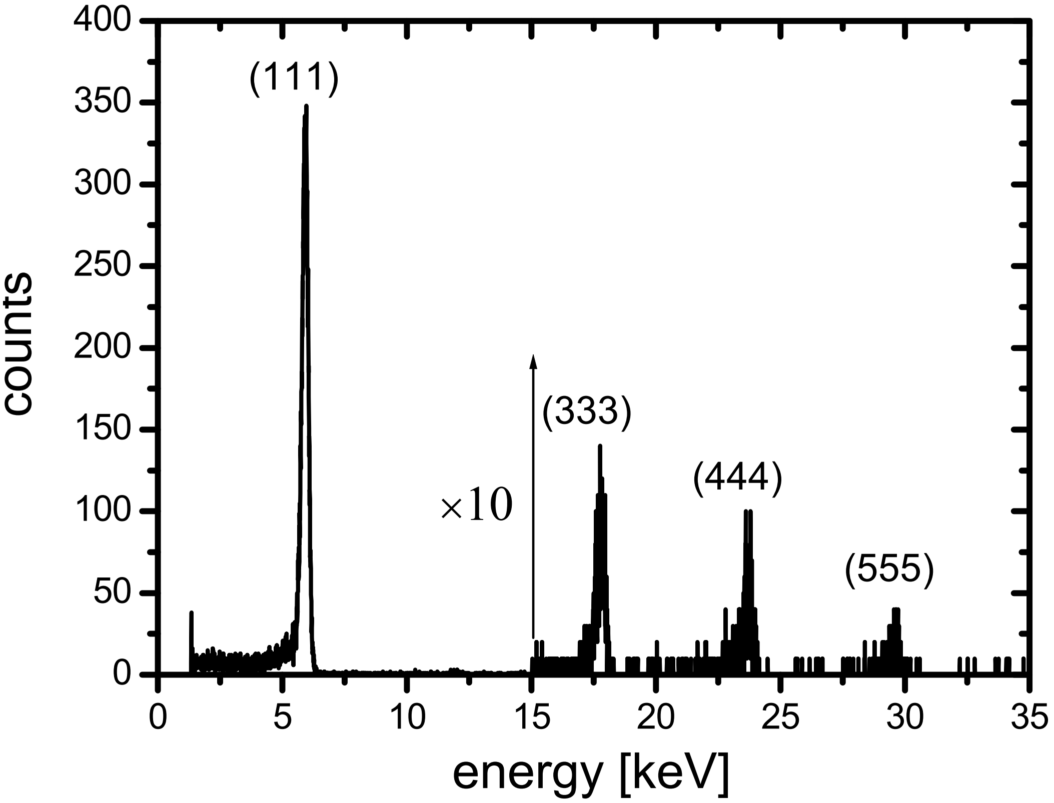

Figure 5.21: The energy spectrum as recorded with a 3 mm × 3 mm × 2 mm cadmium telluride CdZnTe after monochromatization. The Bragg's angle is 19.25° corresponding to an energy of 6 keV for the (111) reflexction. Electron beam current 1 nA, exposure time is 600 sec.

5.4.3 Transverse coherence lengths in horizontal and vertical direction

Fig. 5.22 depicts the radiographs of two polymer strings of the same thickness of 30 μm. In the radiograph (a) the wire is mounted vertically and in (b) horizontally. Although the beam size in horizontal direction is smaller than in the vertical direction, no interference pattern is observed for the vertically mounted polymer string while a nice interference pattern is observed for the horizontally mounted string. Fig. 5.23 shows the normalized intensity profiles of the two strings. The maximum contrast, $\mathrm{C}_{ref} = (I_{max} - I_{min})/(I_{max} + I_{min})$ for the horizontally mounted string is 63.9%, while for the vertically mounted one only 11% . The possibility that the observed effect may be caused by too large a beam spot in horizontal direction has been excluded in additional experiments.

For a beam spot size $\sigma_h = (1.7 \pm 0.1)$ μm the transverse coherence length is, according to the equations $\sigma_h \cdot \theta_{coh} \simeq \lambda/2\pi$ and $\theta_{coh} = L_T/x_{sd}$ for a distance x_{sd}=13.6 m, as

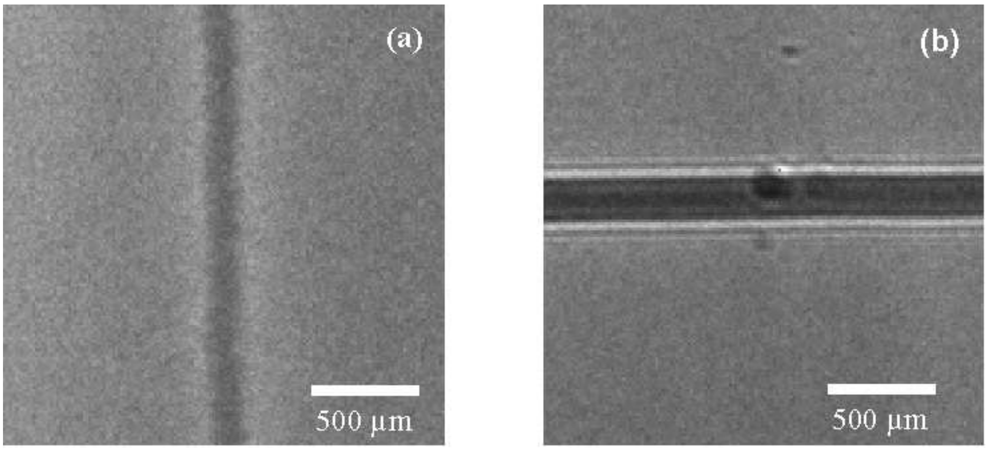

Figure 5.22: Two radiographs of a polymer string of diameter 30 μm. In radiograph (a) the string is mounted vertically, in (b) horizontally. The X-ray source spot size was $\sigma_h = (1.7 \pm 0.1)$ μm in horizontal and $\sigma_v = (3.9 \pm 0.4)$ μm in vertical direction. The electron beam spot size was checked with the wire scanner before and after the imaging in order to be sure that the radiograph deterioration in vertical direction was not caused by to big a spot size in the horizontal direction. The source-to-object distance was $x_{so} = 4.3$ m, and the object-to-detector distance $x_{od} = 9.61$ m. Electron beam current 700 nA, exposure time 1.8 s, 50 frames added.

large as $L_T = 263$ μm (standard deviation). However, only a weak edge enhancement can be observed for the vertically mounted string. The only reasonable explanation for this observation is that the transverse coherence in the horizontal direction is deteriorated by the monochromator crystal. Obviously, in the energy dispersive direction (horizontally) an additional angular divergence is introduced by the crystal.

Fig. 5.24 shows that an angular divergence ψ_{intr} introduced by the crystal results in a virtual spot size in horizontal direction of

$$S_{virt} = \psi_{intr} \cdot x_{sc}, \tag{5.8}$$

with the source-to-monochromator distance x_{sc}, and an apparent spatial resolution of

$$S_r = \psi_{intr} \cdot x_{cd} \quad . \tag{5.9}$$

Let us first discuss whether the angular width of the Darwin-Prins curve might be the reason. With the calculated full width at half maxima of the Darwin-Prins curves of $\triangle\psi_{intr,\sigma} = 46.5$ μrad (FWHM) and $\triangle\psi_{intr,\pi} = 36.4$ μrad (FWHM) for σ and π polarization [SerXX], respectively, a source-to-monochromator distance $x_{sc} = 7.8$ m, a monochromator-to-detector distance $x_{cd} = 5.8$ m, a virtual source size and a spatial resolution of $S_{virt} \approx 360$ μm (FWHM) and $S_r \approx 270$ μm (FWHM) would result, respectively. Such numbers would prevent the observation of interferences at all, in contradiction to the experimental observation. Indeed, according to Eq. (5.7) the

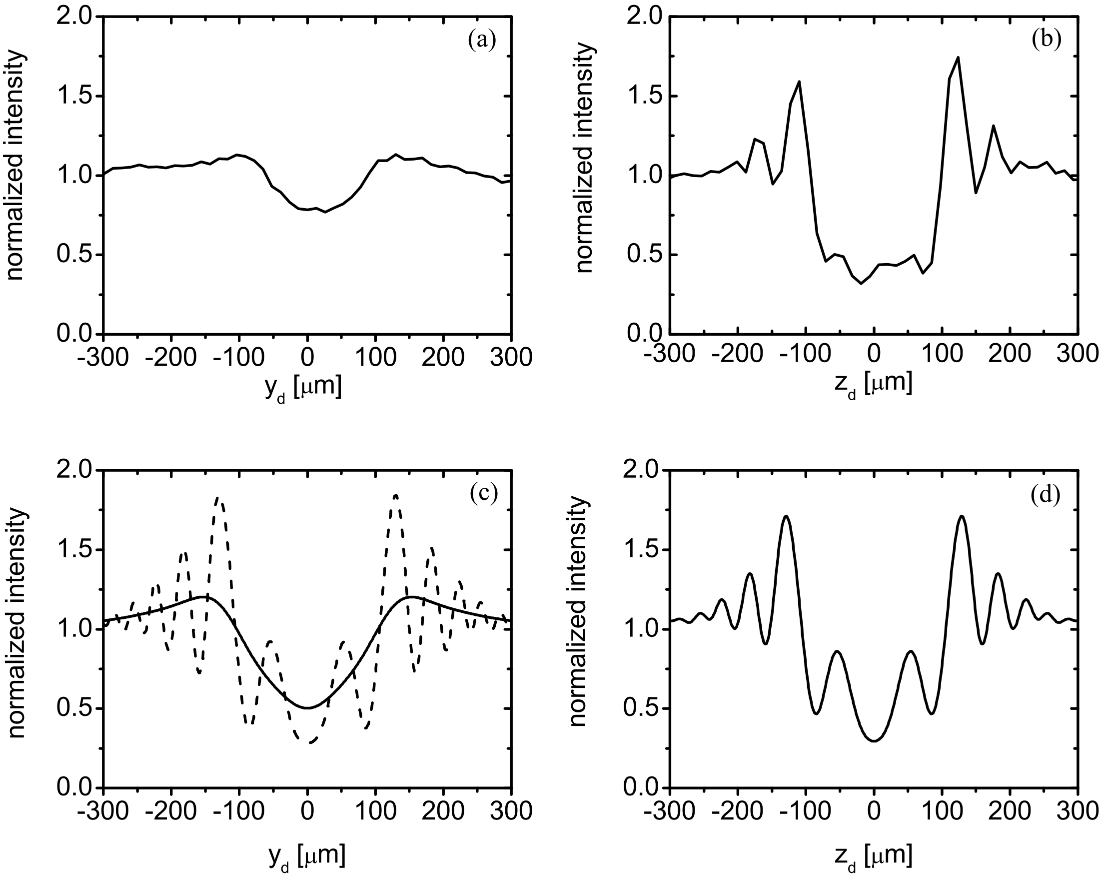

Figure 5.23: Projection in the radiographs shown in the Fig. 5.22. A number of 10 rows resp. columns were added together to improve the statistics. (a) Projection of the vertically mounted string on the horizontal axis, (b) projection of the horizontally mounted string on the vertical axis. Corresponding expected interference pattern are depicted in view graphs (c) and dashed line in (d). Solid line in (d) is calculated interference pattern for the virtual X-ray source spot size $\sigma_{virt} = 37.5$ μm.

reflected power at constant energy $\varepsilon_{\theta x}$ is strictly correlated to the entrance angle θ_x and no angular spreading should occur. However, this equation holds only for plane waves with source and detector at infinity. It remains to be investigated whether for our experimental geometry with source and detector at finite distances an angular spreading could occur, or not.

The spreading angle ψ_{intr} can be estimated by a comparison of the interference pattern observed for the vertical polymer string with a diameter of 30 μm and the simulated one according to Eq. (2.18) taking into account the spatial resolution of the CCD detector. Fig. 5.23 (c) solid line shows the result. From the apparent source size $S_r = 88$ μm which is large in comparison to the pixel size and the horizontal spot size, an $\psi_{intr}=$ 15 μrad follows according to Eq. (5.9), the result is shown in Fig. 5.23 (c) solid line.

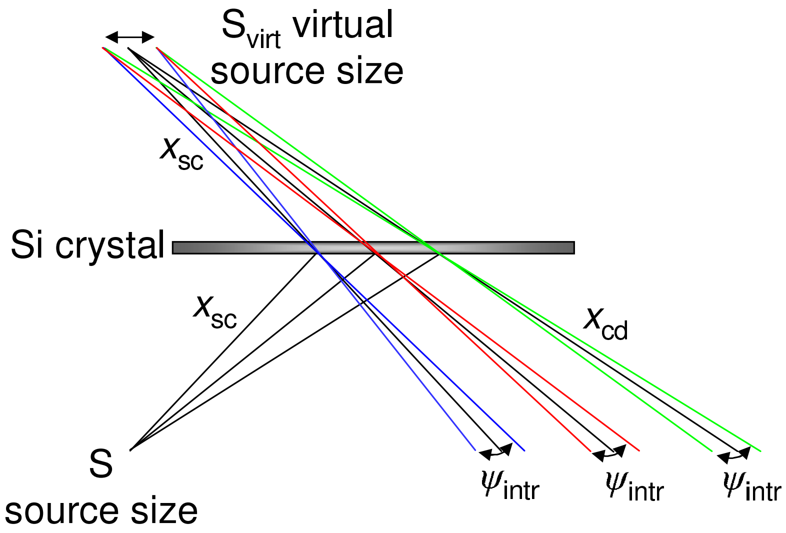

Figure 5.24: Formation of a virtual X-ray spot by an angular divergence in horizontal direction imposed by the silicon single crystal

Whatever the reason for the degradation of the horizontal coherence might be, beside a possible spreading of the reflected power as discussed above also crystal defects may be considered, the vertical coherence is maintained and all experiments described below have been performed with horizontally arranged strings.

5.4.4 Streaks

Fig. 5.25 shows a picture taken with the direct exposure CCD camera without an objects in the transition radiation cone. Cleary vertical streak-like structure can be seen. This structure was investigated in more detail for different photon energies between 5 and 20 keV. Fig. 5.26 shows the results. Radiographs were taken with X-ray films which were digitized as described below in section 5.6, and horizontal stripes with a width of 0.063 mm were projected onto the horizontal y axis. In such a representation the streaks show up as intensity fluctuations. A remarkable feature is that the observed intensity fluctuations obviously depend on the photon energy.

The experimental observations point to surface or intrinsic deformations of the monochromator crystal. The crystal was inspected under an optical microscope but no deformation or inhomogeneities were observed on its surface. Therefore, it must be concluded that the streaks result from deformations or misorientations of the crystal planes inside the crystal (unobservable under an optical microscope), which were formed during the growth of the crystal or during the cutting or mechanical polishing of the crystal surface.

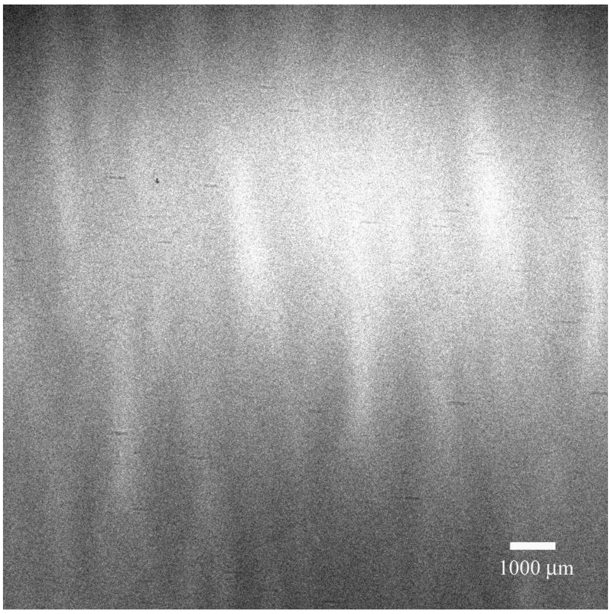

Figure 5.25: Radiograph taken with the CCD camera without an object in the transition radiation cone. Bragg angle 19.25°, photon energy 6 keV. The CCD camera was operated in accumulation mode, exposure time 2 sec, number of single images was 50, electron beam current 160 nA. Clearly observable are vertical streaks.

From the intensity fluctuations shown in Fig. 5.26 information on the bending radius and period of the crystal deformation can be extracted [Chi93, Var96, Kuz99]. It will be assumed that the crystal has wavy structures which form small cylindrical mirrors with certain bending radii R_i, see Fig. 5.27. If a bending radius R_i satisfies the imaging equation [Pod01]

$$\frac{1}{a}+\frac{1}{b}=\frac{1}{f}=\frac{2}{R_i\sin(\theta_B)} \quad . \tag{5.10}$$

with $a = x_{sc} = 5.38$ m the distance source to mirror and $b = x_{cd} = 5.8$ m the distance mirror to detector, X-rays from the source can be locally focused and this way the streaks are formed. The relation between focal length f can be obtained from the geometry of a Rowland circle [Jam65]. From Eq. (5.10) and the Bragg angles as specified in the caption of Fig. 5.26, bending radii between 14 and 55 m can be estimated, the former number belonging to a larger Bragg angle than the latter.

The observation that the spatial period of the streaks decreases as a function of decreasing Bragg angle strongly suggests a common origin in the wavy structure of the crystal. As can be seen from Fig. 5.26, the period y_c of the wavy structure is related to the observed one at the detector plane $y_d(\theta_B)$ by the equation [Bac05]

$$y_c=\frac{x_{cd}}{x_{sc}}\cdot\frac{y_d(\theta_B)}{\sin(\theta_B)} \quad . \tag{5.11}$$

Fig. 5.27 shows a scaling of the streak structures shown in Fig. 5.26 according to this equation with $1/\sin(\theta_B)$. After this scaling the periods are obviously the same. The

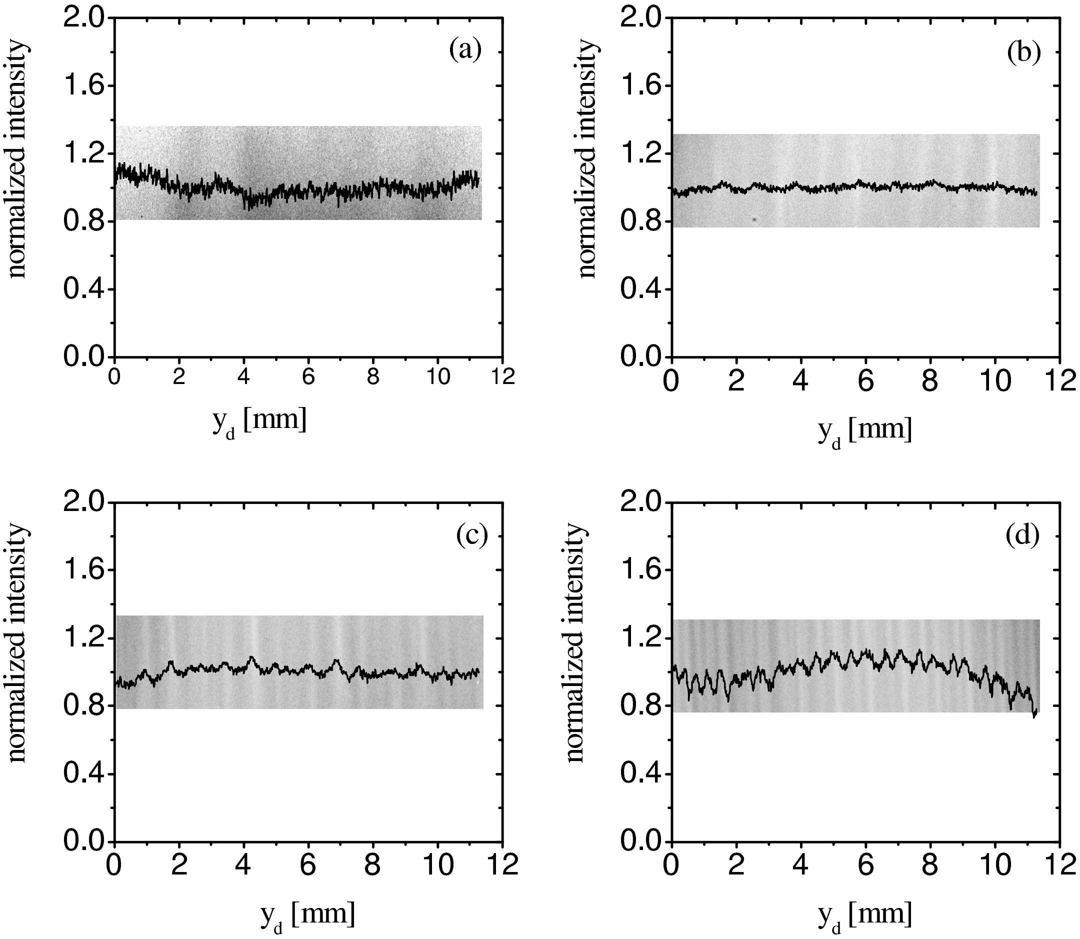

Figure 5.26: Streaks as a function of the X-rays energy recorded with X-ray films, (a) at photon energy of 5 keV, Bragg angle 23.31°, exposure time t_{exp} = 600 s, (b) at 8.23 keV, Bragg angle 13.91°, exposure time t_{exp} = 70 s, (c) at 11.98 keV, Bragg angle 9.51°, exposure time t_{exp} = 100 s, and (d) at 20 keV, Bragg angle 5.86°, exposure time t_{exp} = 600 s. Electron beam current for all radiographs 550 nA, X-ray spot size σ_h = 34 μm and σ_v = 3.4 μm, source-to-object distance x_{sc} = 5.38 m, crystal-to-detector distance x_{cd} = 5.8 m.

results of a quantitative analysis are tabulated in Tab. 5.2. The fact that the bending radius must change as a function of the Bragg angle can be explained by a depth dependence of the bending radius.

To eliminate the effect of the perturbing streaks form the radiograph it must be background corrected. Such a background correction in case of X-ray films is difficult since care must be taken that both exposers are exactly positioned at the same place and that also the exposure time and the film processing are exactly the same. For a direct exposure CCD such a procedure is much simpler since position and current of the electron beam can easily be kept stable over the period of the two exposures with and without the object.

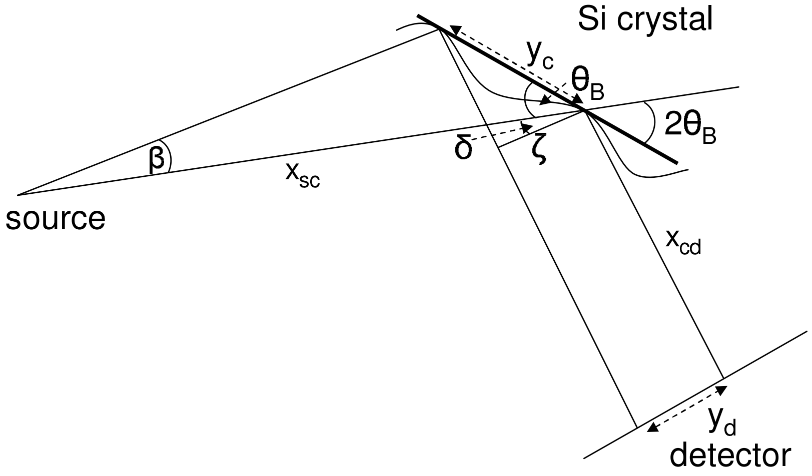

Figure 5.27: Schematic diagram connecting the intrinsic wavy structure in the crystal with the observed one at the detector.

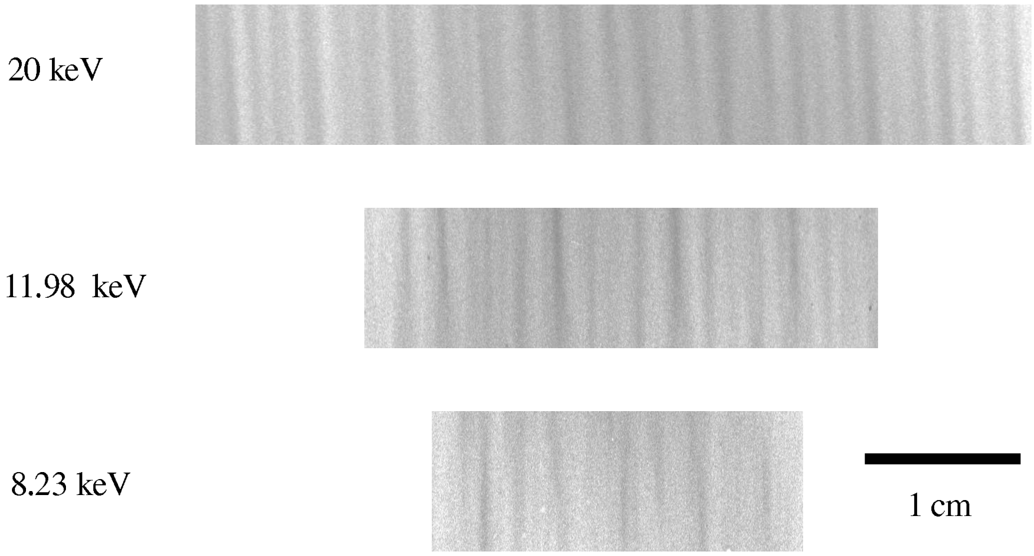

Figure 5.28: The planar morphology of the crystal. The streak structures shown in Fig. 5.26 have been scaled according to $1/\sin(\theta_B)$ as suggested by Eq. (5.11).

Table 5.2: Bragg angles, estimated periods at the detector plane y_d, period y_c of the surface fluctuations on the crystal, and bending radii R_i according to Eq. (5.10).

Bragg angle	y_d [mm]	y_c [mm]	R_i [m]
23.31°	2.1	2.6	14
13.91°	1.3	2.6	23
9.51°	0.8	2.2	33
5.86°	0.5	2.3	54

5.5 Hard X-ray in-line holography with the direct exposure CCD chip

In this section the measurements of hard X-ray in-line holograms are described. Holograms of various linear objects like polymer strings of different diameters or human hairs were taken with the CCD in the direct exposure mode as well as with X-ray films. To facilitate the interpretation of phase contrast radiographs, strongly absorbing objects like tungsten wires of different diameters and a nickel grid of 4 μm thickness, 12 μm width and spacing 40 μm [GooXX] have been investigated as well. All of these objects have been imaged with an optical microscope. Some of the pictures are shown in Fig. 5.29.

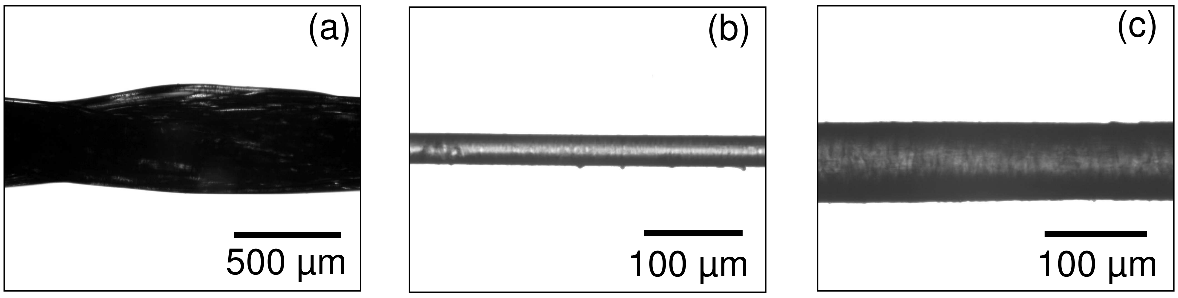

Figure 5.29: Optical microscope pictures of (a) a polymer fiber bundle of average diameter 450 μm which consists of many strings with a small diameter of 30 μm , (b) a polymer string of 30 μm diameter, (c) a human hair of about 80 μm diameter.

5.5.1 Optimization of the beam spot size and measurements

The most important prerequisite for taking high quality holograms is the optimization of the beam spot which must be as small as possible. Therefore, the beam spot size must be carefully prepared. The first step included a minimization of the spot size with the aid of the wire scanner, as described in section 5.2.3.1. In particular, the electrical current of the quadrupole doublet in front of the wire scanner was varied until the scan with the tungsten wire of smallest diameter (4.0 ± 0.4) μm yielded the smallest spot size.

In the next step holograms were taken with the CCD camera. As already mentioned a number of times, a CCD camera allows fast on-line imaging. However, the resolution in the direct exposure mode is limited by the pixel size of 13 μm. To overcome this disadvantage the object can be placed in the X1 beam line of MAMI in a close distance to the X-ray source. In Fig. 5.2 the possible positions an object can be placed are identified. The object frames are mounted perpendicularly with respect to the X-ray beam direction with the exception of the closest distance between source and object $x_{so} = 1.88$ m for which the angle between the normal of the frame and the X-ray beam direction was 46°. In a close distance of the object to the source the hologram will be magnified on expense of a deterioration of the resolution and the visibility of the interference pattern due to the finite beam spot size. However, just this fact can be employed to further optimize the beam spot size. This procedure will be explained in the following.

To quantify the spot size the period of the smallest discernible spacing and the visibility of the fringes can be used. In our experiments the X-ray spot size was estimated from the smallest discernible fringe spacing r_{max} recorded in the interference pattern of transparent objects. With this quantity, the standard deviation of the source size is given by [Car98]

$$\sigma = 0.31 \frac{x_{so}}{x_{od}} r_{max} \quad . \tag{5.12}$$

Fig. 5.31 illustrates the procedure. In Fig. 5.31 (a) more or less only an edge enhancement was observed from which $r_{max} \simeq 117$ μm can be estimated. With the source-to-object distance $x_{so} = 1.88$ m and the object-to-detector distance $x_{od} = 12.03$ m one obtains with Eq. (5.12) $\sigma_v = 6.4$ μm. In Fig. 5.31 (b) the current in the vertical focusing quadrupole was changed while that of the horizontally focusing one was kept constant. An $r_{max} \simeq 52$ μm can be deduced resulting, according to Eq. 5.12, in the X-ray source spot size of $\sigma_v = 2.52$ μm, while with the wire scanner $\sigma_h = (5.9 \pm 0.1)$ μm and $\sigma_v = (2.6 \pm 0.1)$ μm was measured.

In Fig. 5.31 (c) the horizontal quadrupole was optimized as well. With $r_{max} \simeq 26$ μm a $\sigma_v = 1.26$ μm resulted while with the wire scanner $\sigma_h = (19.1 \pm 0.7)$ μm and $\sigma_v = (0.50 \pm 0.05)$ μm was measured, see Fig. 5.30. Another example of such a beam spot measurement is shown in Fig. 5.32. In comparison with wire scanner measurement $\sigma_v = (0.50 \pm 0.05)$ μm, the measured value with the direct exposure CCD deviates significantly. This deviation can be explained by the longitudinal extent of the foil stack which amounts to 2.8 mm. The measured vertical emittances at electron beam energy is $\varepsilon_v = 0.52$ μm mrad, for a micro-focused electron beam spot size $\sigma_v = (0.50 \pm 0.05)$ μm, the corresponding divergence amounts to 1.04 mrad. For the best condition, when the focus is exactly in the middle of the foil stack, the beam spread within the stack amounts to a standard deviation of 1.5 μm, in accord with the observation with direct exposure CCD chip [2].

---

[2] The errors of the fringe method may be in the order of 20%

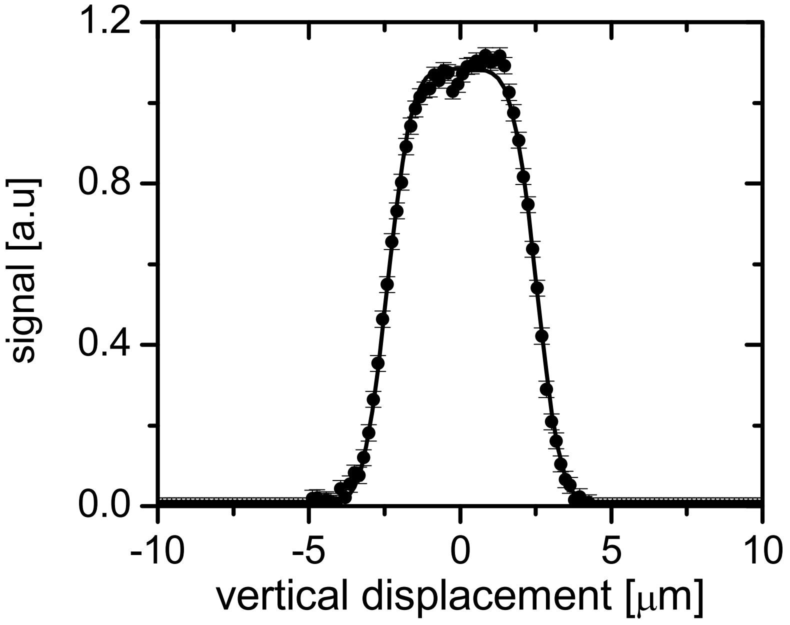

Figure 5.30: Measured electron beam spot size in vertical direction with a (4.0 ± 0.4) μm thick tungsten wire. After deconvolution with the box function of the wire scanner, the electron beam size is (0.50 ± 0.05) μm.

The example of Fig. 5.32 demonstrates that the fringe method for the measurement of the spot size has its practical limits in the spatial resolution of the CCD detector which has a pixel size of (13×13) μm^2. According to Eq. (5.12) the minimum measurable sources size is, therefore, in the order of $\sigma_v = 1.26$ μm.

For comparison, simulations were carried out with the calculations by the program beamoptic. The simulated electron beam size for the measurements shown in Fig. 5.32 is $\sigma_h = 43.2$ μm and $\sigma_v = 0.44$ μm which have to be compared with the wire scanner results $\sigma_h = (19.1 \pm 0.7)$ μm and $\sigma_v = (0.50 \pm 0.05)$ μm. The measured source spot size in the horizontal direction is somewhat better and that in the vertical direction somewhat worse but a better agreement would not be expected.

A very simple method to optimize the beam spot size on-line is to simply count the number of interference fringes. This number exhibits as well the improvement of the focussing as can be seen from Figs. 5.31 and 5.32. For example, in Fig. 5.32 (a) 5 fringes are observed while in Fig. 5.32 (b) for the smaller beam spot 9 fringes. The accuracy of this method can be improved if instead the CCD detectors with a high spatial resolution are used. This will be demonstrated for an X-ray film in section 5.6. However, the on-line capability is lost.

In [Koh00, Koh01] measurements of the transverse coherence length L_T have been reported with standard object, such as homogenous strings with well defined radii and good cylindrical shape and well known refractive index parameters within the object. In our case, the high uncertainty of such object parameters prevented the application

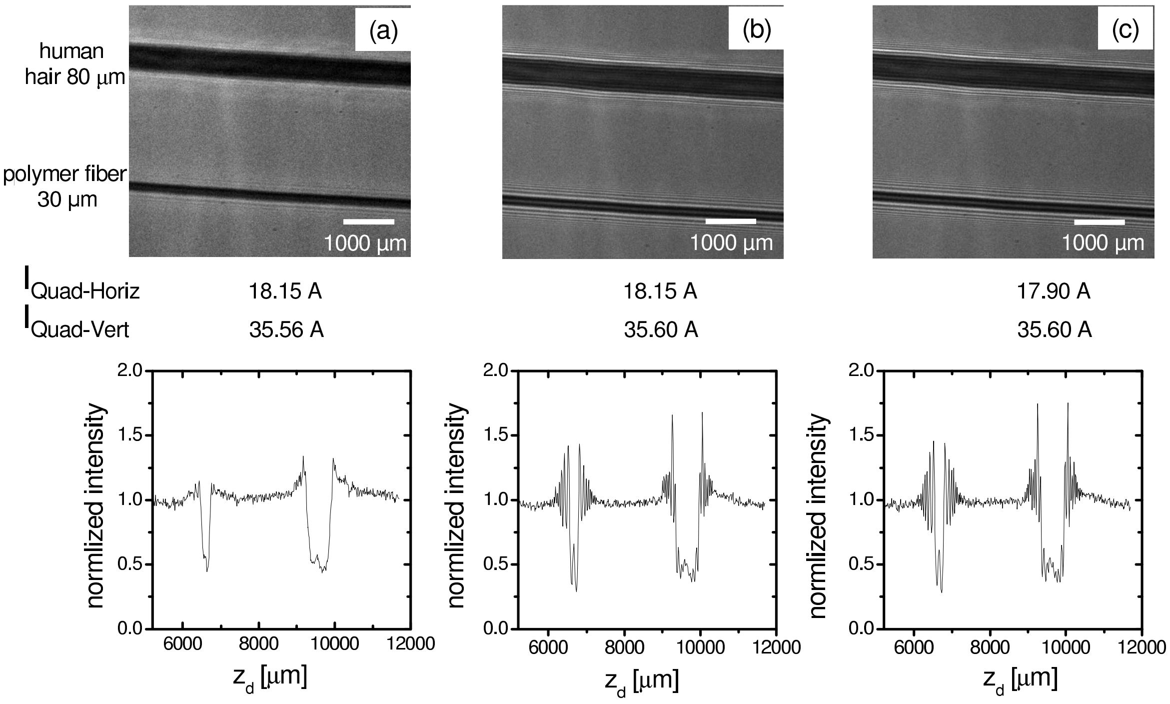

Figure 5.31: Source size minimization with the interference pattern of a human hair of 80 μm diameter and a polymer string of 30 μm diameter. Upper panels show radiographs, lower panels the projected intensity for the polymer string for which 5 columns were added up. The source-to-object distance was $x_{so} = 1.88$ m and the object-to-detector distance $x_{od} = 12.03$ m correspond to a magnification of 7.4 times. The numbers between upper and lower panel are the currents of the horizontally and vertically focusing quadrupoles. Electron beam current 1.21 μA, exposure time 8.1 s, 10 frames added up.

of this approach.

A number of measurements with various strings at different source-object and object-detector distances were performed with the CCD chip and high resolution X-ray films as detectors. The relevant parameters for all measurements are summarized in Table 5.3, the measurements are listed in Table 5.4, and the used strings are collected in Table 5.5.

5.5.2 Analysis

As described in the last section holograms of various strings under various experimental conditions have been taken. The analysis of the holograms is based on a simple model which describes the holograms of strings with arbitrary cross-sectional shapes and optical constants. Particular attention was paid on an thorough understanding of opaque tungsten wires. As will be shown below, holograms of opaque materials with precisely known diameters can be calculated with good reliability and, therefore, may

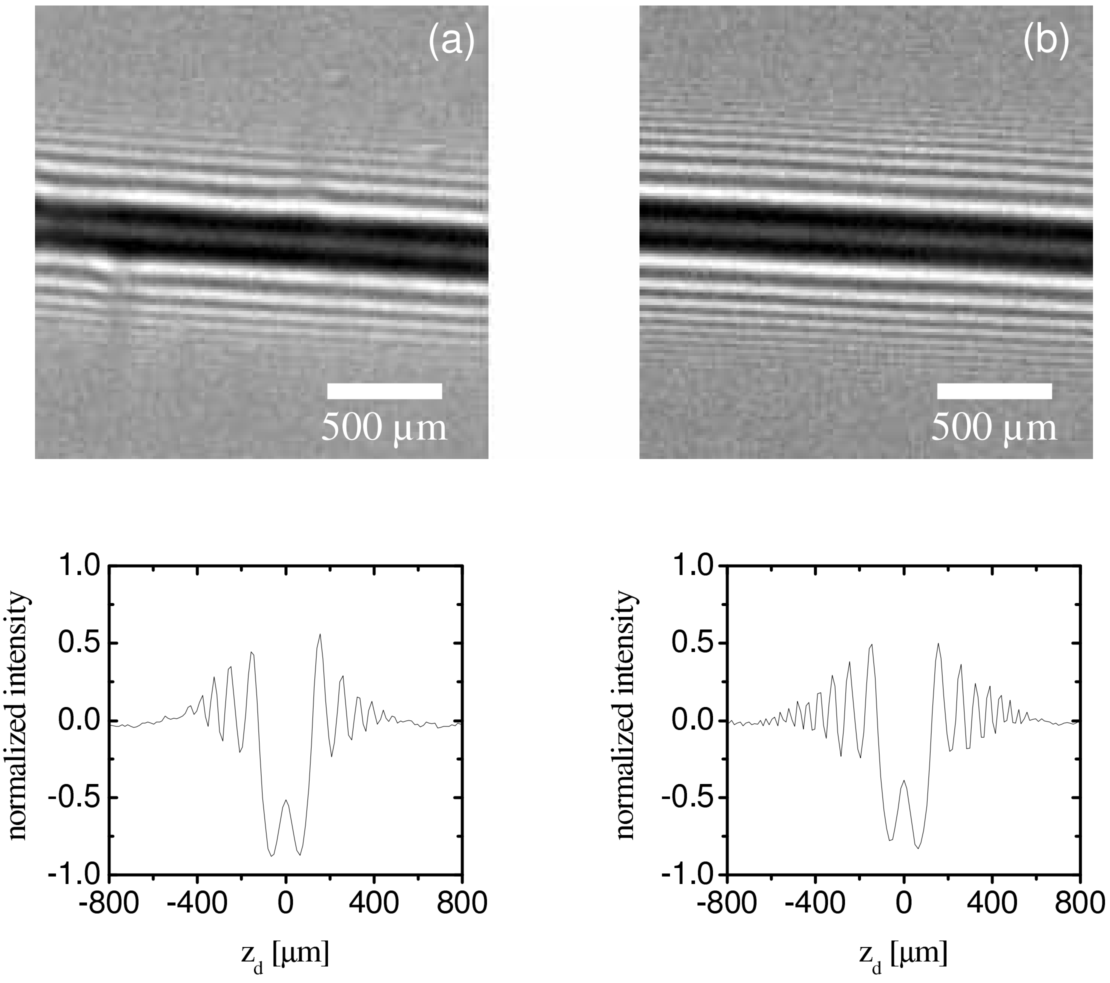

Figure 5.32: Fringe visibility as a function of the X-ray source spot size. Shown are holograms of a polymer string with a diameter of 30 μm for an X-ray source spot size as measured with the wire scanner of (a) $\sigma_h = (5.9 \pm 0.1)$ μm, $\sigma_v = (2.6 \pm 0.1)$ μm, and (b) $\sigma_h = (19.1 \pm 0.7)$ μm, $\sigma_v = (0.50 \pm 0.05)$ μm. The fringe method with Eq. (5.12) yields (a) $\sigma_v = 2.6$ μm, (b) $\sigma_v = 1.26$ μm. The latter value is an estimate which is based on the pixel size, since the smallest distance of resolvable fringes is in the order of one pixel. Source-to-object distance $x_{so} = 1.88$ m, object-to-detector distance 12.03 m, corresponding to a geometrical magnification of 7.4 times. Notice that, the angle between string and beam direction amounts not to 90° but 46°. Electron beam current 500 nA, exposure time 8.1 s per frame, 100 frames added up.

Table 5.3: Experimental parameters of phase contrast and in-line hard X-ray holography.

Electron beam	Electron beam energy	855 MeV and 600 MeV
	Horizontal width(1σ)	(1.9 ± 0.3) μm
	Verticals width (1σ)	(1.6 ± 0.3) μm
	Beam current	max value 2 μA
	Fluctuation of the current	$\leq 3\%$
Radiator	Material	Polyimide
	Number of foils	25
	Thickness of foils [μm]	12.5
	Distance between foils [μm]	100
	Electron beam energy [MeV]	600
Radiator	Material	Polyimide
	Number of foils	30
	Thickness of foils [μm]	25
	Distance between foils [μm]	75
	Electron beam energy [MeV]	855
Spectrometer	Crystal	silicon
	Net plane	[111]
	Energy resolution (FWHM)	(2.4 ± 0.2) eV
	Distance to detector	5.8 m
	Distance to source	7.5 m
Detector	Type	CCD
	Pixel-Dimension	13×13 μm^2
	Number of pixel	1024×1024
	Depletion layer	$\approx 5 - 10$ μm
	Detection efficiency	60% @ (2.5 eV); 50% @ (6.0 keV)
	Energy resolution (FWHM)	127 eV @ 6 keV from ^{55}Fe
X-ray film	Type	Structruix D3 X-ray film, Agfa
	Resolution	approx. 2 μm
	Exposure time	15 min.
Exposure time	Exposure time	7.1 s/image
	Number of images	100 images/single radiograph
	Recording time	1000 s/single radiograph
Raw data	Size of single radiograph	5 MByte

Table 5.4: Compilation of beam times with relevant parameters, such as, date of the measurement, X-ray source spot sizes σ_h, σ_v, sample positions x_{so}, x_{od}, magnification M, and used detectors. Notice that, the angle between string and X-ray beam direction is for the distance $x_{so} = 1.88$ m not 90° but 46°.

Date	σ_h [μm]	σ_v [μm]	x_{so} [m]	x_{od} [m]	M	dectector
April-2004	1.7	3.9	1.88	12.03	7.4	direct exposure CCD
			4.3	9.61	3.23	direct exposure CCD
			10.78	3.13	1.3	direct exposure CCD
			12.71	1.20	1.1	direct exposure CCD
May-2004	5.9	2.6	1.88	12.03	7.4	direct exposure CCD
			4.3	9.61	3.23	direct exposure CCD
			10.78	3.13	1.3	direct exposure CCD
			12.71	1.20	1.1	direct exposure CCD
June-2004	19.1	0.5	1.88	12.03	7.4	direct exposure CCD
			4.3	9.61	3.23	direct exposure CCD
			10.77	3.13	1.3	direct exposure CCD
			12.71	1.20	1.1	direct exposure CCD
June-2004	19.1	0.5	1.88	11.73	7.24	high resolution X-ray film
			4.3	9.31	3.17	
			10.78	2.83	1.26	
			12.71	0.90	1.07	

serve as test objects for various experimental uncertainties as there are, e.g., distances between source and object, and a possible residual bending of the monochromator crystal which may result in a magnification or demagnification of the object. With such uncertainties under control, the much more involved holograms of transparent strings can be analyzed from which, assuming again the precise knowledge of the diameter, optical constants and radial distributions of the optical constants can be extracted.

In this paragraph the generation of the normalized contrast image, which can easily be compared with calculations, is described. Fig. 5.33 shows the picture of a human hair and a polymer string. The original picture (a) still contains streaks. Also dust particles located on the surface of the monochromator or the CCD chip may be imaged as well and may perturb the interpretation of the picture. These adulterations of the picture can be eliminated by subtraction of a picture taken under identical conditions but without the object in the X-ray beam. This background picture was taken immediately after the picture with object under identical conditions. Since the object had to be removed manually during the course of the experiment, the electron beam had to be turned off and the experimental hall B had to be entered. The whole procedure required a time of about 20 minutes. After turning on the beam again, obviously the same experimental conditions were met again since in the resulting contrast image [Kre03] all imperfections are totally removed.

Table 5.5: Imaged objects and their diameters.

object	diameter [μm]
Polymer string	(30 ± 3)
Polymer string	(150 ± 20)
Polymer string	(270 ± 20)
Polymer string	(350 ± 20)
Polymer string	450
Human hair	(80 ± 8)
Tungsten wire	(4 ± 0.4)
Tungsten wire	(10 ± 1)
Tungsten wire	(25 ± 2.5)
Tungsten wire	(40 ± 4)

If, in addition, such a contrast image is normalized to the reference image a normalized contrast image is obtained. The advantage of the latter is that it is corrected for the intensity distribution of the primary X-ray beam over the picture and can directly be compared with calculations on the basis of Eq. (5.1). Two examples of normalized contrast images are shown in Fig. 5.34. It can be seen that because of the large magnification of $M = 7.4$ the pixel resolution of 13 μm imposes no severe restriction.

5.5.3 Results and discussion

5.5.3.1 Holograms of highly absorbing objects

Fig. 5.35 and Fig. 5.36 show holograms of tungsten wires of different diameters. The complex refraction index parameters for a photon energy of 6 keV at which the holograms were taken are $\delta = 8.5 \cdot 10^{-5}$ and $\beta = 1.11 \cdot 10^{-5}$ [CxrXX]. The imaginary part β implies for the wire with the smallest diameter $D = 10$ μm a damping of the intensity to $\exp((4\pi/\lambda) \cdot \beta \cdot D) = \exp(-6.75) = 1.2 \cdot 10^{-3}$ and in particular the thicker wires can be considered as completely opaque. Inspection under an optical microscope revealed a good cylindrical shape, some imperfections in the order of 6 μm were observed for the wire with a diameter of 40 μm. These properties are important for the calculation of the holograms which depend beside the complex refraction index parameters also on the object morphology.

The observed interference pattern results from the interference between diffracted waves at the edge of the wire and undisturbed waves emanating from the source. As already mentioned, from such diffraction pattern information on the X-ray source size, the location of the object and the residual bending of the monochromator crystal can be extracted, provided the diameter of the wire is known.

In the calculations to get the intensity pattern which can be compared with the measurement, the interference pattern according to Eq. (2.18) for a point-like source has

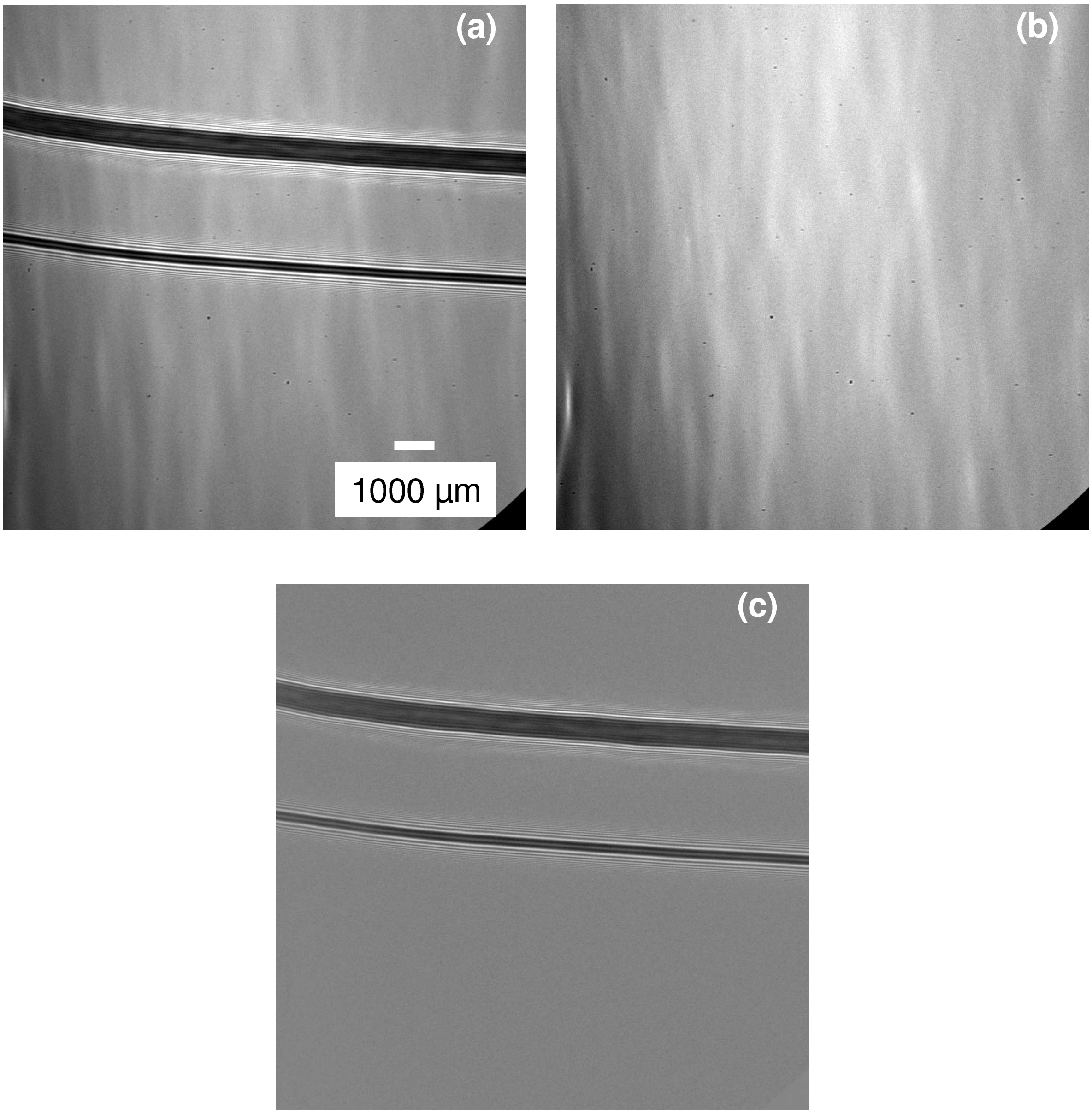

Figure 5.33: Generation of a contrast image from radiographs taken with the CCD camera in the direct exposure mode. A human hair with a diameter of 80 μm and a polymer string of 29.6 μm diameter were positioned in a distance $x_{so} = 1.88$ m from the X-ray source. X-ray spot sizes were $\sigma_h = (19.1 \pm 0.7)$ μm and $\sigma_v = (0.50 \pm 0.05)$ μm, electron beam current 500 nA, exposure time per frame 8.1 s, 100 frames were added up. (a) The original radiograph which clearly shows streaks due to crystal imperfections. Also dust particles on the crystal are clearly observable. (b) The image with the object removed, and (c) the contrast image as obtained by a subtraction of image (b) from image (a).

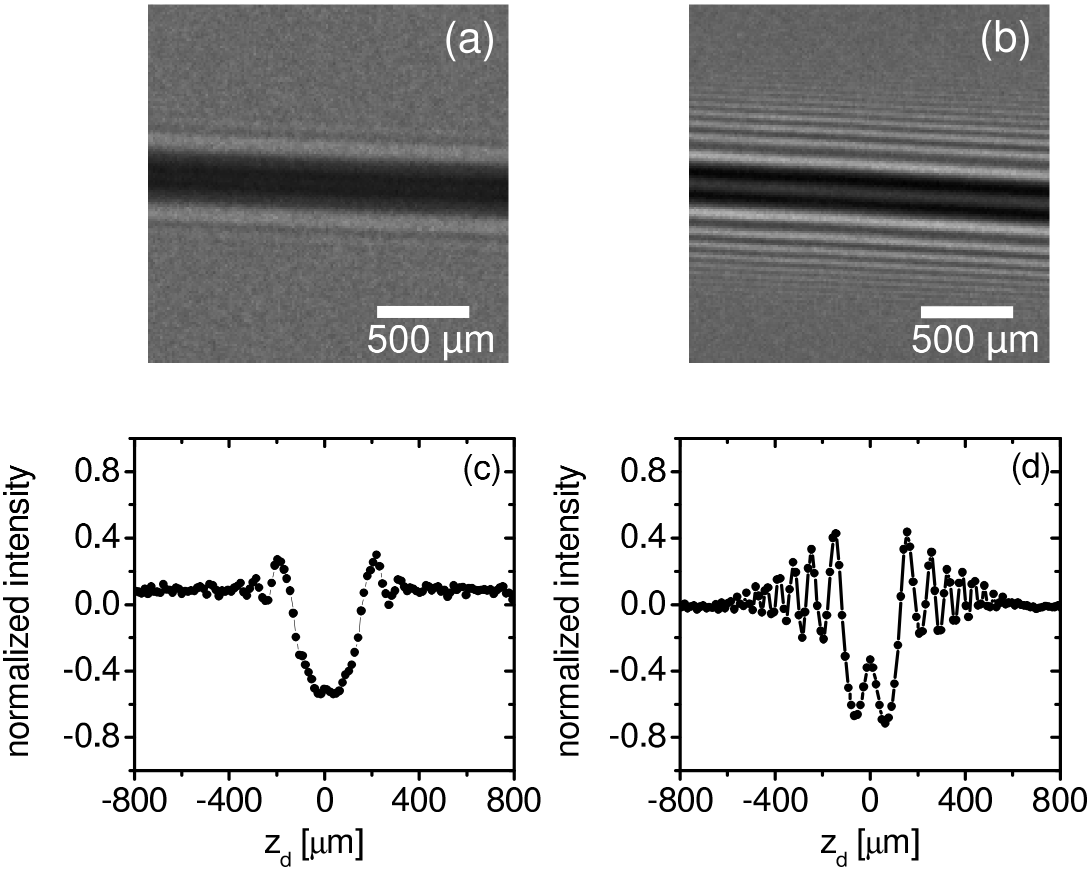

Figure 5.34: Normalized contrast images (holograms) for (a) a tungsten wire of (25±2.5) μm diameter (an opaque object with high absorption) and (b) a nylon wire (a nearly transparent object) of 30 μm diameter which has nearly the same diameter as the tungsten wire. The holograms were recorded at an X-ray energy of 6 keV. The source-to-object distance was x_{so} = 1.88 m and the object-to-detector distance $x_{od} = 12.03$ m, corresponding to a magnification $M = 7.4$. The holograms were taken with the CCD chip at a temperature of -50°C and an electron beam current of 160 nA. Panel (c) depicts the corresponding intensity profile of the holograms of the tungsten wire and (d) that for the polymer string. In the projections 10 columns of the CCD were added up.

been convoluted with the direct exposure CCD spatial resolution which is assumed to have a Gaussian shape with a standard deviation of 8.3 μm and the projected X-ray source profile on the detector which is assumed to be a Gaussian. The monochromator crystal was assumed to be plane. The excellent agreement between measured intensity (points in the graphs (c) and (d) of Fig. 5.35) and calculations confirms that the crystal has a negligible residual bending in the vertical direction and that the measured distances between object-to-source and object-to-detector are correct. From the fit a beam spot size $\sigma_v = (2.5 \pm 0.2)$ μm results which is significantly larger than the beam spot size as measured with the wire scanner. The reason might be a shift of the spot during the measurement. According to Eq. 2.16 a transverse coherence length $L_T = 157$ μm is deduced. Because of this relatively small coherence length the interference fringes get rather weak already at a distance of twice the radius from the wire

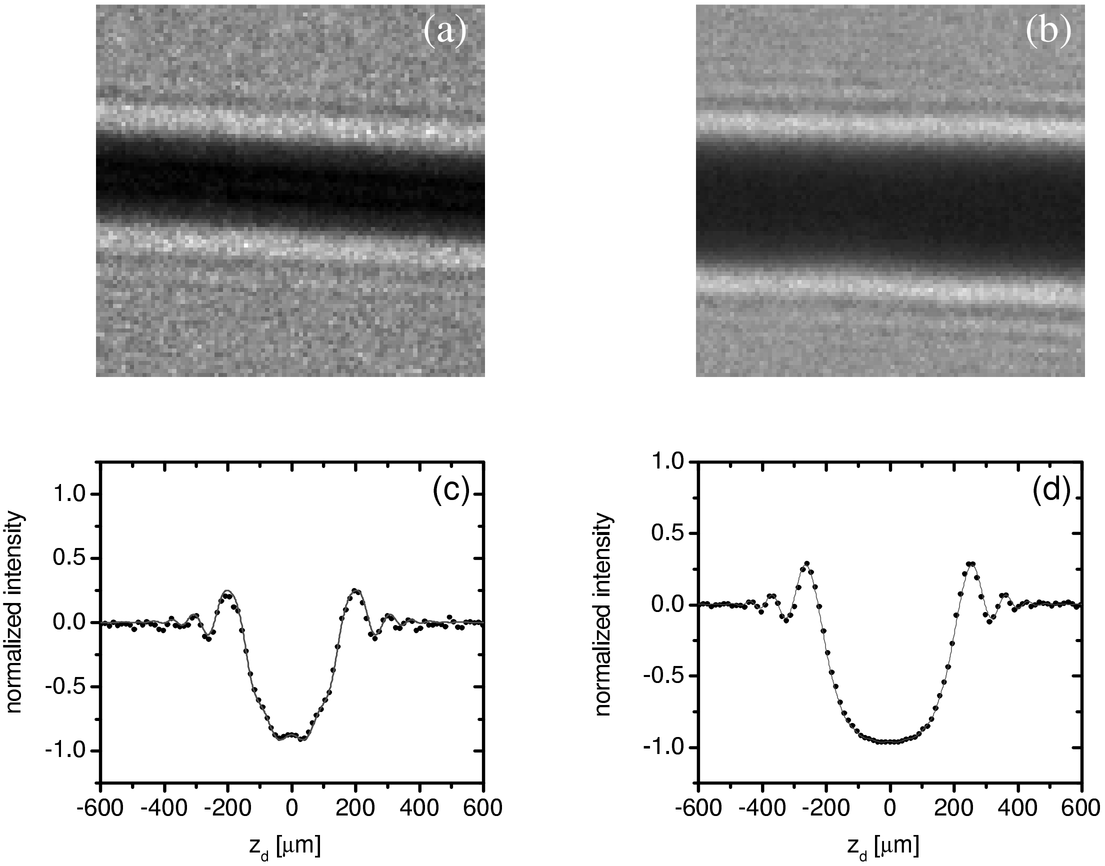

Figure 5.35: Normalized contrast images of two tungsten wires of (a) (25 ± 2.5) μm, and (b) (40 ± 4) μm diameter. Source-to-object distance $x_{so} = 1.88$ m, object-to-detector distance $x_{od} = 12.03$ m, corresponding to a magnification of 7.4 times. The holograms were captured with the direct exposure CCD camera cooled down to -40 $^\circ$C, exposure time 8.1 s, 100 frames added up. Electron beam current 1.4 μA, X-ray spot size $\sigma_h = (19.1 \pm 0.7)$ μm and $\sigma_v = (0.50 \pm 0.05)$ μm as measured with a wire scanner. Diagrams (c) and (d) are the intensity profiles of the holograms, 5 columns added. Points are measurements, solid lines calculated intensities according to Eq. A.42.

center.

A very important feature of these holograms should be mentioned. Despite of the fact that X-ray phase contrast imaging or in-line holography is preferred for low absorbing materials, it could also be used for high absorbing materials such as tungsten. Fig. 5.35 and Fig. 5.36 both reveal a clear edge enhancement due to refraction which increases the contrast. The advantage of the geometrical magnification is, however, that high quality radiographs can be obtained with a detector of moderate spatial resolution, as the CCD camera with a pixel resolution of 13 μm. For a tungsten wire with a diameter of (4.0 ± 0.4) μm which is smaller than the nominal pixel size of the direct exposure CCD camera Fig. 5.36 (c) shows a clearly resolved pattern. Fig. 5.37 confirms this idea for a tungsten wire with a diameter of 4 μm. In a conventional radiography (contact radiography) without geometrical magnification such a wire could not be imaged with

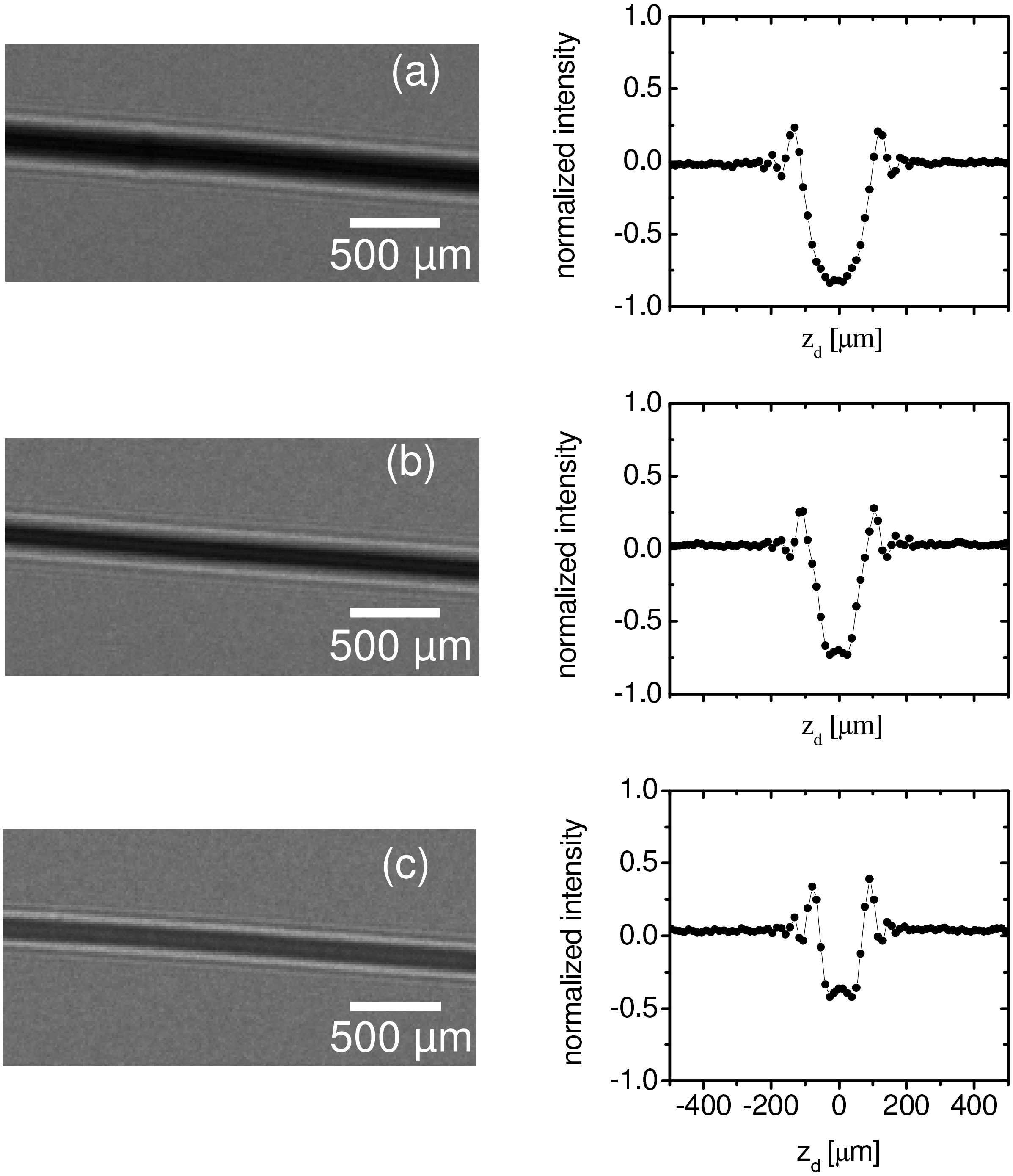

Figure 5.36: Normalized contrast holograms of tungsten wires with diameters (a) (40 ± 4) μm, (b) (25.0 ± 2.5) μm, and (c) (10 ± 1) μm. Source-to-object distance $x_{so} = 4.3$ m, object-to-detector distance $x_{so} = 9.61$ m, corresponding to a magnification of 3.23 times. The holograms were captured with the direct exposure CCD camera cooled down to -40°C, working in accumulated mode. Photon energy 6 keV, X-ray source spot size $\sigma_h = (5.9 \pm 0.1)$ μm and $\sigma_v = (2.6 \pm 0.1)$ μm, electron beam current 600 nA, exposure time 8.1 s, 100 frames added up. Right panels depict the intensity profiles of the holograms, 5 columns added.

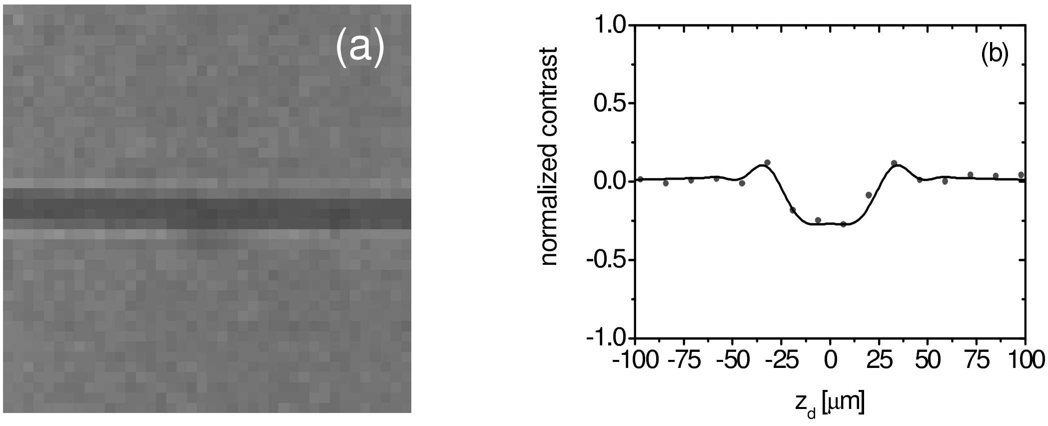

Figure 5.37: Diffraction contrast of a tungsten wire with 4 μm of diameter. The source-to-object distance was $x_{so} = 10.78$ m and the object-to-detector distance $x_{od} = 3.13$ m. Part (a) is a radiograph and (b) the intensity profile. Points represent experimental results, the solid line the simulation.

a detector of this resolution.

In conclusion, two parameters are of importance. These are the X-ray source size projection on the detector which must be as small as possible to avoid degradation of the radiograph and the magnification which is important to overcome the limited resolution of the detector. The position of the sample with respect to X-ray source and X-ray detector must be selected carefully to avoid the radiograph deterioration via the X-ray source projection on the X-ray detector.

5.5.3.2 Holograms of transparent objects

The interference patterns of transparent strings, as polymer wires, are more complicated as that for opaque objects. The complex refraction index parameters for a photon energy of 6 keV, at which the holograms were taken, are typically $\delta = 7.31 \cdot 10^{-6}$ and $\beta = 2.45 \cdot 10^{-8}$ [CxrXX]. The imaginary part β implies for the wire with the largest diameter $D = 350$ μm a damping of the transmitted intensity to $\exp((4\pi/\lambda) \cdot \beta \cdot D) = \exp(-0.52) = 0.59$. The absorbed intensity of 41% is already rather large. Fig. 5.38 shows a normalized contrast radiograph of such a polymer string with a diameter of 350 μm. The absorption contrast in the middle amounts to about 60% which is somewhat larger as the calculated value. The difference may originate from the refraction contrast. Also some fringes on the edges of the string are clearly resolved.

For the thinnest polymer string with a diameter of 30 μm the absorption amounts to at most 4.3%. However, as shown in Figs. 5.39 and 5.40 a contrast of up to 60% with rich interference pattern is observed. The figures show holograms taken at different geometrical magnifications in which the observed structures originate from

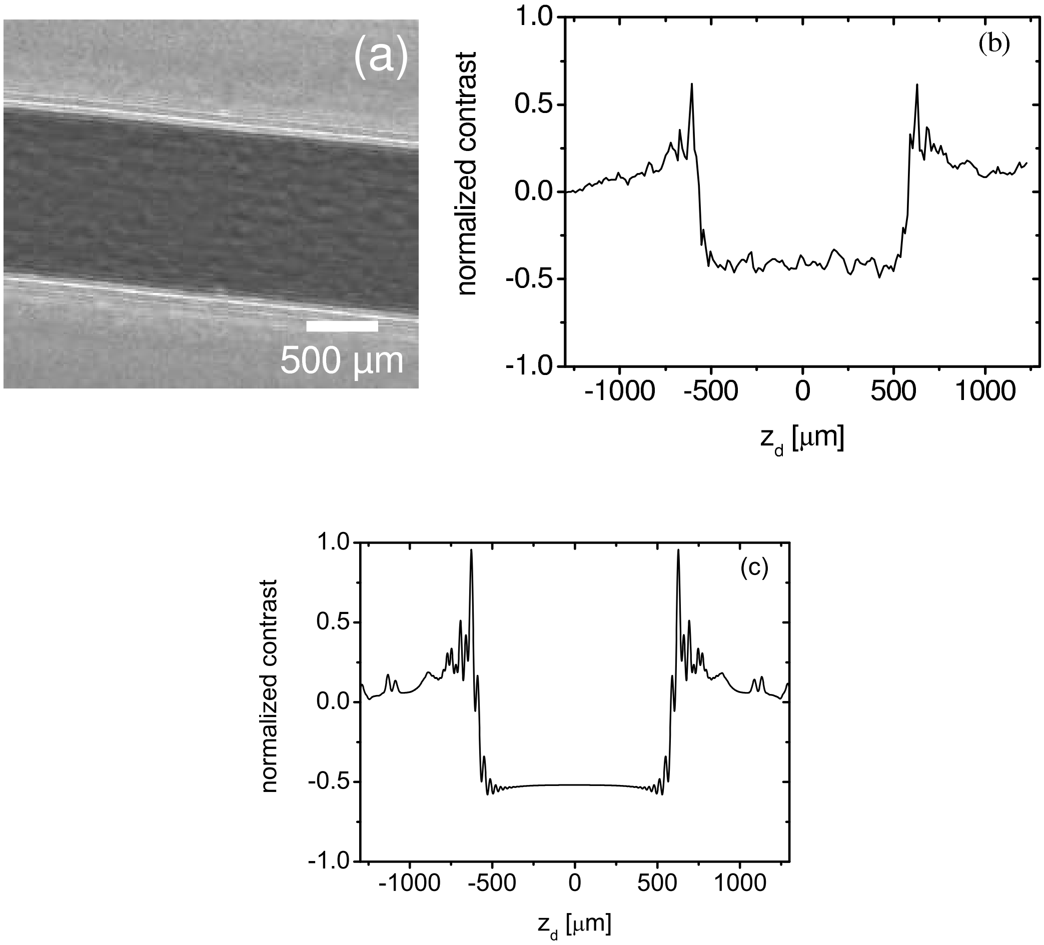

Figure 5.38: (a) Radiograph of a polymer string with a diameter of 350 μm, (b) the intensity profile and (c) the calculated intensity. A number of 10 columns were added up. Source-to-object distance $x_{so} = 4.3$ m at a source-to-detector distance $x_{sd} = 13.91$ m. The X-ray source spot size was $\sigma_h = (5.9 \pm 0.1)$ μm and $\sigma_v = (2.6 \pm 0.1)$ μm. The electron beam current was 200 nA, exposure time 8.1 s, 50 frames added up. The reduction of the intensity in the middle of the string is predominantly caused by conventional absorption.

the interference of the scattered wave by the string with the unperturbed wave from the source.

Some features become apparent in Fig. 5.40 which will be discussed in the following in connection with Fig. 4.1 in which different observation geometries were classified into regions. The contact region (I), the near field region (II) and the intermediate region (III) were discussed in sections 4.1.1, 4.1.2, and 5.1, respectively. Fig. 5.40 (a) and (b) belong to the near field region (II). Although the object-to-detector distance is rather large only an edge enhancement develops since the detector can not resolve the oscillations. Fig. 5.40 (c) and (d) belong to the intermediate region (III) in which fringe pattern develop. Their visibility depends again on the detector resolution. As will be shown in section 5.6 a much better visibility is obtained with a high resolution X-ray film. This discussion demonstrates that the classification into field regions introduced

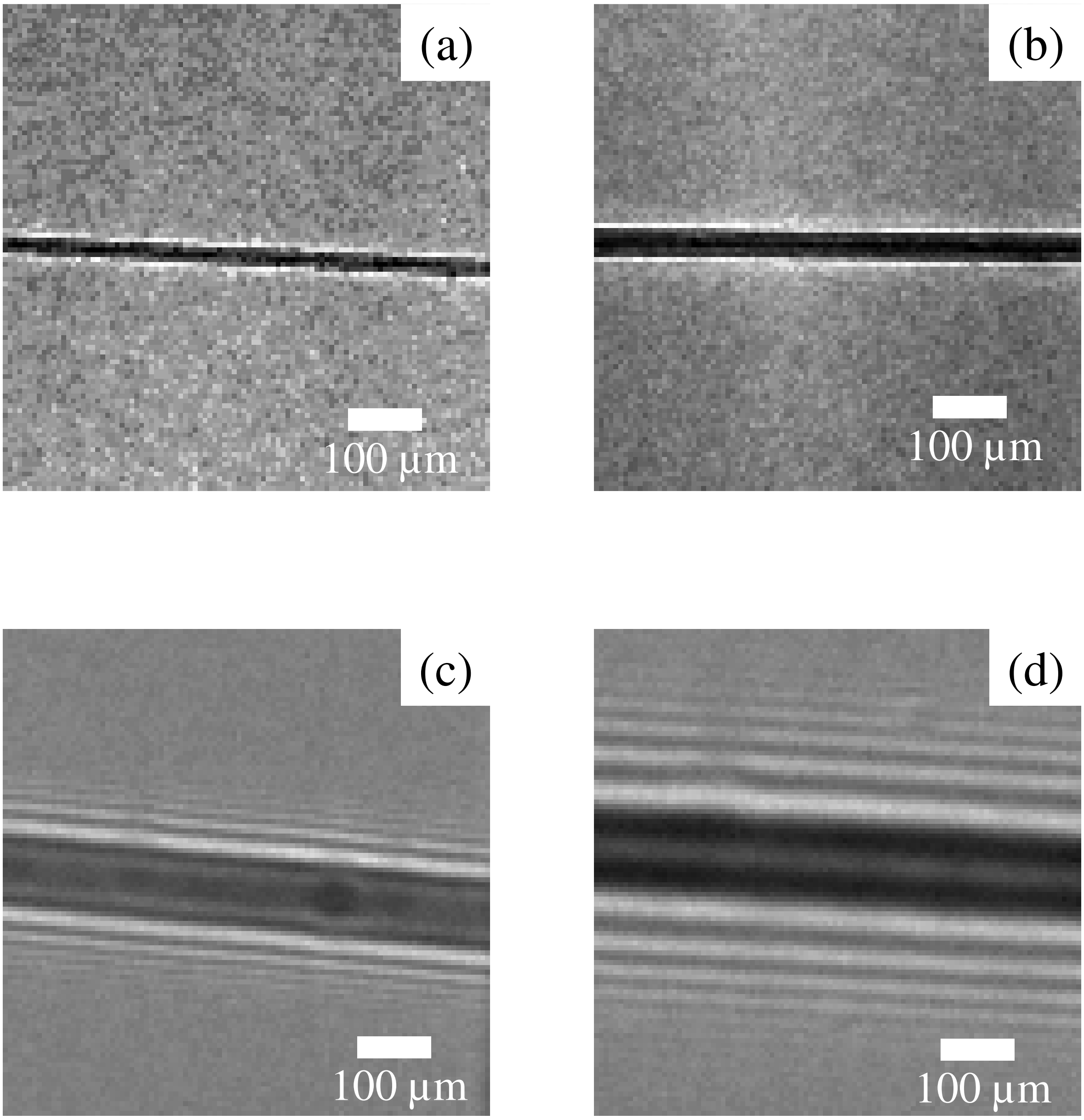

Figure 5.39: Radiographs of a polymer string with a diameter of 30 μm at different object-to-detector distances x_{od}. The source-to-detector distance was $x_{sd} = 13.91$ m. (a) At $x_{od} = 1.20$ m, (b) at $x_{od} = 3.13$ m , (c) at $x_{od} = 9.61$ m and (d) at $x_{od} = 12.03$ m. The X-ray source size was $\sigma_h = (5.9 \pm 0.1)$ μm and $\sigma_v = (2.6 \pm 0.1)$ μm for all radiographs. Radiographs (a) and (b) are not background corrected. The electron beam current was 500 nA, exposure time 2.5 s, 20 frames added up. Radiographs (c) and (d) are background corrected. Exposure time was 8.1 s per frame, electron beam current 500 nA, 100 frames added up.

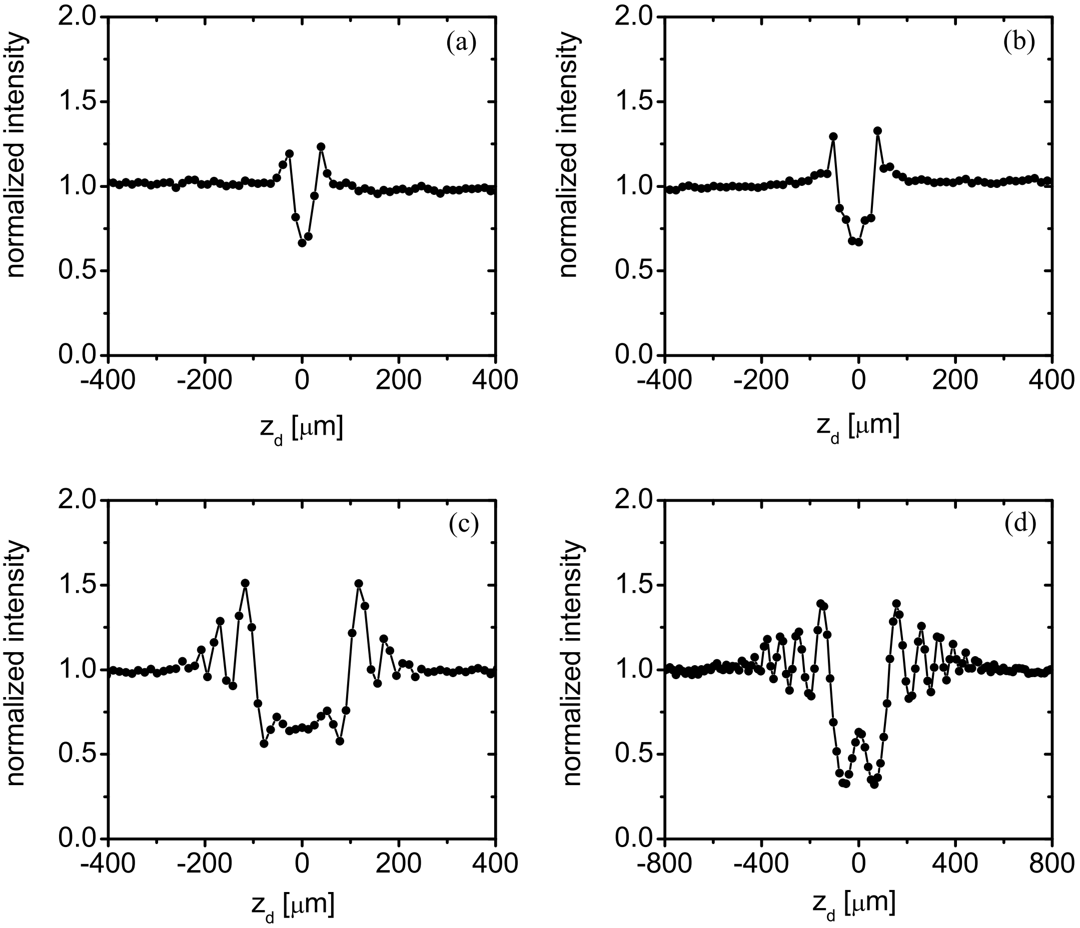

Figure 5.40: Normalized intensity profiles of the radiographs shown in Fig. 5.39. A number of 10 columns were added up. Notice, in view graph (d) the normal of the frame in which the polymer string was fixed made an angle of 46° with the X-ray beam direction.

in Fig. 4.1 depends not only on the spectral distribution of the X-rays but also on the detector resolution.

For the sake of completeness it should be mentioned that in the region (IV) of Fig. 4.1 where the object is close to the source, the integrand in Eq. (4.1) oscillates again rapidly and approaches a δ-function. A measurement would result in a determination of the optical constants δ and β multiplied by the thickness of the object. This might be not a particularly interesting situation.

5.5.4 Applications

As has already been mentioned a number of times, X-rays phase contrast can enhance the visibility of low absorbing details in an object with a low absorbed dose. This way

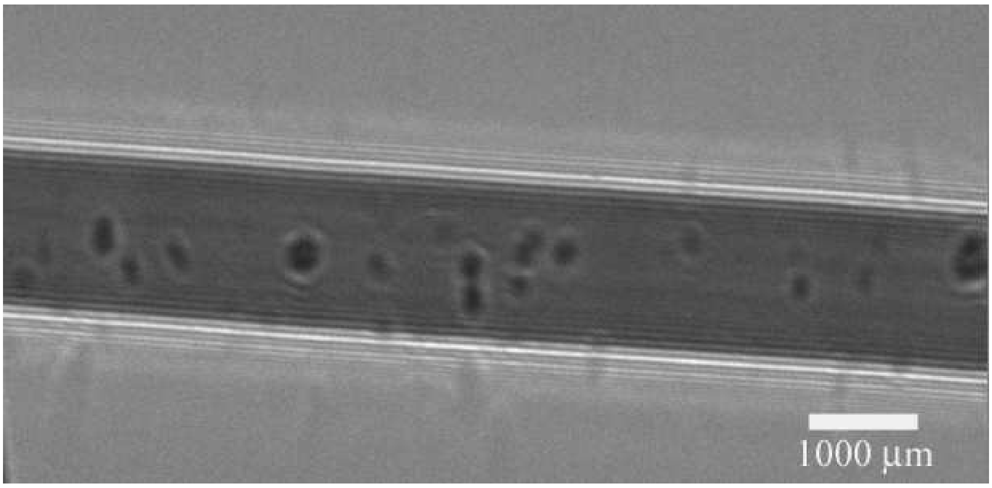

Figure 5.41: A background corrected radiograph (contrast image) of a polymer string of (150 ± 20) μm diameter, supplied by Goodfellow. Source-to-object distance $x_{so} = 1.88$ m, source-to-detector distance $x_{od} = 13.91$ m, corresponding to a magnification of 7.4 times, tilt angle of the object 46°, X-ray source spot size $\sigma_h = (5.9 \pm 0.1)$ μm, and $\sigma_v = (2.6 \pm 0.1)$ μm, electron beam current 600 nA, exposure time 8.1 s, 50 frames added up. Inhomogeneities are clearly seen which may be air bubbles or impurity inclusions with a different density as the string material. The background correction assures that the inhomogeneities do originate from the polymer string and not from dust particles on the monochromator crystal or the detector.

tiny details within the bulk of a sample can be visualized. In this section some examples will be presented which support this statement. The radiographs were all captured with direct exposure CCD in the accumulated mode which allows to produce normalized contrast images. The photon energy was always 6 keV. The strings were mounted horizontally to exploit the benefit of the smaller source size in vertical direction.

Fig. 5.41 shows a radiograph of a polymer string with a diameter of (150 ± 20) μm. According to inspection under an optical microscope the string has nearly ideal cylindrical shape. No deformations or impurities could be observed. However, its radiograph reveals a number of details which must be attributed to un-regularities and inclusions which are clearly visible with high contrast.

Human hairs are interesting phase objects with low absorption. Holograms of human hairs have been taken at different distances. In Fig. 5.42 examples are presented. Inside the hairs interference fringes are observed which assure the small absorption of the 6 keV photons within the hairs.

Fig. 5.43 shows a hologram of a polymer string of 450 μm diameter which consists of thinner strings with a diameter of 30 μm. Interference fringes are clearly observed, moreover the interference fringes from different single strings forming the big string are overlapping. Therefore, the total interference pattern losses resemblance with the original object. Such an object would be an interesting test case for the reconstruction of the 3 D image from the hologram.

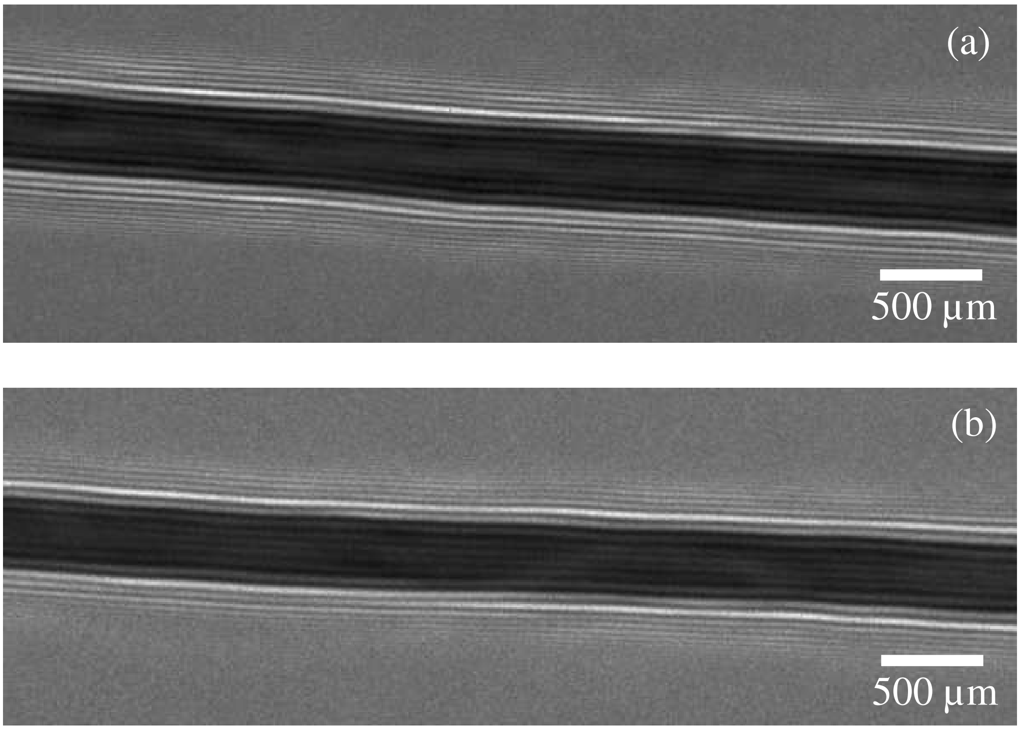

Figure 5.42: Background corrected radiographs (contrast images) of two different human hairs (a) and (b). The diameters are about 80 μm. Source-to-object distance $x_{so} = 1.88$ m, object-to-detector distance $x_{od} = 12.03$ m, X-ray source spot size $\sigma_h = (19.1 \pm 0.7)$ μm, and $\sigma_v = (0.50 \pm 0.05)$ μm, electron beam current 1.4 μA, exposure time 8.1 s per frame, 100 frames added up.

5.6 Hard X-ray in-line holography with high resolution X-ray films

As has been pointed out in the last section 5.5, a direct exposure CCD has the advantage of a good detection efficiency and can be used on-line. However, the spatial resolution in the accumulation mode can not be better than the pixel size of 13×13 μm^2. A high spatial resolution can be obtained with an imaging system with luminescent screens, such as with Gd_2O_2S:Tb, by optical magnification. It preserves the on-line capability. Unfortunately, such a detection system is not well suited in the transition radiation X-ray beam of MAMI as has been demonstrated in section 5.3.4 and appendix C. The reason is the high energy bremsstrahlung background which is emitted simultaneously with the X-rays in the transition radiation foil stack. In this section we demonstrate the possibilities at MAMI with a high resolution X-ray film. The experimental conditions are the same as described in section 5.2, i.e. imaging with transition radiation from a foil stack with a micro-focused 600 MeV electron beam employing a flat silicon single crystal monochromator in Bragg geometry to prepare a monochro-

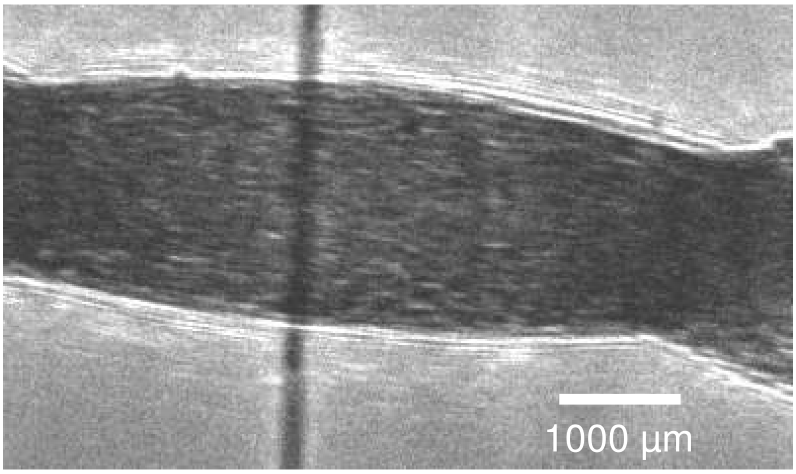

Figure 5.43: Radiograph of a polymer string with a diameter of 450 μm consisting of many thinner strings with a diameter of 30 μm. Source-to-object distance $x_{so} = 4.3$ m, source-to-detector distance $x_{od} = 13.91$ m, X-ray source size $\sigma_h = (5.9 \pm 0.1)$ μm, and $\sigma_v = (2.6 \pm 0.1)$ μm, electron beam current 600 nA, exposure time 1.6 s per frame, 50 frames added up.

matic photon beam with an energy of 6 keV. In the experimental setup only the CCD camera was replaced by the X-ray film.

5.6.1 Characterization of the X-ray film

The principles of image generation with an X-ray film has been described in sections 4.2.2 and 4.4 and will not be repeated here. Nevertheless, it is important to characterize the linearity of the optical density as a function of the deposited energy of the used Structurix D3 X-ray film from Agfa, and also the optical digitization system to extract correct quantified information from the holograms.

5.6.1.1 Photographic density

The primary quantity which is measured by an X-ray film is the photographic density D_p. It is defined as the basis 10 logarithm as $D_p = \log(i_0/i)$ with i_0 the optical light intensity impinging on the film and i the intensity measured by the detector of a densitometer. From this primary quantity the so called fog $D_f = \log(i_0/i_{0f})$ of an unexposed part of the film must be subtracted to obtain the density $D = D_p - D_f = \log(i_{0f}/i)$ which must be related to the exposure b of the film, i.e. the energy per unit area dE/dA deposited by the X-ray photons at a certain location $\overrightarrow{r}$ at the film. In a simple theoretical model [Geo58] the photographic density can be described by

$$D(\overrightarrow{r}) = D_{sat}(1 - \exp(-b(\overrightarrow{r})/b_0)). \tag{5.13}$$

The saturation density D_{sat} and b_0 are characteristic quantities of the X-ray film.

In order to use an X-ray film for a quantitative analysis of radiographs, it is most convenient to operate it in the linear range, in which the photographic density (or blackness) is proportional to the exposure b [Dia74]. To determine this region, the X-ray film was irradiated with X-ray photons from a radioactive ^{55}Fe source with an activity of 1.1 MBq. The source was placed at a distance of about 1 cm from the film. The X-ray film was exposed for different durations in the interval between zero and 600 minutes. The long exposure times result from the low activity of the source and also the low response (detection efficiency) of the film. The X-ray films were processed under the conditions which were specified by the manufacturer [Agf90], i.e. developed in the G128 developer for 5 min, rinsed in running water for 15 min, fixed in a G 328 fixer solution for 5 min, rinsed again in running water for 30 min, and finally dried in hot air. The temperature in the dark room (where the X-ray films were processed) was kept constant at about 20 °C. The described procedure assures that the maximum performance of the developed film can be expected.

The photographic density of the developed X-ray film was measured by using a helium neon laser beam with a wavelength of 632 nm and a digital Luxmeter LM 1301 with an aperture of 3 mm^2 [ElvXX]. The distance between laser and film was 20 cm and between X-ray film and photodiode 3 cm. Fig. 5.44 shows the optical density as a function of the exposure time (characteristic curve). A good linearity of the film Structurix D3 is observed over more than three decades in accord with the product information [Agf90]. With the help of this characteristic curve the linearity of a hologram can be assessed visually by simply demanding that no parts exhibit a blackness which is close to the saturation value.

The X-ray film was digitized with a film scanner (Nikon Coolscan LS 4000 [FilXX]) and with an optical microscope equipped with a high resolution 8-bit CCD camera (F-View XS [OlyXX]). From this system limitations are expected because the dynamical range can not be better than the digitization depth of the ADC (1:256) while the X-ray film has a dynamical range which is more than a factor of 10 better (3.5 decades corresponding to 1:3160). Since, in addition, the illumination time was selected automatically by the scanner after the part of interest of the picture and the optical magnification were selected, the holograms were digitized at various positions of the string, similarly as described in section 4.4. Along the imaged strings the exposure is changing and the sector with the best contrast was selected for further analysis. Examples are shown in Fig. 5.45, and 5.46. Generally, the contrast is best for a low exposure.

5.6.1.2 Spatial resolution

The spatial resolution of a hologram has two contributions which are the intrinsic resolution of the X-ray film and the resolution of the optical microscope. Different

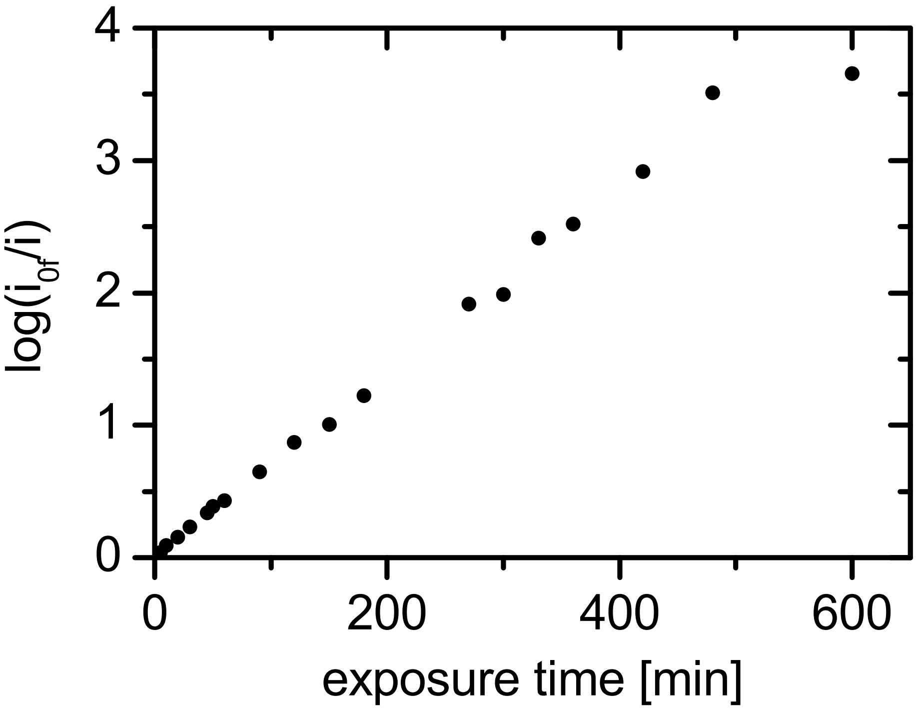

Figure 5.44: Photographic density $\log(i_{0f}/i)$ as a function of the exposure time of the X-ray film Structurix D3. The film was exposed to a ^{55}Fe source.

objective lens with magnifications (4×) and (10×) were used since, for example, the objective with magnification (4×) can not resolve the interference pattern for the objects mounted close to the X-ray film. Therefore, the resolution had to be determined for these different magnifications. In a first step, the effective pixel size was determined with a standard object micrometer scale [LinXX]. For the objective lens magnifications (4×) and (10×), one pixel corresponds to 1.27 μm and 0.52 μm, respectively. In a second step, the spatial resolution was measured with the aid of a razor blade edge. The measured edge spread function, an example is shown in Fig. 5.47, was fitted with the function

$$f(y) = c_1 + \frac{c_2}{2}(1 + \mathrm{erf}(\frac{y_0 - y}{\sqrt{2}\sigma_{sc}})) \tag{5.14}$$

with c_1, c_2, y_0, and σ_{sc} fit variables from which only the latter, which is the standard deviation of the resolution, is of physical importance. The results are $\sigma_{sc,4} = (4.1 \pm 0.1)$ μm and $\sigma_{sc,10} = (1.60 \pm 0.01)$ μm.

According to [Koc98], it is possible to estimate the spatial resolution for an imaging system from the interference pattern [3]. The procedure is similar to the beam spot optimization procedure described in section 5.5.1. The pattern of the holographic

---

[3] In the beginning it was tried to measure the spatial resolution with the edge spread function for a razor-blade. The razor-blade was mounted in contact with the film and illuminated with a point like light source of 500 μm diameter, placed in a distance of 70 cm from the film. This arrangement minimizes the deterioration of the edge by diffraction or the light source size projection on the

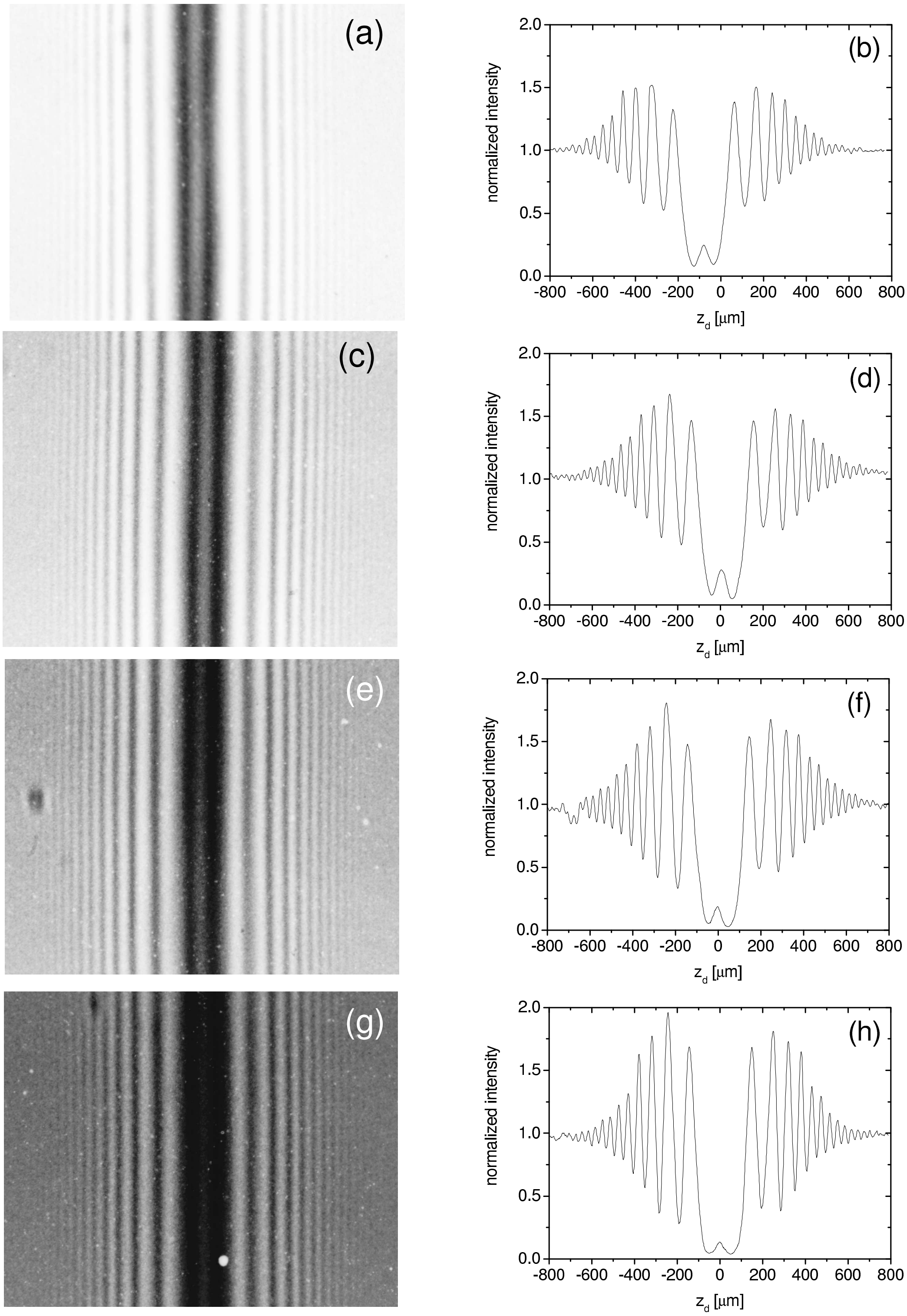

Figure 5.45: Different sectors of a radiograph (left) and projections (right) of a string of 30 μm diameter corresponding to various exposures. Source-to-object distance $x_{so} = 1.88$ m, object-to-detector distance $x_{od} = 11.73$ m, corresponding geometrical magnification is 7.24 times, electron beam current 500 nA, exposure time 15 min. 100 rows were summed up. The change in blackness from top to bottom is due to the change of the X-ray flux incident on the different sectors. The contrast reaches a maximum in panels (g), respectively (h), where the exposure was lowest. The radiograph was digitized with an optical microscope of magnification (4×).

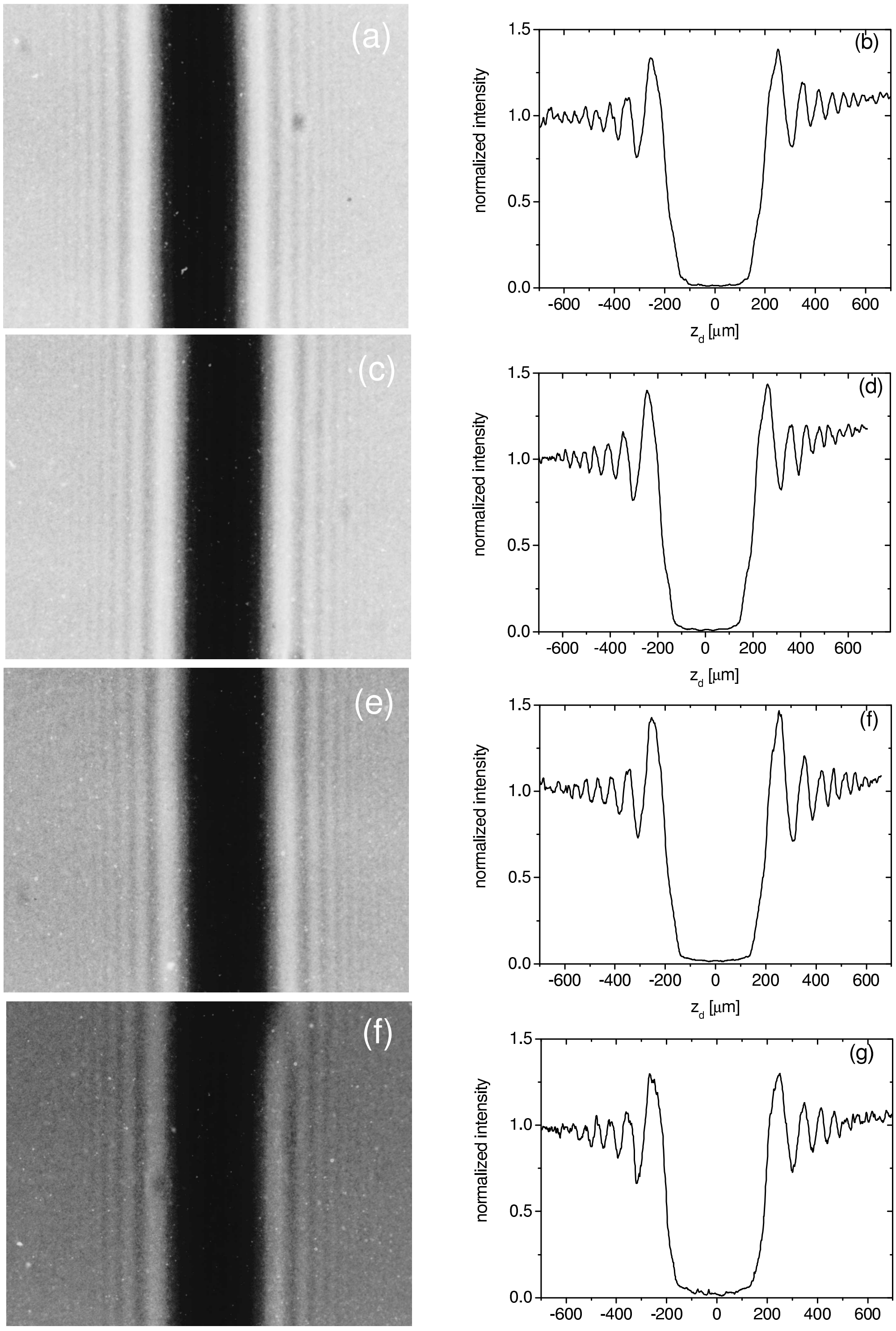

Figure 5.46: Different sectors of a radiograph(left) and projections (right) of a tungsten wire of (40 ± 4) μm diameter corresponding to various exposures. Source-to-object distance $x_{so} =$ 1.88 m, object-to-detector distance $x_{od} = 11.73$ m, corresponding geometrical magnification is 7.24 times, electron beam current 500 nA, exposure time 15 min. 200 rows were summed up. The change in blackness from top to bottom is due to the change of the X-ray flux incident on the different sectors. The contrast reaches a maximum in panels (e) respectively (f). The radiograph was digitized with an optical microscope of magnification (4×).

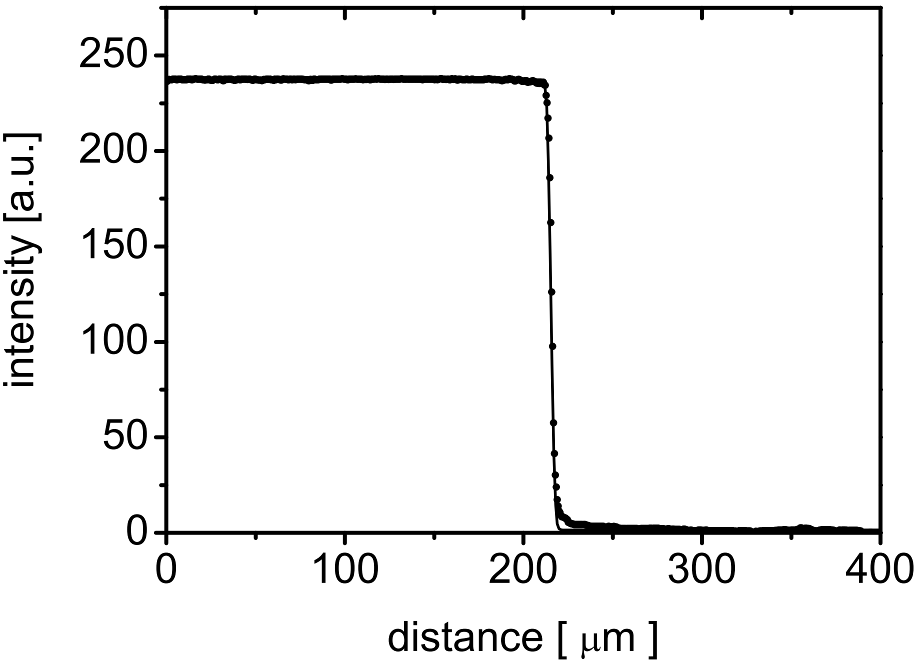

Figure 5.47: Edge spread function to determine the spatial resolution of the optical microscope with objective lens magnification of (10×). Points are measurements, the solid line a fit with Eq. (5.14). The measured spatial resolution amounts to $\sigma_{sc} = (1.60 \pm 0.01)$ μm corresponding to (3.77 ± 0.02) μm (FWHM). The illumination and exposure time of the CCD camera were adjusted before measurements to avoid saturation.

images of a weakly absorbing object, a polyamide string with (150 ± 20) μm diameter, is shown in Fig. 5.48. The experimental interference pattern is compared with the theoretical calculation of a point X-ray spot and after that is convoluted with the spatial resolution of X-ray film and the optical microscope together. The vertical X-ray source size projection on the detector plane is $\sigma_v^{'} = \sigma_v \cdot x_{od}/x_{so} = 0.035$ μm. With such a small effective source size the main deterioration in the fringe visibility arises from the spatial resolution of the film. The X-ray film was scanned under the optical microscope with magnification (10×). Fig. 5.48 (b) shows the experimental intensity profile of the radiograph (solid line) show the theoretical calculation (dashed line). The best agreement was obtained with $\sigma_{exp} = (2.0 \pm 0.2)$ μm. The spatial resolution of the direct exposure X-ray film Structurix D3 after de-convolution with the spatial resolution of the optical microscope ($\sigma_{sc,10} = 1.6 \pm 0.01$ μm) is then $\sigma_f = \sqrt{\sigma_{exp}^2 - \sigma_{sc,10}^2} = (1.2 \pm 0.4)$ μm. In comparison with the direct exposure CCD chip the spatial resolution of the X-ray film is about a factor of 6 better.

---

film. However, this technique was unsuccessful because the Structurix D3 film is double coated. This leads to light scattering within the film which results in a spread of the edge.

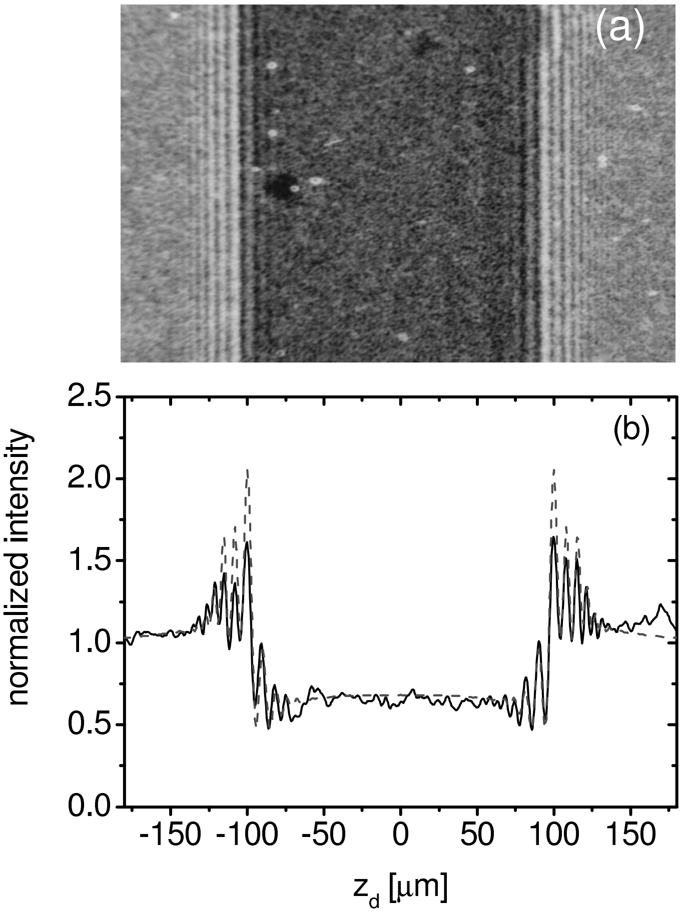

Figure 5.48: Spatial resolution of the direct exposure D3 Structurix D3. (a) Hologram of a polyamide string with (150 ± 20) μm mounted horizontally at object-to-detector distance $x_{od} = 0.9$ m. The source-to-detector distance $x_{sd} = 12.71$ m. The X-ray source size, as measured with the wire scanner, was $\sigma_h = (19.1 \pm 0.7)$ μm and $\sigma_v = (0.50 \pm 0.05)$ μm. The X-ray photon energy was 6 keV, the exposure time 15 min, electron beam current 500 nA. (b) The normalized intensity profile, 100 rows are added together to improve statistics. The radiograph was digitized with an optical microscope of magnification (10×).

5.6.2 X-ray source size determination from X-ray holograms

The X-ray source spot size can be estimated from the fringe visibility of a polyamide string in a hologram [Koh00]. The string should be positioned in a close distance to the source and far away from the X-ray film, in order to make the hologram sensitive to the projected beam spot size on the film rather than to its spatial resolution. Here the approach of [Koh00] is followed since at the most favorable closest distance $x_{so} = 1.88$ m, with a geometrical magnification of 7.24 times, the string was not mounted perpendicularly to the wire but under an angle of 46°. In a strict sense, the formalism presented in appendix A.2 to calculate the diffraction pattern in the Fresnel approximation does not apply [4].

The approach of [Koh00] is based on the measured fringe visibility $V(z_d) = (I_{max} - I_{min})/(I_{max} + I_{min})$ at a position at the hologram $z_d > 1.5R_m$, with $R_m = R \cdot x_{sd}/x_{so}$ the projected radius R of the string. The visibility of a fringe is calculated [Koh00] as

$$V_0(z_d) = \frac{2A(z_d)}{1 + A^2(z_d)} \; , \tag{5.15}$$

where

$$A(z_d) = \frac{g(z_d) f^{1/2}(z_d)}{[1 + f(z_d)]^{1/2}} \qquad \text{and} \quad f(z_d) = \frac{(2\delta x_{od})^2 R_m}{(z_d - R_m)^3} \; . \tag{5.16}$$

The function $g(z_d)$ is obtained from the enhanced stationary phase technique. It takes values between 1, for fringes near the fiber shadow edge, and 0.5 for fringes far away from the edge. With these quantities the source size S (FWHM) can be calculated according to

$$S = \frac{2}{\pi} \frac{\lambda x_{sd}}{(|z_d| - R_m)} \ln^{1/2} \left(\frac{|V_0(z_d)|}{V(z_d)}\right) \; . \tag{5.17}$$

The measurements with a polyamide string of 30 μm diameter is shown in Fig. 5.45 (g) and (h). The complex refraction index parameters are $\delta = 7.24 \cdot 10^{-6}$ and $\beta = 2.42 \cdot 10^{-8}$ at an X-ray photon energy of 6 keV. The measured visibility at $z_d = 365$ μm is $V(z_d) = 0.49$ and with $g(z_d) = 0.75$ from Eq. (5.17) a standard deviation $\sigma_v = (1.4 \pm 0.5)$ μm is calculated.

With the wire scanner the electron beam spot size amounted to $\sigma_v = (0.50 \pm 0.05)$ μm while the simulated one with the aid of program Beamoptic gave $\sigma_v = 0.44$ μm. While this measurement agrees within the errors with the expectation, the measured X-ray beam spot size $\sigma_v = 1.4$ μm is significantly larger. The most probable explanation for these findings is the longitudinal extent of the foil stack, in which the X-rays are produced, which amounts to 2.8 mm. With the measured vertical beam emittance $\varepsilon_v = 0.52$ μm mrad at 600 MeV electron energy, the beam has, with $\sigma_v = (0.50 \pm 0.05)$ μm, a divergence of 1.04 mrad. Assuming that the focus is located in the center of the foil stack the beam spreads within the stack to a standard deviation of 1.5 μm, in accord with the observation.

5.6.3 Results and discussions

5.6.3.1 Holograms for transparent objects

Holograms of transparent objects like polyamide strings with different diameters and human hairs were recorded at different source-to-object and object-to-detector distances. The X-ray photon energy was 6 keV corresponding to a wavelength $\lambda = 2.067$

---

[4] In a perhaps quite good approximation the increased thickness of the elliptical wire can be taken into account by an appropriate scaling of the thickness. However, possible effects of the variable distance x_{so} along the string remain to be investigated.

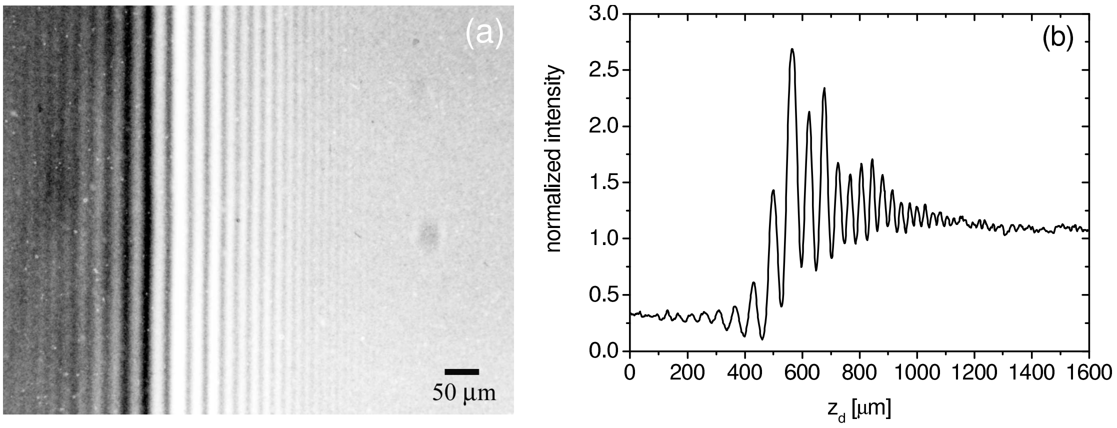

Figure 5.49: (a) Radiograph of a polyamide string of a diameter of (150 ± 20) μm. Source-to-object distance $x_{so} = 1.88$ m, object-to-detector distance $x_{od} = 11.73$ m, corresponding magnification 7.24 times, X-ray source size $\sigma_h = (19.1 \pm 0.7)$ μm and $\sigma_v = (0.50 \pm 0.05)$ μm. The X-ray film was digitized with an optical microscope with a magnification 4× in order to maintain a good resolution. Therefore, only part of the hologram was in the field of view. (b) Intensity profile 200 rows added up.

Å. This low X-ray energy was selected to increase the transversal coherence length. The complex refraction index parameters at this energy for polyamide are $\delta = 7.24 \cdot 10^{-6}$ and $\beta = 2.42 \cdot 10^{-8}$. The maximum absorption $(1 - \exp[-(4\pi\beta D)/\lambda])$ within the string is about 19.8% for the string with the diameter $D = 150$ μm, and the absorption contrast is not of major importance. Fig. 5.49 (a) shows a part of a hologram for a polyamide (Nylon) string of a diameter (150 ± 20) μm mounted at the source-to-object distance $x_{so} = 1.88$ m. A large number of about 18 interference fringes can be seen, as demonstrated in Fig. 5.49 (b). In this radiograph the main deterioration in the fringe visibility results from the X-ray spot size. Therefore, such holograms are also well suited to measure the spot size using Eq. (5.12). For example the minimum discernable distance between two adjacent fringes is about 24 μm and the estimated X-ray source size is $\sigma_v = 1.12$ μm.

Fig. 5.50 (a) and (b) show hologram and intensity profiles, respectively, again for the nylon string with a diameter of (150 ± 20) μm for which the distance between source and object was increased to $x_{so} = 4.3$ m. The calculation on the basis of the Kirchhoff-Fresnel integral Eq. (2.18) is shown in Fig. 5.50 (c). By comparison of the measured and the calculated profile deviations become apparent. They could arise from density or morphological inhomogeneities of the polyamide string, or inappropriate assumptions on the electron beam spot size.

To throw light on this matter, larger parts of the hologram for the polyamide string with a diameter of 150 μm are shown in Fig. 5.51. Clear density fluctuations can be seen in the geometrical shadow of the string. Such fluctuations could not be observed with the aid of an optical microscope. To further investigate the origin of such fluctuations, two

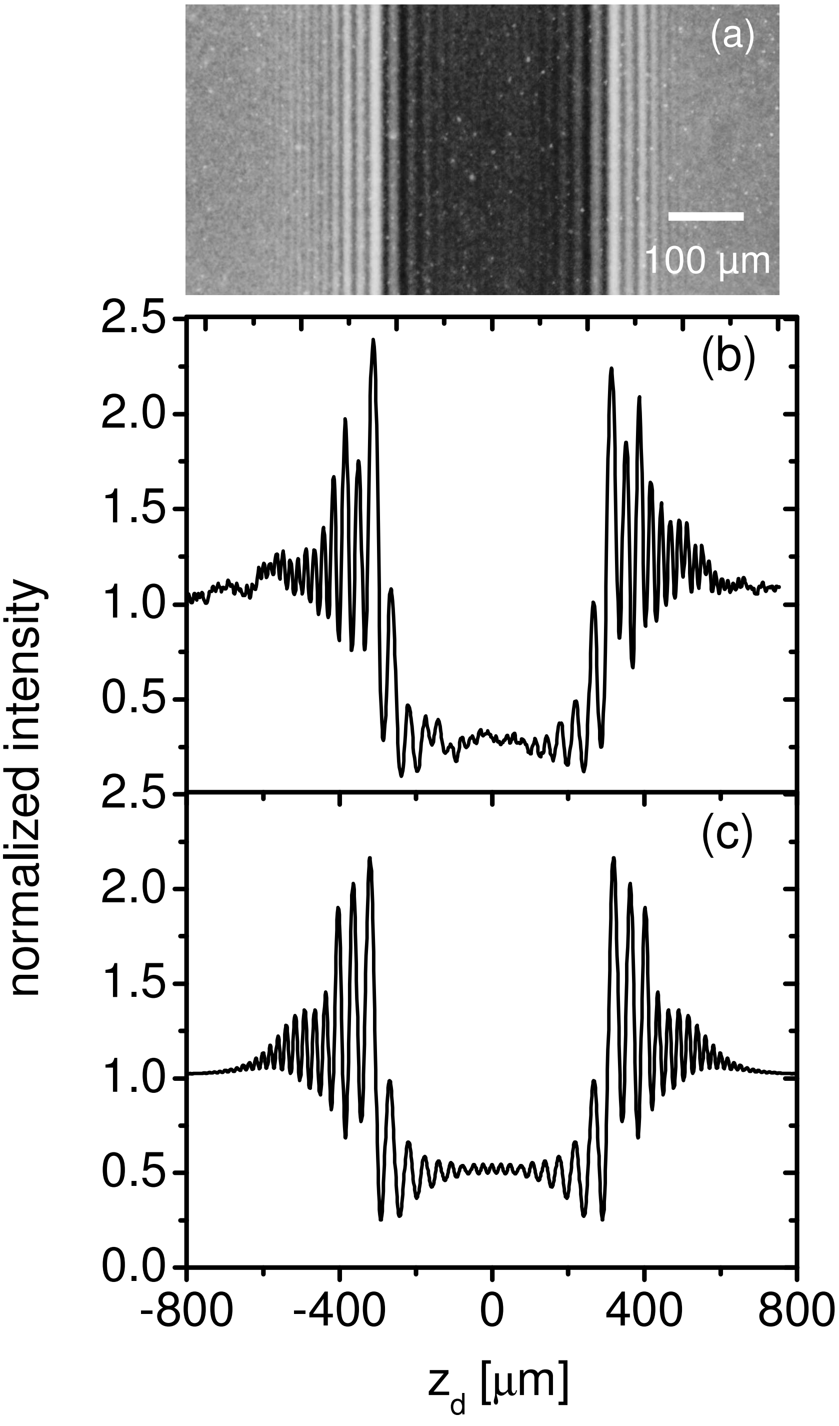

Figure 5.50: (a) Radiograph of a polyamide string of a diameter of (150 ± 20) μm. Source-to-object distance $x_{so} = 4.3$ m, object-to-detector distance $x_{od} = 9.31$ m, corresponding geometrical magnification 3.17 times, X-ray source size $\sigma_h = (19.1 \pm 0.7)$ μm and $\sigma_v = (0.50 \pm 0.05)$ μm. The X-ray film was digitized with an optical microscope with a magnification 4×. (b) Intensity profile, 200 rows added up. (c) Calculated intensity profile of the radiograph. The spatial resolution of the X-ray source spot size of $\sigma_v = (0.50 \pm 0.05)$ μm, of the film of $\sigma_f = (1.2 \pm 0.4)$ μm, and the optical resolution of ($\sigma_{sc,4} = 4.1 \pm 0.1$ μm) were incorporated into the calculations.

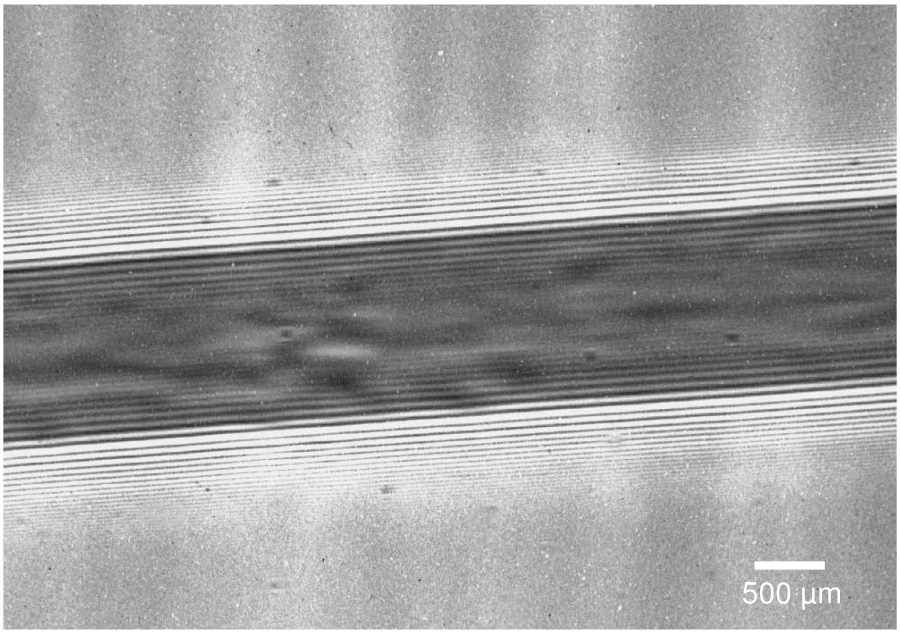

Figure 5.51: Radiograph of a polyamide string of (150 ± 20) μm diameter at object-to-detector distance x_{od} = 11.73 m. the source-to-detector distance was x_{od} = 13.61 m. The X-ray energy was 6 keV, X-ray source size σ_h = (19.1 ± 0.7) μm, σ_v = (0.50 ± 0.05) μm, electron beam current 500 nA and exposure time was 15 min. The radiograph was digitized the film scanner (Nikon Coolscan LS 4000).

different polyamide strings were imaged. The first string was supplied by Goodfellow. It has a diameter of 270 μm. The other one is a fishing line with a diameter of 350 μm. Fig. 5.52 shows a comparison of the holograms. The polyamide string from Goodfellow, Fig. 5.52 (a), shows a rather good homogeneity. However, in Fig. 5.52 (b), the fishing line, much more irregularities are present. To be sure that the intensity fluctuations in the middle part of the string originate from the objects themselves, the objects were removed and a radiograph taken without them. No intensity fluctuations were observed. They may originate from density fluctuations or shape deformations within the string, i.e., the string may not be a perfect and homogeneous cylinder.

There are two possibilities to analyze holograms of strings. In the first one, calculations on the basis of the Fresnel-Kirchhoff integrals can be performed in which assumptions about the density and morphology of the string are incorporated. The right solution can be found by trial and error. Such calculations went beyond the scope of this experimental thesis work. The second one is based on reconstruction algorithms to find the phase profile produced by the transparent object. One of these is the modified Gerchberg-Saxton algorithm [Ger72] which is an iterative method with which the phase information can be found from two holograms which were taken at different distances between object and detector. Therefore, holograms of a polyamide string with a diameter of 30 μm and of human hairs were taken at different object-to-detector distances. The holograms are shown in Fig. 5.53 and and 5.54.

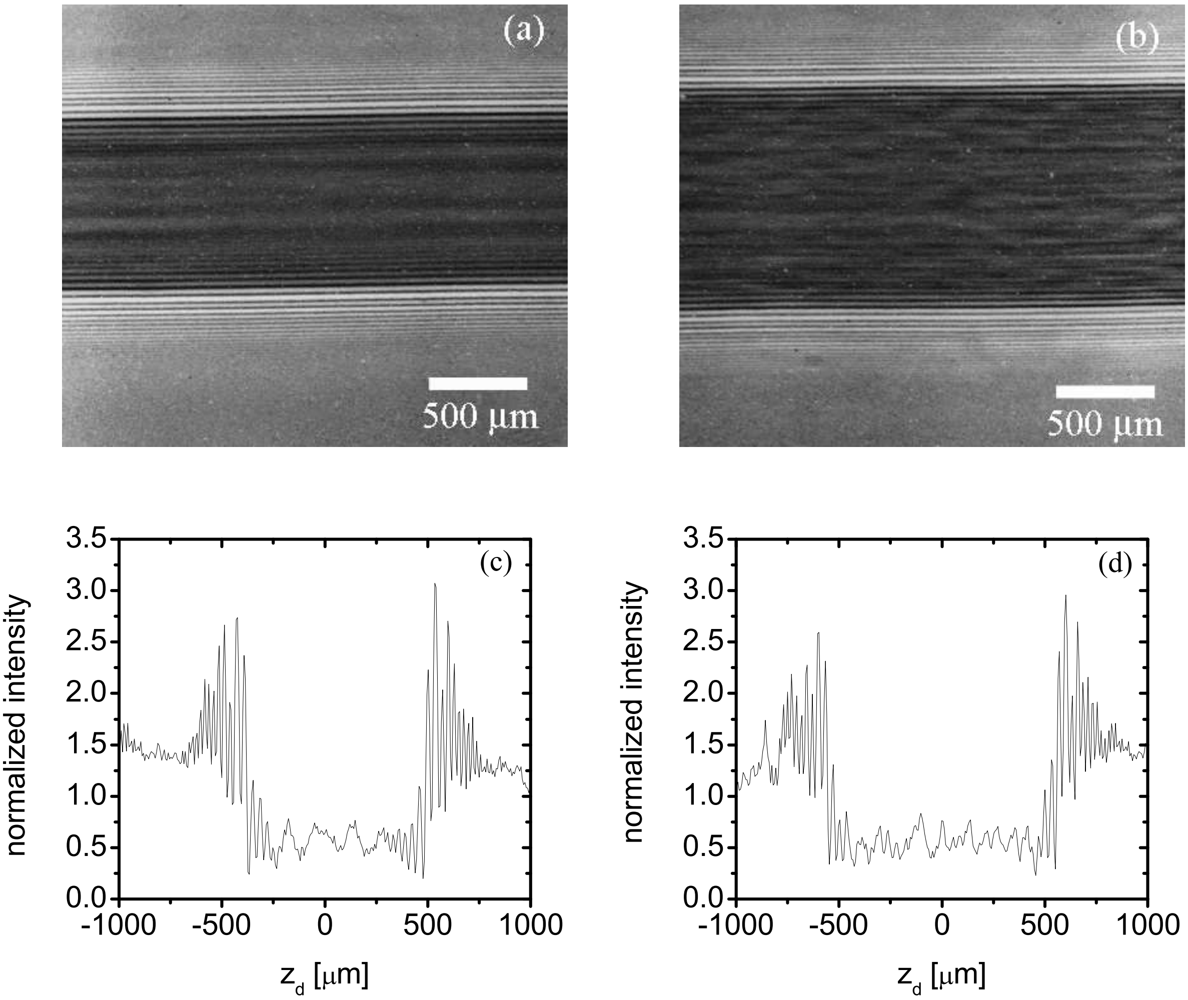

Figure 5.52: Radiographs of two different polyamide strings. (a) A string from Goodfellow with a diameter of 270 μm, (b) a fishing line with a diameter of 350 μm. The source-to-object distance was $x_{so} = 4.3$ m, object-to-detector distance $x_{od} = 9.31$ m, X-ray spot size $\sigma_h = (19.1 \pm 0.7)$ μm, $\sigma_v = (0.50 \pm 0.05)$ μm, electron beam current 500 nA, and exposure time 15 min. Normalized intensity profiles of the radiographs . (c) For a 270 μm polyamide string and (d) for 350 μm, 50 rows are summed up. The films were scanned with a film scanner of (Nikon Coolscan LS 4000).

The selected distances cover different imaging regimes. For the contact regime the contrast would be $(1 - \exp[-(4\pi\beta D)/\lambda]) = 4.26$ % and the absorption contrast of the polyamide string with a diameter of $D = 30$ μm can be neglected. In the near field region, at an object-to-detector distance $x_{od} = 0.9$ m, Fig. 5.53 (a) and (b), the interference pattern produced by both edges have only very little overlap. The reason is that the size of the first Fresnel zone $\sqrt{\lambda x_{od}} = 13.6$ μm is smaller than the diameter of the string. However, at the largest distance $x_{od} = 11.73$ m, Fig. 5.53 (g) and (h), one obtains for the first Fresnel zone $\sqrt{\lambda x_{od}} = 49.2$ μm and the interference pattern from both edges do overlap. The resemblance between the original object and the radiograph is more or less lost. Both limiting cases may be of particular interest for the reconstruction of the phase profile. However, also this issue went beyond the scope of this experimental thesis work.

5.6.3.2 Holograms for opaque objects

Opaque objects are interesting test objects since the interference patterns arise only from the diffraction at the object boundaries. The distribution within the object is invisible and the reconstruction reduces to a two dimensional problem which can, in principle, much easier be solved as the three dimensional one of transparent objects. Combining the hard X-ray imaging of opaque objects with a large geometrical magnification and a micro-focused X-ray spot size, detailed information on objects with micrometer dimensions should be obtainable.

Holograms of highly absorbing objects such as tungsten wires (atomic number Z = 74) of different diameters were recorded at different object-to-detector distances for the source-to-detector distance $x_{sd} = 13.61$ m. At a photon energy of 6 keV the complex refraction index parameters are $\delta = 8.52 \cdot 10^{-5}$ and $\beta = 1.11 \cdot 10^{-5}$. The maximum absorption in a tungsten wire with a diameter of 40 μm is $(1 - \exp[-(4\pi\beta D)/\lambda]) =$ 1-$1.9 \cdot 10^{-12}$, i.e., the object can be regarded in a very good approximation as completely opaque. For a wire with a diameter of 4 μm the absorption is $(1 - \exp[-(4\pi\beta D)/\lambda])$ = 93.3 %, meaning that the object is not completely opaque.

Fig. 5.55 shows holograms of a tungsten wire with a diameter of 40 μm, taken at different distances. The interference patterns are produced due to diffraction at edges and interference with the unperturbed wave. Fig. 5.56 shows holograms of a tungsten wire with a diameter of (4.0 ± 0.4) μm taken at a object-to-detector distance of $x_{od} =$ 2.83 m. The calculations shown in 5.56 (c) on the basis of the Kirchhoff-Fresnel integral were convoluted with a spot size of (0.5 ± 0.05) μm, the spatial resolution of the X-ray film $\sigma_f = (1.2 \pm 0.4)$ μm and finally the spatial resolution of the optical microscope $\sigma_{sc,10} = (1.60 \pm 0.01)$ μm. In contrast to Fig. 5.37, taken with the direct exposure CCD camera, where just an edge enhancement occurred, 4 fringes are observed here with the high resolution X-ray film.

Fig. 5.57 show radiographs of a nickel grid (atomic number Z=28) which demonstrates the importance of the beam spot size. The complex refraction index parameters are

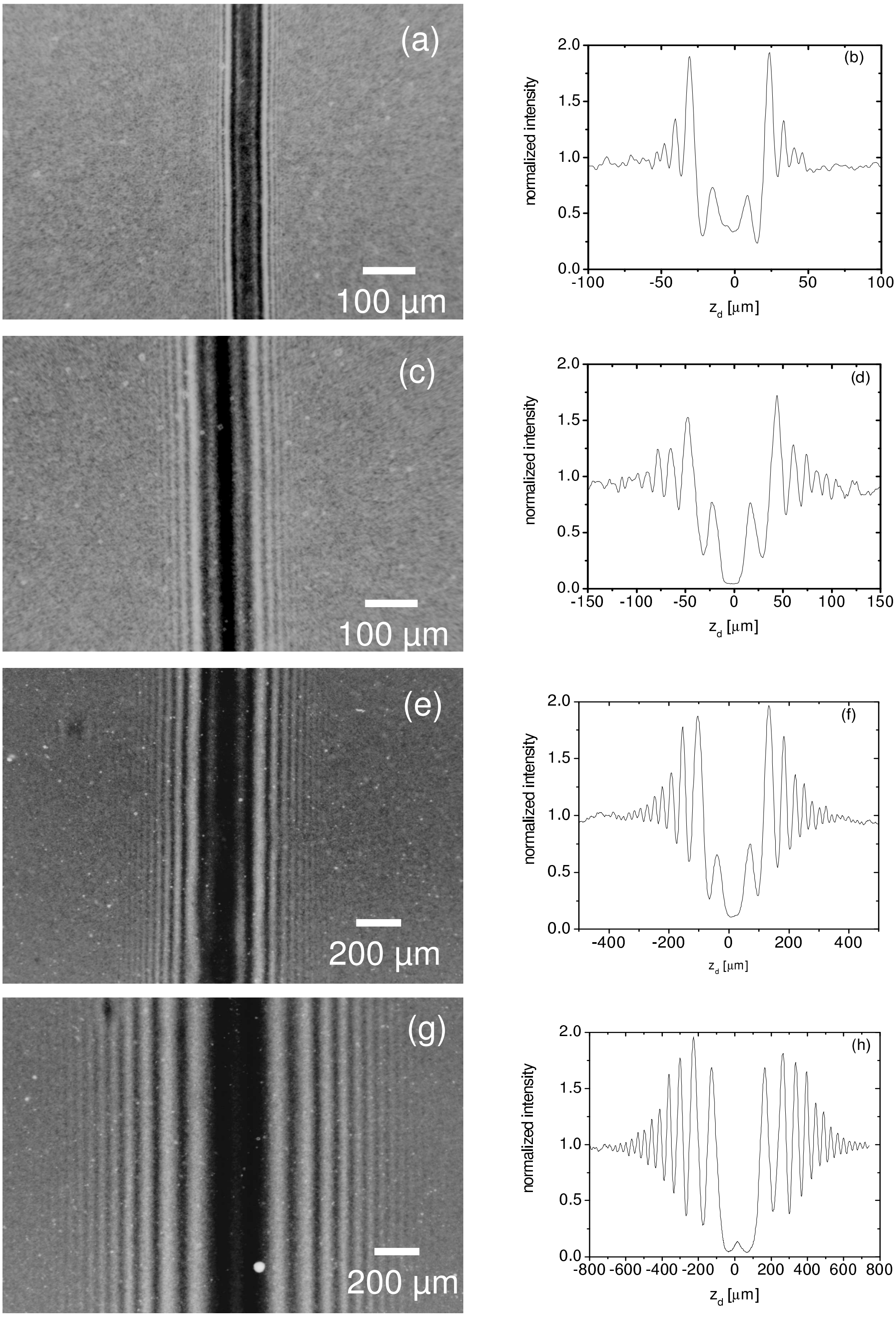

Figure 5.53: Radiographs of the polyamide string of 30 μm diameter at different positions. (a) $x_{od} = 0.9$ m, (c) $x_{od} = 2.83$ m, (d) $x_{od} = 9.31$ m and (g) $x_{od} = 11.73$ m. The intensity profiles are shown on the right side. The intensity profiles are shown at the right side, 200 rows added up. The X-ray film was digitized with an optical microscope (a) and (b) with a magnification of 10 times, (c) and (d) with a magnification of 4 times.

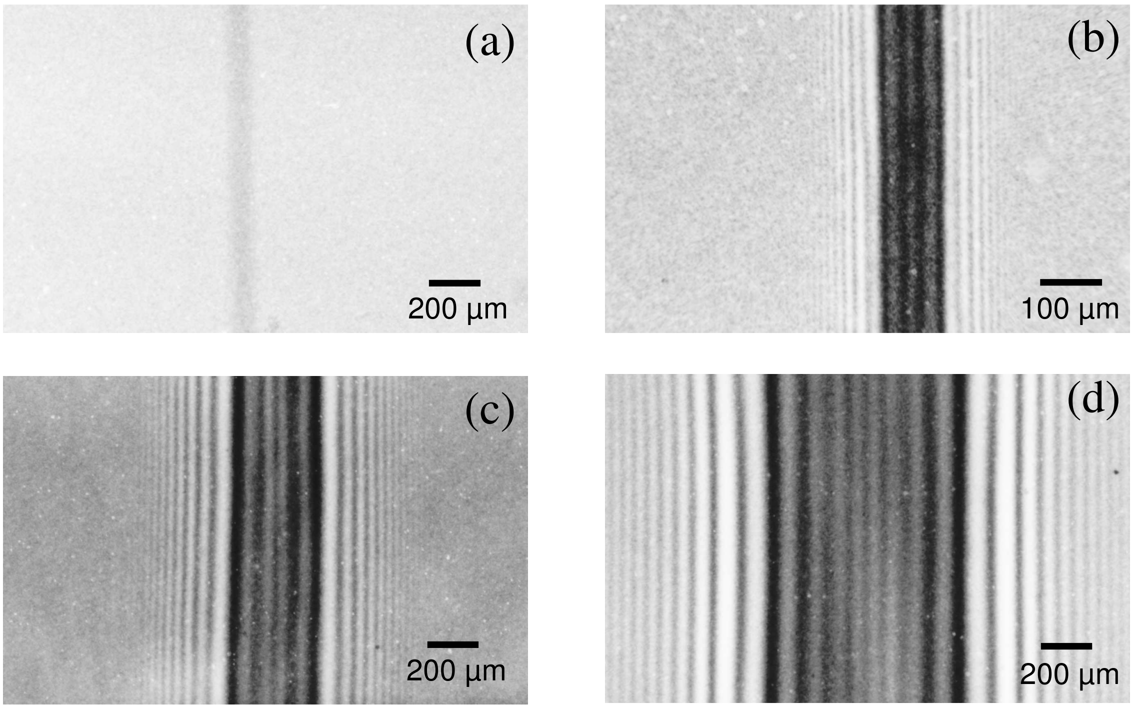

Figure 5.54: Radiograph of a human hair with a diameter of 80 μm at different distances. The X-ray spot size was $\sigma_h = (19.1 \pm 0.7)$ μm, and $\sigma_v = (0.50 \pm 0.05)$ μm. The object-to-detector distances were $x_{od} = 0.002$ m (a), $x_{od} = 2.83$ m (b), $x_{od} = 9.31$ m (c), $x_{od} = 11.73$ m (d). The source-to-detector distance was always $x_{so} = 13.61$ m. The X-ray film was digitized with an optical microscope (a), (c) and (d) with a magnification of (4×), (b) with a magnification of (10×).

$\delta = 4.7 \cdot 10^{-5}$ and $\beta = 1.56 \cdot 10^{-6}$. The absorption of the grid is $(1 - \exp[-(4\pi\beta t_{Ni})/\lambda])$ $= 31.6\%$.

In Fig. 5.57 (c) the vertical intensity profile of the grid disappears. This fact can be explained by the large beam spot size in horizontal direction, which amounts to $\sigma_h = (19.1 \pm 0.7)$ μm. The corresponding X-ray spot size projection on the detector plane is $\sigma_{h-proj} = (41.35 \pm 1.65)$ μm. A further contribution originate from the virtual beam spot size of 37.5 μm of the crystal monochromator, see section 5.4.3.

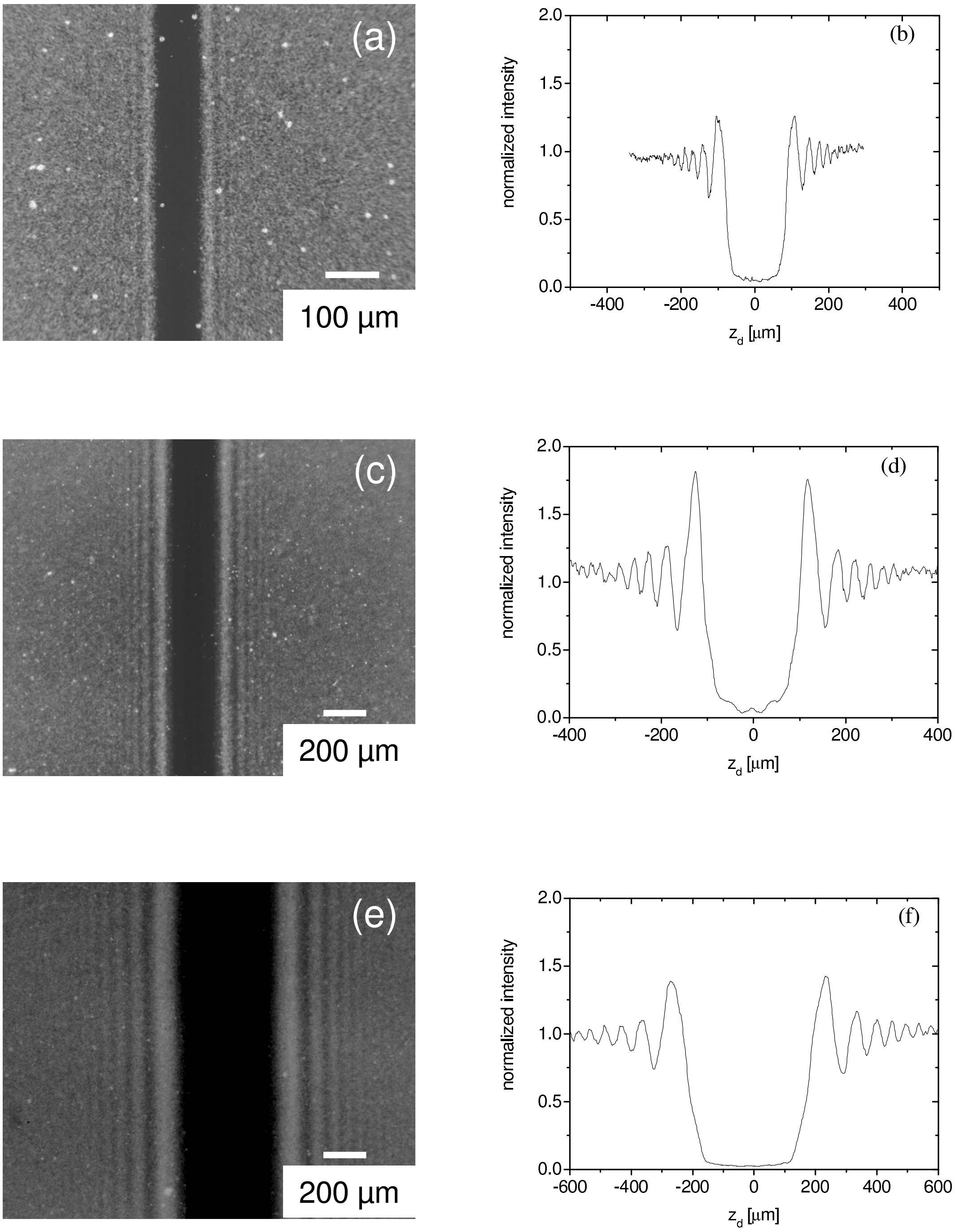

Figure 5.55: Radiograph of a tungsten wire of (40 ± 4) μm diameter. X-ray photon energy is 6 keV, X-ray source size was $\sigma_h = (19.1 \pm 0.7)$ μm, and $\sigma_v = (0.50 \pm 0.05)$ μm. The object-to-detector distance (a) $x_{od} = 2.83$ m, (c) $x_{od} = 9.31$ m and (e) $x_{od} = 12.71$ m. The radiograph is recorded with an X-ray film and digitized with optical microscope of magnifications (10×) (a), and (4×) (c), (e).

5.7 Concluding remarks

At third generation synchrotron radiation sources X-ray phase contrast imaging and hard X-ray in-line holography become a routine technique for beam quality monitoring, characterization of the optical elements, sample alignment and a number of similar applications [Grz99, Gur96, Ste03].

At MAMI, a brilliant X-ray beam has been prepared on the basis of transition radiation. The high transverse coherence length arises from the micro-focused electron beam in combination with a relative long source-to-detector distance. The longitudinal coherence has been obtained by the (111) reflection at a flat silicon single crystal in Bragg geometry. Streaks have been observed which probably originate from deformations in the crystal lattice planes of the monochromator crystal (wavy structures). It has been demonstrated that the direct exposure CCD chip provides a highly efficient on-line detector. It was used to monitor the electron beam size by observing the smallest visible interference fringe spacings or the number of fringes.

Direct exposure CCD camera chips have, compared with X-ray films, the big advantage that they have a good linearity over a wide dynamical range, a good signal-to-noise ratio, and that they are on-line capable. Contrast images can easily be generated in which all parasitic background, which originates not from the object, can be eliminated. The on-line capability allowed a minimization of the beam spot size. The disadvantage of a moderate spatial resolution in comparison to an X-ray film could be alleviated by a geometrical magnification which resulted in an effective pixel size of 1.86 μm. Unfortunately, the spatial resolution is larger than one pixel because of split events.

Density fluctuations and shape deformation of low absorbing materials have been observed with photons of 6 keV energy. The reconstruction of 3-D images from the holograms is a difficult task [Ger72, Koh97] and was outside the scope of this work.

X-ray radiography using coherent X-rays enhances also the visibility of the highly absorbing materials via diffraction at edges. This was demonstrated with tungsten wires of various thicknesses between 4 and 40 μm diameter. In combination with a high geometrical magnification this effect would allow the observation of small highly absorbing features with micrometer size in an object to be investigated.

It has been shown in this section 5.6 that X-ray films, in combination with the micro-focused and monochromized transition radiation X-ray source at MAMI, are useful detectors. The main advantage in comparison with the direct exposure CCD chip is the resolution. For the X-ray film Structurix D3 the standard deviation of the resolution was measured to be $\sigma_f = (1.2 \pm 0.4)$ μm, which is about a factor of 6 better than for the direct exposure CCD chip. With the small effective X-ray spot size in vertical direction of $\sigma_v = (1.4 \pm 0.5)$ μm and a geometrical magnification of up to 7.24 high quality holograms of tiny transparent and opaque objects were taken. The exposure times at a photon energy of 6 keV were about the same for the direct exposure CCD chip and the X-ray film.

The main disadvantage of the X-ray film is the missing on-line capability, which, in particular, makes the production of normalized contrast images more difficult. This problem can be solved in future experiments by a precise positioning procedure of the film with which the hologram and the reference picture are taken with the aid of suitable absorption markers. The often stated disadvantage of a limited dynamical range, for the Structurix D3 film about 1:3000, was in the experiments of this work not the limiting factor since the final dynamical range of 1:256 was defined by the optical scanning microscope with which the developed X-ray film was digitized. This problem can be solved by using a setup similar to that described in appendix C in which the Gd_2O_2S:Tb luminescent screen is replaced by the X-ray film. The Marconi CCD47-10 chip is well suited as an optical detector with a dynamical range of about 16 bits or 1:65500. With a magnification of the optics of about a factor of 5 times, the effective pixel resolution of 2.6 μm (standard deviation) of the CCD will be in the order of the X-ray film resolution.

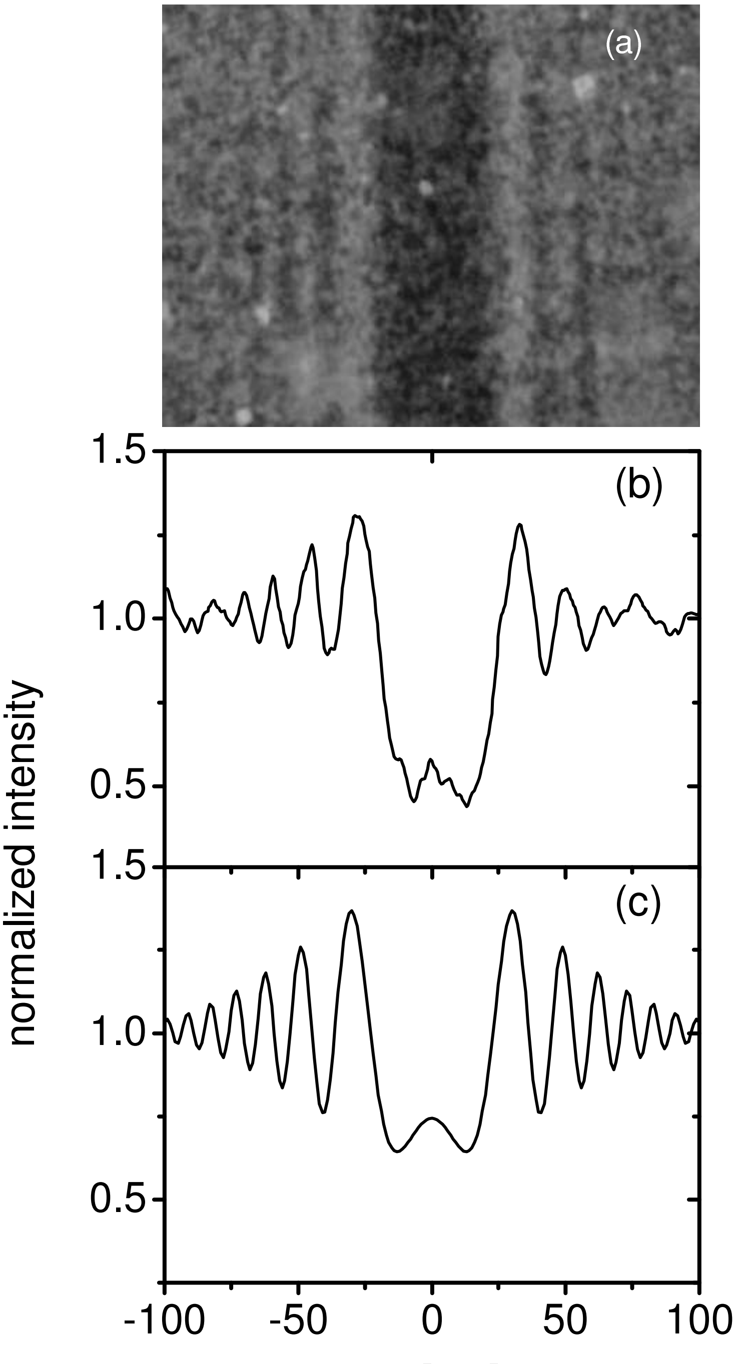

Figure 5.56: (a) Radiograph of a tungsten wire with a diameter of (4.0 ± 0.4) μm. Source-to-object distance $x_{so} = 10.78$ m, object-to-detector distance $x_{od} = 2.83$ m, corresponding geometrical magnification 1.26 times, electron beam current 500 nA, exposure time 15 min. The radiograph was digitized with an optical microscope of magnification (10×). (b) The intensity profile, 200 rows were summed up, (c) the calculated intensity profile.

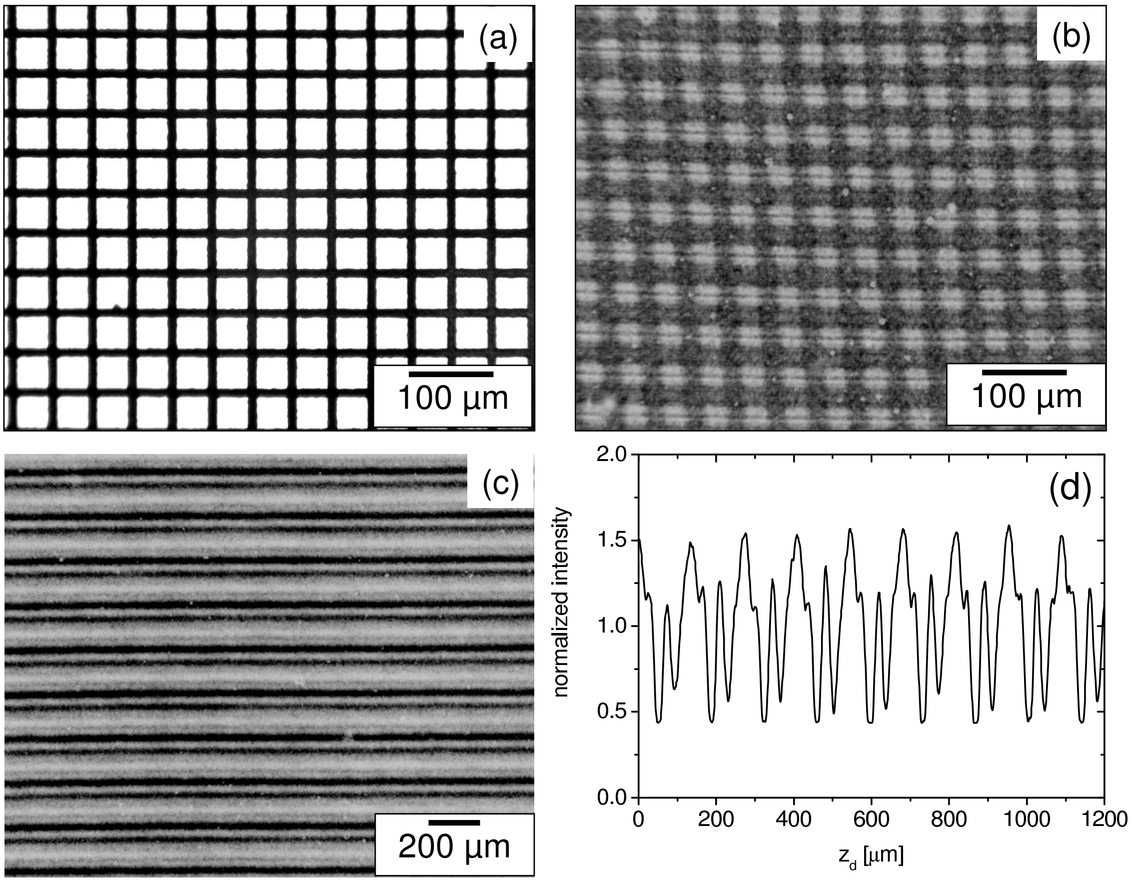

Figure 5.57: Pictures of a nickel grid with 4 μm thickness, width of 12 μm and spacing of 40 μm. (a) Image taken with an optical microscope with (10×) magnification. (b) Radiograph at source-to-object distance $x_{so} = 12.71$ m while the object-to-detector distance $x_{od} = 0.9$ m, geometrical magnification 1.07 times. The radiograph was scanned with an optical microscope with magnification (10×). (c) Radiograph at source-to-object distance $x_{so} = 4.3$ m while the object-to-detector distance $x_{od} = 9.31$ m, geometrical magnification 3.17 times. The radiograph was scanned with an optical microscope with magnification (4×) . (d) Vertical intensity profile of radiograph (c). X-ray photon energy 6 keV, electron beam current 500 nA, exposure time 15 min, X-ray source size was $\sigma_h = (19.1 \pm 0.7)$ μm, and $\sigma_v = (0.50 \pm 0.05)$ μm.

6 Outlook

Any work on X-ray holography at MAMI must, in some sense, bear comparison with modern synchrotron radiation sources such as ESRF, APS and Spring8. At these facilities nanofocusing parabolic refractive X-Ray lenses [Sch03], and two dimensional X-ray wave guides [Jar05] are being developed with which X-ray spot sizes in the order of 50 nm can be prepared. The question arises which dimensions, at least in principle, in future can be achieved with a transition radiation source at MAMI.

To achieve at a given emittance a small beam spot size the divergence of the electron beam must be large. It will be required that the angular spread of the electron beam should not be too large and must not exceed the angle $2/\gamma$ (standard deviation). With the measured emittances at a electron beam energy of 600 MeV $\varepsilon_h = 2.3$ μm mrad and $\varepsilon_v = 0.52$ μm mrad in horizontal and vertical direction, respectively, beam spot sizes of $\sigma_h = 1.35$ μm and $\sigma_v = 0.31$ μm result [1]. A decrease of the spot size into these dimensions should be achievable by micro-focusing the beam spot size by means of miniaturized quadrupoles of a small focal length. Such devices are currently being developed at the LMU München [Hab05] and will be tested at MAMI in the next future. A further improvement should be obtainable if the X-ray beam spot size is demagnified by a crystal optics, as schematically shown in Fig. 6.1. The longitudinal dimension l_{tr} of the transition radiator must fulfill the condition $l_{tr} \leq \sigma_v \gamma$, i.e. must not exceed $l_{tr} = 364$ μm. Typically, it consists only of a few foils with a thickness of about 12 μm and a spacing of about 100 μm. At a demagnification of 5× the virtual beam spot sizes would be in the order $\sigma_{h,virt} = 270$ nm and $\sigma_{v,virt} = 62$ nm, i.e. in the order of what is envisaged at synchrotron radiation facilities with two dimensional X-ray wave guides.

However, it should be stressed that the degradation of the transverse coherence by the crystal in horizontal direction, which has been mentioned in section 5.4.3, must be solved. If this would be possible, the angle in which coherent X-rays of a photon energy of 6 keV, or $\lambda = 2.067$ Å, are emitted would be, according to the equation $\sigma_{h,v} \cdot \theta_{coh} \simeq \lambda/2\pi$, about $\theta_{coh,h} = 0.12$ mrad and $\theta_{coh,v} = 0.84$ mrad in horizontal and vertical direction, respectively. At a source-to-crystal distance of $x_{sc} = 7.8$ m, a crystal-to-detector distance of $x_{cd} = 5.8$ m, and a demagnification factor $M = 5\times$ the focal length of the demagnifying crystal is $f = x_{sc}/(M-1) = 1.95$ m. At a distance between

---

[1] These numbers are well above the theoretical diffraction limit. For a transition radiation source with an opening angle of the radiation of $\theta = 2/\gamma = 1.7$ mrad, $\gamma = 1174$ for 600 MeV electrons, one obtains at a photon energy of 6 keV, or $\lambda = 2.067$ Å, according to the relation $\sigma_{spot}\theta = \lambda/(2\pi)$ a spot size $\sigma_{spot} = 19.4$ nm.

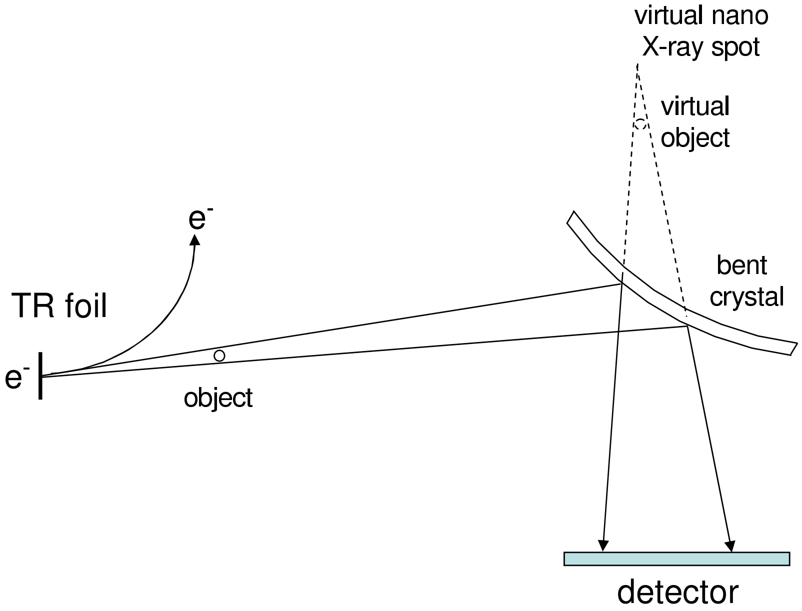

Figure 6.1: Demagnifying crystal optics to produce a nanofocus at MAMI. The source-to-crystal distance is x_{sc}, the crystal to detector distance x_{cd}, and the demagnification factor M. Then, the focal length of the crystal must be $f = x_{sc}/(M-1)$ and the virtual source-to-crystal distance is $x_{sc,virt} = x_{sc}/M$. Focal length, bending radius R of the crystal and Bragg angle θ_B are connected by the equation $f = (R/2)\sin\theta_B$. The object can be placed between X-ray source and crystal or crystal and detector.

the virtual source and detector $x_{sc,virt} = x_{sc}/M + x_{cd} = 7.36$ m an elliptical area with semiaxes of 0.9 mm × 6.2 mm could be coherently illuminated.

A Refraction and diffraction of X-rays by a cylindrical string

A.1 Refraction in the approximation of geometrical optics

In this appendix the intensity profile behind a cylindrical string, which is illuminated by a point like X-ray source, will be calculated in the approximation of geometrical optics. It will be assumed that the X-rays are refracted by the object. This approach might be a good approximation at experimental conditions in which interference patterns are smeared out, i.e., if the object is illuminated with polychromatic X-rays, or if the projected source size or the detector resolution are too large resp. too bad. The geometrical configuration is depicted in Fig. A.1.

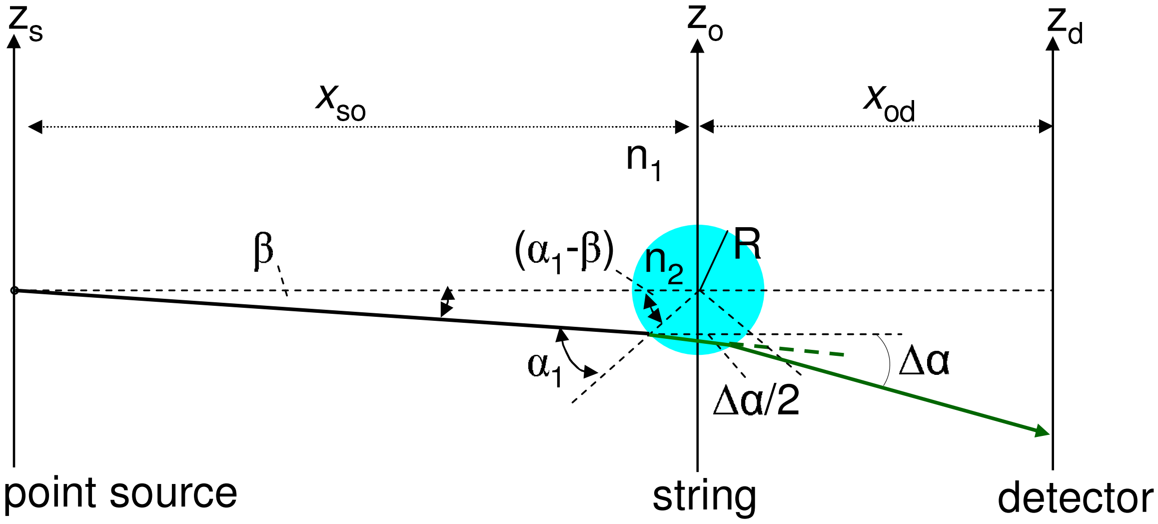

Figure A.1: Refraction of X-rays by a cylindrical string of radius R and refraction index n_2 embedded in a medium with refraction index n_1. The angle α_1 is the angle of incidence with respect to the surface normal of the string, α_2 is the refraction angle in the string. From these angles the deflection angle $\Delta\alpha/2$ of the incident ray can be calculated which is assumed to be doubled at the exit.

By using Snell's law

$$n_1 \sin\alpha_1 = n_2 \sin\alpha_2 \tag{A.1}$$

where

$$n_1 = 1 - \delta_1 + i\beta_1 \quad \text{and} \quad n_2 = 1 - \delta_2 + i\beta_2 \ ,$$

neglecting absorption, i.e. $\beta_1 = \beta_2 = 0$, and assuming $\delta_1, \delta_2 \ll 1$ one obtains

$$\sin(\alpha_2) = \frac{1-\delta_1}{1-\delta_2}\sin\alpha_1 \quad \Rightarrow \quad \sin\alpha_2 = (1 - \delta_1 + \delta_2)\sin\alpha_1 \ . \tag{A.2}$$

With $\alpha_2 = \alpha_1 + \Delta\alpha/2$ and $\Delta\alpha/2$ a small quantity for hard X-rays the equation

$$\sin\alpha_2 = \sin(\alpha_1 + \frac{\Delta\alpha}{2}) = \sin\alpha_1 \cos\frac{\Delta\alpha}{2} + \cos\alpha_1 \sin\frac{\Delta\alpha}{2} \tag{A.3}$$

reduces to

$$\sin\alpha_1 + \frac{\Delta\alpha}{2}\cos\alpha_1 = [1 + (\delta_2 - \delta_1)]\sin\alpha_1 \tag{A.4}$$

or

$$\frac{\Delta\alpha}{2}\cos\alpha_1 = (\delta_2 - \delta_1)\sin\alpha_1 \ . \tag{A.5}$$

The total deflection angle $\Delta\alpha$ is assumed to be doubled at the exit interface of the string, which probably is a rather good approximation, and is given by

$$\Delta\alpha = 2(\delta_2 - \delta_1)\frac{\sin\alpha_1}{\cos\alpha_1} \quad . \tag{A.6}$$

The spatial coordinate z_d of the ray at the detector plane becomes

$$z_d = z_o(1 + x_{od}/x_{so}) + \text{sign}(z_o)\cdot\Delta\alpha\cdot x_{od} = z_o(1 + x_{od}/x_{so}) + \text{sign}(z_o)\cdot 2\cdot(\delta_2 - \delta_1)x_{od}\frac{\sin\alpha_1}{\cos\alpha_1} \ . \tag{A.7}$$

with z_0 the spatial coordinate of the ray at the object, in front of the string, see Fig. A.1. Without any restriction of generality, only positive values of z_0 will be assumed in the following. For the distance between source and object x_{so} large against the radius R of the string, i.e. $\beta \ll 1$, in good approximation $\sin(\alpha_1 - \beta) \approx \sin\alpha_1$ holds. By eliminating in this equation $\sin\alpha_1$ and $\cos\alpha_1$ with the expressions

$$z_o = R\sin\alpha_1 \Rightarrow \sin\alpha_1 = \frac{z_o}{R} \Rightarrow \cos\alpha_1 = \sqrt{1 - (\frac{z_o}{R})^2} \tag{A.8}$$

and dividing both sides by R one obtains

$$\frac{z_d}{R} = \frac{z_o}{R}(1 + x_{od}/x_{so}) + 2\frac{x_{od}}{R}(\delta_2 - \delta_1)\frac{z_o/R}{\sqrt{1 - (z_o/R)^2}} \quad . \tag{A.9}$$

With the substitutions $z_d/R = \xi, \ z_o/R = \xi_1, \ 2(\delta_2 - \delta_1)x_{od}/R = A$ Eq. (A.9) reads

$$\xi = \xi_1(1 + x_{od}/x_{so}) + A\frac{\xi_1}{\sqrt{1 - \xi_1^2}}. \tag{A.10}$$

The scattered intensity distribution dN/dz_d at the detector plane is connected with the primary intensity distribution dN_0/dz_0 without the string by the expression,

$$\frac{dN}{dz_d} = \frac{dN}{dz_o}\frac{dz_o}{dz_d} = \frac{dN_0}{dz_d} \cdot \frac{(1 + x_{od}/x_{so})}{d\xi/d\xi_1} \ . \tag{A.11}$$

With

$$\frac{d\xi}{d\xi_1} = (1 + x_{od}/x_{so}) + \frac{A}{\sqrt{1-(\xi_1^2)}} + A\xi_1[-\frac{1}{2}\frac{-2\xi_1}{(1-\xi_1^2)^{\frac{3}{2}}}] \tag{A.12}$$

$$\frac{d\xi}{d\xi_1} = (1 + x_{od}/x_{so}) + \frac{A}{(1-\xi_1^2)^{\frac{3}{2}}} \tag{A.13}$$

and substitution of Eq. (A.13) into Eq. (A.11) one obtains for the scattered intensity distribution

$$\frac{dN}{d(z_d/R)} = \frac{dN_0}{d(z_d/R)}\frac{(1 + x_{od}/x_{so})}{(1 + x_{od}/x_{so}) + A/(1-(z_o/R)^2)^{\frac{3}{2}}} \ . \tag{A.14}$$

The normalized total intensity distribution $I_n^{(\omega)}$ at the detector plane is given by

$$\begin{aligned} I_n^{(\omega)}(z_d/R,\omega) &= \theta(\frac{z_d}{R\cdot(1 + x_{od}/x_{so})} - 1) + \frac{dN}{d(z_d/R)}/\frac{dN_0}{d(z_d/R)} = \\ &= \theta(\frac{z_d}{R\cdot(1 + x_{od}/x_{so})} - 1) + \frac{(1 + x_{od}/x_{so})}{(1 + x_{od}/x_{so}) + A(\omega)/(1-(z_o/R)^2)^{\frac{3}{2}}} \end{aligned} \tag{A.15}$$

with z_0/R a solution of the equation

$$\frac{z_d}{R} = \frac{z_o}{R}(1 + x_{od}/x_{so}) + A(\omega)\frac{z_o/R}{\sqrt{1-(z_o/R)^2}} \ , \tag{A.16}$$

$\theta(x)$ the unit step function, equal to zero for $x < 1$ and 1 for $x \geq 1$, and $A = A(\omega) = 2(x_{od}/R)(\delta_2(\omega) - \delta_1(\omega))$. In the final intensity distribution $I_n(z_d/R)$ the frequency spectrum of the primary polychromatic X-ray beam and the response of the X-ray detector has to be taken into account. It is obtained by an integration with an appropriate normalized distribution function $f(\omega)$ and reads

$$I_n(z_d/R) = \int I_n^{(\omega)}(z_d/R,\omega)f(\omega)d\omega \ . \tag{A.17}$$

A typical example of such an intensity distribution, assuming an unlimited spatial resolution of the detector and a point-like X-ray source is shown in Fig. A.2.

The edge enhancement can clearly be recognized. The step-like increase of the intensity at $z_d/R = 1$ originates from the assumption $\lambda \to 0$ and, therefore, is unrealistically steep. To understand the decrease of the intensity for $z_d/R < 1$ it is worthwhile to notice that the string acts in some sense as a de-focusing cylindrical lens since in the X-ray region the index of refraction is less than unity. The focal length f in the center of the string is given by the lens makers formula [Hec89]

$$\frac{1}{f} = -\frac{2(\delta_2 - \delta_1)}{R} \ . \tag{A.18}$$

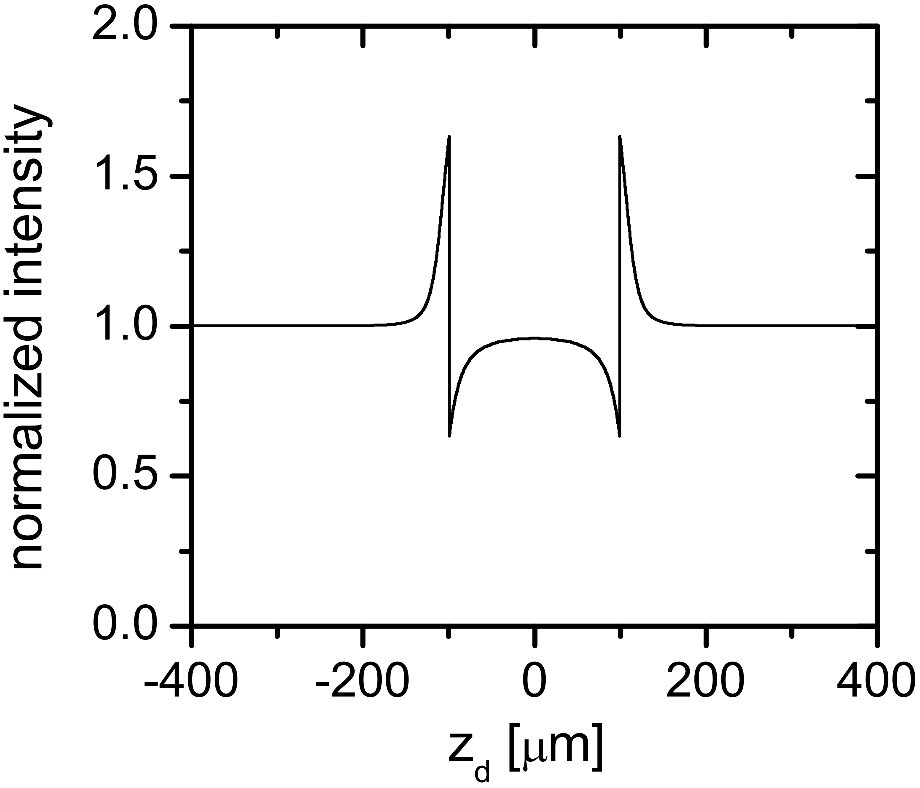

Figure A.2: Calculated intensity profile of a polymer wire with a diameter of 30 μm illuminated with a point like source. Calculations are based on geometrical optics as outlined in this appendix. The object-to-detector distance is $x_{so} = 1.92$ m and the object-to-detector distance $x_{od} = 11.68$ m, the corresponding magnification is 7.1 times. X-ray photon energy 19.6 keV, the complex refraction index parameters are $\delta = 6.8 \cdot 10^{-7}$ and $\beta = 2.6 \cdot 10^{-10}$.

A.2 Diffraction in the Fresnel approximation of wave optics

The wave field emanating from the point source in the geometry of Fig. (A.1) is in the Fresnel approximation at the object given by

$$E_0(y_o, z_o) = E_A \exp(ik\frac{y_o^2 + z_o^2}{2x_{so}}), \tag{A.19}$$

with $E_A = (A/x_{so}) \exp(ikx_{so})$, $k = 2\pi/\lambda$ the wavenumber, and A the amplitude. Let us assume that our object consists of "flat" elements which are positioned in space at various distances x_{so} from the source. Each of these elements may be described by a transmission function $Q(y_o, z_o)$ which is defined in the complete object plane. This will be discussed in detail below. By using Kirchhoff's integral the wave field at the detector plane is given by

$$E(y_d, z_d) = h_0 \int\limits_{-\infty}^{\infty}\int\limits_{-\infty}^{\infty} E_0(y_o, z_o)Q(y_o, z_o)\exp\Big(i\frac{k}{2x_{od}}[(y_d-y_o)^2+(z_d-z_o)^2]\Big)dy_o dz_o, \tag{A.20}$$

with $h_0 = (-i/\lambda x_{od})\exp(ikx_{od})$. Inserting Eq. (A.19) one obtains

$$\begin{aligned} E(y_d, z_d) &= h_0 E_A \int\limits_{-\infty}^{\infty}\int\limits_{-\infty}^{\infty} \exp\Big(ik\frac{y_o^2+z_o^2}{2x_{so}}\Big)Q(y_o, z_o)\exp\Big(i\frac{k}{2x_{od}}[(y_d-y_o)^2+(z_d-z_o)^2]\Big)dy_o dz_o \\ &= h_0 E_A \int\limits_{-\infty}^{\infty}\int\limits_{-\infty}^{\infty} \exp\Big(i\frac{k}{2}[\frac{y_o^2}{x_{so}}+\frac{(y_d-y_o)^2}{x_{od}}]\Big) \\ &\qquad \cdot Q(y_o, z_o)\exp\Big(i\frac{k}{2}[\frac{z_o^2}{x_{so}}+\frac{(z_d-z_o)^2}{x_{od}}]\Big)dy_o dz_o\ . \end{aligned} \tag{A.21}$$

With the identities

$$\frac{y_o^2}{x_{so}} + \frac{(y_d-y_o)^2}{x_{od}} = \frac{x_{sd}}{x_{so}x_{od}}(y_o - y_d\frac{x_{so}}{x_{sd}})^2 + \frac{y_d^2}{x_{sd}} \tag{A.22}$$

and

$$\frac{z_o^2}{x_{so}} + \frac{(z_d-z_o)^2}{x_{od}} = \frac{x_{sd}}{x_{so}x_{od}}(z_o - z_d\frac{x_{so}}{x_{sd}})^2 + \frac{z_d^2}{x_{sd}} \tag{A.23}$$

one obtains

$$\begin{aligned} E(y_d, z_d) &= \frac{A}{x_{sd}}\exp(ikx_{sd})\exp(ik\frac{y_d^2+z_d^2}{2x_{sd}})\cdot\frac{-ix_{sd}}{\lambda x_{so}x_{od}}\cdot \\ &\int\limits_{-\infty}^{\infty}\int\limits_{-\infty}^{\infty} \exp\Big(ik\frac{x_{sd}}{2x_{so}x_{od}}[(y_o-y_d\frac{x_{so}}{x_{sd}})^2+(z_o-z_d\frac{x_{so}}{x_{sd}})^2]\Big)Q(y_o, z_o)dy_o dz_o\ . \end{aligned} \tag{A.24}$$

In the first line the unperturbed wave $E_0(y_d, z_d) = (A/x_{sd})\exp(ikx_{sd})\exp(ik(y_d^2 + z_d^2)/(2x_{sd})$ at the detector position in a distance x_{sd} from the source can be recognized. The second line describes the modification of this wave by the object. In the following we assume that the object is an one-dimensional string for which the transmission function can be written as $Q(y_o, z_o) = Q(z_o)$. Then Eq. (A.24) separates into

$$\begin{aligned} E(y_d, z_d) = E_0(y_d, z_d)\frac{-ix_{sd}}{\lambda x_{so}x_{od}} &\int\limits_{-\infty}^{\infty} \exp\Big(ik\frac{x_{sd}}{2x_{so}x_{od}}(y_o-y_d\frac{x_{so}}{x_{sd}})^2\Big)dy_o \\ \cdot &\int\limits_{-\infty}^{\infty} \exp\Big(ik\frac{x_{sd}}{2x_{so}x_{od}}(z_o-z_d\frac{x_{so}}{x_{sd}})^2\Big)Q(z_o)dz_o\ . \end{aligned} \tag{A.25}$$

The calculation of the integral

$$I_y = \int\limits_{-\infty}^{\infty} \exp\Big(i\frac{\pi\cdot x_{sd}}{\lambda x_{so}x_{od}}(y_o - y_d\frac{x_{so}}{x_{sd}})^2\Big)dy_o \tag{A.26}$$

yields with the well known expression $\int\limits_{-\infty}^{\infty} \exp(-i\beta t^2)dt = \sqrt{-i\pi/\beta}$, $\beta = -\pi x_{sd}/(\lambda x_{so} x_{od})$, $t = y_o - y_d \; x_{so}/x_{sd}$, $dt = dy_o$

$$I_y = \sqrt{\frac{\lambda x_{so} x_{od}}{-i x_{sd}}} \tag{A.27}$$

and Eq. (A.25) can be rewritten as

$$E(y_d, z_d) = E_0(y_d, z_d) \sqrt{\frac{-i x_{sd}}{\lambda x_{so} x_{od}}} \int\limits_{-\infty}^{\infty} Q(z_o) \exp\Big(ik \frac{x_{sd}}{2 x_{so} x_{od}} (z_o - z_d \frac{x_{so}}{x_{sd}})^2 \Big) dz_o \; . \tag{A.28}$$

Let us assume that $Q(z_o)$ can be subdivided into three regions according to

$$Q(z_o) = \begin{cases} 1 & \text{for} \quad |z_o| > R \\ q(z_o) & \text{for} \quad -R < z_o < R \; . \end{cases} \tag{A.29}$$

Then, Eq. (A.28) can be reshaped into

$$\begin{aligned} E(y_d, z_d) \;\; = \;\; & E_0(y_d, z_d) \sqrt{\frac{-i x_{sd}}{\lambda x_{so} x_{od}}} \Big[\int\limits_{-\infty}^{\infty} \exp\Big(ik \frac{x_{sd}}{2 x_{so} x_{od}} (z_o - z_d \frac{x_{so}}{x_{sd}})^2 \Big) dz_o + \\ & \int\limits_{-R}^{R} [q(z_o) - 1] \exp\Big(ik \frac{x_{sd}}{2 x_{so} x_{od}} (z_o - z_d \frac{x_{so}}{x_{sd}})^2 \Big) dz_o \Big] \; . \end{aligned} \tag{A.30}$$

The first integral can be calculated and gives the same result as Eq. (A.27). Then, the final result for the normalized wave field at the detector plane reads

$$\frac{E(y_d, z_d)}{E_0(y_d, z_d)} = 1 + a(z_d) \tag{A.31}$$

with

$$a(z_d) = -\sqrt{\frac{-i x_{sd}}{\lambda x_{so} x_{od}}} \int\limits_{-\infty}^{\infty} p(z_o) \exp\Big(ik \frac{x_{sd}}{2 x_{so} x_{od}} (z_o - z_d \frac{x_{so}}{x_{sd}})^2 \Big) dz_o \tag{A.32}$$

and

$$p(z_o) = [1 - q(z_o)] \cdot \theta(1 - |z_o|/R), \tag{A.33}$$

the complementary transmission function of the object. With this function the object plane can be regarded as opaque for $|z_o| > R$ and transparent at the object, i.e. for $|z_o| \leq R$. If illuminated the amplitude $a(z_d)$ describes a kind of slit diffraction, however, with the complementary transmission function of the object placed into the slit. For the limiting cases of a transparent and an opaque object the complementary transmission function is zero and one, respectively. The former corresponds to $a(z_d) = 0$, the latter to Fresnel diffraction for an illuminated slit.

The exponent of the exponential in Eq. (A.32) can be expanded as

$$k\frac{x_{sd}}{2x_{so}x_{od}}(z_o - z_d\frac{x_{so}}{x_{sd}})^2 = k\frac{x_{sd}}{2x_{so}x_{od}}(z_o^2 - 2z_oz_d\frac{x_{so}}{x_{sd}} + (z_d\frac{x_{so}}{x_{sd}})^2)\ . \tag{A.34}$$

and Eq. (A.32) with Eq. (A.34) rewritten in

$$\begin{aligned} a(z_d) \quad &= \quad -\exp\Big(ik\frac{x_{so}}{2x_{od}x_{sd}}z_d^2\Big) \\ &\cdot\sqrt{\frac{-ix_{sd}}{\lambda x_{so}x_{od}}}\cdot\int\limits_{-\infty}^{\infty} p(z_o)\exp\Big(ik\frac{x_{sd}}{2x_{so}x_{od}}z_o^2\Big)\exp\Big(-i\frac{kz_d}{x_{od}}z_o\Big)dz_o\ \ . \end{aligned} \tag{A.35}$$

The second line

$$\sqrt{\frac{-ix_{sd}}{\lambda x_{so}x_{od}}}\cdot\int\limits_{-\infty}^{\infty}\tilde{p}(z_o)\exp\Big(-i\tilde{z}_dz_o\Big)dz_o\ \ . \tag{A.36}$$

contains a Fourier integral of the modified complementary transmission function

$$\tilde{p}(z_o) = p(z_o)\exp\Big(ik\frac{x_{sd}}{2x_{so}x_{od}}z_o^2\Big) \tag{A.37}$$

in the reduced space coordinate $\tilde{z}_d = k\ z_d/x_{od}$. The exponential in the first line of Eq. (A.35) oscillates rapidly with increasing z_d and contains, in essence, the holographic information on the distance of the transparent object to the source x_{so}, or the object to the detector $x_{od} = x_{sd} - x_{so}$.

Let us discuss under which conditions the integral transform Eq. (A.36) reduces to a simple Fourier transform of $p(z_o)$. Generally, this is the case if $\pi x_{sd}z_o^2/(\lambda x_{so}x_{od}) = (\pi z_o^2/\lambda)(1/x_{so} + 1/x_{od}) \leq (\pi R^2/\lambda)(1/x_{so} + 1/x_{od}) \ll \pi$ holds. In terms of Fresnel numbers

$$N_F' = \frac{R^2}{\lambda x_{so}}, \qquad N_F'' = \frac{R^2}{\lambda x_{od}} \tag{A.38}$$

this condition can also be formulated as $N_F = N_F' + N_F'' \ll 1$. At a constant source-to-detector distance x_{sd} the total Fresnel number N_F is large for either $x_{od} \ll x_{sd}$ or $x_{so} \ll x_{sd}$, and it is minimal at $x_{od} = x_{so} = x_{sd}/2$. For the latter case $N_F = 4R^2/(\lambda x_{sd}) \ll 1$ or $R \ll \sqrt{\lambda x_{sd}/4}$ must be fulfilled. For $x_{sd} = 13.6$ m, $\lambda = 2$ Å an $R \ll 26.0\ \mu$m results. This condition was generally not fulfilled in our experiments.

A remark may be appropriate under which conditions Eq. (A.35) is equivalent to the Fraunhofer approximation. This is the case if, in addition, the exponential in the first line of Eq. (A.35) reduces to one which is the case if the observation region obeys the inequality $z_d \ll \sqrt{\lambda x_{sd}x_{0d}/(x_{so})}$. Under the assumptions made above this means that $z_d \ll \sqrt{\lambda x_{sd}} = 52.2\ \mu$m. This condition was also not fulfilled in our experiments.

In summary, since neither of the above discussed conditions were fulfilled in general in our experiments, Eq. (A.35) can not be simplified to the Fraunhofer approximation and Eq. (A.36) not to a Fourier transform of $p(z_o)$.

The normalized contrast image

$$I_{norm}(z_d) = |E(y_d, z_d)/E_0(y_d, z_d)|^2 - 1 \;=\; 2\Re[a(z_d)] + |a(z_d)|^2 \tag{A.39}$$

separates into a "holographic diffraction pattern" $2\Re[a(z_d)]$ which essentially contains the information on the distance, and a "classical diffraction pattern" $|a(z_d)|^2$ of the complementary transmission function $p(z_o)$ of the object. This separation is illustrated in Fig. 5.1 for a homogeneous string with radius R for which $q(z_o)$ is given by

$$q(z_o) = \exp\Big(\frac{-4\pi(i\delta+\beta)}{\lambda}\sqrt{R^2 - z_o^2}\Big). \tag{A.40}$$

The results derived in this appendix on the basis of Kirchhoff's integral Eq. (A.20), which can also be obtained in a system theoretical approach by an expansion of the wave behind the object into paraboloidal elementary waves (Fresnel approximation), see [Sal91, Eq. (4.1-14)], agrees with the results reported by [Koh01].

For a string with the transmission function Eq. (A.40) the Eq. (A.32) reads with the substitution $z_o/R = \sin\theta$, $dz_o = R\cos\theta d\theta$

$$\begin{aligned} a(z_d) = \exp\Big(ik\frac{x_{so}}{2x_{od}x_{sd}}z_d^2\Big)R\sqrt{\frac{-ix_{sd}}{\lambda x_{so}x_{od}}}\int\limits_{-\pi/2}^{\pi/2}\Big(\exp\Big(\frac{-4\pi(i\delta+\beta)}{\lambda}z_{sh}(\cos\theta)\Big)-1\Big) \\ \cdot\exp\Big(ik\frac{x_{sd}}{2x_{so}x_{od}}R\sin\theta(R\sin\theta - 2z_d\frac{x_{so}}{x_{sd}})\Big)\cos\theta d\theta. \end{aligned} \tag{A.41}$$

with $z_{sh}(\cos\theta) = R\cos\theta$. This representation has the advantage that it can easily be generalized for non-circular surfaces of the string. For that purpose a shape function $z_{sh}(\cos\theta) = R(a\;\cos^n\theta) + b\;\cos^m\theta)$ has been introduced with n, m and a arbitrary real numbers, and b determined from the normalization condition $\pi R^2 = 2R\int\limits_{-\pi/2}^{\pi/2} z_{sh}(\cos\theta)\cos\theta d\theta$. With such an ansatz also radial inhomogeneities of the density as well as δ or β may be described.

In the foregoing calculations a point source has been assumed. In reality, only finite sources with a profile $s(z_d)$ are available and, therefore, the calculated intensity profile must be convoluted with the X-ray source projection function at the detector plane $s_{proj}(z_d) = (x_{od}/x_{so})\;s(z_d)$. In addition, also the detector has a finite spatial resolution which is in the order of the pixel size and the resulting intensity profile must be once more convoluted with the detector spatial response function $r(z_d)$ to get the final profile which can be compared with the measured ones. The convoluted normalized contrast image is written as

$$\bar{I}_{norm}(z_d) = I_{norm}(z_d) * (s_{proj}(z_d) * r(z_d)). \tag{A.42}$$

In the calculations Gaussian profiles with standard deviations σ_s and σ_d were assumed for both, the source profile and the detector response function, respectively. This has the advantage that the double convolution in Eq. (A.42) reduces to a single one with a Gaussian of variance $\sigma^2 = ((x_{od}/x_{so})\sigma_s)^2 + \sigma_d^2$.

B Further results of refraction contrast radiography

Figs. B.1, B.2 and B.3 show refraction contrast radiographs of a nylon string with a diameter of 30 μm at different object-to-detector distances. If the object is in close contact with the film, no contrast is observed since the absorption is only 0.1%. At an object-to-detector distance of 0.5 m the contrast starts to builds up but is still small, $C_{ref} = (4.1 \pm 2.9)$ %. At a larger object-to-detector distance $x_{od} = 3.27$ m the contrast increases to $C_{ref} = (15.7 \pm 2.6)$ %, and reaches at $x_{od} = 5.5$ m the value $C_{ref} = (20.1 \pm 2.9)$ %. Also here a broadening of the edge is observed which is due to the increasing size of the projected X-ray source spot at the detector plane.

The most interesting feature of the radiographs shown in Figs. B.1, B.2, B.3 is that an edge enhancement or phase contrast can be observed with a polychromatic X-ray beam also for a rather thin polymer wire with a diameter of 30 μm. In the following a comparison will be given between the interpretation of the experimental results according to the geometrical and wave optical interpretation. Figs. B.1 (c) , B.2 (c) and B.3 (c) show calculations with the geometrical model presented in subsection 4.1.3. Beam spot sizes and X-ray film resolution, including the scanner resolution, have been taken as measured. For the sake of convenience the X-ray spectrum has been approximated by a delta-function at the mean photon energy $\hbar\omega$=19.6 keV. Figs. B.1 (d) , B.2 (d) and B.3 (d) show calculations with the wave optical model presented in subsection A.2. Again, beam spot sizes and X-ray film resolutions, including the scanner resolution, have been taken as measured. The calculations were performed with an approximation of the detected X-ray spectrum shown in Fig. 4.6 which was approximated with 22 discrete values in the energy range between 8 and 30 keV. The measured contrast C_{ref} at different object-to-detector distances x_{od} are shown together with calculations in the framework of geometrical and wave optics in Fig. B.4.

It can be seen from Fig. B.4 that the calculations based on wave optics overestimate and that one on the geometrical optics underestimate the measurements. But it should be mentioned that, even when the wave optical correction is omitted in the geometrical model, the calculations are too low. Clearly, limitations of the geometrical model become apparent. The higher values of the wave optical calculations indicate that in the digitization of the measurement with the polymer string with a diameter of 30 μm is worse as has been assumed.

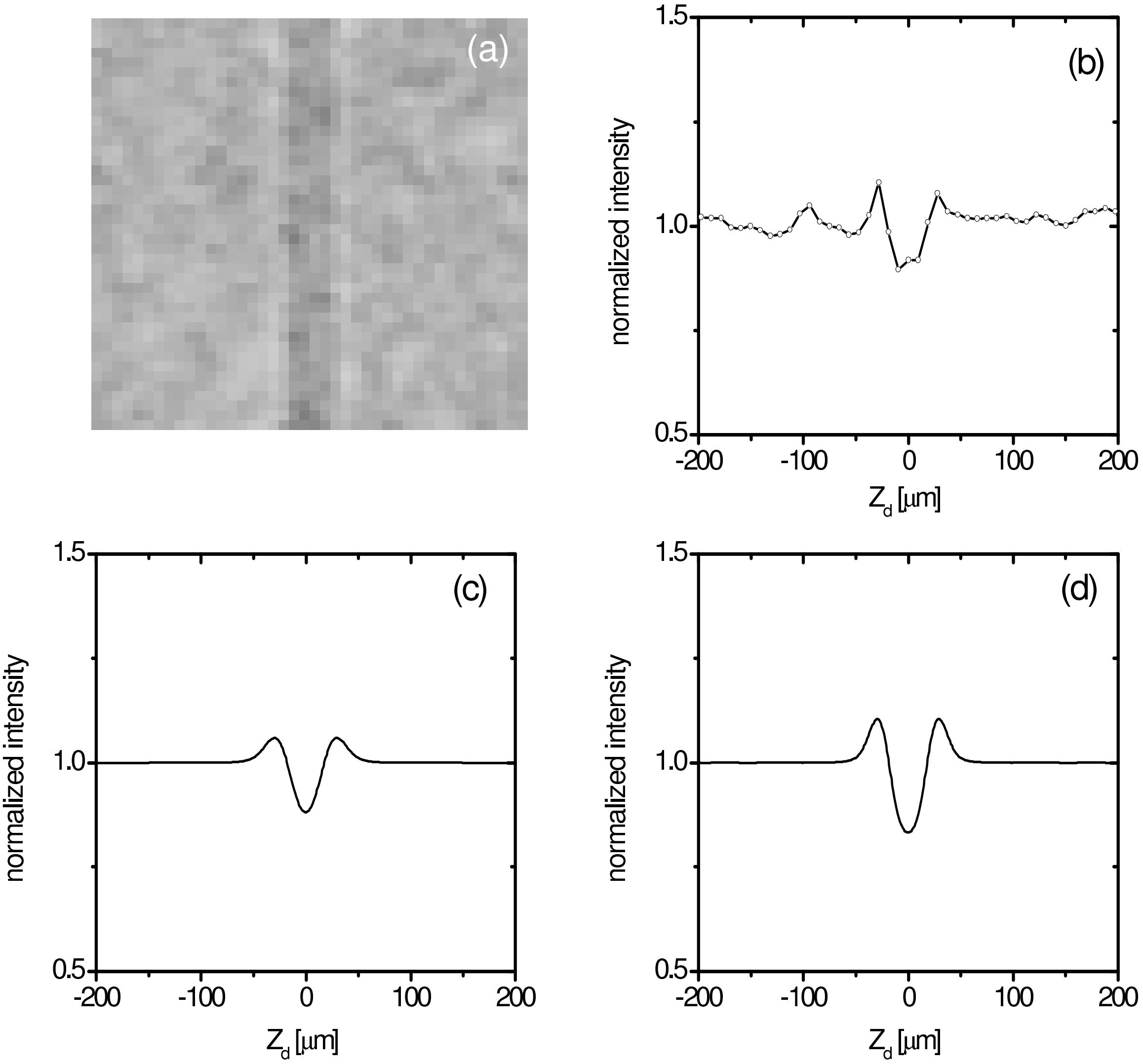

Figure B.1: (a) Refraction enhanced radiograph of a polymer string with a diameter 30 μm at an object-to-detector distance $x_{od} = 2.0$ m, and a source-to-detector distance $x_{sd} = 11.38$ m. The polychromatic X-ray beam from transition radiation with spectral distribution shown in Fig. 3.5 has been used. At the spectrally weighted energy of 19.6 keV the refractive index parameters are $\delta = 7.2 \cdot 10^{-7}$ and $\beta = 2.74\ 10^{-10}$. The electron beam current was 6 nA, the exposure time amounted to 60 sec. X-ray source sizes were $\sigma_h = (8.6 \pm 0.1)$ μm and $\sigma_v = (7.5 \pm 0.1)$ μm in horizontal and vertical direction, respectively. The radiograph (a) was captured by an X-ray film of type Mamoray MR5 II PQ (Agfa). The developed film was digitized by an X-ray scanner of type Super CoolScan 2700 ED (Nikon) with a pixel size of $9.4 \cdot 9.4$ μm^2. (b) Intensity profile for which 100 vertical pixels were added together to improve the statistics. (c) Normalized intensity profile according to geometrical optics as described in subsection 4.1.3 with the following parameters: film and scanner resolution $\sigma_d = (10.0 \pm 0.4)$ μm, and the wave optical contribution $\sigma_w = \sqrt{\lambda x_{sd} x_{od}/(2\pi x_{so})} = 4.94$ μm with $\lambda = 0.633$ Å. (d) Same as (c) on the basis of wave optics

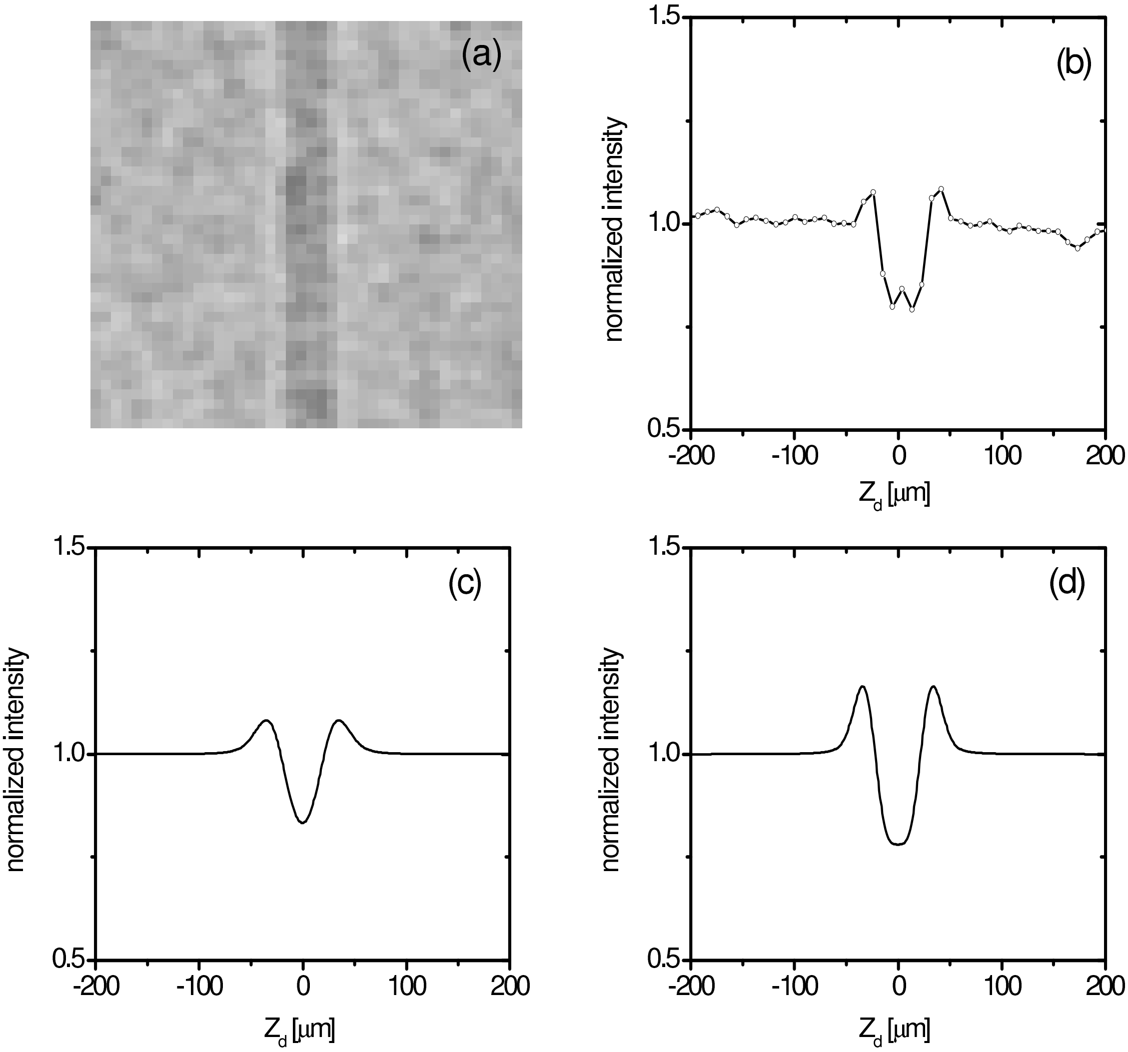

Figure B.2: (a) Refraction enhanced radiograph of a polymer string with a diameter of 30 μm at an object-to-detector distance $x_{od} = 3.27$ m. For further explanations see caption of Fig. B.1.

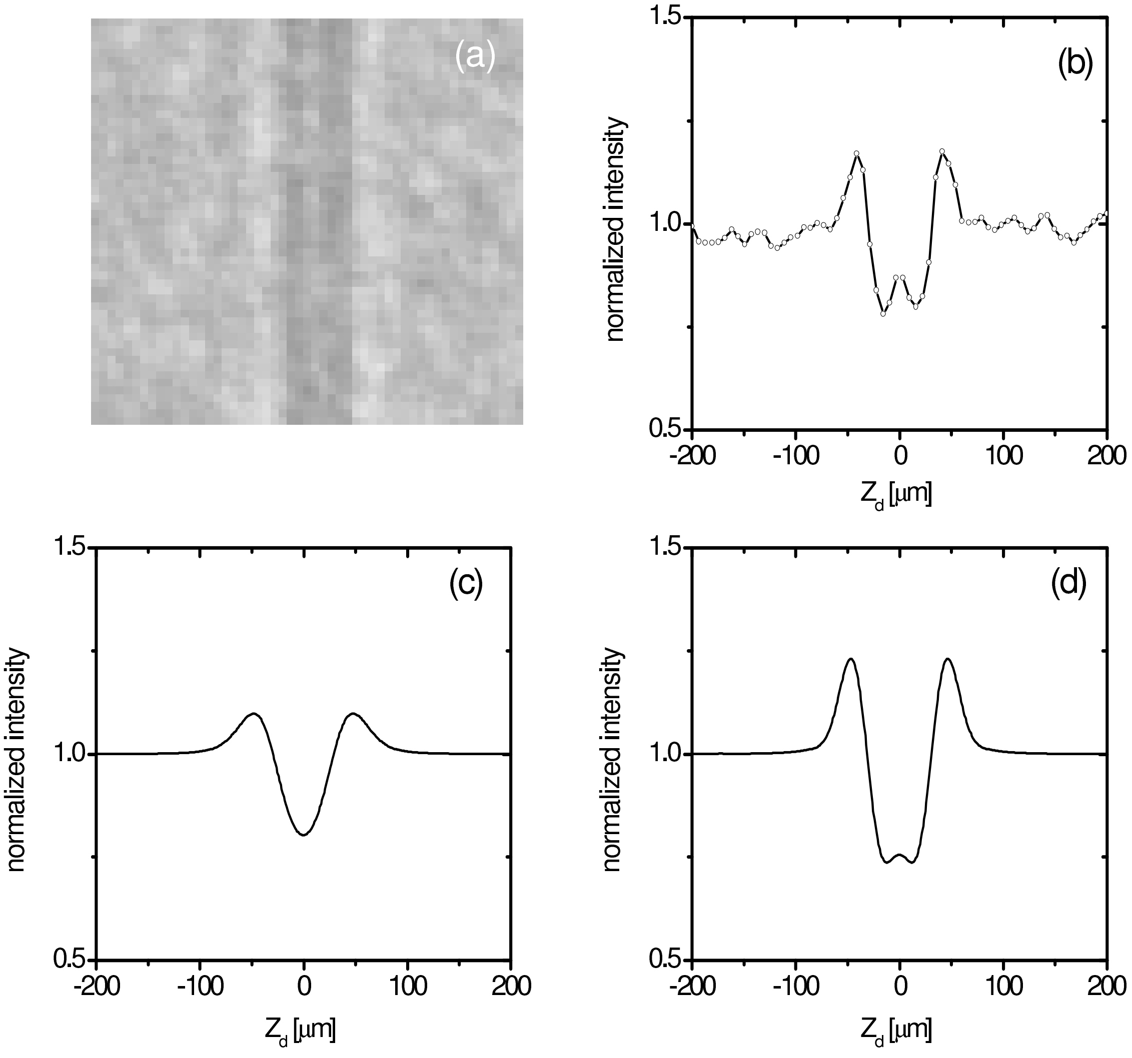

Figure B.3: (a) Refraction enhanced radiograph of a polymer string with a diameter of 30 μm at an object-to-detector distance $x_{od} = 5.5$ m. For further explanations see caption of Fig. B.1.

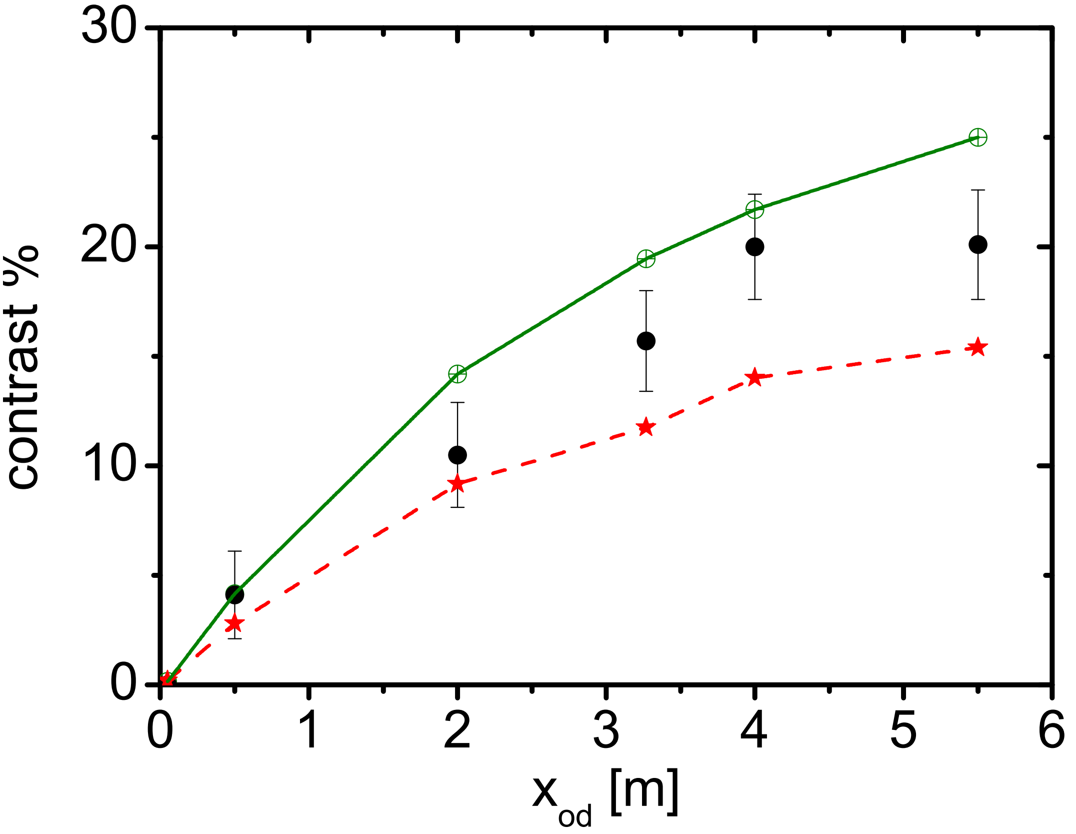

Figure B.4: Contrast C_{ref} for a polymer string of 30 μm diameter as a function of the object-to-detector distance x_{od}. The source-to-detector distance x_{so} = 11.38 m was kept constant during the measurements. Error bars are measurements, crossed circles calculations with the wave optical model with a beam spot size σ_h = 8.6 μm and a total X-ray film resolution of σ_f = 1.96 μm, and a scanner resolution of σ_p = 9.77 μm. Stars designate calculations according to geometrical optics.

C X-ray imaging with a Gd_2O_2S:Tb luminescence screen

The direct-exposure CCD camera as image detector has a spatial resolution which is limited by the pixel size, in the present case 13 × 13 μm^2. Consequently, fringes of holograms with spacings smaller than the pixel size will be blurred or invisible. However, the spatial resolution even with such a CCD as detector can be improved if the X-rays are converted by a suitable luminescent converter screen into visible light and the resulting picture is being magnified via an optical microscope. The finite pixel size of the CCD camera turns out to be negligibly small if high enough a magnification is chosen. Such systems have been described in different works [Bus94, Koc98, And96], and resolutions in the order of 0.8 μm (FWHM) were reported. In the following, the experiences with such a system at MAMI, employing a transition radiation beam which is contaminated with high energy bremsstrahlung photons, will be described.

C.1 Experimental set-up

The setup employed at MAMI is depicted in Fig. C.1. The transition radiation X-rays produced by the 6 keV foil stack, described in chapter 3, at an electron beam energy of 600 MeV are converted by a Gd_2O_2S:Tb luminescent screen of 4 μm or 12 μm [APSXX] thickness into visible light which is partly collected by an optical lens and conveyed to the CCD camera [And96, Gia89, Kan97, Swa73]. To avoid direct exposure of the CCD chip to bremsstrahlung photons, with which the transition radiation X-ray beam is contaminated, the light is reflected behind the lens by a 45° mirror into the CCD chip. The CCD chip is placed in an evacuated chamber at a pressure of 10^{-8} mbar. The light enters the chamber through a 5 mm thick glass window. Upstream the whole system is shielded with a lead wall of 20 cm thickness. The wall has a hole with an area of 7.5×8.2 cm^2 through which the X-rays enter into the imaging system. The whole system is made light tight by stainless steel bellows which allow an easy preadjustment of the luminescent screen and the CCD camera head which are mounted on an optical bench. The entrance window at the converter screen is closed with two aluminized Hostaphan foils of 250 μg/cm^2 thickness covered with 20 μg/cm^2 aluminum. The whole imaging system is mounted on a positioning stage which allows to adjust the image detector position with respect to the X-ray beam.

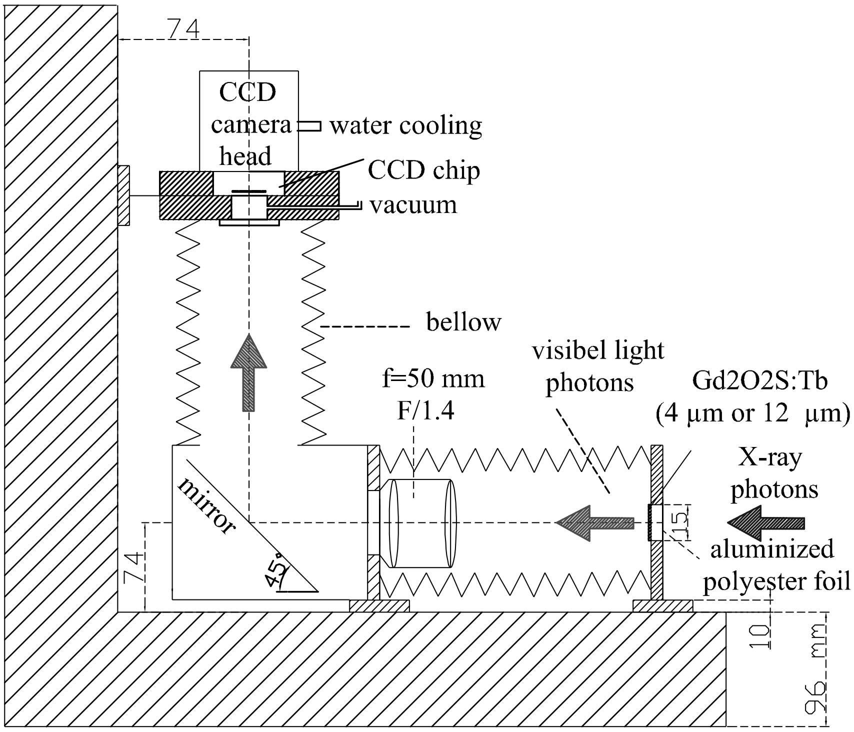

Figure C.1: Imaging system (not to scale). X-ray photons impinge from the right onto the Gd_2O_2S:Tb luminescent screen of 4 and 12 μm thickness for polychromatic and monochromatic X-ray detection, respectively. An $f = 50$ mm Canon camera lens with F-number of 1.4 has been used. The principal points are located in front of the lens. The picture at the luminescent screen can be focused remotely by a mechanical drive at the lens. For a detailed description of the CCD camera head see section 5.3.

C.2 Test of the X-ray imaging system and measurements

C.2.1 Off-line tests

The optical axis of the system was adjusted with the aid of a laser beam. In the geometry of Fig. C.1, the magnification can be chosen between 1 to 6 times resulting in an effective pixel size between 13 μm and 2.62 μm. The spatial resolution of the system is, in addition, affected by the thickness of the phosphor screen and the quality of the imaging lens. The optics and CCD camera system was tested with a standard Siemens star [LinXX] with minimum spatial resolution of 8.7 μm which replaced the luminescent screen. Thereafter, the complete system with a converter screen was tested with alpha particles from an ^{241}Am source. The source was located at a distance of 1 cm from the luminescent screen in air. An optimum resolution of 7 μm (FWHM) was found with a 4 μm thick converter screen at a magnification of 3.5.

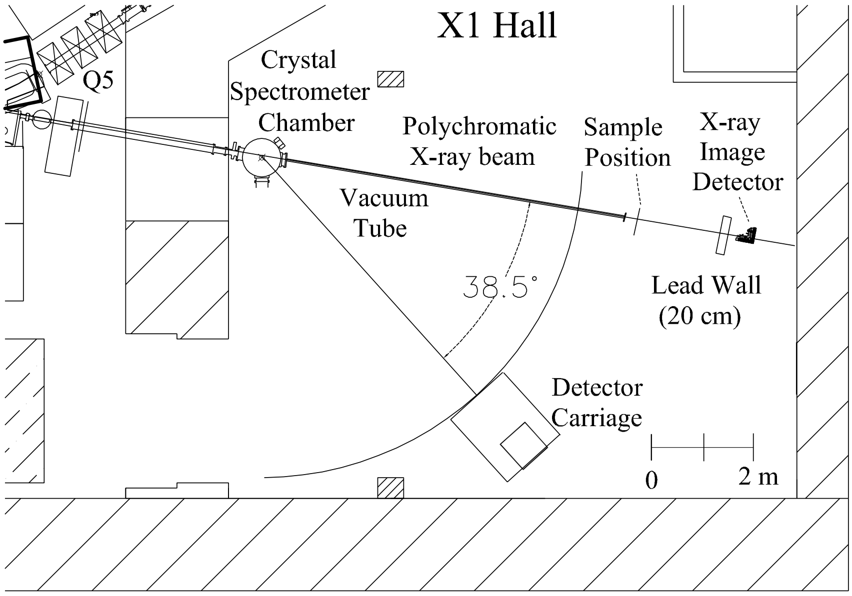

Figure C.2: Layout of the experimental area in the X1 hall to test the X-ray imaging detector with luminescent screen with polychromatic X-rays in the forward direction and with monochromatic X-rays (6 keV) under 38.5°. For the latter the imaging system is mounted on the detector carriage which allows the selection of the Bragg angle and consequently the X-ray energy.

C.2.2 On-line measurements with polychromatic X-rays

First on-line experiments with X-rays were performed with a polychromatic X-ray beam in forward geometry, using the 6 keV foil stack at an electron beam energy of 600 MeV, with the emission spectrum as shown in Fig. 3.6. The geometrical arrangement is shown in Fig. C.2. To avoid absorption losses of the low energy X-rays in air, an additional aluminum vacuum tube of 60 mm diameter and 8 m length was mounted between crystal spectrometer chamber and X-ray detection system. The exit window was made of a 25 μm thick polyimide foil. A distance of 2 m is kept free between exit window and detection system in order to easily position the samples to be investigated.

At first, a green leaf was positioned in a distance $x_{od} = 1.8$ m from the luminescent screen. The resulting radiograph is shown in Fig. C.3. Although the edge enhancement is still visible, the resolution apparently is rather bad. In addition, the intensity seems to fluctuate strongly between adjacent pixels. To find the reason for this rather poor result, an experiment to determine the spatial resolution has been performed next.

Fig. C.4 depicts a measurement of the spatial resolution of the imaging system using the so called edge spread function (ESF) technique. Part of the luminescent screen was covered with an iron slit of 30 mm width and 400 μm thickness and complex refraction index parameters $\delta = 3.958 \cdot 10^{-5}$ and $\beta = 1.0538 \cdot 10^{-6}$. The thickness is large enough

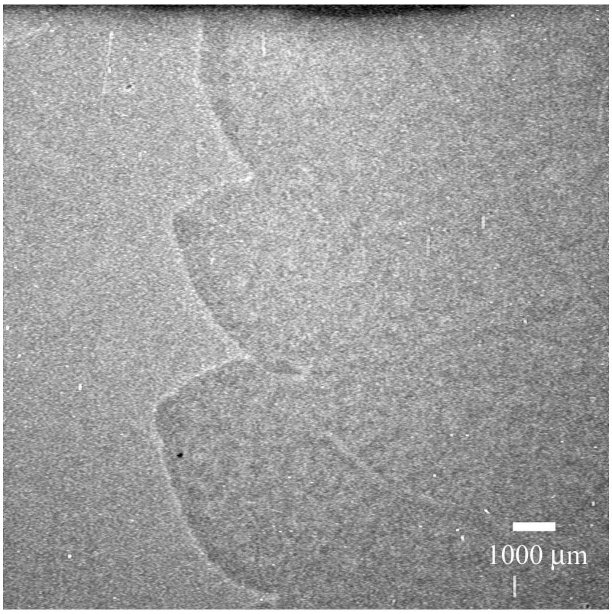

Figure C.3: A green leaf radiograph as recorded with the imaging system shown in Fig. C.1. The CCD camera was cooled down to -40 °C. Object-to-detector distance $x_{od} = 1.8$ m, source-to-object distance $x_{so} = 14.01$ m, geometrical magnification 1.13 times, optical magnification 3.5 times, electron beam energy 600 MeV, 6 keV foil stack, electron beam current 100 nA, exposure time 125 s.

to absorb X-rays with an energy of 6 keV completely $(1 - \exp[-(2\pi\beta R)/\lambda] = 1)$. A small distance between slit and luminescent screen of 25 mm was chosen. At a distance of 15.9 m between source and detector a possible deterioration of the resolution due to the X-ray source size, which is in the μm range, can completely be neglected. With a magnification of the optics of 3.5 times the effective pixel size is 3.8 μm^2.

Fig. C.4 (b) shows, the edge spread function obtained with a 4 μm thick of Gd_2O_2S:Tb luminescent screen. The intensity profile was averaged over 100 neighboring rows to improve the statistics. The data have been fitted with the function

$$f(y) = c_1 + \frac{c_2}{2} \cdot \left(1 + \operatorname{erf}(\frac{y_0 - y}{\sigma\sqrt{2}})\right) \quad . \tag{C.1}$$

Here the constant c_1 corresponds to the background level in the non-illuminated domain, and c_2 to the difference of the intensities far from the edge in the illuminated and non-illuminated domain. The spatial resolution of the system is the standard deviation σ in the argument of the error function. The best fit procedure results to $\sigma = (19.5 \pm 0.5)$ μm or 45.8 μm (FWHM) which is unexpectedly large in comparison to the estimation of the contributions from the effective pixel size of 3.8 μm^2 and 4 μm^2 from the luminescent screen of 4 μm thickness.

To further explore the reason for this result, in Fig. C.5 (a) the horizontal intensity profile of just one horizontal row of the radiograph Fig. C.4 (a) is shown. Strong intensity fluctuations are seen on top of the smooth intensity levels in the illuminated and

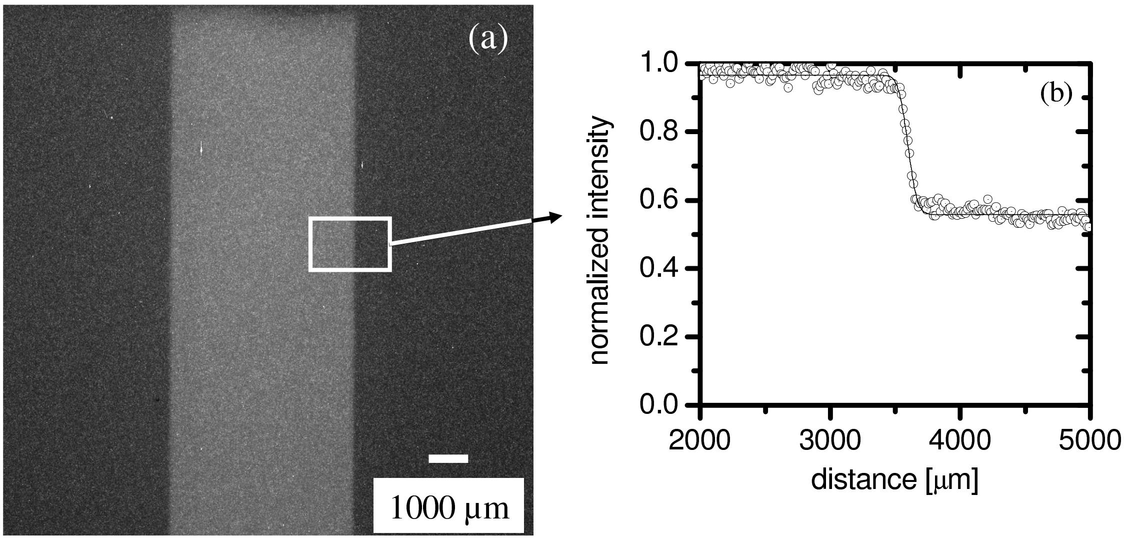

Figure C.4: Measurement of the spatial resolution of the X-ray imaging system with a 4 μm thick Gd_2O_2S:Tb luminescent screen at a magnification of the optics of 3.5 times. An iron slit of 1.4 mm width was positioned in a distance of 25 mm from the luminescent screen . (a) Radiograph as taken with the cooled CCD camera (-40 °C) at an electron beam current of 100 nA, an exposure time $t_{exp} = 30$ s, X-ray spot size of $\sigma_h = 2.49$ μm and $\sigma_v = 3.8$ μm. (b) Edge spread function (ESF) derived from the right edge of the slit by averaging over 100 neighboring horizontal rows of the CCD detector. The points are experimental results, the solid lines show the best fit with the function Eq. (C.1). The standard deviation of the resolution is $\sigma = (19.5 \pm 0.5)$ μm.

non-illuminated domains. It is just this noise which is suspected of having deteriorated the spatial resolution of the system. Such large intensity fluctuations do not result from the dark current or the read out noise of the CCD camera. [1] The electronic offset of the ADC is (544±15) counts which is much smaller than the offset of about 6000 in the non-illuminated domain of the CCD camera. Therefore, it must be concluded that the excess noise is produced by an external source.

It is highly probable that such a noise source has its origin in the high energy bremsstrahlung background with which the transition radiation X-ray beam is contaminated. If the bremsstrahlung photons hit matter, as the 8 m long additional aluminum vacuum tube or materials of the X-ray detector system, electromagnetic showers will be generated. To further localize the background source, the aluminum tube was removed, however, the background decreased only by a few per cent. Thereafter, the entrance opening in the lead shielding of the X-ray detector system was closed with an addi-

---

[1] The CCD camera was cooled down to -40 °C. The dark current at this temperature is 0.1 eles/pixel/s, i.e. at an exposure time $t_{exp} = 30$ s the noise is 3 eles/pixel. The read out time was 1.02 seconds per frame, which corresponds to an additional read out noise of 6.8 eles/pixel (rms). The total number of 9.8 eles/pixel corresponds at a pulse hight sensitivity of 0.36 counts/eles to 3.5 ADC channels which are here called counts.

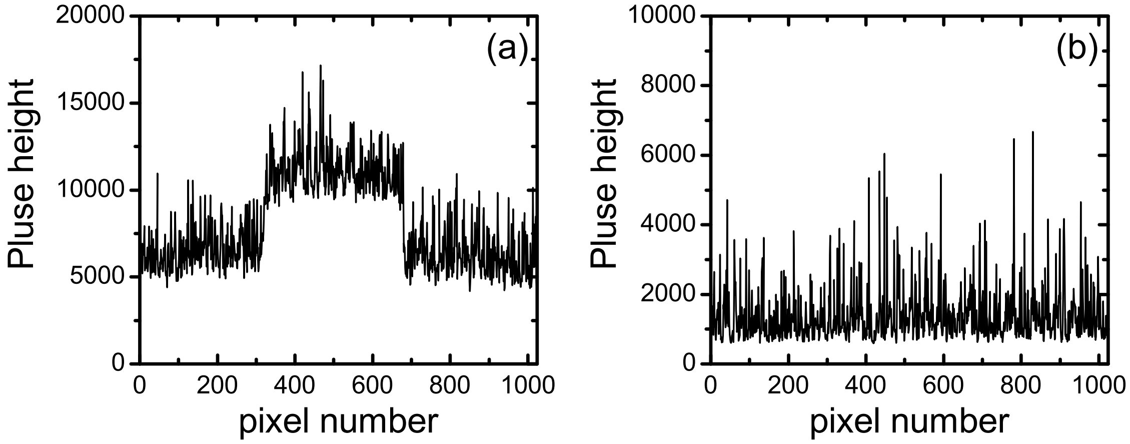

Figure C.5: Horizontal intensity profiles along just one single row of the CCD camera, (a) of the marked row of the radiograph Fig. C.4 (a), and (b) of one row with the entrance hole of the X-ray detector system blocked with an additional 10 cm thick lead shielding. The CCD camera was cooled down to -40 °C in both cases, electron beam current 200 nA, exposure time $t_{exp} = 30$ s.

tional 10 cm thick lead wall which corresponds to 17.86 radiation lengths [Tsa74]. The effect of this shielding is shown in Fig. C.5 (b). The background level decreased in comparison to the open detector system by about a factor of 12, but the pulse heights of the spikes remain about the same. These features will be discussed in the following.

It seems to be reasonable to assume that the electromagnetic showers are produced in the material of the X-ray detector system in front of and in the lens system itself. Electrons and positrons may produce visible Cerenkov radiation in the glass body of the lens which could be detected by the CCD camera chip. Also optical transition radiation, produced by the shower electrons or positrons at the boundaries of the single lenses of the lens system as well as the flat 45° mirror, might contribute. This light could contribute to the increase of the background level in the open X-ray detection system in comparison to the shielded one.

It remains to explain the large fluctuation or spikes on top of the continuous background level. It seems reasonable to assume that these are produced by electrons and positrons of the shower which are scattered into the CCD chip and penetrate the 10 μm thick depletion layer. At an ionization energy loss of 1.8 keV/(mg/cm^2) the deposited energy is 4.2 keV which creates 1150 electron-hole pairs in a pixel, assuming a mean energy of 3.65 eV for the generation of one electron-hole pair in silicon. With the pulse height sensitivity of 0.36 counts/eles one obtains a total pulse height of 414 counts per electron passing a pixel. The larger signals can be explained under the assumption that several electrons pass a single pixel during the exposure time. Since such double or multiple events remain small numbers their statistical fluctuations are large.

C.2.3 On-line measurements with monochromatic X-rays

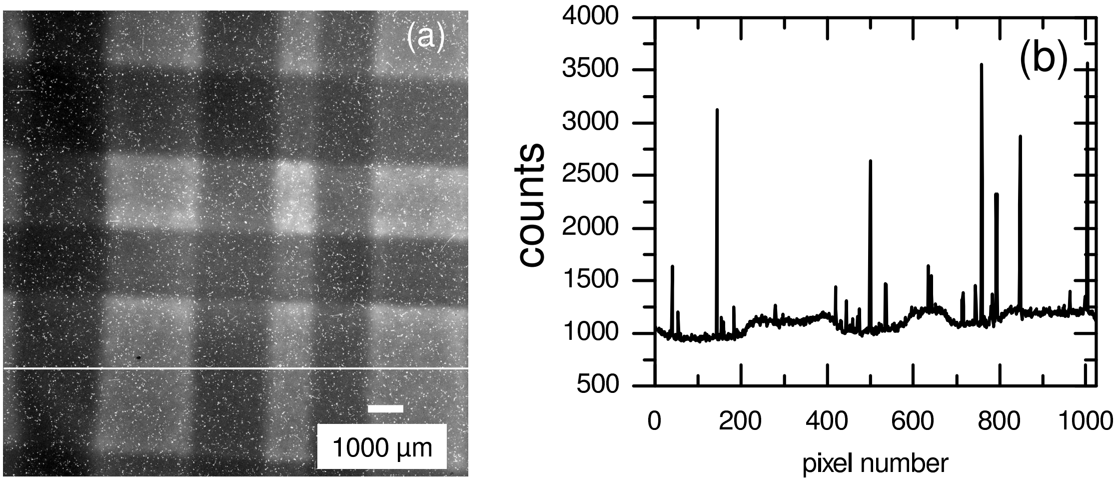

Figure C.6: (a) Radiograph of different polymer strings imaged with monochromatic X-rays of 6 keV energy. (b) Intensity profile along the white line in the radiograph (a). For the overall geometrical arrangement see Fig. C.2. The X-ray source size was $\sigma_h = (19.1 \pm 0.7)$ μm and $\sigma_v = (0.50 \pm 0.05)$ μm, the source-to-object distance $x_{so} = 4.3$ m, the object-to-detector distance $x_{od} = 9.3$ m corresponding to a geometrical magnification of 3.17 times. The magnification of the imaging system was 1.8 times. The electron beam current was 1 μA and the exposure time 300 s. The white points observed on the radiograph result from interactions of electrons and positrons in the CCD, created in electromagnetic showers from high energy bremsstrahlung photons in the experimental area.

Since the bremsstrahlung is concentrated in forward direction at an opening angle in the order of $1/\gamma = 0.85$ mrad (for 600 MeV electrons) with respect to the electron beam direction, an observation at much larger angles may be favorable. Large observation angles must be chosen, anyway, for experiments with monochromatic X-rays. For a photon energy of 6 keV the Bragg angle for the (111) plane of a silicon single crystal monochromator amounts to 19.25° and the X-ray beam is deflected by angle 38.5°, see Fig. C.2. The disadvantage of this geometry is the low X-ray photons flux. Therefore, electron beam current and exposure time must be increased to compensate for the decrease of the X-ray flux.

Fig. C.6 shows a radiograph taken with monochromatic X-rays of different polymer strings. On the radiograph white points can be recognized which resulted from background in the experimental hall which is strongly dependent on the electron beam current and the thickness of the foil stack The CCD detector was not shielded with lead . Comparing Fig. C.6 and Fig. C.5, it can be concluded that the offset level in case of monochromatic X-rays is smaller by about a factor of 6 than the offset level in case of the polychromatic X-rays although the exposure time and the electron beam current in case of monochromatic X-rays was 10 times larger than for polychromatic X-rays.

The very big spikes can obviously not be explained by ionization losses of electrons and positrons.

The effective pixel size of the CCD detector at the magnification of the optical microscope of 1.8 corresponds to 7.22 μm^2. However, the spatial resolution of the system is obviously rather bad. The reason was found in an experimental mistake. The lens was mounted in wrong direction with respect to the nominal light pass in which it is not corrected for abberations.

C.3 Conclusions

The experiments described in this section have shown that the X-ray imaging system with a Gd_2O_2S:Tb luminescence screen and a CCD camera chip as light sensor is not well suited as a high spatial resolution detection system in the transition radiation X-ray beam of MAMI. The reason is the high energy bremsstrahlung background which is emitted simultaneously with the X-rays in the transition radiation foil stack. Since the bremsstrahlung production cross section scales with Z^2 this background could be diminished by employing foils with lower atomic numbers Z as, e.g., beryllium or lithium. In addition, a sophisticated shielding of the CCD chip may help as well to suppress the background. However, we refrained from an optimization of this type of detector system since it would require a great deal of developments and tests.

D Derivation of Eq. (5.11)

Consider the geometry of Fig. 5.27 which shows the connection between the streak on the silicon crystal and the observed fluctuations on the detector plane. The angle between the incident ray and crystal's surface, α, is calculated as

$$\alpha = \frac{\pi}{2} - 2\theta_B + \theta_B \quad , \tag{D.1}$$

$$\alpha = \frac{\pi}{2} - \theta_B \quad . \tag{D.2}$$

Now α could be written as a function of Bragg's angle

$$\cos\alpha = \cos(\frac{\pi}{2} - \theta_B) = \sin\theta_B \quad . \tag{D.3}$$

$$\cos\alpha = \frac{\xi}{y_c} \quad . \tag{D.4}$$

The geometry of the Fig. 5.27 leads to

$$\frac{y_d}{x_{sc} + x_{cd}} = \frac{\xi}{x_{sc}} \quad . \tag{D.5}$$

By substitution from Eq. (D.4) in Eq. (D.5), we get,

$$\frac{y_d}{x_{sc} + x_{cd}} = \frac{y_c \sin\theta_B}{x_{sc}} \quad . \tag{D.6}$$

Finally the streak's separations on the crystal plane is expressed as,

$$y_c = \frac{x_{sc}}{x_{sc} + x_{cd}} \cdot \frac{y_d}{\sin\theta_B} \quad , \tag{D.7}$$

which is equivalent to the Eq. (5.11).

Bibliography

[Aga91] B. K. Agarwal, *X-Ray Spectroscopy*, second edition, Berlin, Springer, 1991.

[Agf90] Agfa-Gevaert N. V., *Industrielle Radiografie*, B-2510 Mortsil-Belgien (1990).

[Akh98] A. I. Akhieser, N. F. Shul'ga, *Coherent Effects in Scattering and Radiation of High-Energy Particles in Crystals*, Physics Reviews **19** (1998) 1.

[And96] D. A. Maidment and M. Yaffe, *Analysis of signal propagation in optically coupled detectors for digital mammography: II. Lens and fiber optics*, Phys. Med. Biol. **41** (1996) 475.

[AndXX] http://www.andor-tech.com/germany/products/oem.cfm

[APSXX] http://www.appscintech.com/home/index.html

[Arf98] F. Arfelli, M. Assante, V. Bonvicini, A. Bravin, G. Cantatore, E. Castelli, L. Dalla Palmaz, M. Di Michiel, R. Longox, A. Olivox, S. Panix, D. Pontoni, P. Poropat, M Prestx, A Rashevskyx, G Trombay, A. Vacchix, E. Vallazza and F. Zanconati, *Low-dose phase contrast x-ray medical imaging*, Phys. Med. Biol. **43** (1998) 2845.

[Ari94] V. Aristov and A. Erko, *X-ray microscopy IV*, Bogorodskii Pechatnik, Chernogolovka 1994.

[Bac94] H. Backe, S. Gampert, A. Grendel, H. J. Hartmann, W. Lauth, Ch. Weinheimer, R. Zahn, F. R. Buskirk, H. Euteneuer, K. H. Kaiser, G. Stephan, Th. Walcher, *Resonant transition radiation in the X-ray region from a low emittance 855 MeV electron beam*, Z. Phys. **A 349** (1994) 87.

[Bac96] H. Backe, K. H. Brenzinger, F. Buskirk, S. Dambach, Th. Doerk, N. Eftekhari, H. Euteneuer, F. Görgen, C. Herberg, F. Hagenbuck, K. Johann, K. H. Kaiser, O. Kettig, G. Knies, G. Kube, W. Lauth, B. Limburg, J. Lind, H. Schöpe, G. Stephan, Th. Walcher, Th. Tonn, and R. Zahn, *Transition Radiation in the X-Ray Region from a low Emittance 855 MeV Electron Beam* in R.L.Johnson, H. Schmidt-Böcking, B.F. Sonntag, editors, *X-Ray and Inner-Shell Processes: 17th International Conference*, AIP conference proceeding 389, AIP Press, Woodbury, New York, 1997.

[Bac98] H. Backe, private communications, Institut für Kernphysik, Universität Mainz, 1998.

[Bac01] H. Backe, private communications, Institut für Kernphysik, Universität Mainz, 2000.

[Bac02] H. Backe, private communications, Institut für Kernphysik, Universität Mainz, 2002.

[Bac05] H. Backe, private communications, Institut für Kernphysik, Universität Mainz, 2005.

[Bau86] M. W. Bautz, G. E. Berman, J. P. Doty and G. R. Ricker, *A CCD X-Ray Detector Performance Model.* SPIE Vol. 688 Multilayer Structures and Laboratory X-Ray Laser Reasearch, 1986.

[Bea74] J. H. Beaumont, M. Hart, *Multiple Bragg reflection monochromators for synchrotron x-radiation*, J. Phys. **E 7** (1974) 823.

[Ber68] G. Bertolini and A. Coche, *Semiconductor Detectors*, Wiley Interscience, New York, 1986.

[Bon65] U. Bonse and M. Hart, *An X-ray Interferometer*, Appl. Phys. Lett. **6**, (1965) 155.

[Bor75] M. Born and E. Wolf, *Principle of Optics*, 5th ed. Pergamon, Oxford, 1975.

[Boy77] W. Boyle and G. Simth, *Charge coupled semiconductor devices*, Bell System Tech. J. 49 (1970) 587.

[Bus94] F. Busch, *Auflösungsvermögen einer Mikrotomographiekamera für Röntgen-Synchrotronstrahlung*, Ph. D. dissertation, Unverysity of Dortmund, Germany, 1994.

[CanXX] http://www.canon.com.

[Car77] W. H. Carter and E. Wolf, *Coherence and radiometry with quasihomogeneous planar sources*, J. Opt. Soc. Am. **67**, (1977) 785.

[Car98] C. Raven, *Microimaging and Tomography with High Energy Coherent Synchrotron X-Rays* , Shaker Verlag, 1998.

[Cat89] A. Caticha, *Transition-diffracted radiation and the Cerenkov emission of x-rays*, Phys. Rev. **A 40** (1989) 4322.

[Cha97] D. Chapman, W. Thomlinson, R. E. Johnston, D. Washburn, E. Pisano, N. Gmür, Z. Zhong, R. Menk, F. Arfelli and D. Sayers, *Diffraction enhanced x-ray imaging*, Phys. Med. Biol. **42** (1997) 2015.

[Che74] M. L. Cherry, G. Hartmann, D. Müller, T. A. Prince *Transition radiation from relativistic electrons in periodic radiators*, Phys. Rev. **D 10** (1974) 3594.

[Chi93] Y. Chikaura and Y. Suzuki, *X-ray reconstruction topography for observation of the orientation distribution in a single crystal*, J. Appl. Cryst. **26** (1993) 219.

[Col96] P. Cloetens, R. Barrett, J. Baruchel, J. Guigay and M. Schlenker, *Phase objects in synchrotron radiation hard x-ray imaging*, J. Phys. D: Appl. Phys. **29** (1996) 133.

[Com35] A. H. Compton, S. K. Allison, *X–rays in theory and experiment*, second edition, D. van Nostrand Company Inc., Princetown, New Yersey, 1935.

[CxrXX] http://www.cxro.lbl.gov/optical_constants

[Deb88] K. Debertin and R. G. Helmer, *Gamma-and X-Ray Spectrometery with Semiconductor Detectors*, North-Holland, 1988.

[Dia74] J. C. Dainty and R. Shaw, *Image Science*, Academic Press, London, 1974.

[ElvXX] http://www.shop.elv.de.

[Fab75] C. W. Fabjan, W. Struczinkski, *Coherent emission of transition radiation in periodic radiators*, Phys. Lett. **B 57** (1975) 483.

[FilXX] http://www.filmscanner.infoNikonSuperCoolscan4000ED.html.

[Fra45] I. M. Frank and V. L. Ginzburg, *Radiation of a uniform moving electron due to its transition from one medium into another*, J. Phys. USSR **9** (1945) 107.

[Hab05] D. Habs, M. Schrammet, et al., private communication, LMU München , 2005.

[Hag95] F. Hagenbuck, *Entwurf eines Strahlführungssystems und strahloptische Messungen am Elektronenstrahl des Mainzer Mikrotrons*, Diplomarbeit, Institut für Kernphysik, Universität Mainz, 1995.

[Hag01] F. Hagenbuck, *Entwicklun eines neuartigen bildgebenden Verfarens zur digitalen Subtraktionsradiographie mit Übergangsstrahlung am Mainzer Mikrotron MAMI*, Dissertation, Institut für Kernphysik, Universität Mainz, 2001.

[Har71] M. Hart, *Bragg reflection x ray optics*, Rep. Prog. Phys., **34** (1971) 435.

[Har96] P. Hariharan, *Optical Holography, Principles, techniques, and application*, Second Edition, Cambridge University Press, (1996).

[Hec89] E. Hecht, *Optik*, zweite Auflage, Addison–Wesley, Bonn, Paris, Reading, Massachusetts, 1987.

[Hen86] B. L. Henke, J. Y. Uejio, G. F. Stone, C. H. Dittmore, F. G. Fujiwara, *High-energy x-ray response of photographic films: models and measurement*, J. Opt. Soc. Am. B. **11** (1986) 1540.

[Hen93] B. L. Henke, E. M. Gullikso, J. C. Davis, *X-ray interactions: photoabsorption, scattering, transimission and reflection at E=50-30000 eV, Z=1-93*, Data and Nucl. Data Tabl. 54 (1993) 181.

[Hu01] Z. W. Hu, B. Lai, Y. S. Chu, Z. Cai, D. C. Mancini, B. R. Thomas, and A. A. Chernov, *Phase Sensitive X-Ray Diffraction Imaging of Defects in Biological Macromolecular Crystals*, Phys. Rev. Lett. **87** (2001) 148101.

[Hwu99] Y. Hwu, H. H. Hsieh, M. J. Lu, W. L. Tsai, H. M. Lin, W. C. Goh, B. Lai, J. H. Je, C. K. Kim, D. Y. Noh, H. S. Youn, G. Tromba and G. Margaritondo, *Coherence-enhanced synchrotron radiology: Refraction versus diffraction mechanisms*, J. App. Phys. **86 (8)** (1999) 4613.

[Gab49] D. Gabor, *A new microscopic principle*, Nature **161** (1948) 777.

[Geo58] Georg Joos, Erwin Schopper, *Grundriss der Photographie und ihrer Anwendungen besonders in der Atomphysik*, Akademische Verlagsgesellschaft M. B. H. Frankfurt am Main 1958.

[Ger72] R. W. Gerchberg and W. O. Saxton, *A Practical Algorithm for the Determination of phase from Image and Diffraction Plane Pictures*, Optik **35** (1972) 237.

[Gia89] G. E. Giakoumakis, C. D. Nomicos and P. X. Sandilos, *Absolute efficiency of* $Gd_2O_2S : Tb$ *screens under fluoroscopic conditions*, Phys. Med. Biol., **34 (6)** (1989) 673.

[GooXX] http://www.goodfellow.com/csp/active/gfHome.csp.

[Grz99] Grzegorz Kowalski, Moreton Moore and Stuart Nailer, *Application of x-ray phase-contrast imaging to polycrystalline CVD diamond*, J. Phys. D: Appl. Phys. **32** (1999) A166.

[Gur96] T. E. Gureyev, K. A. Nugent, *Phase retrieval with the transport-of-intensity equation. II. Orthogonal series solution for nonuniform illumination* , J. Opt. Soc. Am. A, (1996) 1670.

[Ing95] V. N. lngal and E. A. Beliaevskaya, *X-ray plane-wave topography observation of the phase contrast from a non-crystalline object* , J. Phys. D Appl. Phys. **28** (1995) 2314.

[Jac83] J. D. Jackson, *Klassische Elektrodynamik*, zweite Auflage, Walter de Gruyter, Berlin, New York, 1983.

[Jam65] R. W. James, *The optical Principles of the Diffraction of X-rays.* Cornell University Press, 1965.

[Jar05] A. Jarre, C. Fuhse, C. Ollinger, J. Seeger, R. Tucoulouand T. Salditt, *Two-Dimensional Hard X-Ray Beam Compression by Combined Focusing and Waveguide Optics*, Phys. Rev. Lett. **94**, (2005) 074801.

[Joh95] K. Johann, *Aufbau eines Monochromators für 33 keV Röntgenstrahlung am 855 MeV Elektronenbeschleuniger MAMI*, Diplomarbeit, Institut für Kernphysik, Universität Mainz, 1995.

[Kan97] I. Kandarakis, D. Cavouras, G. S. Panayiotakis, D. Triantis and C. D. Nomicos, *An Experimental method for determination of spatial-frequncey-dependent detective quantum efficiency (DQE) of scintillators used in X-ray imaging detectors*, Nucl. Inst. and Meth. in Phys. Res. A, **399** (1997) 335.

[Ket00] O. Kettig, *Entwicklung und Test eines Röntgeninterferometers auf der Basis von Übergangsstrahlung*, Dissertation, Institut für Kernphysik, Universität Mainz, 2000.

[Koc98] A. Koch, C. Raven, P. Spanne and A. Snigirev *X-ray imaging with submicrometer resolution employing transparent luminescent screens*, J. Opt. Soc. Am. **15(7)** (1998) 1940.

[Koh97] V. Kohn, *The method of phase retrieval of complex wavefield from two intensity measurements applicable to hard X-ray*, Physica Scripta, **56**, (1997)14.

[Koh00] V. Kohn, I. Snigireva and A. Snigirev, *Direct Measurement of Transverse Coherence Length of Hard X Rays from Interference Fringes*, Phys. Rev. Lett. **85** (2000) 2745.

[Koh01] V. Kohn, I. Snigireva, and A. Snigirev, *Interferometric characterization of spatial coherence of high energy synchrotron X-rays*, Optics Communications **198** (2001) 293.

[Kot99] C. J. Kotre and I. P. Birch, *Phase contrast enhancement of x-ray mammography: a design study*, Phys. Med. Biol. **44** (1999) 2853.

[KPHXX] http://www.kph.uni-mainz.de/information/introduction/prospekt.pdf.

[Kph89] Institut für Kernphysik, *Jahresbericht 1988-1989*, Universität Mainz, 1989.

[Kph93] Institut für Kernphysik, *Jahresbericht 1992-1993*, Universität Mainz, 1993.

[Kre03] H. J. Kreuzer and R. A. Pawlitzek, *Digital in-line holography*, Europhysics News **34(2)** (2003).

[Kun01] C. Kunz, *Synchrotron radiation: third generation sources*, J. Phys.: Condens. Matter **13** 7499 (2001).

[Kuz99] S. Kuznetsov, I. Snigireva, A. Souvorov and A. Snigirev, *New Features of X-Ray Bragg Diffraction Topography with Coherent Illumination*, phys. stat. sol. (a) **172** (1999) 3.

[Len94] B. Lengeler, *Experimental determination of the dispersion correction f´(E) to the atomic scattering factor*, in G. Materlik, C.J. Sparks, K. Fischer, editors, *Resonant anomalous x–ray scattering*, Elsevier Science B.V., Amsterdam, 1994.

[Lew04] R. A. Lewis, *Medical phase contrast x-ray imaging: current status and future prospects*, Phys. Med. Biol. **49** (2004) 3573.

[Lin97] J. Lind, *Aufbau eines Monochromators für Röntgenstrahlung mit gebogenem Silizium–Einkristall*, Diplomarbeit, Institut für Kernphysik, Universität Mainz, 1997.

[LinXX] http://www.linos-katalog.de.

[Lui05] Chenglin Liu, Yuan Zhang, Xinyi Zhang, Wentao Yang, Weijun Peng, Daren Shi, Peiping Zhu, Yulian Tian, Wanxia Huang, *X-ray diffraction-enhanced imaging of uterine leiomyomas*, Med Sci Monit, **11**(2005) 33.

[Mah95] A. Mahendrasingam, C. Martin, W. Fuller, D. J. Blundell, D. Mackerron, R. J. Rule, R. J. Oldman, J. Liggat, C. Riekel and P. Engström, *Microfocus X-ray Diffraction of Spherulites of Poly-3-hydroxybutyrate*, J. Synchrotron rad. **2** (1995) 308.

[May02] S. C. Mayo, P. R. Miller, S. W. Wilkins, T. J. Davis, D. Gao, T. E. Gureyev, D. Paganin, D. J. Parry, A. Pogany and A. W. Stevenson, *Quantitative X-ray projection microscopy: phase-contrast and multi-spectral imaging*, J. Microscopy 207:2 (2002) 79.

[May03] S. C. Mayo, T. J. Davis, T. E. Gureyev, P. R. Miller, D. Paganin, A. Pogany, A. W. Stevenson, S. W. Wilkins, *X-ray phase-contrast microscopy and microtomography*, Opt.Exp. **11** (2003) 2289.

[Mcn92] I. McNulty, J. Kirz, C. Jacobsen, E. H. Anderson, M. R. Howells and D. P. Kern, *High-Resolution Imaging by Fourier Transform X-ray hologray*, Science, **256** (1992) 1009.

[Mic93] A. G. Michette, *X–rays and their properties*, in A. G. Michette, C. J. Buckley, editors, *X–ray science and technology*, Insitute of Physics Publishing, Bristol, Philadelphia, 1993.

[MirXX] http://www.data.it/support/data_sheets/e2vtech/47-10back.pdf

[Mom95] A. Momose, *Demonstration of phase-contrast x-ray computed tomography using an x-ray interferometer*, Nucl. Inst. and Meth. in Phys. Res. A **352** (1995) 622.

[Mom02] Atsushi Momose, Tohoru Takeda, Yuji Itai, *Blood Vessels: Depiction at Phase-Contrast X-ray Imaging without Contrast Agents in the Mouse and Rat—Feasibility Study*, Radiology **217** 2000) 593.

[Mon04] D. S. Montgomery, A. Nobile, and P. J. Walsh, *Characterization of National Ignitition Facility cryogenic beryllium capsules using x-ray phase contrast imaging*, Rev. Sci. Instrum. **75** (2004) 3986.

[Mor02] K. Mori, N. Sekine, H. Sato, D. Shimao, H. Shiwaku, K. Hyodo, H. Sugiyama, M. Ando, K. Ohashi, M. Koyama and Y. Nakajima, *Application of synchrotron X-ray imaging to phase objects in orthopedics*, J. Synchrotron Rad. **9** (2002) 143.

[OlyXX] http://www.olympus.pl/pliki/mikroskopy/dokumenty/LM_cameras_ENG.pdf.

[PhyXX] http://physics.nist.gov/PhysRefData/XrayMassCoef/ComTab/kodak.html

[PicXX] http://www.picotech.com/pc_oscilloscope.html.

[Pin84] Z. G. Pinsker, *Dynamical scattering of x-rays in crystals*, Springer, Heidelberg, 1984.

[ProXX] http://www.proxitronic.de/

[Pod01] S. G. Podorov1, O. Renner, O. Wehrhan and E. Förster, *Optimized polychromatic x-ray imaging with asymmetrically cut bent crystals*, J. Phys. D **34** (2001) 2363.

[Rö96] W. K. Röntgen, *On a new kind of rays*, Nature, **53** (1896) 274.

[Roy84] Roy E. Rand, *Recirculating electron accelerators* Harwood Academic Publishers, New York, 1984.

[Rul97] P. Rullhusen, X. Artru, P. Dhez, *Novel Radiation Sources Using Relativistic Electrons, from Infrared to X-Rays: From Infrared to X-Rays*, Series on Synchrotron Radiation Techniques and Applications, Vol. 4, 1997.

[Sal91] B. E. A. Saleh, M. C. Teich, *Fundamentals of photonics* , New York, (1991).

[Sch03] C. G. Schroer, M. Kuhlmann, U. T. Hunger, T. F. Günzler, O. Kurapova, S. Feste, F. Frehse, B. Lengeler, M. Drakopoulos, A. Somogyi, A. S. Simionovici, A. Snigirev, I. Snigireva, C. Schug and W. H. Schröder, *Nanofocusing parabolic refractive x-ray lenses*, Appl. Phys. Letters 82 (2003) 1485.

[SerXX] http://sergey.gmca.aps.anl.gov/

[ShvXX] I. Shvedunve, INP/MAV, Moskow, private communication, July, (2000).

[SICXX] http://www.sico.at/

[Sin95] A. Snigirev, I. Snigireva, V. Kohn, S. Kuznetsov and I. Schelokov, *On the possibilities of x-ray phase contrast microimaging by coherent high-energy synchrotron radiation*, Rev. Sci. Instrum. **66** (1995) 5486.

[Sin96] A. Snigirev, I. Snigireva, V. Kohn, S. M. Kuznetsov. *On the requirements to the instrumentation for the new generation of the synchrotron radiation sources. Beryllium windows*, Nucl. Instr. and Meth. in Phys. Res. A, **370 (2-3)** (1996) 634.

[Spa99] P. Spanne, C. Raven, I. Snigireva and A. Snigirev, *In-line holography and phase-contrast microtomography with high energy x-rays*, Phys. Med. Biol. **44** (1999) 741.

[Spy02] G. Spyrou1, G. Tzanakos, G. Nikiforides1 and G. Panayiotakis1, *A Monte Carlo simulation model of mammographic imaging with x-ray sources of finite dimensions*, Phys. Med. Biol. **47** (2002) 917.

[Ste03] A. W. Stevenson, T. E. Gureyev, D. Paganin, S. W. Wilkins, T. Weitkamp, A. Snigirev, C. Rau, I. Snigireva, H. S. Youn, I. P. Dolbnya, W. Yun, B. Lai, R. F. Garrett, D. J. Cookson, K. Hyodo and M. Ando, *Phase-contrast X-ray imaging with synchrotron radiation for materials science applications*, Nucl. Inst. and Meth. in Phys. Res. B, **199** (2003) 427.

[Sto70] E. Storm, H.I. Israel, *Photon cross sections from 1 keV to 100 MeV for elements Z=1 to Z=100*, Atom. Data and Nucl. Data Tabl. **A 7** (1970) 565.

[Suz02] Y. Suzuki, N. Ysgi, K. Uesugi, *X-ray refraction-enhanced imaging and method for phase retrieval for a simple object*, J. Synchrotron Rad. **9** (2002) 160.

[Swa73] R. K. Swank, *Calculation of modulation transfer function of x-ray fluorescent screens*, Applied Optics, **12 (8)** (1973) 1865.

[Tak98] T. Takeda, A. Momose, E. Ueno and Y. Itai, *Phase-contrast X-ray CT image of breast tumor*, J. Synchrotron Rad. **5** (1998) 1133.

[Ter72] M. L. Ter–Mikaelian, *High–energy electromagnetic processes in condensed media*, Wiley–Interscience, New York, London, Sydney, Toronto, 1972.

[Tsa74] Y. S. Tsai, *Pair production and bremsstrahlung of charged leptons*, Rev. Mod. Phys. 46, 815 (1974).

[Tsu02] H. Tsunemia, J. Hiragaa, E. Miyata, *Application of a finite size of the charge cloud shape generated by an X-ray photon inside the CCD*, Nucl. Inst. and Meth. in Phys. Res. A **477** (2002) 155.

[Tur04] L. D. Turner, B. B. Dhal, J. P. Hayes, A. P. Mancuso, K. A. Nugent, D. Paterson, R. E. Scholten, C. Q. Tran1 and A. G. Peele, *X-ray phase imaging: Demonstration of extended conditions with homogeneous objects*, OPTICS EXPRESS, **12** (2004) 2960.

[Var96] I. A. Vartanyants, J. A. Pitney, J. L. Libbert, and I. K. Robinson, *Reconstruction of surface morphology from coherent x-ray reflectivity* , Phys. Rev. **B 55** (1997) 13193.

[Wil92] K. Wille, *Physik der Teilchenbeschleuniger und Synchrotronstrahlungsquellen*, B. G. Teubner, Stuttgart 1992.

[Wil96] S. W. Wilkins, T. E. Gureyev, D. Gao, A. Pogany and A. W. Stevenson, *Phase-contrast imaging using polychoromatic hard X-rays*, Nature (London), **384** (1996) 335.

[Xiz03] Xizeng Wu and Hong Liu, *Clinical implementation of x-ray phase-contrast imaging: Theoretical foundations and design considerations*, Medical Physics **30**, (2003) 2169.

[Zah94] R. Zahn, *Messung resonanter Übergangsstrahlung im Röntgenbereich mit einem 855 MeV Elektronenstrahl geringer Emittanz*, Dissertation, Institut für Kernphysik, Universität Mainz, 1994.

List of Figures

List of Tables